Computational Electromagnetics in Microwave Remote Sensing

by

Wai Chung Au

B.A., Trinity College, Cambridge University
June 1988

M.S., Massachusetts Institute of Technology
February 1991

Submitted to the Department of Aeronautics and Astronautics
in Partial Fulfillment of the Requirements for the Degree of

DOCTOR OF PHILOSOPHY

at the

MASSACHUSETTS INSTITUTE OF TECHNOLOGY

September 1994

© Massachusetts Institute of Technology 1994
All rights reserved

Signature of Author _____
Department of Aeronautics and Astronautics
June 6, 1994

Certified by _____
Professor Walter M. Hollister
Thesis Committee Chairman, Department of Aeronautics and Astronautics

Certified by _____
Professor Jin A. Kong
Thesis Supervisor, Department of Electrical Engineering and Computer Science

Certified by _____
Dr. Robert T. Shin
Thesis Supervisor, Lincoln Laboratory

Certified by _____
Professor Mark Drela
Department of Aeronautics and Astronautics

Accepted by _____
Professor Harold Y. Wachman
Chairman, Department Graduate Committee

MASSACHUSETTS INSTITUTE
OF TECHNOLOGY

SEP 21 1994

LIBRARIES ARCHIVES

Computational Electromagnetics in Microwave Remote Sensing

by

Wai Chung Au

Submitted to the Department of Aeronautics and Astronautics
on June 6, 1994, in partial fulfillment of the
requirements for the degree of
Doctor of Philosophy

Abstract

The use of microwaves for remote sensing has shown promising results in geophysical applications. The advantages of using microwave frequencies over optical frequencies are largely due to their abilities to penetrate clouds and vegetation canopies and to provide day-and-night coverage. Microwave remote sensing techniques can be used to monitor the atmosphere and the surfaces of the earth with a potential for applications in monitoring global climate changes. This thesis focuses on the importance of vegetation structure in electromagnetic wave scattering and applications of branching structures in simulations of vegetation canopies. Although the fractional volume of the scatterers is low in a vegetation canopy, vegetation usually exhibits locally dense properties due to clustering. Mutual interactions between components of a cluster are important and neglected in the classical independent scattering model. To characterize the medium, Maxwell's equations are solved exactly by method of moments (MoM) for a single cluster to include the collective scattering and absorption effects, and radiative transfer theory is employed to account for the incoherent interactions between clusters. The algorithms for solving large systems of equations for electromagnetic wave scattering problems are also addressed in this thesis.

A volume scattering model using scatterers with multi-scale branching structures is developed to investigate the scattering characteristics of vegetation canopies. The branching scatterer is first approximated by a thin and perfectly conducting wire structure. The MoM formulation based on the reaction integral equations is employed in the calculation. The frequency, angle, and polarization dependences of the electromagnetic scattering characteristics of the branching structure are studied. A flat frequency response is obtained and a similar trend observed in experimental data from forests suggests that the multi-scale scatterers are a good model for the vegetation canopy. In the next step, a more realistic model consisting of dielectric cylinders is developed. The volume integral equation of the electric field is derived from Maxwell's equations and solved numerically by MoM to obtain the scattering characteristics of dielectric structures. Good agreement between the model and the experimental data is obtained at X-band frequency.

The absorption and scattering of a single cluster calculated using the numerical method can be several times larger than those calculated using the classical independent scattering model. The MoM formulation provides a means to accurately calculate scattering functions of branching vegetation clusters. With the scattering functions as elements of the phase matrix and the extinction matrix, radiative transfer theory is applied to calculate the backscattering coefficients for a two-layer structure with planar interfaces. The radiative transfer equations are solved by an iterative method to the first order. It is shown that the coherent scattering model, which accounts for the coherent scattering effect while neglecting the multiple scattering effect on the induced currents on the cylinder, provides a good estimate for co-polarized returns. For cross-polarized returns, both the independent and coherent scattering models are shown to be less accurate. Cross-polarized returns are strongly influenced by interactions between the components of the cluster and the approximate methods do not account for this effect.

The radiative transfer equations for passive remote sensing are solved numerically by the discrete eigenanalysis method, which accounts for the multiple scattering effects. The brightness temperatures of the random medium containing discrete vegetation clusters overlying the planar bottom surfaces are calculated. Numerical results show that the coherent scattering model gives a better estimate of the brightness temperatures than the independent scattering model for half-space cases. Both the independent and coherent scattering models underestimate the optical depth of the random medium layer.

Three-dimensional electromagnetic wave scattering problems involve systems of linear equations with a large number of unknowns. Two iterative methods are developed and implemented on a parallel virtual machine (PVM). Both methods are variants of the conjugate gradient method; one is good for solving block tridiagonal systems while the other works for general complex matrix problems. PVM is a macro library code that runs on a UNIX network. The use of PVM provides access to increased CPU power as well as memory, making it possible to solve problems which normally cannot be solve on a single machine. Numerical experiments are performed and a high efficiency in the parallelization of the block tridiagonal solver is achieved.

Thesis Supervisor: Jin A. Kong
Title: Professor of Electrical Engineering

Thesis Supervisor: Robert T. Shin
Title: Assistant Group Leader, Lincoln Laboratory

Acknowledgments

First of all, I would like to express my sincerest thanks to my thesis supervisor, Professor Jin A. Kong. His encouragement, support and guidance throughout my work are deeply appreciated.

Many thanks to Dr. Robert Shin for helping me with research problems and in improving my technical writing and presentation. To Professor Walter Hollister for serving as my thesis committee chairman; I enjoyed the satellite engineering course very much. To Professor Mark Drela for his support throughout my six years at MIT.

To Dr. Gerald Minerbo for his enlightening and stimulating discussions during the summers I worked at Schlumberger-Doll Research. To Dr. Tarek Habashy for the support when I worked at Schlumberger. Thank you both for coming up to MIT and serving as my external readers.

To Professor Leung Tsang for his ideas and insight, without which this thesis work will not be as complete.

To Dr. Michael Prange for his advice and suggestions in developing PVM programs and to the computer staff at Schlumberger for their help.

It is a privilege to work in the Electromagnetic Wave Theory Group. Thanks to all members of the group for making this environment so enjoyable. To Dr. Eric Yang for discussions on computer information and for serving as my General Examination committee member. To Chih-Chien Hsu for verifying my results with his RT program, to Joel Johnson for proof reading my thesis. To Dr. Lars Bomholt for bringing more funs to our group. Thanks also to Dr. Kung-Hau Ding, Dr. Jean-Claude Souyris, Dr. John Oates, Dr. Ali Tassoudji, Dr. Murat Veysoglu, Kevin Li, Li-Fang Wang, Hong-Tat Ewe, Ante Salcedo, Sean Shih, Yan Zhang. Many thanks to the group's secretary Kit Wah Lai for all her help.

To former group members: Dr. David Arnold, Dr. Bob Atkins, Phillipe Berisset, Pierre Coutu, Professor Hsiu-Chi Han, Greg Hwang, Dr. Cheung-Wei Lam, Dr. Laurence Lee, Harold Lim, Alex Mou, Dr. Son Nghiem, Dr. David Sheen, Tony Triolo, Dr. Jake Xia, Dr. Yi Yuan, Dr. Simon Yueh.

To my friends in Boston, especially my housemates Ka-Shun Wong and Alex Fung. To brothers and sisters in Allston Church and to Dr. Norman Lee and his family.

I am deeply indebted to my parents, my sister Virginia, my brothers Wilfred and Wai-Ling for their love and support throughout my life.

This work was supported by NASA contracts 958461 and NAGW-1617, and Office of Naval Research grant N00014-92-J-1616. Schlumberger-Doll Research provided the computer facilities for the PVM research.

To my parents

Contents

Abstract 3

Acknowledgments 5

Dedication 7

Table of Contents 9

List of Figures 13

List of Tables 21

1 Introduction 23

1.1 Introduction 23

1.2 Description of the Thesis 27

2 Electromagnetic Waves Scattering for a Multi-Scale Branching Structure: Conducting Case 29

2.1 Introduction 29

2.2 Formulation 30

2.2.1 Reaction Integral Equation 30

2.2.2 Thin Wire Approximation 31

2.3 Method of Solution 32

2.4 Multi-Scale Branching Structure 34

2.5 Results and Summary 35

3 Method of Moments Approach for a Thin Dielectric Cylinder Structure **47**

3.1 Introduction 47

3.2 Formulation 48

3.3 Method of Solution 50

3.3.1 Point Matching Method 50

3.3.2 Numerical Evaluation of Matrix Elements 51

3.3.3 Thin Cylinder Considerations 54

3.4 Results and Discussion 55

3.5 Summary 59

4 Radiative Transfer Theory for Active Remote Sensing: Discrete Scatterer Model **75**

4.1 Introduction 75

4.2 Vector Radiative Transfer Equation for Active Remote Sensing 77

4.3 Phase Matrix and Extinction Matrix 78

4.4 Iterative Solution for Vector Radiative Transfer Equation 80

4.4.1 Zeroth Order Solution 81

4.4.2 First Order Solution 84

4.5 Theoretical Results and Discussion 86

4.6 Summary 89

5 Absorption Enhancement and Radiative Transfer Theory for Passive Remote Sensing **103**

5.1 Introduction 103

5.2 Vector Radiative Transfer Equation 105

5.3 Method of Solution 106

5.4 Absorption Enhancement 112

5.5 Brightness Temperature Calculation 114

5.6 Summary 117

6 Iterative Solvers for Large Linear Systems of Equations in Parallel Virtual Machine **147**

6.1 Introduction 147

6.2 Iterative Solver for Block Tridiagonal Systems of Equations 149

6.2.1 Method of Solution 150

6.2.2 Implementation 153

6.3 Iterative Solver for Unsymmetric Linear Systems of Equations 155

6.3.1 Method of Solution 156

6.3.2 Implementation 157

6.4 Numerical Experiments 157

6.5 Summary 160

7 Summary **167**

A Notations **171**

B Mutual Impedance of Sinusoidal Monopoles **177**

B.1 Nonplanar-Skew Case 177

B.2 Parallel Monopole Mutual Impedance 179

References **181**

Biographical Note **191**

List of Figures

2-1 Decomposition of a scattering problem into incident and scattered fields. 38

2-2 Piecewise sinusoidal basis function as a function of l. 39

2-3 A segment for the test source. 39

2-4 Basic building block of the scatterer (first stage scatterer). 40

2-5 Second stage scatterer. 40

2-6 Third stage scatterer. 41

2-7 Backscattering cross sections as a function of incidence angle θ, with $\phi = 45^o$ – vertical polarization. 42

2-8 Backscattering cross sections as a function of incidence angle θ, with $\phi = 45^o$ – horizontal polarization. 43

2-9 Average backscattering cross sections for different stage scatterers – vertical polarization. 44

2-10 Average backscattering cross sections for different stage scatterers – horizontal polarization. 45

3-1 Scattering problem for an inhomogeneous material body. 61

3-2 Backscattering cross sections as a function of incidence angle of a cylinder of length $l = 10$ cm, radius $r = 0.5$ cm, and $\epsilon = (3 + i0.5)\epsilon_o$ at 3 GHz with subcells of different aspect ratio ($= 2r/\Delta l$) using dipole approximation. Aspect ratio = 0.5,1.0,1.5,2.0 for horizontal polarization. 62

3-3 Backscattering cross sections as a function of incidence angle of a cylinder of length $l = 10$ cm, radius $r = 0.5$ cm, and $\epsilon = (3 + i0.5)\epsilon_o$ at 3 GHz with subcells of different aspect ratio ($= 2r/\Delta l$) using dipole approximation. Aspect ratio = 0.5,1.0,1.5,2.0 for vertical polarization. 63

3-4 Backscattering cross sections as a function of incidence angle of a cylinder of length $l = 10$ cm, radius $r = 0.5$ cm, and $\epsilon = (3 + i0.5)\epsilon_o$ at 3 GHz with subcells of different aspect ratio ($= 2r/\Delta l$) using numerical integration to evaluate matrix elements. Aspect ratio = 0.5,1.0,1.5,2.0 for horizontal polarization. 64

3-5 Backscattering cross sections as a function of incidence angle of a cylinder of length $l = 10$ cm, radius $r = 0.5$ cm, and $\epsilon = (3 + i0.5)\epsilon_o$ at 3 GHz with subcells of different aspect ratio ($= 2r/\Delta l$) using numerical integration to evaluate matrix elements. Aspect ratio = 0.5,1.0,1.5,2.0 for vertical polarization. 65

3-6 Comparison of backscattering cross sections as a function of incidence angle as computed by THINC and body of revolution code using surface integral approach. Cylinder length $l = 10$ cm, radius $r = 0.5$ cm, and $\epsilon = (3 + i0.5)\epsilon_o$ at 3 GHz for horizontal polarization. 66

3-7 Comparison of backscattering cross sections as a function of incidence angle as computed by THINC and body of revolution code using surface integral approach. Cylinder length $l = 10$ cm, radius $r = 0.5$ cm, and $\epsilon = (3 + i0.5)\epsilon_o$ at 3 GHz for vertical polarization. 67

3-8 Absorption, extinction and total scattering cross sections as a function of incidence angle for a cylinder of length $l = 10$ cm, radius $r = 0.5$ cm and $\epsilon = (3 + i0.5)\epsilon_o$ at 3 GHz for horizontal polarization. 68

3-9 Absorption, extinction and total scattering cross sections as a function of incidence angle for a cylinder of length $l = 10$ cm, radius $r = 0.5$ cm and $\epsilon = (3 + i0.5)\epsilon_o$ at 3 GHz for vertical polarization. 69

3-10 Experiment setup for microwave coherent propagation in cylindrically shaped forest components. 70

3-11 Comparison of theoretical extinction cross section of bare twigs and experimental data as a function of incidence angle θ_i for a cylinder of length 10 cm, radius 1.5 mm, at 9 GHz. ϵ is chosen to be $(11 + i4)\epsilon_o$. 71

3-12 Comparison of theoretical loss factor and measurements as a function of polarization angle ψ_i, $(\theta_i = 90^o)$ for Scots pine. 72

3-13 Comparison of theoretical loss factor and measurements as a function of polarization angle ψ_i, $(\theta_i = 90^o)$ for Norway spruce twigs. 73

3-14 Comparison of theoretical loss factor and measurements as a function of polarization angle ψ_i, $(\theta_i = 90^o)$ for Douglas fir twigs. 74

4-1 Configuration of two layer medium with planar interfaces containing discrete scatterers. 91

4-2 Four scattering mechanisms for single volume scattering in the presence of a reflective boundary. 92

4-3 Configuration of the cluster. Center cylinder: length = 10 cm, radius = 0.3 cm; branching cylinder: length = 2 cm, radius = 0.15 cm, branching angle $\beta = 45^o$; permittivity of the cluster = $(11 + i4)\epsilon_o$; frequency is 5.3 GHz; incidence angle = θ_i. 93

4-4 Absorption cross section as a function of incidence angle for vertical polarization. Number of branches is 10. Curves are normalized by $(\sigma_{ah}(90^o))_{ind}$ with the numerical value of -39.5 dBsm. Frequency is 5.3 GHz. 94

4-5 Absorption cross section as a function of incidence angle for vertical polarization. Number of branches is 10. Curves are normalized by $(\sigma_{sh}(90^o))_{ind}$ with the numerical value of -43.2 dBsm. Frequency is 5.3 GHz. 95

4-6 Backscattering coefficients for a two-layer medium — σ_{hh}, fractional volume $f = 0.5\%, \epsilon_s = (11 + i4)\epsilon_o$. Scattering layer has a thickness $d = 0.25$m and underlying half-space is flat and has a permittivity $\epsilon_{soil} = (10 + i2)\epsilon_o$. Frequency is 5.3 GHz. Number of branches for the scatterers is 10. 96

4-7 Backscattering coefficients for a two-layer medium — σ_{vv}, fractional volume $f = 0.5\%, \epsilon_s = (11 + i4)\epsilon_o$. Scattering layer has a thickness $d = 0.25$m and underlying half-space is flat and has a permittivity $\epsilon_{soil} = (10 + i2)\epsilon_o$. Frequency is 5.3 GHz. Number of branches for the scatterers is 10. 97

4-8 Backscattering coefficients for a two-layer medium — σ_{hv}, fractional volume $f = 0.5\%, \epsilon_s = (11 + i4)\epsilon_o$. Scattering layer has a thickness $d = 0.25$m and underlying half-space is flat and has a permittivity $\epsilon_{soil} = (10 + i2)\epsilon_o$. Frequency is 5.3 GHz. Number of branches for the scatterers is 10. 98

4-9 Backscattering coefficients for a two-layer medium — σ_{hv} at nadir, as a function of branching angle β. Fractional volume $f = 0.5\%, \epsilon_s = (11 + i4)\epsilon_o$. Scattering layer has a thickness $d = 0.25$m and underlying half-space is flat and has a permittivity $\epsilon_{soil} = (10 + i2)\epsilon_o$. Frequency is 5.3 GHz. Number of branches for the scatterers is 10. 99

4-10 Backscattering coefficients for a two-layer medium — σ_{hv} as a function of the center cylinder diameter. Fractional volume $f = 0.5\%, \epsilon_s = (11 + i4)\epsilon_o$. Scattering layer has a thickness $d = 0.25$m and underlying half-space is flat and has a permittivity $\epsilon_{soil} = (10 + i2)\epsilon_o$. Frequency is 5.3 GHz. Number of branches for the scatterers is 10. 100

4-11 Backscattering coefficients for a two-layer medium — σ_{vv} at nadir as a function of branching angle β. Fractional volume $f = 0.5\%, \epsilon_s = (11 + i4)\epsilon_o$. Scattering layer has a thickness $d = 0.25$m and underlying half-space is flat and has a permittivity $\epsilon_{soil} = (10 + i2)\epsilon_o$. Frequency is 5.3 GHz. Number of branches for the scatterers is 10. 101

4-12 Backscattering coefficients for a two-layer medium — σ_{vv} as a function of the center cylinder diameter. Fractional volume $f = 0.5\%, \epsilon_s = (11 + i4)\epsilon_o$. Scattering layer has a thickness $d = 0.25$m and underlying half-space is flat and has a permittivity $\epsilon_{soil} = (10 + i2)\epsilon_o$. Frequency is 5.3 GHz. Number of branches for the scatterers is 10. 102

5-1 Geometrical configuration of the problem. 119

5-2 Configuration of the cluster. Center cylinder: length = 10 cm, radius = 0.3 cm; branching cylinder: length = 2 cm, radius = 0.15 cm, branching angle $\beta = 45^o$; permittivity of the cluster = $(11 + i4)\epsilon_o$; frequency is 5.3 GHz; incidence angle = θ_i. 120

5-3 Absorption cross section as a function of incidence angle for horizontal polarization. Number of branches is 10. Curves are normalized by $(\sigma_{ah}(90^o))_{ind}$ with the numerical value of -39.5 dBsm. 121

5-4 Absorption cross section as a function of incidence angle for vertical polarization. Number of branches is 10. Curves are normalized by $(\sigma_{ah}(90^o))_{ind}$ with the numerical value of -39.5 dBsm. 122

5-5 Absorption cross section as a function of incidence angle for horizontal polarization. Number of branches is 48. Curves are normalized by $(\sigma_{ah}(90^o))_{ind}$ with the numerical value of -30.7 dBsm. 123

5-6 Absorption cross section as a function of incidence angle for vertical polarization. Number of branches is 48. Curves are normalized by $(\sigma_{ah}(90^o))_{ind}$ with the numerical value of -30.7 dBsm. 124

5-7 Cross sections as a function of incidence angle for horizontal polarization. The number of branches is 48. 125

5-8 Cross section as a function of incidence angle for vertical polarization. Number of branches is 48. 126

5-9 Absorption cross sections as a function of incidence angle for horizontal polarization. Number of branches is 48. Center cylinder is removed from the cluster. Curves are normalized by $(\sigma_{ah}(90^o))_{ind}$ with the numerical value of -30.9 dBsm. 127

5-10 Absorption cross section as a function of incidence angle for vertical polarization. Number of branches is 48. Center cylinder is removed from the cluster. Curves are normalized by $(\sigma_{ah}(90^o))_{ind}$ with the numerical value of -30.9 dBsm. 128

5-11 Brightness temperature of a half-space medium embedded with vertically oriented scatterers — T_{Bh}, $f = 0.5\%, \epsilon_s = (11 + i4)\epsilon_o$. Frequency is 5.3 GHz. Number of branches for the scatterers is 10. 129

5-12 Brightness temperature of a half-space medium embedded with vertically oriented scatterers — T_{Bv}, $f = 0.5\%, \epsilon_s = (11 + i4)\epsilon_o$. Frequency is 5.3 GHz. Number of branches for the scatterers is 10. 130

5-13 Ratio of κ_a to κ_e for horizontal polarization — case 1. 131

5-14 Ratio of κ_a to κ_e for vertical polarization — case 1. 132

5-15 Brightness temperature of a half-space medium embedded with vertically oriented scatterers — T_{Bh}, $f = 0.5\%, \epsilon_s = (11 + i8)\epsilon_o$. Frequency is 5.3 GHz. Number of branches for the scatterers is 10. 133

5-16 Brightness temperature of a half-space medium embedded with vertically oriented scatterers — T_{Bv}, $f = 0.5\%, \epsilon_s = (11 + i8)\epsilon_o$. Frequency is 5.3 GHz. Number of branches for the scatterers is 10. 134

5-17 Brightness temperature of a two-layer medium — T_{Bh}, $f = 0.5\%, \epsilon_s = (11 + i4)\epsilon_o$. Scattering layer has a thickness $d = 0.25$m and underlying half-space is flat and has a permittivity $\epsilon_{soil} = (16 + i4)\epsilon_o$. Frequency is 5.3 GHz. Number of branches for the scatterers is 10. 135

5-18 Brightness temperature of a two-layer medium — T_{Bv}, $f = 0.5\%, \epsilon_s = (11 + i4)\epsilon_o$. Scattering layer has a thickness $d = 0.25$m and underlying half-space is flat and has a permittivity $\epsilon_{soil} = (16 + i4)\epsilon_o$. Frequency is 5.3 GHz. Number of branches for the scatterers is 10. 136

5-19 Brightness temperature of a two-layer medium — T_{Bh} at observation angle = 8.4°, $f = 0.5\%, \epsilon_s = (11 + i4)\epsilon_o$. Underlying half-space is flat and has a permittivity $\epsilon_{soil} = (16 + i4)\epsilon_o$. Frequency is 5.3 GHz. Number of branches for the scatterers is 10. 137

5-20 Brightness temperature of a two-layer medium — T_{Bv} at observation angle = 8.4° as a function of canopy thickness d, $f = 0.5\%, \epsilon_s = (11 + i4)\epsilon_o$. Underlying half-space is flat and has a permittivity $\epsilon_{soil} = (16 + i4)\epsilon_o$. Frequency is 5.3 GHz. Number of branches for the scatterers is 10. 138

5-21 Brightness temperature of a half-space medium — T_{Bh}, $f = 0.5\%, \epsilon_s = (11 + i4)\epsilon_o$. Frequency is 5.3 GHz. Number of branches for the scatterers is 48. 139

5-22 Brightness temperature of a half-space medium — T_{Bv}, $f = 0.5\%, \epsilon_s = (11 + i4)\epsilon_o$. Frequency is 5.3 GHz. Number of branches for the scatterers is 48. 140

5-23 Brightness temperature of a two-layer medium — T_{Bh}, $f = 0.5\%, \epsilon_s = (11 + i4)\epsilon_o$. Scattering layer has a thickness $d = 0.25$m and underlying half-space is flat and has a permittivity $\epsilon_{soil} = (16 + i4)\epsilon_o$. Frequency is 5.3 GHz. Number of branches for the scatterers is 48. 141

5-24 Brightness temperature of a two-layer medium — T_{Bv}, $f = 0.5\%, \epsilon_s = (11 + i4)\epsilon_o$. Scattering layer has a thickness $d = 0.25$m and underlying half-space is flat and has a permittivity $\epsilon_{soil} = (16 + i4)\epsilon_o$. Frequency is 5.3 GHz. Number of branches for the scatterers is 48. 142

5-25 Brightness temperature of a half-space medium — T_{Bv}, $f = 0.5\%, \epsilon_s = (11 + i4)\epsilon_o$. Frequency is 5.3 GHz. Number of branches for the scatterers is 48. Branching angle β is 15°. 143

5-26 Brightness temperature of a two-layer medium — T_{Bv}, $f = 0.5\%, \epsilon_s = (11 + i4)\epsilon_o$. Scattering layer has a thickness $d = 0.25$m and underlying half-space is flat and has a permittivity $\epsilon_{soil} = (16 + i4)\epsilon_o$. Frequency is 5.3 GHz. Number of branches for the scatterers is 48. Branching angle β is 15^o. 144

5-27 Brightness temperature of a half-space medium — T_{Bv}, $f = 0.5\%, \epsilon_s = (11 + i4)\epsilon_o$. Frequency is 5.3 GHz. Number of branches for the scatterers is 48. Branching angle β is 75^o. 145

5-28 Brightness temperature of a two-layer medium — T_{Bv}, $f = 0.5\%, \epsilon_s = (11 + i4)\epsilon_o$. Scattering layer has a thickness $d = 0.25$m and underlying half-space is flat and has a permittivity $\epsilon_{soil} = (16 + i4)\epsilon_o$. Frequency is 5.3 GHz. Number of branches for the scatterers is 48. Branching angle β is 75^o. 146

6-1 Block diagram showing the modules of BICONG. 162

6-2 Flow chart for BICONG. 163

6-3 Geometrical configuration of the test problem 1. 164

6-4 Geometrical configuration of the test problem 2. 165

A-1 Illustration of the wave vector and the horizontal and vertical polarization vectors. 175

B-1 Nonplanar skew monopoles. 178

B-2 Parallel monopoles. 180

List of Tables

3.1 Characteristics of the coniferous needles. 60

6.1 Performance of BICONG with different preconditioner. 159
6.2 Breakdown of time spent in the calculation. 159
6.3 Performance of BICONG in a homogeneous platform. 160
6.4 Performance of BICONG with and without load balancing. 160

Chapter 1

Introduction

1.1 Introduction

Remote sensing of earth terrain at microwave frequency has been actively pursued since the 1960s [1]. Microwave frequency has the advantages over optical frequency in their abilities to penetrate clouds and vegetation canopies and to provide day-and-night coverage. Microwave remote sensing is an important tool for monitoring the atmosphere and the surfaces of the earth with a potential for applications in monitoring global climate changes. It provides a means to infer the global carbon cycle [2], the water cycle [3], climatic and geologic processes [4], ocean circulation and air-sea interactions [5]. The carbon cycle refers to the paths and rates of exchange of carbon between the Earth's atmosphere, oceans and terrestrial life. Remote sensing of vegetative terrain can provide information on the types and amounts (biomass) [6] of vegetation in that region as well as the soil moisture [7, 8] underneath the vegetation. The biomass of the vegetation plays an important role in the carbon cycle. The estimations of soil moisture, snow and ice cover enable better understanding the water cycle. One of the applications of remote sensing of ocean surface is to determine the wind speed and direction [9, 10] and ocean floor [11]. In polar region, the monitoring the iceberg formation and movement is necessary for safe navigation [12]. The improvement in radar technology has led to the use of multiple frequency, multi-polarization radar measurements at variable incidence angles [13, 14]. Development

of accurate theoretical models for the interpretation of experimental data from active and passive remote sensors is essential in deriving algorithms for extracting physical parameters of interest from the measurements. In this thesis, we focus on the remote sensing of vegetation canopies, and a new model is developed for the calculation of electromagnetic scattering from a medium containing branching vegetation structures.

With advances in computer technology and new development of sophisticated numerical algorithms, rigorous numerical solutions for electromagnetic wave phenomena in complex media can be more readily obtained. Numerical solutions not only provide a means for studying electromagnetic wave phenomena, but also allows verification of various approximate analytical models. In this thesis, computational electromagnetics is applied for the study of microwave remote sensing of vegetation.

There are basically two types of microwave sensors, namely active and passive sensors. Active sensors, such as radars and scatterometers, transmit a microwave signal and measure the received signal. Passive sensors, like radiometers, do not transmit any signal, but instead measure the microwave radiation emitted from an object or a region. When a scene, such as terrain, is observed by a microwave radiometer (through its antenna beam), the radiation received by the antenna is partly due to the scene itself and partly due to the reflected radiation. For active sensing, the important parameters are the backscattering coefficients, while for passive remote sensing the quantity of interest is the brightness temperature [1].

Various theoretical models have been developed to characterize the electromagnetic wave scattering properties of vegetation canopies. These models can be broadly categorized into either the wave theory model or the radiative transfer theory model. In the wave theory, one starts out with Maxwell's equations, and then introduces the scattering and absorption properties of the medium. Considerably complicated system of equations are solved under various approximations. The dyadic Green's function formulation is frequently used to form an integral equation to calculate the scattered field. In the case of weakly scattering media, the Born approximation is used, in which a small perturbation series is truncated to obtain solutions to different

orders. When the fluctuation of the permittivity of the medium is large, strong fluctuation theory can be used in which an effective permittivity is introduced to account for the attenuation due to the scattering and the absorption in the medium [15]. The distorted Born approximation is then used to calculate the scattered fields [16, 17]. Radiative transfer theory, on the other hand, is based on the energy transport equation. It is assumed that there is no correlation between the fields so that their intensities rather than their amplitudes are summed. The intensities are expressed in terms of the Stokes parameters, and the propagation characteristics can be described by an integro-differential equation. The scattering and absorption properties of the medium are described through the phase matrix and the extinction matrix, both of which can be obtained by either considering a homogeneous background embedded with discrete scatterers, or by considering a medium with random permittivity fluctuations. In the discrete scatterer case, a configuration average over the size, the shape and the orientation distribution of the scatterers has to be considered. In the continuous random medium model, the important parameters are the mean, variance and spatial correlation function of the permittivity. The basic limitation of the radiative transfer theory is that the coherent effects or phase relations between the scatterers are not included. However, it has the advantage of simplicity and, if solved numerically, it can also account for multiple scattering effects. Both analytical and numerical methods, such as analytical iterative method and Gaussian quadrature method, can be used to solve the radiative transfer equation.

Radiative transfer theory has been used to model vegetation canopies [1, 18, 19]. The extinction matrix and the phase matrix in the radiative transfer equations are derived using the discrete scatterer model with approximations of the scattering functions and with the assumption of sparse distribution. Trunks, branches and needleleaves are usually modeled as dielectric cylinders [20, 21], while the leaves of deciduous trees are modeled as thin dielectric disks [20, 22]. The scattered and internal fields are calculated using various approximations, such as the physical optics approximation [22, 23] and the finite cylinder approximation [19, 20].

Classical radiative transfer theory assumes that particles scatter independently.

This assumption is based on the random phase of scattering by different particles and is valid if the particle separations are large compared to the wavelength. Although the fractional volume of the scatterers is low in a vegetation canopy, vegetation usually exhibits locally dense properties due to clustering. The incoherent addition of scattering intensities due to many components of the vegetation cluster neglects the mutual interactions between the components. Clustered scatterers, as in branches and leaves in a vegetation canopy, can exhibit coherent scattering effect since the arrangement of the scatterers are confined in a region comparable to the wavelength. The collective scattering behavior of branching vegetation was first studied by Yueh et al [24]. In that model, the internal fields of the scatterers were assumed to be the same as that of independent scattering and the focus of the study was on the coherent scattering enhancement. The collective coherent scattering behavior is taken into account by including the relative phase shifts of the scattered fields from different scatterers due to their relative positions with each other. A significant difference compared to the independent scattering model was observed. However, since the internal field in the model was assumed to be the same as the independent scattering model, the mutual interaction (multiple scattering) was not included.

In this thesis, we study the effect of mutual interaction in the scattering behavior of locally dense vegetation. The radiative transfer theory is modified by defining the phase matrix and extinction coefficient as, respectively, the bistatic cross section per unit volume of space and the extinction cross section per unit volume of space. The limit of the volume of space is taken such that the collective scattering effects of the particles within the volume are taken into account. The scattering functions of the scatterers within the volume of space are obtained from the numerical solution of Maxwell's equations, and hence all the interactions between different components of the cluster are retained. Because of low fractional volume, the interaction between two remotely separated scatterers is small, thus the use of radiative transfer theory is justified. Flat surface boundary conditions are imposed for both the active and the passive cases, so that surface transmission and reflection are described by the Fresnel coefficients and can be easily incorporated into the radiative transfer equations. Ana-

lytical iterative solution method is used in the active case to calculate backscattering coefficients and Gaussian quadrature method is used in the passive case to calculate brightness temperatures.

1.2 Description of the Thesis

In Chapter 2, a volume scattering model using scatterers with multi-scale branching structures is developed to investigate the scattering characteristics of a vegetation canopy. The branching scatterer is approximated by a thin, perfectly conducting wire structure. The method of moments (MoM) formulation based on the reaction integral equations [25-30] is employed in the calculation. The frequency, angle and polarization dependences of the electromagnetic scattering characteristics of the branching structure is studied.

The perfectly conducting case considered in Chapter 2 provides a computationally efficient solution to study the frequency, angle and polarization dependences of a multi-length scale scattering structure. In Chapter 3, a more realistic model of dielectric cylinder is considered. A code based on the MoM for the volume integral equation is developed to solve the scattering problem of arbitrarily connected thin dielectric cylinder structures. Simulations of vegetation canopies of bare twigs of deciduous trees and needle-shaped leaves of coniferous trees are carried out. It also provides an accurate numerical solution against which other approximate solutions can be checked.

Using the scattering functions of an individual branching scatterer obtained by the MoM, radiative transfer theory is applied to calculate backscattering coefficients (Chapter 4) and brightness temperatures (Chapter 5) of a random medium with discrete scatterers. The first order iterative solution of the vector radiative transfer equations with flat surface boundary conditions is derived in Chapter 4. The results are compared with those obtained from the independent scattering model and the coherent scattering model [24]. The effects of both the multiple scattering between the components of the clustering structure and the coherent interference within the

structure are addressed.

In Chapter 5, the solution for the vector radiative transfer equations for passive remote sensing is derived using Gaussian quadrature method. Mutual interactions between the components of the structure result in an increase in the internal electric field. This effect, absorption enhancement, is studied in Chapter 5. Scattering functions based on the independent scattering model and the coherent scattering model are used in the brightness temperature calculation for comparison. The effects of absorption and scattering associated with the clustering on the brightness temperature are studied. The significance of layer thickness on thermal emission is also examined.

The calculations of the scattering functions, phase matrix and extinction matrix are computationally expensive. Not only do the calculations require considerable computational power but they also require a large computer memory. In Chapter 6, the use of parallel virtual machine (PVM) to solve complex matrix problems arising from electromagnetic scattering is described. PVM is a macro library code that runs on a UNIX network. The use of PVM provides access to increased CPU power as well as memory, making it possible to solve large problems which normally cannot be solved on a single machine. Methods for solving the complex matrix problems with a general structure or a block tridiagonal structure, as implemented in PVM, are described in Chapter 6. Iterative methods based on variants of the preconditioned conjugate gradient method are used. The performance of the parallel solvers is evaluated in terms of computational costs as well as communication costs over the network. Numerical experiments are carried out to evaluate the effectiveness of different preconditioners. The notations adopted in this thesis are given in Appendix A.

Chapter 2

Electromagnetic Waves Scattering for a Multi-Scale Branching Structure: Conducting Case

2.1 Introduction

A volume scattering model using scatterers with multi-scale branching structures is developed to investigate the scattering characteristics of a vegetation canopy. A branching scatterer shows a closer resemblance to a tree than the randomly oriented cylinder model. It provides a realistic simulation of vegetation patterns, and its structure is also very important in the electromagnetic scattering behavior. In general, vegetation consists of components with a variety of length scales. The present model may provide a means of describing electromagnetic scattering from vegetation canopy.

The branching scatterer is approximated by a thin, perfectly conducting wire structure. The method of moments (MoM) formulation based on reaction integral equations [25-30] is employed in the calculation. The MoM has been used successfully to treat problems in a variety of areas within the general field of electromagnetics. The earlier efforts have dealt with the general treatment in the frequency domain problems involving analysis and design of radiation and scattering systems consisting of arbitrarily bent and interconnected thin wires and rods [25]. It has been shown that

for radiation problems, the current distributions on the wires can be determined along with appropriate near- and far-field patterns and input impedances corresponding to the feed point [29]. For scattering problems, the current distributions can again be computed along with the desired scattered fields and radar cross sections [30]. In this chapter, the method is applied to investigate frequency, angle, and polarization dependencies of the electromagnetic scattering characteristics from the branching model.

2.2 Formulation

A computer code for scattering and radiating problems is developed based on Richmond's reaction integral equations formulation [25, 26]. The derivation of the MoM is shown in this section. The term "thin wire" implies a wire of length L and radius a with $L/a \gg 1$ and $a \ll \lambda$, where λ is the wavelength. A perfect conductor is assumed. Finite conductivity case can be dealt with by adding the surface impedance.

2.2.1 Reaction Integral Equation

We adopt the notations shown in Fig. 2-1. $\overline{E}, \overline{H}$ are the total fields; $\overline{E}^i, \overline{H}^i$ are the incident fields due to $\overline{J}_i, \overline{M}_i$; $\overline{E}^s, \overline{H}^s$ are the scattered field due to $\overline{J}_s, \overline{M}_s$ on the scatterer surface.

We have

$$\overline{E} = \overline{E}^i + \overline{E}^s \tag{2.1}$$

$$\overline{H} = \overline{H}^i + \overline{H}^s \tag{2.2}$$

We first start with the assumption that $\overline{M}_i = 0$ and the surface S is perfectly conducting. We begin with the implicit integral equation

$$\overline{J} = \overline{J}_i + \overline{J}_s \tag{2.3}$$

where the domain can be considered to be the entire space including the surface S

and the volume V_i occupied by the electric source $\overline{J}_i$. We have now replaced the scatterer enclosed by the surface S with an equivalent surface current $\overline{J}_s$ on S. In this equivalent problem the total field inside the scatterer vanishes.

$$\overline{E} = 0 \qquad \text{in } V \tag{2.4}$$

Taking the symmetric product with $\overline{E}^m$ (the E field due to the test source $\overline{J}_m$) on both sides of equation (2.3) over the entire domain

$$\int \overline{J} \cdot \overline{E}^m dv = \int_{V_i} \overline{J}_i \cdot \overline{E}^m dv + \int_S \overline{J}_s \cdot \overline{E}^m ds \tag{2.5}$$

But by reciprocity

$$\int \overline{J} \cdot \overline{E}^m dv = \int \overline{J}_m \cdot \overline{E} dv \tag{2.6}$$

The right hand side equation (2.6) is zero because $\overline{E} = 0$ in V (from equation (2.4)) and $\overline{J}_m = 0$ outside V and on S because the test source $\overline{J}_m$ is in the interior region of V. We have

$$\int_{V_i} \overline{J}_i \cdot \overline{E}^m dv + \int_S \overline{J}_s \cdot \overline{E}^m ds = 0 \tag{2.7}$$

Repeating the same process and replacing the test field $\overline{E}^m$ with $\overline{H}^m$ and $\overline{J}_i$ with $\overline{M}_i$, we obtain another equation. Combining them by the superposition theorem, we obtain the reaction integral equation in which the assumption of $\overline{M}_i = 0$ is not needed.

$$\int_{V_i} (\overline{J}_i \cdot \overline{E}^m - \overline{M}_i \cdot \overline{H}^m) dv + \int_S (\overline{J}_s \cdot \overline{E}^m - \overline{M}_s \cdot \overline{H}^m) ds = 0 \tag{2.8}$$

2.2.2 Thin Wire Approximation

Equation (2.8) can be simplified for a thin wire structure by selecting an intrinsic co-ordinate system $(\hat{n}, \hat{\phi}, \hat{l})$, where $\hat{n}$ is the outward normal, $\hat{\phi}$ is the circumferential direction and $\hat{l}$ is the axial direction. The surface current $\overline{J}_s$ is approximated by the thin wire assumption

$$\overline{J}_s(\overline{r}) = \frac{\overline{I}_l(l)}{2\pi a} \tag{2.9}$$

i.e., $\overline{J}_s$ has no variation in the circumferential direction.

For a wire with finite conductivity,

$$\overline{E}_t = Z_s \overline{J}_s \tag{2.10}$$

where Z_s is the surface impedance on the wire and $\overline{E}_t$ is the tangential component of the electric field.

The magnetic current $\overline{M}_s$ can then be related to the electric current in the following way,

$$\begin{aligned} \overline{M}_s &= -\hat{n} \times \overline{E} \\ &= Z_s \overline{J}_s \times \hat{n} \\ &= \frac{Z_s I(l) \hat{\phi}}{2\pi a} \end{aligned} \tag{2.11}$$

The integral equation (2.8) can be written as

$$-\int_o^L I(l)(E_l^m - Z_s H_\phi^m) dl = V_m \tag{2.12}$$

where L is the overall wire length

$$V_m = \int_V (\overline{J}_i \cdot \overline{E}^m - \overline{M}_i \cdot \overline{H}^m) dv \tag{2.13}$$

$$E_l^m = \frac{1}{2\pi} \int_o^{2\pi} \hat{l} \cdot \overline{E}^m d\phi \tag{2.14}$$

$$H_\phi^m = \frac{1}{2\pi} \int_o^{2\pi} \hat{\phi} \cdot \overline{H}^m d\phi \tag{2.15}$$

2.3 Method of Solution

The unknown current $I(l)$ is approximated by a set of basis functions $B_1, B_2, \cdots, B_N$ as follows:

$$\overline{I}(l) = \sum_{n=1}^{N} I_n \overline{B}_n(l)$$

We select a basis function as follows:

$$B_1(l) = \frac{\hat{l}_1 P_1(l) \sinh \gamma(l - l_1)}{\sinh \gamma d_1} + \frac{\hat{l}_2 P_2(l) \sinh \gamma(l_3 - l)}{\sinh \gamma d_2}$$

$$\gamma = i\omega\sqrt{\mu\epsilon}$$

$$P_1(l) = \begin{cases} 1 & l_2 > l > l_1 \\ 0 & \text{otherwise} \end{cases}$$

$$P_2(l) = \begin{cases} 1 & l_3 > l > l_2 \\ 0 & \text{otherwise} \end{cases}$$

The notations are shown in Fig. 2-2.

The reason for choosing sinusoidal functions as basis functions is that sinusoidal basis functions have a simple closed-form expression for the radiated field and the current vanishes at wire ends.

Employing the Galerkin's method, i.e., choosing the same weighting function as the basis function, the integral equation is then reduced to a matrix equation.

$$\sum_{n=1}^{N} I_n Z_{mn} = V_m \qquad m = 1, 2, \cdots, N \tag{2.16}$$

where

$$Z_{mn} = -\int_n B_n(l)(E_l^m - Z_s H_\phi^m) dl$$

with

$$V_m = \int_V (\overline{J}_i \cdot \overline{E}^m - \overline{M}_i \cdot \overline{H}^m) dv$$

$$E_l^m = \frac{1}{2\pi} \int_o^{2\pi} \hat{l} \cdot \overline{E}^m d\phi$$

$$H_\phi^m = \frac{1}{2\pi} \int_o^{2\pi} \hat{\phi} \cdot \overline{H}^m d\phi$$

In order to generate the impedance matrix, the (E_l^m, H_ϕ^m) due to the test source are

required. Fig. 2-3 shows a typical segment for the test source.

$$I(l) = \frac{I_1 \sinh \gamma(l_2 - l) + I_2 \sinh \gamma(l - l_1)}{\sinh \gamma d} \tag{2.17}$$

The fields due to this current are found to be

$$\begin{aligned}
E_\phi &= H_\rho = H_l = 0 \\
E_\rho &= \frac{\eta}{4\pi \sinh \gamma d}\Big[(I_1 e^{-\gamma R_1} - I_2 e^{-\gamma R_2}) \sinh \gamma d \\
&\quad + (I_1 \cosh \gamma d - I_2) e^{-\gamma R_1} \cos\theta_1 + (I_2 \cosh \gamma d - I_1) e^{-\gamma R_2} \cos\theta_2\Big] \\
E_l &= \frac{\eta}{4\pi \sinh \gamma d}\Big[(I_1 - I_2 \cosh \gamma d)\frac{e^{-\gamma R_2}}{R_2} \\
&\quad + (I_2 - I_1 \cosh \gamma d)\frac{e^{-\gamma R_1}}{R_1}\Big] \\
H_\phi &= \frac{1}{4\pi\rho \sinh \gamma d}\Big[(I_1 \cos\theta_1 \sinh \gamma d + I_1 \cosh \gamma d - I_2) e^{-\gamma R_1} \\
&\quad + (I_2 \cos\theta_2 \sinh \gamma d + I_2 \cosh \gamma d - I_1) e^{-\gamma R_2}\Big]
\end{aligned}$$

In the implementation of the computer program, numerical integration is used to calculate Z_{mn}. It is found that the convergence is slow if the segments n and m are colinear or parallel. For a long wire, the program will automatically divide the long segment into smaller segments with length less than a prescribed fraction of wavelength (usually 0.1λ). Hence, significant computation time is used in filling up the impedance matrix. Richmond [27, 28, 31] has suggested an efficient way to fill the matrix which involves an exponential integral. It is given in Appendix B.

2.4 Multi-Scale Branching Structure

In order to study the structure of vegetation, a branching scatterer with different length scales is formed and the scattering patterns over a range of frequencies and angles are investigated. Mandelbrot [32] shows examples of umbrella trees with infinitely thin stems. This is the simple form of a fractal tree. The tree skeleton has a close resemblance to a botanical tree. The branching scatterer consists of two parts:

branching tips and branches. Fig. 2-4 shows the basic building block for the construction of the branching scatterer used in this chapter. We regard it as the first stage of the branching scatterer. The second and the third stages of the scatterers are shown in Figs. 2-5 and 2-6, respectively. The rule for the formation of the next stage is that a scaled basic building block is placed on every branching tip of the previous stage. The inter-branch angle takes the same value at every fork. It can be varied over a wide range and hence a variety of scatterer shapes can be formed without changing the scaling factor for the building blocks. In the calculation, we choose the branching angle to be 45^o from the vertical and each branch is separated from the adjacent ones by 90^o in the azimuthal direction. The scale factor is chosen to be 0.5. That is, the reduced building block placed on the branch tip is half the size of the previous one. With this restriction, a deterministic branching scatterer can be formed with self-avoidance property. The construction of a random fractal tree is more complicated because the addition of any branch has to be considered as a global process in which the proximity of any existing branch has to be checked in order to ensure that branches do not overlap. An algorithm for constructing random fractal trees is given by Oppenheimer [33]. In this chapter, only deterministic branching scatterers are considered. The frequency response of multi-scale branching scatterers can be illustrated by such scatterers without the complexity of full random fractal tree models.

2.5 Results and Summary

In this section, the backscattering cross sections of multi-scale branching structures obtained with the method of moments are presented. First, we consider the backscattering cross sections for the first stage and the third stage scatterers as a function of incidence angle. The incidence angle in ϕ is fixed at 45^o and θ varies from 0^o to 180^o. The length of the branch of the first stage scatterer is 43.75 cm. The third stage scatterer is built up from a building block of branch length 25 cm, and the scale ratio is 0.5. The scaled building blocks of branch length 12.5 cm are then placed on the

branch tips. The further scaled building blocks of branch length 6.75 cm are placed on the branch tips of the second stage scatterer. The first and third stage scatterers then have the same longest branch length. The frequency is 1.6 GHz. The results are shown in Figs. 2-7 and 2-8. The backscattering cross section is normalized by the square of the wavelength. The curves are similar in shape. The higher stage curve is shifted upward and has several more side lobes. The average backscattering cross section can provide a better comparison because Figs. 2-7 and 2-8 are only confined to the $\phi = 45^o$ plane.

Figs. 2-9 and 2-10 show the average backscattering cross sections of different stage scatterers as a function of frequency for vertical and horizontal polarizations, respectively. It should be noted that the average cross section has the unit of dBsm in this case as we want to show the frequency dependence. The average backscattering cross section is calculated by integrating over the upper hemisphere of the scatterer; it is given by

$$\sigma_{p,ave} = \int_0^{2\pi} \int_0^{\frac{\pi}{2}} \sigma_{pp}(\theta, \phi) \sin\theta d\theta d\phi \tag{2.18}$$

where $p = v, h$. The same first and third stage scatterers are used and the second stage scatterer is made to have the same dimension for the largest length scale. At low frequencies, the scatterers behave like Rayleigh scatterers as shown in the slopes of all the curves in this region. Above the first resonance frequency, there is a series of peaks for each curve. The peak corresponds to the resonance frequency for a given length scale. It is observed that a higher stage scatterer has less number of peaks and has a relatively flat curve. The reason is that a higher stage scatterer has more branches and consists of components with a larger variety of length scales, which resonate at different frequencies and hence give rise to a relatively flat curve.

A preliminary study has been carried out for the frequency response of multi-scale branching scatterers. The given scatterer models the shape of a vegetation cluster but not its electric properties. Vegetation clusters are made of dielectric materials while the present model is for a conducting material. However, the trend of a flat frequency response curve is obtained in the calculation which is observed in

experimental data [34]. As a next step, a dielectric scatterer model is developed in the next chapter to study branching, multi-scale scatterers in electromagnetic waves scattering.

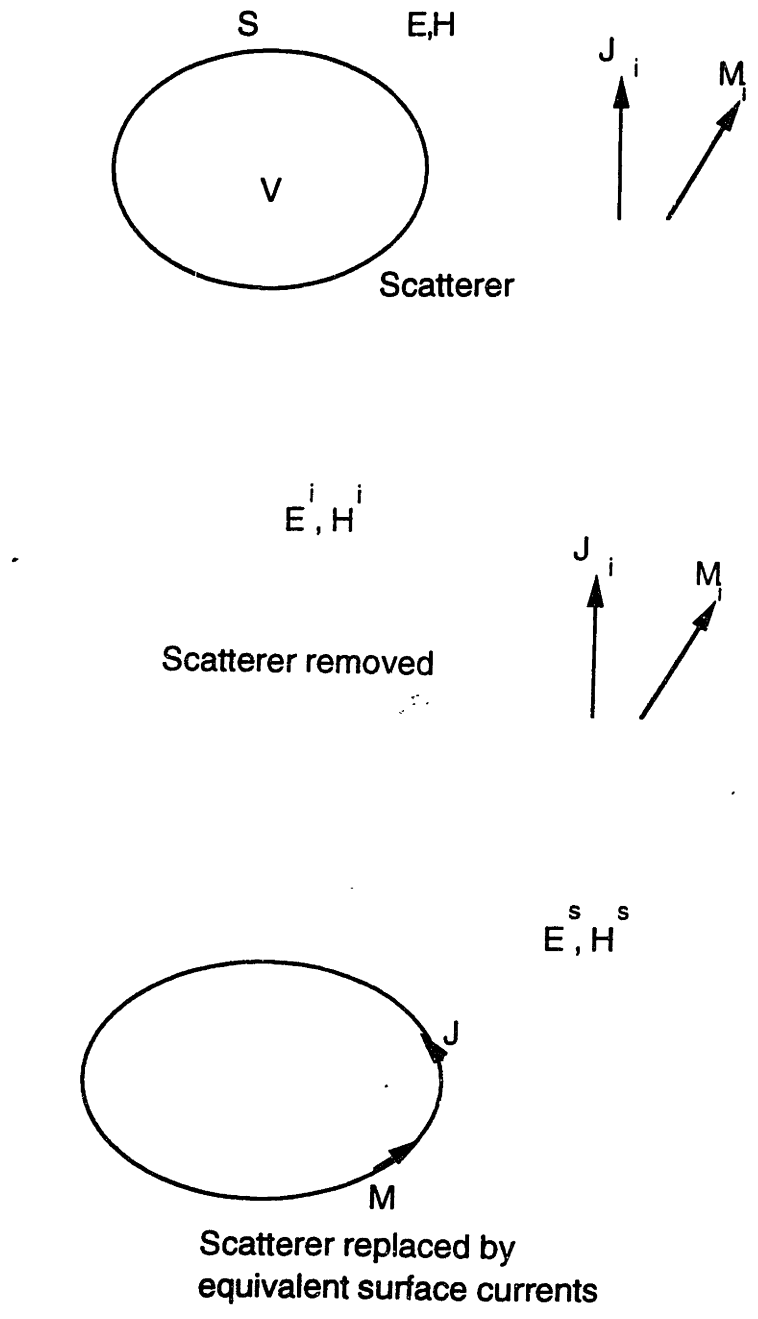

Figure 2-1: Decomposition of a scattering problem into incident and scattered fields.

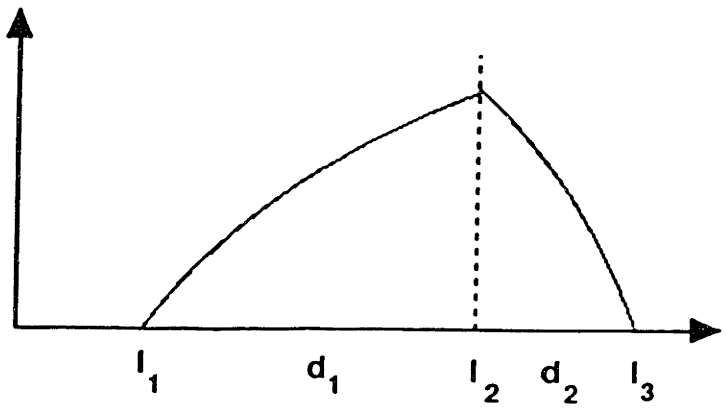

Figure 2-2: Piecewise sinusoidal basis function as a function of l.

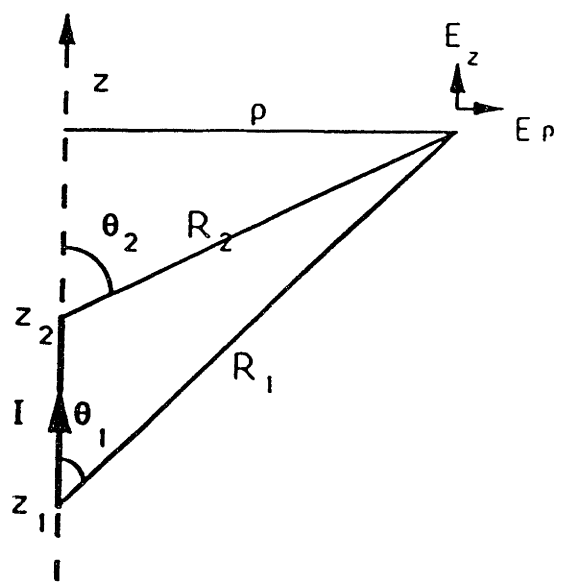

Figure 2-3: A segment for the test source.

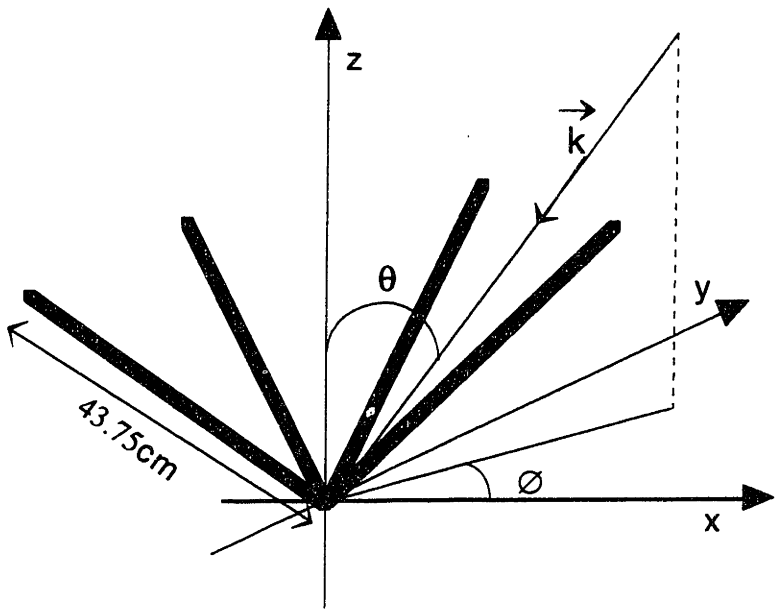

Figure 2-4: Basic building block of the scatterer (first stage scatterer).

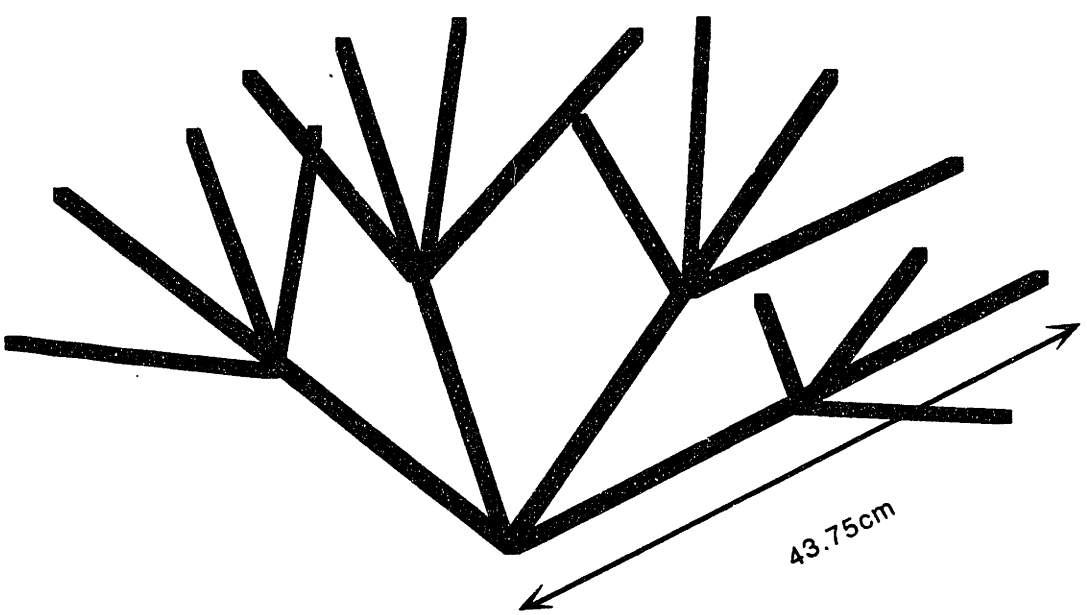

Figure 2-5: Second stage scatterer.

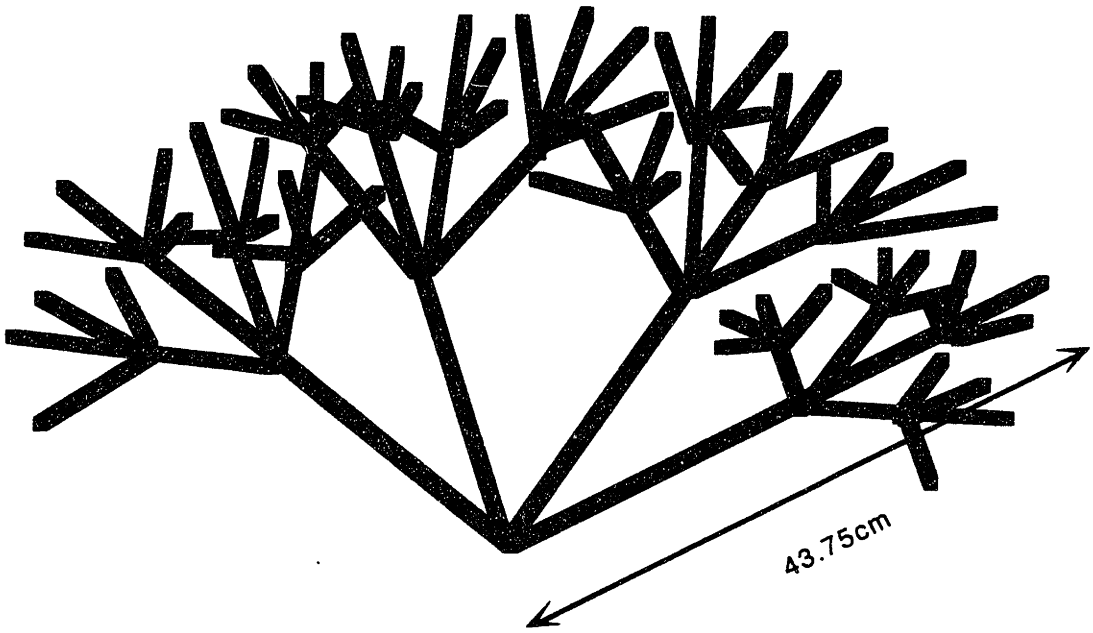

Figure 2-6: Third stage scatterer.

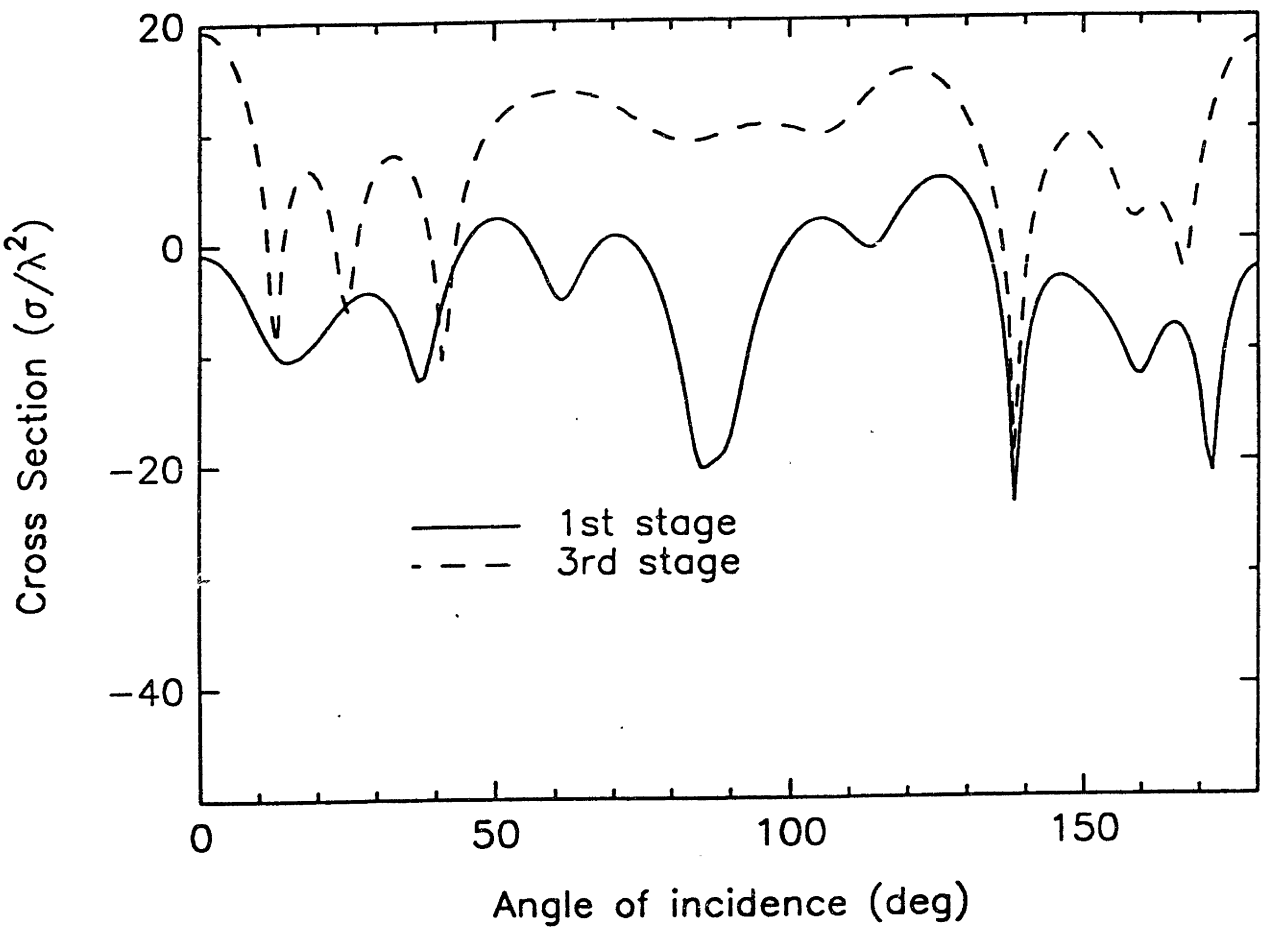

Figure 2-7: Backscattering cross sections as a function of incidence angle θ, with $\phi = 45^o$ – vertical polarization.

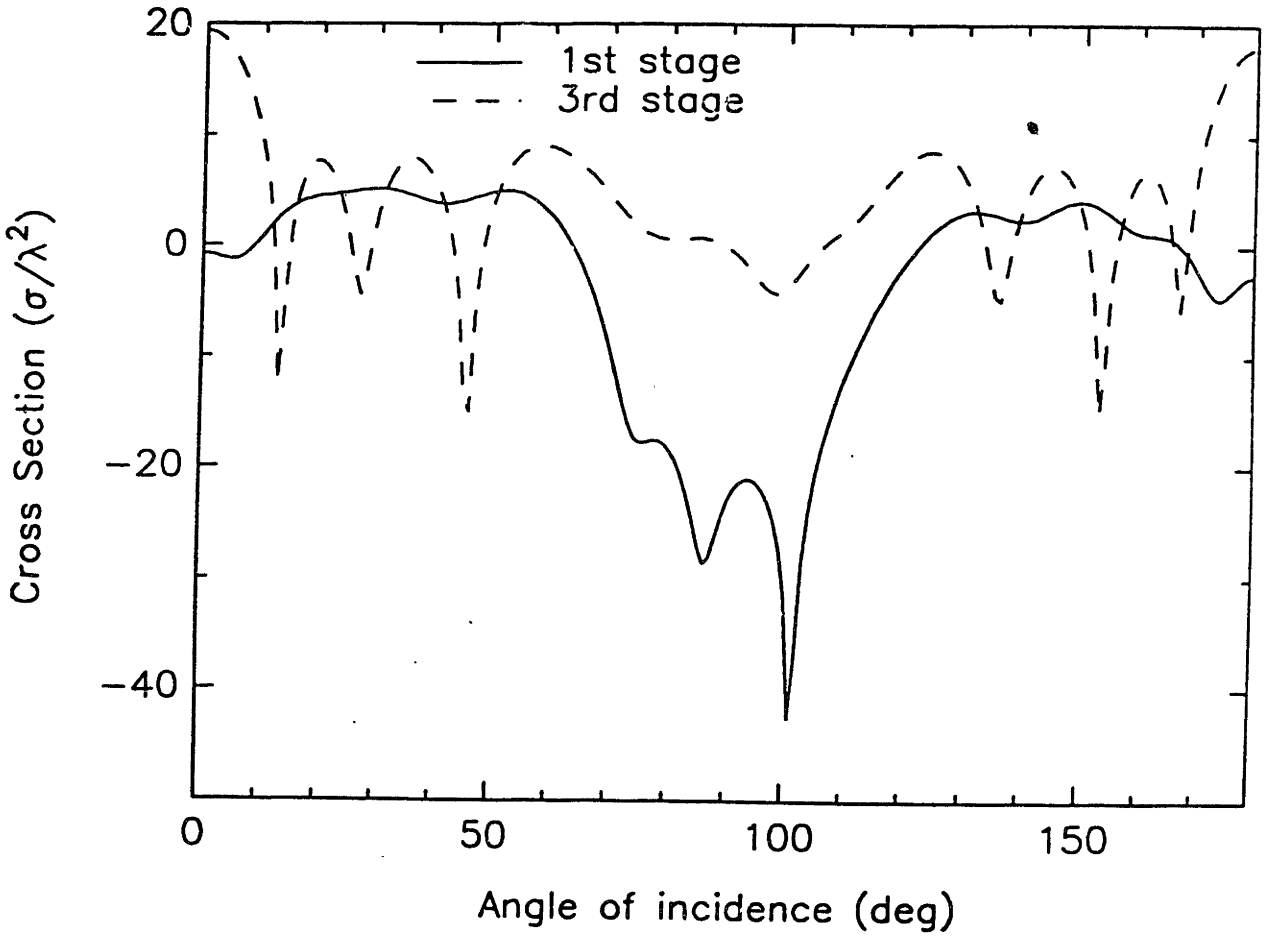

Figure 2-8: Backscattering cross sections as a function of incidence angle θ, with $\phi = 45^o$ – horizontal polarization.

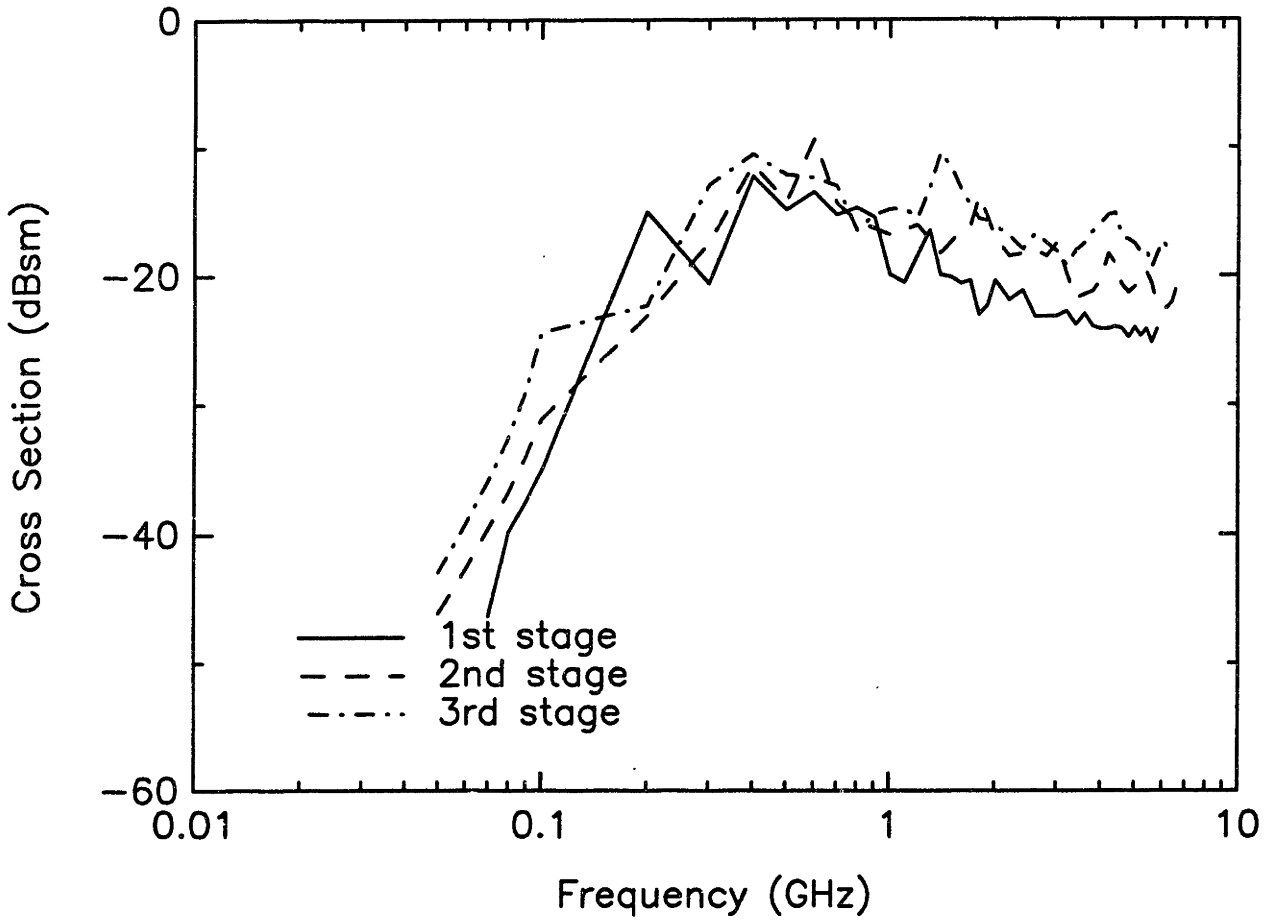

Figure 2-9: Average backscattering cross sections for different stage scatterers – vertical polarization.

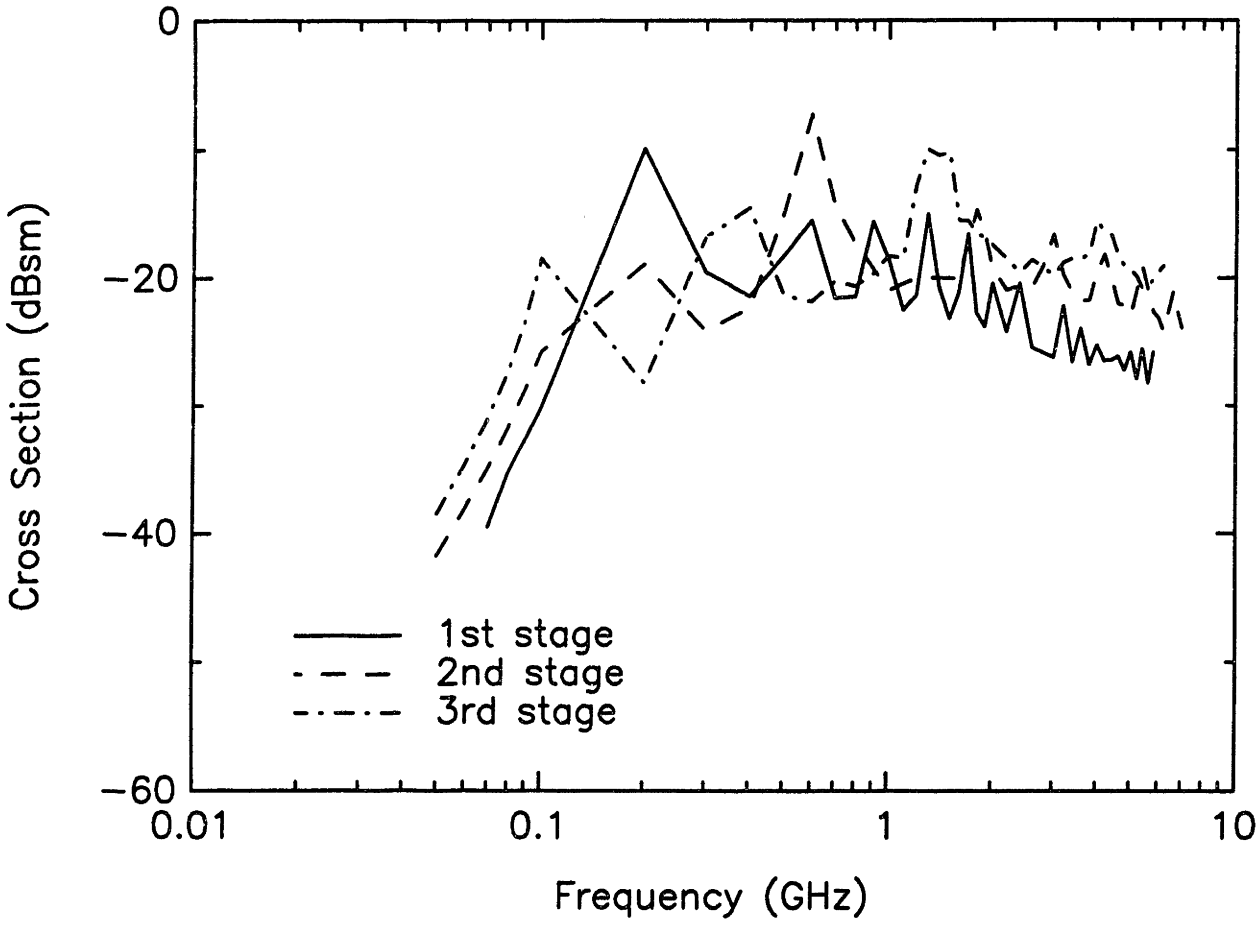

Figure 2-10: Average backscattering cross sections for different stage scatterers – horizontal polarization.

Chapter 3

Method of Moments Approach for a Thin Dielectric Cylinder Structure

3.1 Introduction

Electromagnetic scattering from dielectric scatterers has been a subject of interest for many years because of their wide range of applications. A variety of techniques have been developed for analyzing electromagnetic scattering by objects of different shapes and properties. Among them are surface integral methods [35, 36], volume integral methods [37, 38], and unimoment [39, 40] or hybrid methods [41, 42] which couple finite element methods with surface integral methods. The surface integral method is well-suited for homogeneous bodies. On the other hand, the volume integral method and the finite element method are versatile for highly inhomogeneous media. In volume integral methods, the unknowns in the problem are expressed in terms of volume currents flowing inside the bodies. The volume current consists of the conduction current as well as the displacement current induced by the total field. The volume integral equation is then approximated by a matrix equation. In order to solve for the volume current, a full matrix inversion has to be carried out. In the finite element method, a sparse matrix with a much larger size is involved. The choice

among various methods depends on the particular application.

In this chapter, we develop a method to solve thin dielectric structures with applications in remote sensing. A thin dielectric cylinder structure model is used to simulate natural vegetation canopy of bare twigs of deciduous trees and needle-shaped leaves of coniferous trees. Averaging over orientations of different realizations is necessary in order to obtain reliable results.

In section 3.2, the volume integral formulation is discussed. The discussion is then followed by the method of solution in section 3.3 which gives details of the formation of the matrix equation. Numerical results are presented in section 3.4 and comparisons with experimental data is made. Section 3.5 summarizes this chapter.

3.2 Formulation

In this section, the formulation of the volume integral equation of the electric field is derived from Maxwell's equations [30]. The volume integral equation is well suited for solving scattering problems of inhomogeneous bodies. In Fig. 3-1, a scatterer of volume V, permittivity ϵ and permeability μ is in region V_1 bounded by the surface S_1, which may be infinitely large. The scatterer can be replaced by equivalent electric and magnetic volume currents $\overline{J}_{eq}$ and $\overline{M}_{eq}$ in the following way. In the presence of the scatterer, we have

$$\nabla \times \overline{H} = -i\omega\epsilon\overline{E} + \overline{J} \tag{3.1}$$

$$\nabla \times \overline{E} = i\omega\mu\overline{H} - \overline{M} \tag{3.2}$$

By replacing the scatterer with $\overline{J}_{eq}$ and $\overline{M}_{eq}$

$$\nabla \times \overline{H} = -i\omega\epsilon_o\overline{E} + \overline{J}_{eq} + \overline{J} \tag{3.3}$$

$$\nabla \times \overline{E} = i\omega\mu_o\overline{H} - \overline{M}_{eq} - \overline{M} \tag{3.4}$$

For equations (3.1) and (3.2) to be equivalent to equations (3.3) and (3.4), we need

$$\overline{J}_{eq} = -i\omega(\epsilon - \epsilon_o)\overline{E} \tag{3.5}$$

$$\overline{M}_{eq} = -i\omega(\mu - \mu_o)\overline{H} \tag{3.6}$$

Equations (3.5) and (3.6) state the volume equivalence theorem which is valid for material bodies that are inhomogeneous since ϵ and μ can be a function of position $\overline{r}$. With the equivalent currents, the scattered fields can be expressed in terms of $\overline{\overline{G}}_e$ and $\overline{\overline{G}}_m$, which are the electric and magnetic dyadic Green's functions subject to the boundary conditions [43].

$$\overline{E}^s = i\omega\mu \int_V \overline{\overline{G}}_e \cdot \overline{J}_{eq}\, dv' - \int_V \overline{\overline{G}}_m \cdot \overline{M}_{eq}\, dv' \tag{3.7}$$

$$\overline{H}^s = i\omega\epsilon \int_V \overline{\overline{G}}_e \cdot \overline{M}_{eq}\, dv' + \int_V \overline{\overline{G}}_m \cdot \overline{J}_{eq}\, dv' \tag{3.8}$$

The total fields $\overline{E}$ and $\overline{H}$ are equal to the sum of the incident and the scattered fields.

$$\overline{E} = \overline{E}^i + \overline{E}^s \tag{3.9}$$

$$\overline{H} = \overline{H}^i + \overline{H}^s \tag{3.10}$$

Substituting equations (3.7) and (3.8) into equations (3.9) and (3.10), we obtain the following volume integral equations.

$$\overline{E} = \overline{E}^i + i\omega\mu \int_V \overline{\overline{G}}_e \cdot \overline{J}_{eq}\, dv' - \int_V \overline{\overline{G}}_m \cdot \overline{M}_{eq}\, dv' \tag{3.11}$$

$$\overline{H} = \overline{H}^i + i\omega\epsilon \int_V \overline{\overline{G}}_e \cdot \overline{M}_{eq}\, dv' + \int_V \overline{\overline{G}}_m \cdot \overline{J}_{eq}\, dv' \tag{3.12}$$

Now we let S_1 recede to infinity so that the region V_1 becomes unbounded. The Green's functions can be expressed as

$$\overline{\overline{G}}_e(\overline{r},\overline{r}') = (\overline{\overline{I}} + \frac{1}{k^2}\nabla\nabla)g(\overline{r},\overline{r}') \tag{3.13}$$

$$\overline{\overline{G}}_m(\overline{r},\overline{r}') = \nabla \times [\overline{\overline{I}}g(\overline{r},\overline{r}')] \tag{3.14}$$

where $\overline{\overline{I}}$ is the identity matrix and $g(\overline{r},\overline{r}')$ is the scalar Green's function given by

$$g(\overline{r},\overline{r}') = \frac{e^{ik|\overline{r}-\overline{r}'|}}{4\pi|\overline{r}-\overline{r}'|} \tag{3.15}$$

For scattering problem of a dielectric body of permittivity ϵ and permeability μ_o, we have

$$\overline{J}_{eq} = i\omega(\epsilon_o - \epsilon)\overline{E} \tag{3.16}$$

$$\overline{M}_{eq} = 0 \tag{3.17}$$

Substituting into equation (3.11), we obtain

$$\frac{\overline{J}_{eq}}{i\omega(\epsilon_o - \epsilon)} - i\omega\mu_o \int_V \overline{\overline{G}}_e \cdot \overline{J}_{eq}\, dv' = \overline{E}^i \tag{3.18}$$

where V is the volume of the scatterer. This is a Fredholm integral equation of the second kind, in which the unknown $\overline{J}_{eq}$ is present both inside and outside the integral.

3.3 Method of Solution

3.3.1 Point Matching Method

To solve equation (3.18), moment method with a point matching as testing is used. $\overline{J}_{eq}(\overline{r})$ is expressed in a set of basis functions, $\overline{B}_j(\overline{r})$, defined as

$$\overline{B}_j(\overline{r}) = \sum_{k=1}^{3} \hat{u}_k P_j(\overline{r}) \tag{3.19}$$

where

$$P_j(\overline{r}) = \begin{cases} 1 & \text{for } \overline{r} \in V_j \\ 0 & \text{otherwise} \end{cases} \tag{3.20}$$

and $\hat{u}_k$ denotes unit vectors $\hat{x}$, $\hat{y}$, and $\hat{z}$ in a rectangular coordinate system. The scatterer is divided into N subvolumes, in which the equivalent current is assumed to

be constant. Thus

$$\overline{J}_{eq}(\overline{r}) = \sum_{j=1}^{N}\sum_{k=1}^{3} \alpha_{jk}(\overline{B}_j(\overline{r}) \cdot \hat{u}_k)\hat{u}_k \tag{3.21}$$

Discretizing $\overline{J}_{eq}$ in terms of the basis functions, equation (3.18) can be expressed in a compact form,

$$\sum_{j=1}^{N}\sum_{k=1}^{3} \alpha_{jk}\overline{\overline{L}}(B_j^k(\overline{r})) = \overline{E}^i(\overline{r}) \tag{3.22}$$

where

$$\overline{\overline{L}} \cdot \overline{J} = \frac{\overline{\overline{I}} \cdot \overline{J}}{i\omega(\epsilon_o - \epsilon)} - \int_V i\omega\mu_o \overline{\overline{G}}_e \cdot \overline{J}\, dv'$$

and

$$B_j^k = (\overline{B}_j(\overline{r}) \cdot \hat{u}_k)\hat{u}_k$$

To determine $3N$ unknown α's, a delta weighting function (thus, the term point matching) is used to form the matrix equations

$$\overline{W}_p^n = \delta(\overline{r} - \overline{r}_p)\hat{u}_n \tag{3.23}$$

where $\overline{r}_p$ is a representative point inside the subvolume V_p.

Taking the inner product of equation (3.22), we get

$$\sum_{j=1}^{N}\sum_{k=1}^{3} \alpha_{jk} Z_{jk}^{pn} = V^{pn} \tag{3.24}$$

where

$$\begin{aligned} Z_{jk}^{pn} &= < \overline{W}_p^n, \overline{\overline{L}} B_{jk} > \\ V^{pn} &= < \overline{W}_p^n, E_n^i \hat{u}_n >= E_n^i(\overline{r}_p) \\ < \overline{f}, \overline{g} > &= \int_V \overline{f} \cdot \overline{g}\, dv \end{aligned}$$

3.3.2 Numerical Evaluation of Matrix Elements

To calculate the matrix elements Z in equation (3.24), the singularity of the Green's function must be handled with care. The problem of handling the singularity of the

Green's functions has been addressed in the literature [44, 45]. Difficulties with the numerical evaluation of the Green's function of an infinitesimally small volume has also been reported [46]. For this reason, we choose to use a finite size exclusion volume in the calculation.

In equation (3.22), the integral of the Green's function operating on the equivalent current $\overline{J}_{eq}$ involves integration of a scalar Green function and its second derivatives. Mathematically,

$$I = \int_V \overline{\overline{G}}(\overline{r}, \overline{r}') \cdot \overline{J} dv' \tag{3.25}$$

where

$$\overline{\overline{G}} = \begin{bmatrix} 1 + \frac{1}{k^2}\left(\frac{\partial^2}{\partial x_1'^2}\right) & \frac{1}{k^2}\left(\frac{\partial^2}{\partial x_1' \partial x_2'}\right) & \frac{1}{k^2}\left(\frac{\partial^2}{\partial x_1' \partial x_3'}\right) \\ \frac{1}{k^2}\left(\frac{\partial^2}{\partial x_2' \partial x_1'}\right) & 1 + \frac{1}{k^2}\left(\frac{\partial^2}{\partial x_2'^2}\right) & \frac{1}{k^2}\left(\frac{\partial^2}{\partial x_2' \partial x_3'}\right) \\ \frac{1}{k^2}\left(\frac{\partial^2}{\partial x_3' \partial x_1'}\right) & \frac{1}{k^2}\left(\frac{\partial^2}{\partial x_3' \partial x_2'}\right) & 1 + \frac{1}{k^2}\left(\frac{\partial^2}{\partial x_3'^2}\right) \end{bmatrix} g(\overline{r}, \overline{r}')$$

and g is defined in (3.15).

The second derivatives can be explicitly expressed as

$$\frac{\partial^2 g}{\partial x_m' x_n'} = k^2 \cos\theta_m \cos\theta_n \left[-1 - \frac{3i}{kR}\left(1 + \frac{i}{kR}\right)\right] + \delta_{mn} \frac{ik^2}{kR}\left(1 + \frac{i}{kR}\right) g(R) \tag{3.26}$$

where

$$R = |\overline{r} - \overline{r'}|$$

$$\cos\theta_n = \frac{x_n' - x_n}{R}$$

and δ_{mn} is the kronecker delta function.

It can be observed that $g(\overline{r})$ has an R^{-1} singularity at $R = 0$ and its second derivatives have an R^{-3} singularity at that point. The R^{-3} singularity is not generally integrable. The integral is well-defined provided the current density $\overline{J}$ satisfies the Hölder condition at the obervation point [47]. A function $J(\overline{r}')$ is said to satisfy the Hölder condition at $\overline{r}$ if there are three positive constants c, A and α, such that

$$|J(\overline{r}') - J(\overline{r})| \leq AR^{\alpha} \tag{3.27}$$

for all points $\overline{r}'$ for which $R \leq c$.

The major difficulty in evaluating the integral in (3.25) arises from the terms with the second derivatives of the scalar Green's function. The integration of the scalar Green's function which has an R^{-1} integrable singularity can be carried out numerically using an open end quadrature formula [48]. The integral

$$I_{mn}(\overline{r}) = \int_V \frac{\partial^2 g}{\partial x'_m \partial x'_n} J(\overline{r}') dv' \tag{3.28}$$

is evaluated using an approach similar to that given by Lee [46]. The integral can be separated into three terms,

$$\begin{aligned} I_{mn} &= \int_{V-V_\epsilon} J(\overline{r}') \frac{\partial^2 g}{\partial x'_m \partial x'_n} dv' + \int_{V_\epsilon} \Big[J(\overline{r}') \frac{\partial^2 g}{\partial x'_m \partial x'_n} \\ &\quad - J(\overline{r}) \frac{\partial^2 g_o}{\partial x'_m \partial x'_n} \Big] dv' + J(\overline{r}) \int_{V_\epsilon} \frac{\partial^2 g_o}{\partial x'_m \partial x'_n} dv' \end{aligned} \tag{3.29}$$

where

$$g_o(R) = \frac{1}{4\pi R}$$

Volume V_ϵ is an arbitrary volume inside V containing the observation point $\overline{r}$.

The first integral can be carried out numerically since there is no singularity in it. The second integral can be rewritten as

$$\int_{V_\epsilon} \Big[J(\overline{r}') - J(\overline{r}) \Big] \frac{\partial^2 g}{\partial x'_m \partial x'_n} dv' + J(\overline{r}) \int_{V_\epsilon} \frac{\partial^2 (g - g_o)}{\partial x'_m \partial x'_n} dv' \tag{3.30}$$

Now by choosing the flat pulse function as the basis function to approximate $\overline{J}(\overline{r})$, we have

$$\overline{J}(\overline{r}) = \overline{J}(\overline{r}') \qquad \text{for} \qquad \overline{r}, \overline{r}' \in V_l \tag{3.31}$$

and

$$g - g_o = \frac{1}{4\pi R} \Big[ikR + \frac{1}{2}(ikR)^2 + \cdots \Big] \tag{3.32}$$

in the neighborhood of $R = 0$.

The second derivative of $(g - g_o)$ is given by,

$$\frac{\partial^2(g-g_o)}{\partial x'_m \partial x'_n} = \frac{1}{4\pi}\Big[\frac{k^2}{2R}\cos\theta_m\cos\theta_n + \frac{k^4 R}{3!}\cos\theta_n\cos\theta_m + \cdots + \delta_{mn}\Big(\frac{-k^2}{2R} - \frac{ik^3}{3} + \frac{k^4 R}{3!} + \cdots\Big)\Big] \tag{3.33}$$

with δ_{mn} as the kronecker delta function.

Now that the integral has an R^{-1} singularity, and it can be handled in the same manner as that of the scalar Green's function. The third integral in (3.29) can be converted to a surface integral that depends on the shape of the exclusion volume V_ϵ and the observation point:

$$\int_{V_\epsilon} \frac{\partial^2 g_o}{\partial x'_m \partial x'_n} dv' = \frac{1}{4\pi}\int_{S_\epsilon} \frac{(\hat{x}_m \cdot \hat{n})(\hat{x}_n \cdot \hat{R})}{R} ds' \tag{3.34}$$

where

$$\hat{R} = \frac{\overline{r}' - \overline{r}}{|\overline{r}' - \overline{r}|}$$

and $\hat{n}$ is the outward normal to the exclusion volume.

3.3.3 Thin Cylinder Considerations

The discussion of the previous subsection is applicable to any arbitrarily shaped scatterer. However, certain assumptions were made when the computer code was developed. The code is developed primarily for electrically thin cylinder structures, i.e. $ka \ll 1$, k being the free space wavenumber and a the representative radius of the cylinder structure. In the discretization process, the structure is divided into cylindrically shaped subcells. It is then natural to use an exclusion volume of cylindrical shape. The exclusion volume is chosen to be a cylinder of radius a and length b, where b is the minimum of the length of the cylindrical subcell and one fortieth of the wavelength. The restriction on b is required because of the dimensions of the subcell and the validity of the approximation in (3.33). The aspect ratio of the subcell is an important factor in evaluating matrix elements. When the matrix elements for

non-diagonal terms are evaluated by discrete dipole approximation [49], i.e.

$$\begin{aligned} I_{mn} &= \int_{V_n} \overline{\overline{G}}(\overline{r},\overline{r}') \cdot \overline{J} dV' \\ &\approx G_{x_p x_q}(\overline{r}_m,\overline{r}_n)\Delta V_n \end{aligned} \tag{3.35}$$

where

$$G_{x_p x_q}(\overline{r},\overline{r}') = i\omega\mu_o(\delta_{pq} + \frac{1}{k^2}\frac{\partial^2}{\partial x_p \partial x_q})g(\overline{r},\overline{r}')J_q(\overline{r}_n) \tag{3.36}$$

inconsistent results are obtained with different aspect ratios as shown in Figs. 3-2 and 3-3. Similar phenomena were reported by Su [50] for a two dimensional case. The problem can be alleviated by carrying out numerical integration for the matrix elements that involve neighboring subcells. Figs. 3-4 and 3-5 show the results with the implementation of numerical integration for evaluating all matrix elements. In order to speed up the process of setting up the matrix, the dipole approximation can be made when two subcells are far apart.

3.4 Results and Discussion

The numerical results are first verified by comparing to results from another MoM code for body of revolution geometries based on the surface integral formulation [51]. The observation of the optical theorem (as known as extinction theorem) is also checked. After that, the computer code is applied to model branching vegetation clusters. The theoretical results are then compared with experimental data.

The backscattering cross sections of a cylinder of permittivity $\epsilon = (3 + i0.5)\epsilon_o$, length $l = \lambda$, radius $a = \lambda/10$ at 3 GHz as a function of incidence angle are shown in Figs. 3-6 and 3-7. The results agree very well with that from the body of revolution code. In Figs. 3-8 and 3-9, the total scattering cross section, absorption cross section, their sum and the extinction cross section are plotted for the same cylinder. The extinction cross section is calculated from the optical theorem given by [1]

$$\sigma_{epp} = \frac{4\pi}{k_o} Im\{f_{pp}(\theta_i,\theta_i)\}, \qquad p = v,h \tag{3.37}$$

where k_o is the free space wavenumber, and f_{pp} is the scattering function in the forward scattering direction. By energy conservation, the extinction cross section is equal to sum of the absorption and the total scattering cross sections.

The model is then applied to model vegetation clusters. The theoretical results are compared with X-band experiments on cylindrically shaped forest components [52]. The experiment was carried out under laboratory conditions in which the parameters of the vegetation components can be measured and controlled. Transmission measurements were performed on simulated canopies composed of bare deciduous twigs and leafy coniferous branches at 9 GHz. The system consisted of transmitting and receiving antennas. The antennas were linearly polarized. The vertically oriented vegetation samples were placed on a Styrofoam frame in one or several rows between the two antennas (Fig. 3-10). Parameters for the samples are given in Table 3.1. Measurements were performed with vegetative targets and the transmitted powers were recorded. Different samples were used and averaged to give the received power P_1. After removing the targets, the reference power P_o was then recorded. The loss factor, $L(\theta_i, p)$, is defined as the one way transmission loss through the vegetation canopy for the incidence angle θ_i with a polarization angle p, such that

$$L(\theta_i, p) = 10 \log \frac{P_o}{P_1} \quad . \tag{3.38}$$

For the theoretical calculation, Foldy's approximation [1, 53, 54] is employed to account for the attenuation introduced by the medium. The propagation of the coherent wave with E_h and E_v as the horizontal and the vertical components of the electric field is governed by the following equations:

$$\frac{dE_v}{ds} = (ik_o + M_{vv})E_v + M_{vh}E_h \tag{3.39}$$

$$\frac{dE_h}{ds} = M_{hv}E_v + (ik_o + M_{hh})E_h \tag{3.40}$$

where s is the distance along the direction of propagation, and

$$M_{jl} = \frac{i2\pi n_o}{k_o} < f_{jl}(\theta, \phi; \theta, \phi) > \qquad j, l = v, h \tag{3.41}$$

with (θ, ϕ) as the direction of propagation, n_o the number density of the scatterers, and $<>$ denotes ensemble average over the orientation and size distribution of the scatterers. For vegetation canopy that exhibits azimuthal symmetry, there is no coupling between the horizontal and vertical components of the coherent field. Hence the cross-polarized components M_{hv} and M_{vh} are zero. The effective propagation constants are given by

$$k_p = k_o - iM_{pp} \qquad p = v, h \tag{3.42}$$

The effective propagation constants are then used to calculate the loss factor [55]. The received power for a linearly polarized wave transmitted through the medium with the effective propagation given in (3.42) at the incidence angle of θ_i is given by

$$P_r = C_r |\cos\psi_i \cos\psi_r e^{-i\delta_v d/\cos\theta_i} + \sin\psi_i \sin\psi_r e^{-i\delta_h d/\cos\theta_i}|^2 \tag{3.43}$$

where

$$C_r = \frac{1}{\eta_o} G_r \frac{\lambda_o^2}{4\pi} \tag{3.44}$$

$$\delta_p = iM_{pp} \qquad p = v, h \tag{3.45}$$

and G_r is the gain, η_o is the intrinsic wave impedance, λ_o is the wavelength, d is the depth of the medium, and ψ_i and ψ_r are respectively the polarization angles for the incident wave and the receiving antenna. The polarization angle is defined to be the angle between the incident polarization vector and the vertical. Hence, 0^o corresponds to the vertical polarization, and 90^o corresponds to the horizontal polarization. The reference received power is measured with the vegetative target removed, i.e. δ_p are zero. The loss factor for the co-polarized transmitted field is measured with $\psi_i = \psi_r$

and is given as

$$L(\theta_i, \psi_i) = |\cos^2\psi_i e^{-\kappa_{ev}d/2\cos\theta_i} + \sin^2\psi_i e^{-\kappa_{eh}d/2\cos\theta_i} e^{i\Delta\beta d/\cos\theta_i}|^{-2} \tag{3.46}$$

where

$$\kappa_{ep}(\theta_i) = \frac{4\pi}{k_o} n_o Im(< f_{pp}(\theta;\theta) >) \tag{3.47}$$

and

$$\Delta\beta = (2\pi k_o) n_o [Re(< f_{hh}(\theta;\theta) >) - Re(< f_{vv}(\theta;\theta) >)] \tag{3.48}$$

The dielectric constant of the leaves is determined using the Ulaby and El Rayes' model [56] according to the water content of the leaves reported in reference [52]. The method of moments code is used to calculate the scattering function of the vegetation samples. Realizations of the vegetation sample are made according to the parameters given in Table 3.1. Averaging over different realizations is performed to obtain average scattering amplitudes. In Fig. 3-11, we show the comparison of the theoretical calculations and experimental data for the attenuation of vertically oriented bare twigs as a function of incidence angle. Good agreement is observed. In Figs. 3-12 through 3-14, we compare the theoretical loss factors with the measurements as a function of the polarization angles at an incidence angle of 90^o for different species. For the calculation, the needles are assumed to be entirely responsible for the measured attenuation. Hence only the needle characteristics are incorporated in the model and the central twig is neglected. The needles are assumed to have the same circular cross section with radius a. The needle orientation for different coniferous species was estimated [52] and the probability density function is used to generate a vegetation sample. Only the center one third portion of the structure is used in the calculation due to the limitation of computer resources. The number of twigs used in the vegetative target is not reported, therefore only a qualitative study is carried out. The theoretical curve is adjusted to the experimental curve by choosing a suitable number of scatterers, n_o, in equation (3.46). Scots pine twigs (Fig. 3-12), which are mostly oriented at 30^o from the vertical, have the most variation with polarization

angle, while Norway spruce twigs (Fig. 3-13) have less variation. Douglas fir twigs (Fig. 3-14) have a planophil distribution (more horizontal orientation) and hence they have more attenuation for the horizontal polarization. The discrepancies for the results of Scots pine and Douglas fir twigs are larger than that of Norway spruce twigs. The distribution function of the branching angle is unknown and it can be the main source of error. Scots pine and Douglas fir may have a larger deviation from their mean value given in reference [52] and hence larger discrepancies are observed. The comparison between the model and experimental data shows that the attenuation behavior of vegetation components at X-band microwaves can be predicted reasonably well by scattering functions obtained from the method of moments calculation.

3.5 Summary

A method of moments code based on the volume integral equation of the electric field is formulated and developed to compute both the scattered fields and absorption cross sections by thin cylinder structures. It is able to solve for scattering and absorption of complex cylinder structures with complex permittivity illuminated at an arbitrary angle of incidence by a linearly polarized plane wave. It has been applied to calculate the scattering function for coniferous leaves and the theoretical attenuations using the Foldy's approximation for sparse medium. A good agreement between the model and observations is obtained at X-band for various forest components. An important application of the model would be in the study of clustering effects exhibited by vegetation, since the model accounts for the mutual interactions between the components of the structure. The model can also be used to construct the phase matrix and extinction matrix in the radiative transfer equations, which can then be used to calculate scattering and emission from a vegetation canopy.

Species Parameters	Scots pine	Norway spruce	Douglas fir
Needle azimuth distribution	uniform	quasi uniform	quasi uniform
Needle elevation distribution	extremophil 30^o	extremophil 45^o	planophil 70^o
Needle length cm	5.4	1.8	2.3
Needle thickness mm	0.7	0.8	0.3
Needle width mm	1.5	1.2	1.2
Needle density N/cm	10.5	13.9	18.8
twig diameter cm	1.0	0.36	0.28

Table 3.1: Characteristics of the coniferous needles.

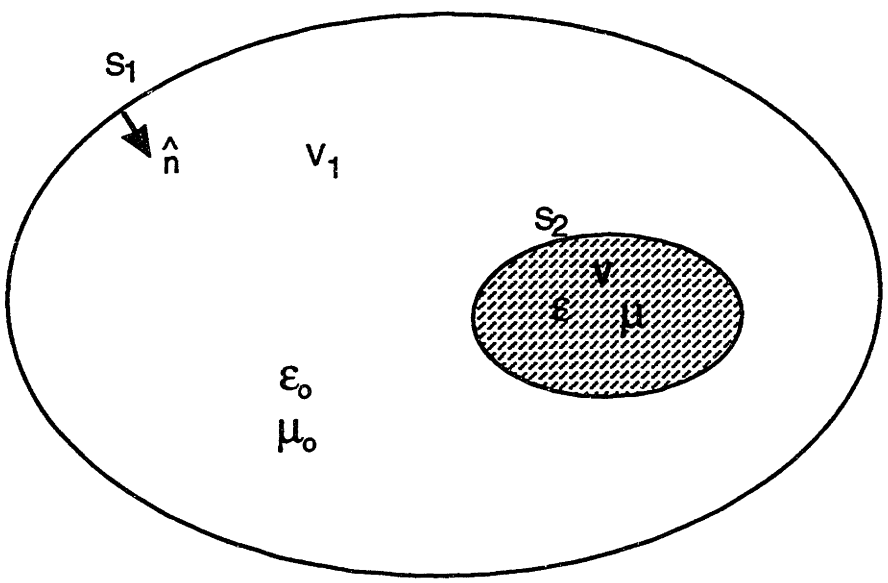

Figure 3-1: Scattering problem for an inhomogeneous material body.

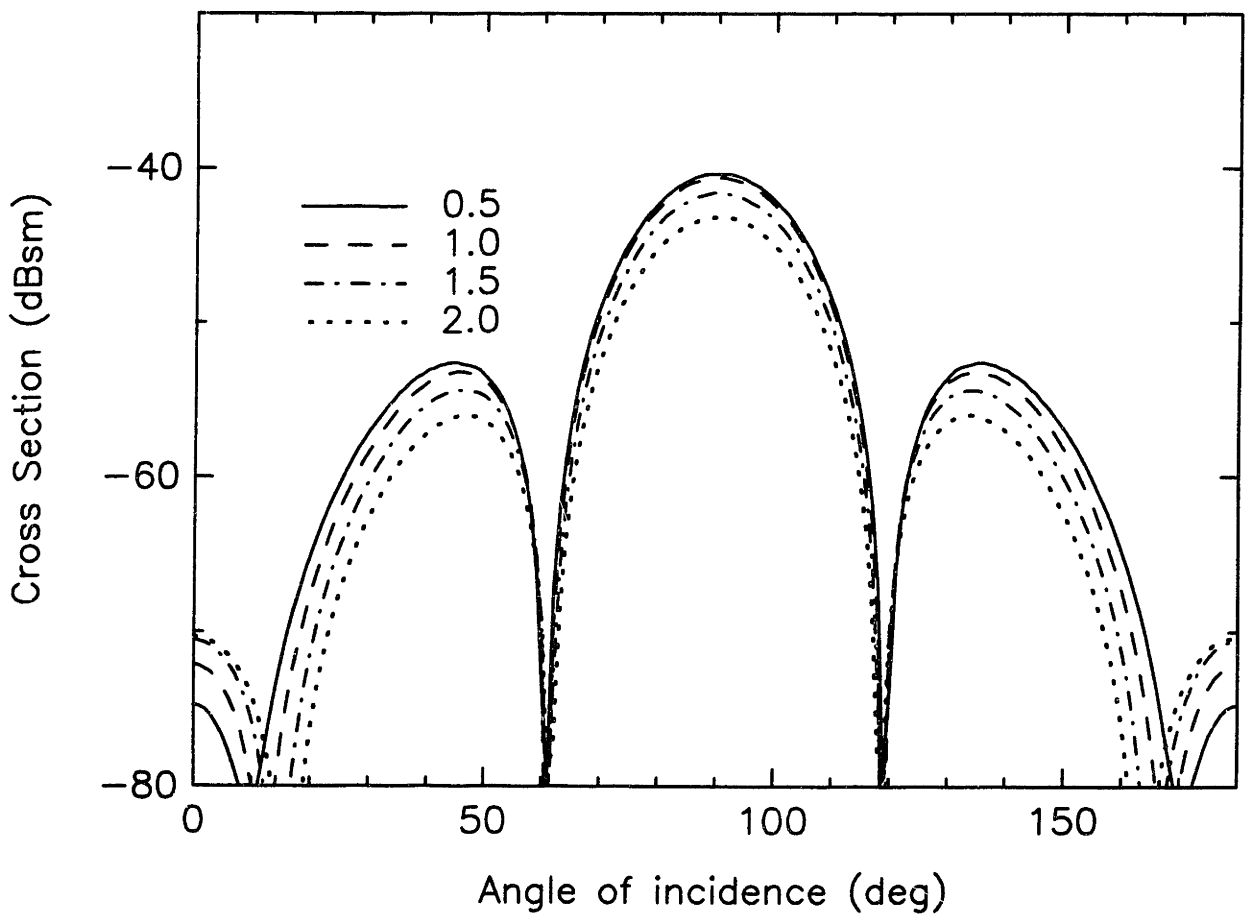

Figure 3-2: Backscattering cross sections as a function of incidence angle of a cylinder of length $l = 10$ cm, radius $r = 0.5$ cm, and $\epsilon = (3 + i0.5)\epsilon_o$ at 3 GHz with subcells of different aspect ratio ($= 2r/\Delta l$) using dipole approximation. Aspect ratio = 0.5,1.0,1.5,2.0 for horizontal polarization.

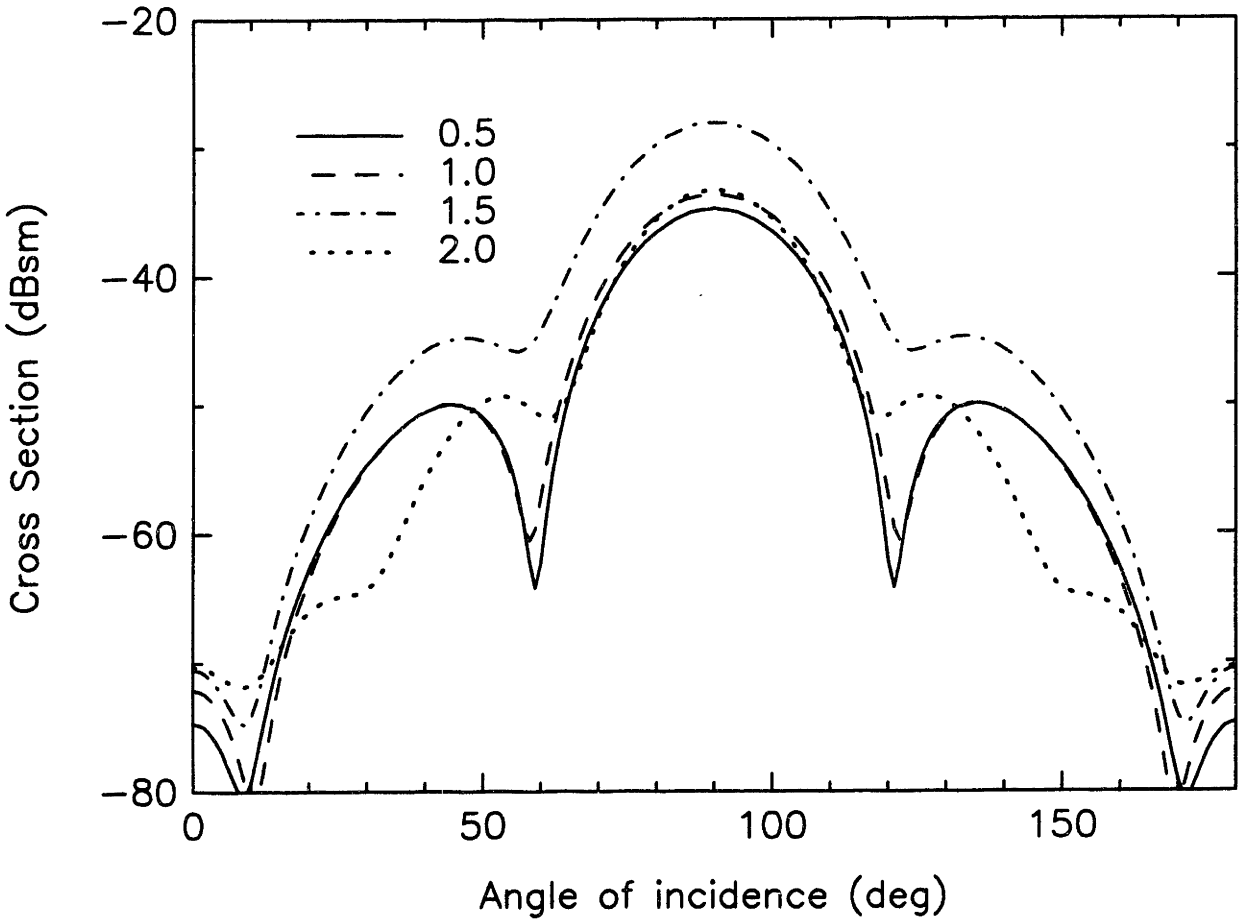

Figure 3-3: Backscattering cross sections as a function of incidence angle of a cylinder of length $l = 10$ cm, radius $r = 0.5$ cm, and $\epsilon = (3 + i0.5)\epsilon_o$ at 3 GHz with subcells of different aspect ratio ($= 2r/\Delta l$) using dipole approximation. Aspect ratio = 0.5,1.0,1.5,2.0 for vertical polarization.

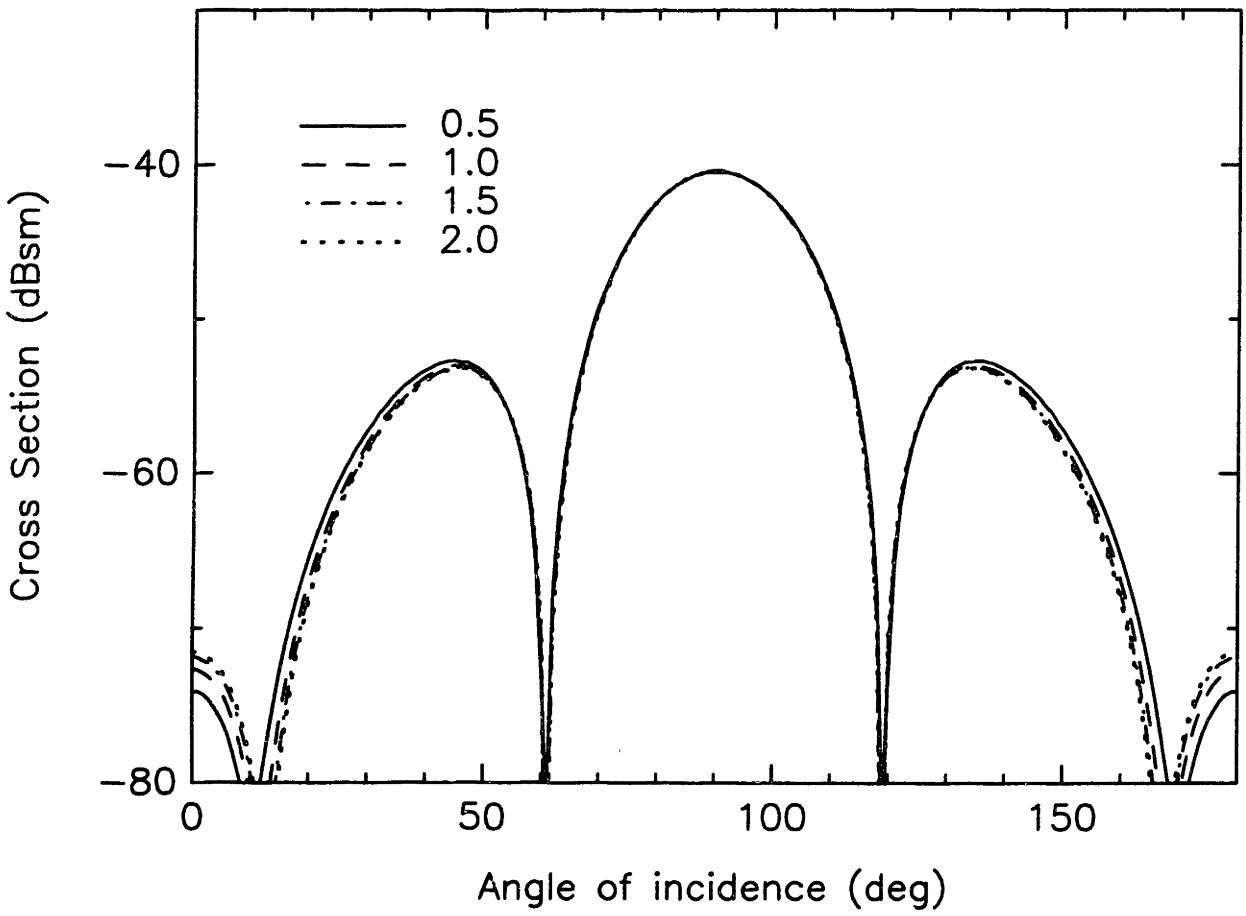

Figure 3-4: Backscattering cross sections as a function of incidence angle of a cylinder of length $l = 10$ cm, radius $r = 0.5$ cm, and $\epsilon = (3 + i0.5)\epsilon_o$ at 3 GHz with subcells of different aspect ratio ($= 2r/\Delta l$) using numerical integration to evaluate matrix elements. Aspect ratio = 0.5,1.0,1.5,2.0 for horizontal polarization.

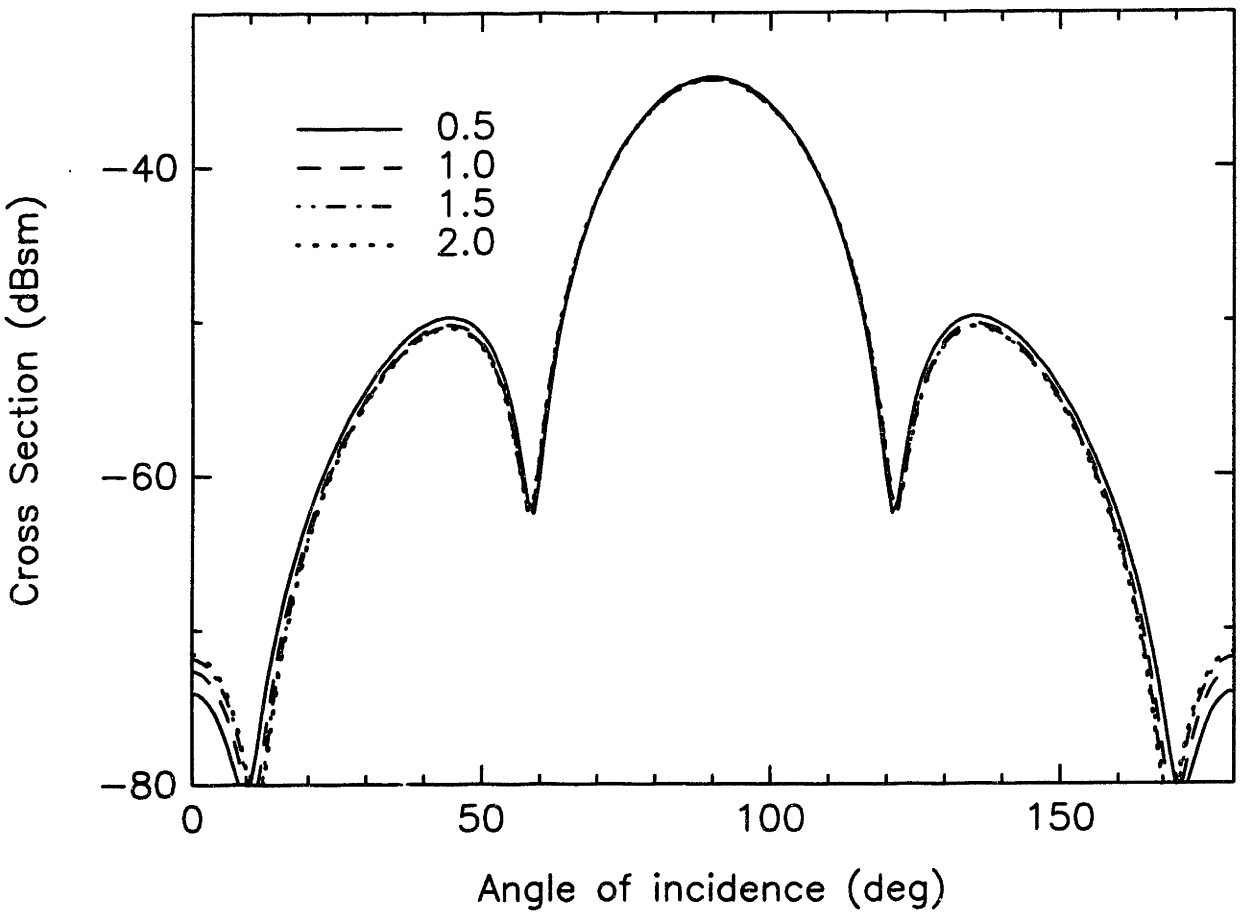

Figure 3-5: Backscattering cross sections as a function of incidence angle of a cylinder of length $l = 10$ cm, radius $r = 0.5$ cm, and $\epsilon = (3 + i0.5)\epsilon_o$ at 3 GHz with subcells of different aspect ratio ($= 2r/\Delta l$) using numerical integration to evaluate matrix elements. Aspect ratio = 0.5,1.0,1.5,2.0 for vertical polarization.

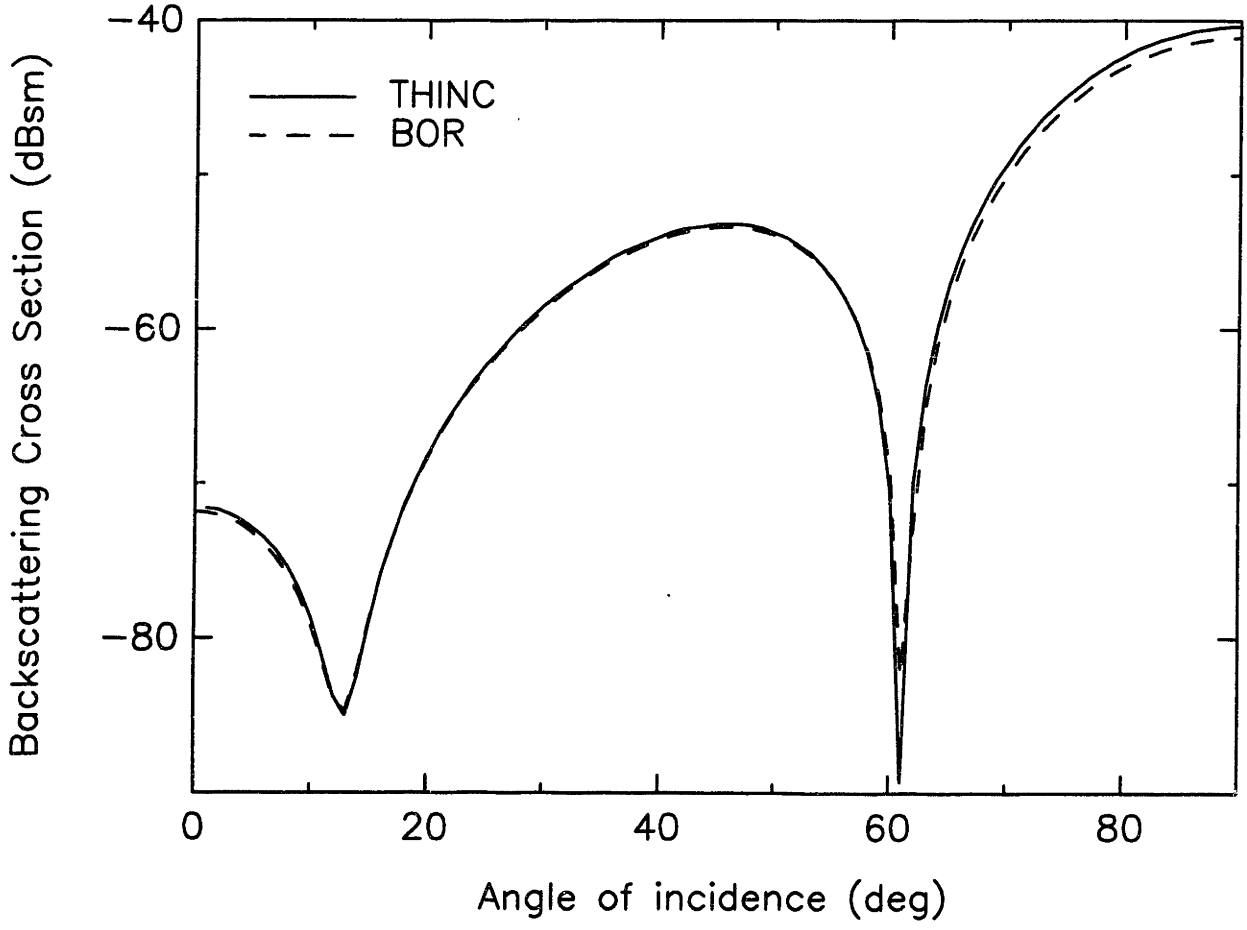

Figure 3-6: Comparison of backscattering cross sections as a function of incidence angle as computed by THINC and body of revolution code using surface integral approach. Cylinder length $l = 10$ cm, radius $r = 0.5$ cm, and $\epsilon = (3 + i0.5)\epsilon_o$ at 3 GHz for horizontal polarization.

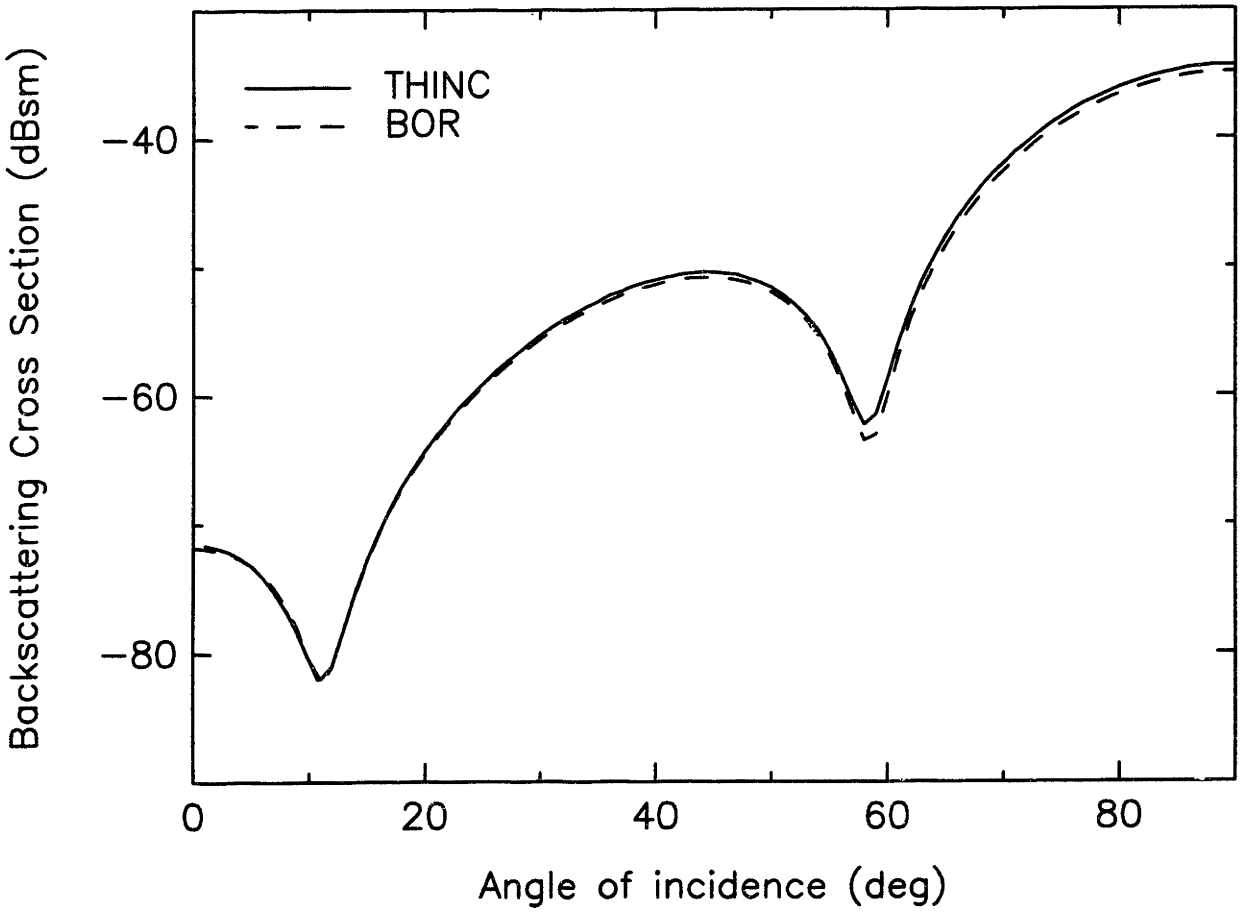

Figure 3-7: Comparison of backscattering cross sections as a function of incidence angle as computed by THINC and body of revolution code using surface integral approach. Cylinder length $l = 10$ cm, radius $r = 0.5$ cm, and $\epsilon = (3 + i0.5)\epsilon_o$ at 3 GHz for vertical polarization.

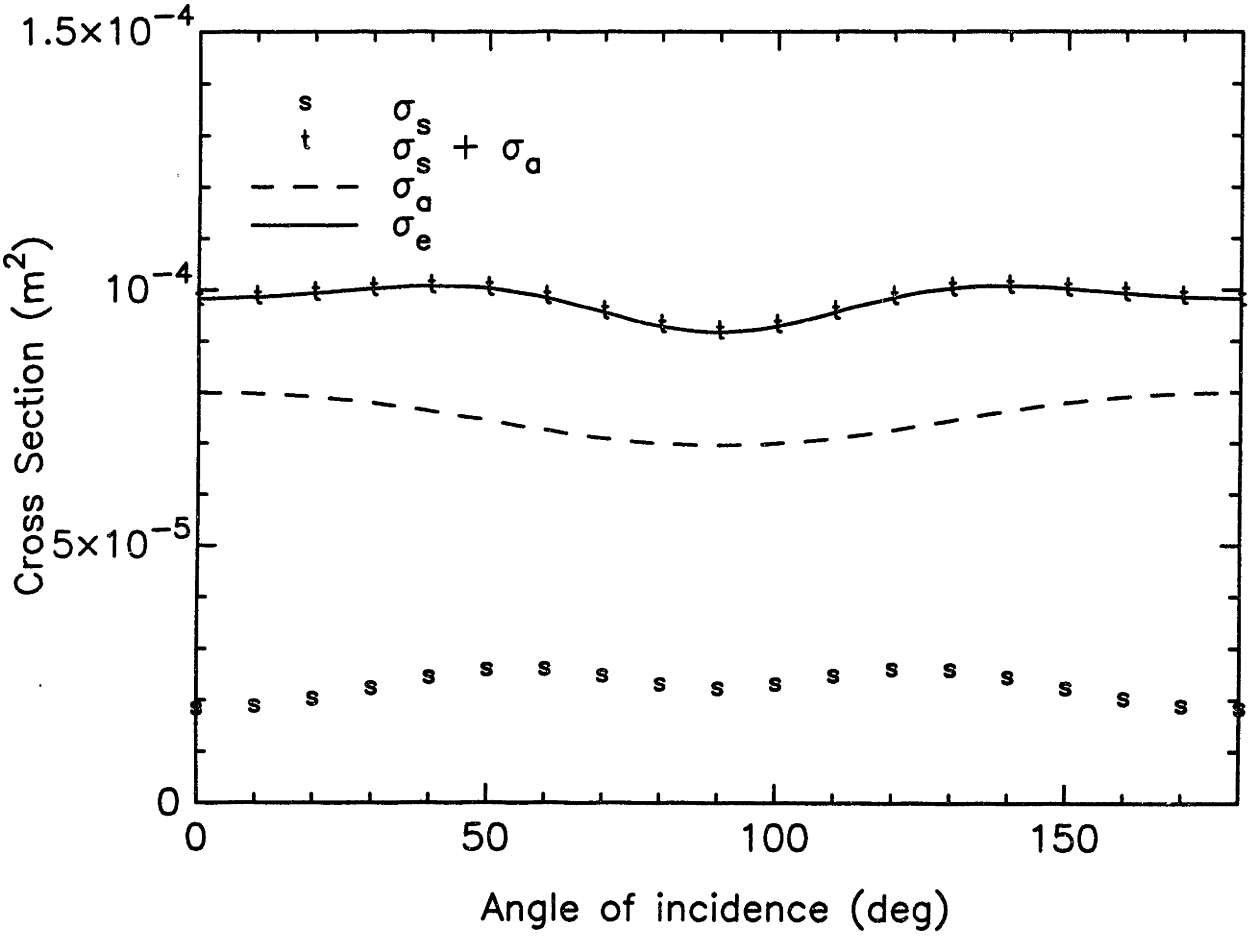

Figure 3-8: Absorption, extinction and total scattering cross sections as a function of incidence angle for a cylinder of length $l = 10$ cm, radius $r = 0.5$ cm and $\epsilon = (3 + i0.5)\epsilon_o$ at 3 GHz for horizontal polarization.

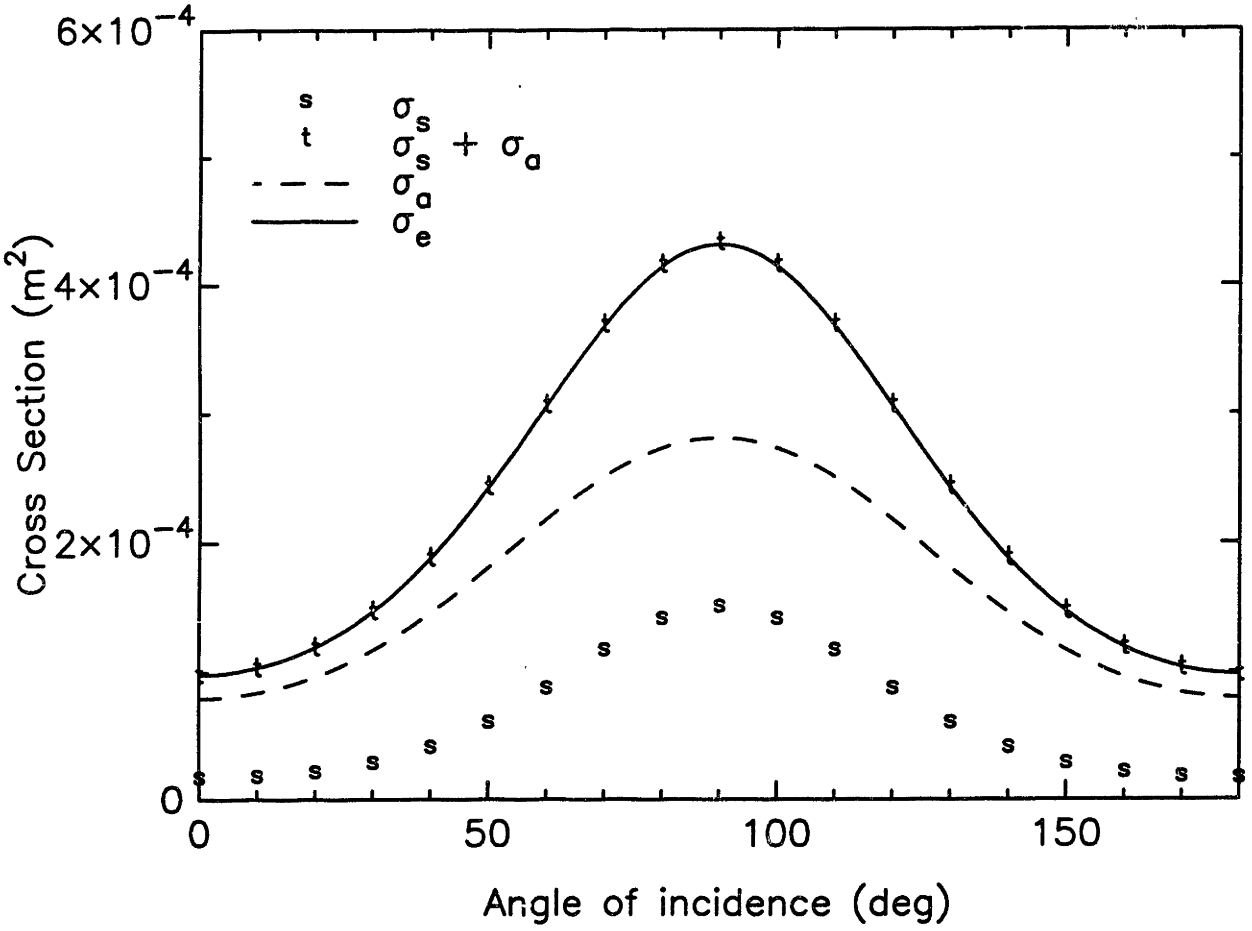

Figure 3-9: Absorption, extinction and total scattering cross sections as a function of incidence angle for a cylinder of length $l = 10$ cm, radius $r = 0.5$ cm and $\epsilon = (3 + i0.5)\epsilon_o$ at 3 GHz for vertical polarization.

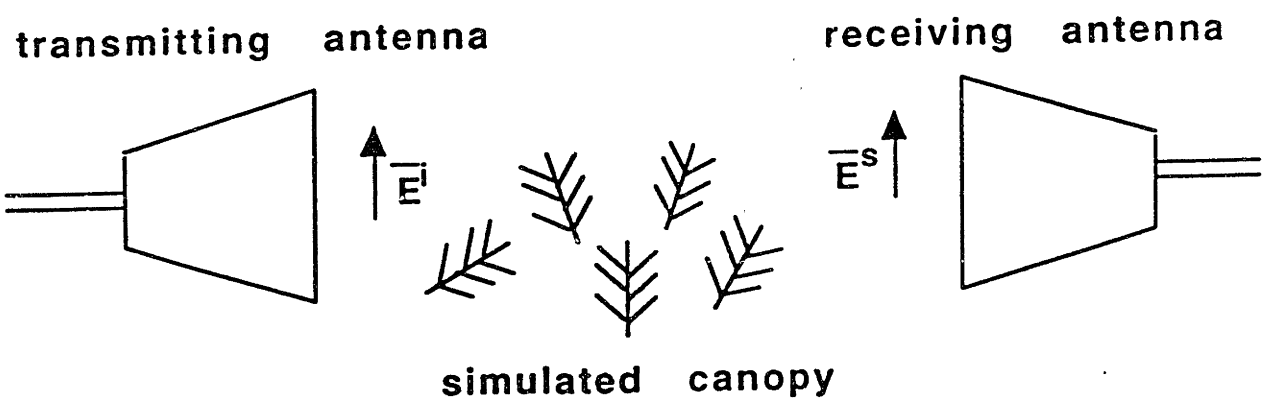

Figure 3-10: Experiment setup for microwave coherent propagation in cylindrically shaped forest components [52].

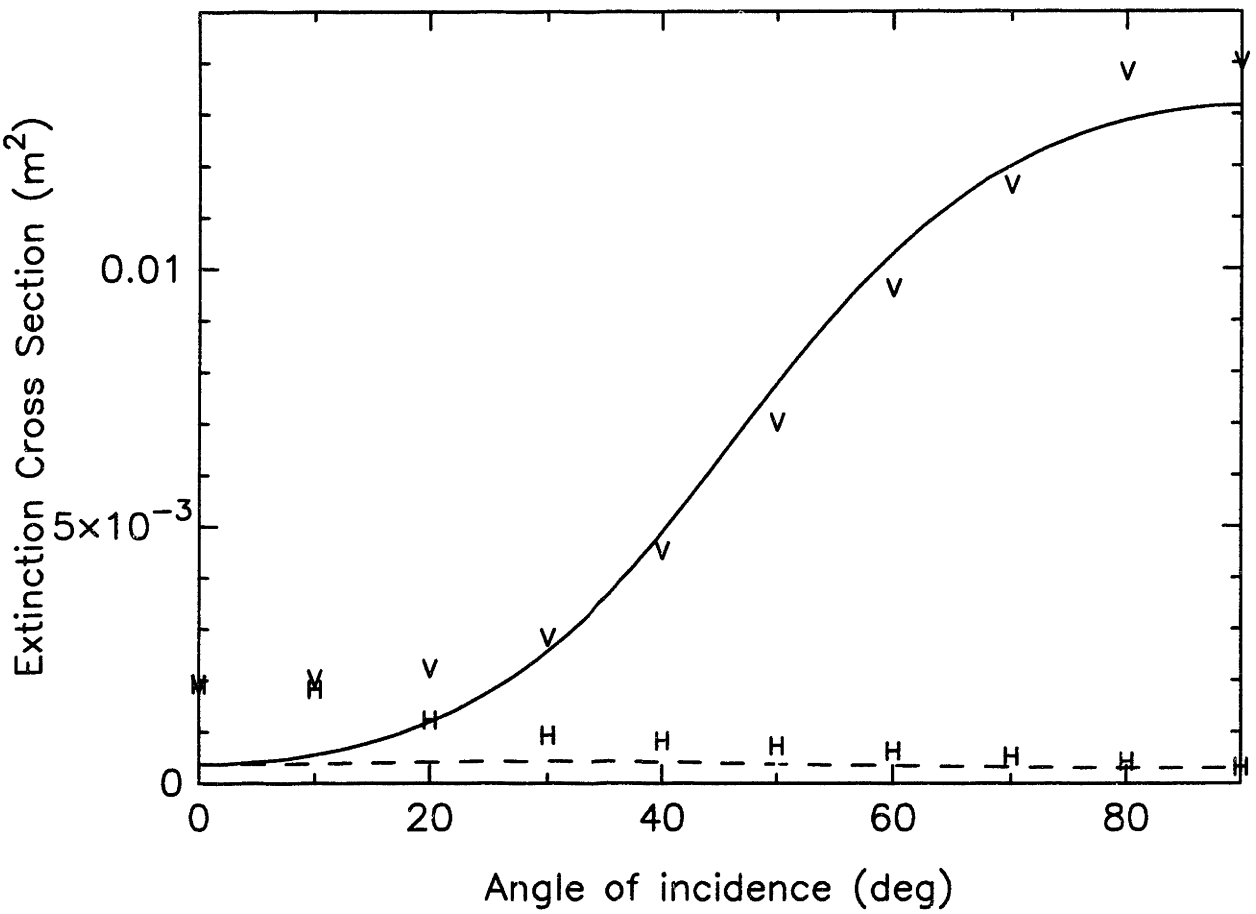

Figure 3-11: Comparison of theoretical extinction cross section of bare twigs and experimental data as a function of incidence angle θ_i for a cylinder of length 10 cm, radius 1.5 mm, at 9 GHz. ϵ is chosen to be $(11 + i4)\epsilon_o$.

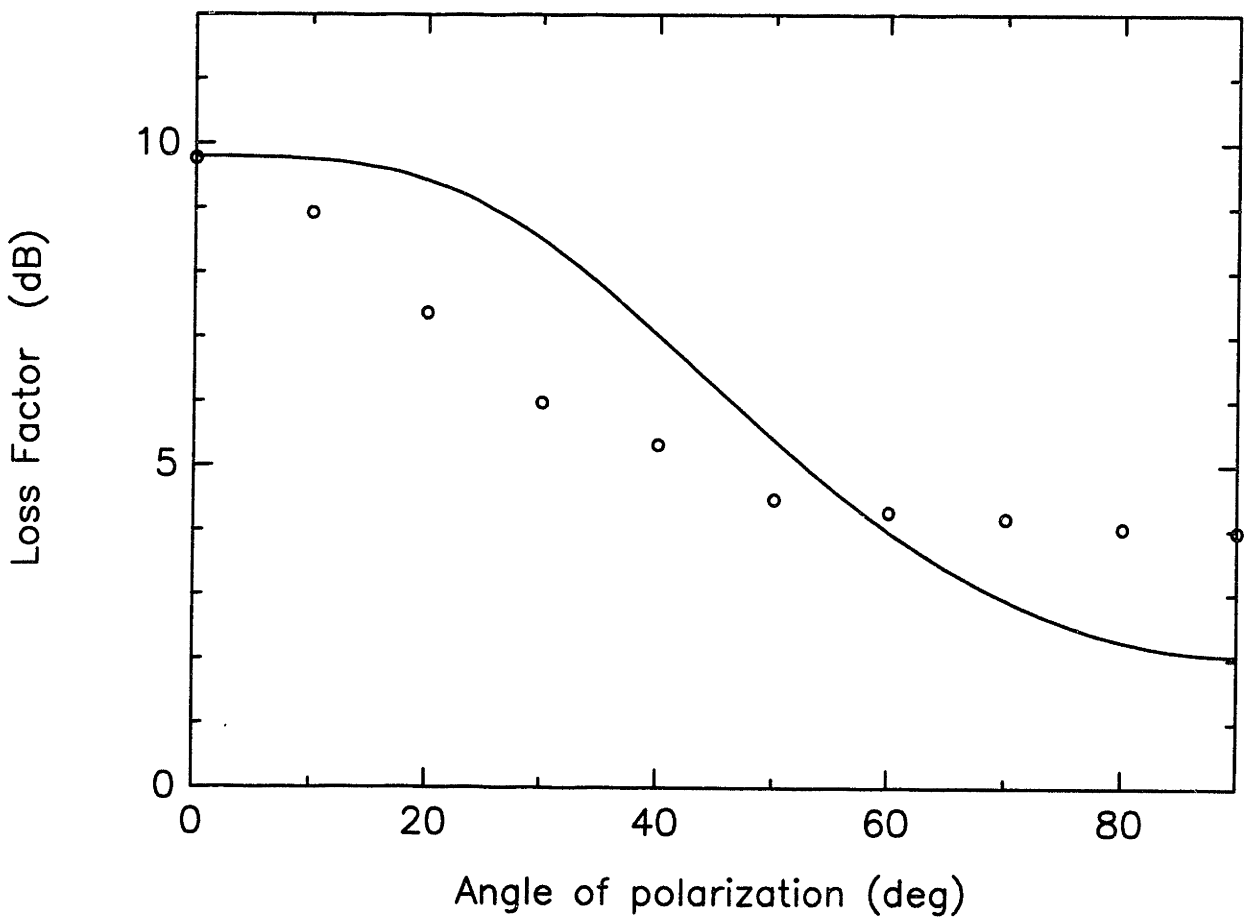

Figure 3-12: Comparison of theoretical loss factor and measurements as a function of polarization angle ψ_i, ($\theta_i = 90^o$) for Scots pine.

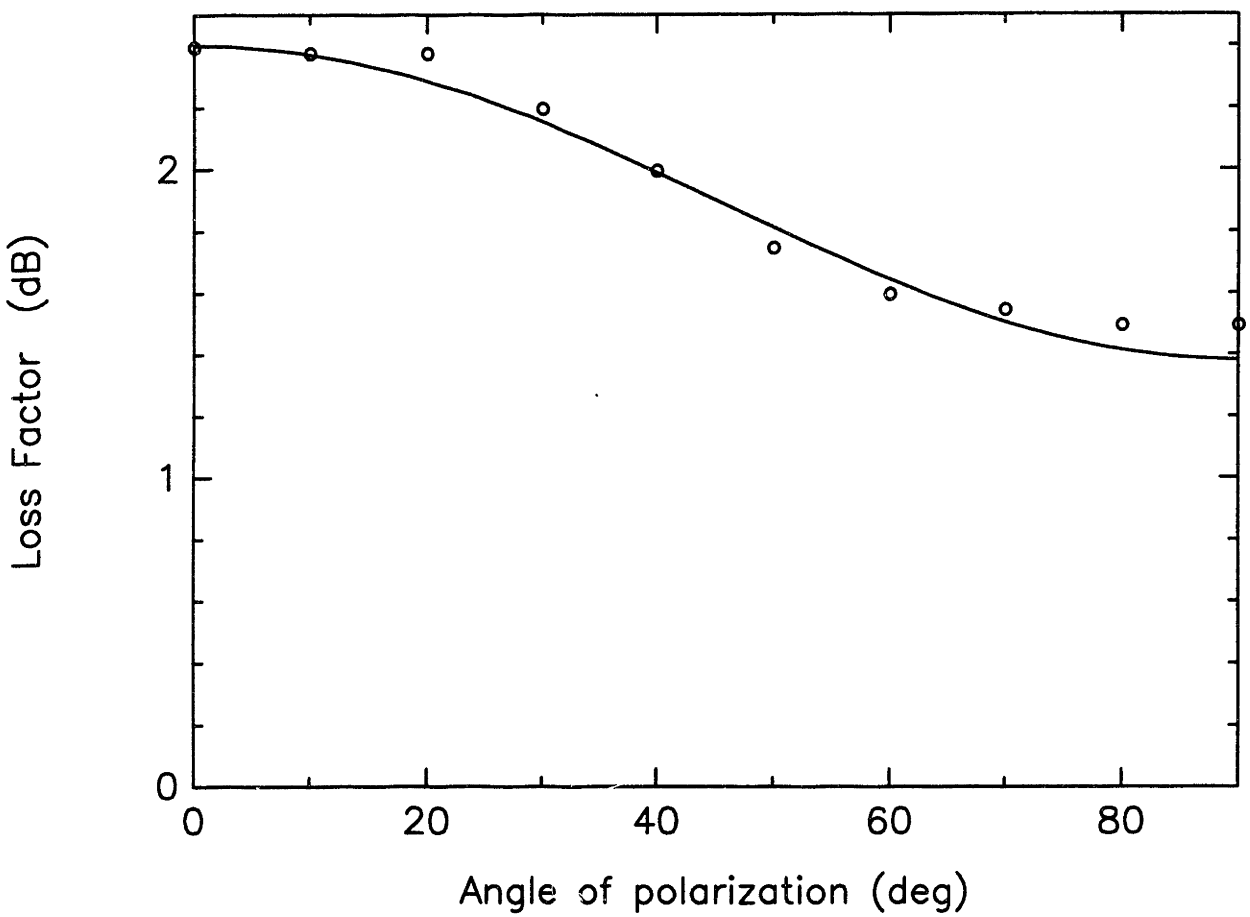

Figure 3-13: Comparison of theoretical loss factor and measurements as a function of polarization angle ψ_i, ($\theta_i = 90^o$) for Norway spruce twigs.

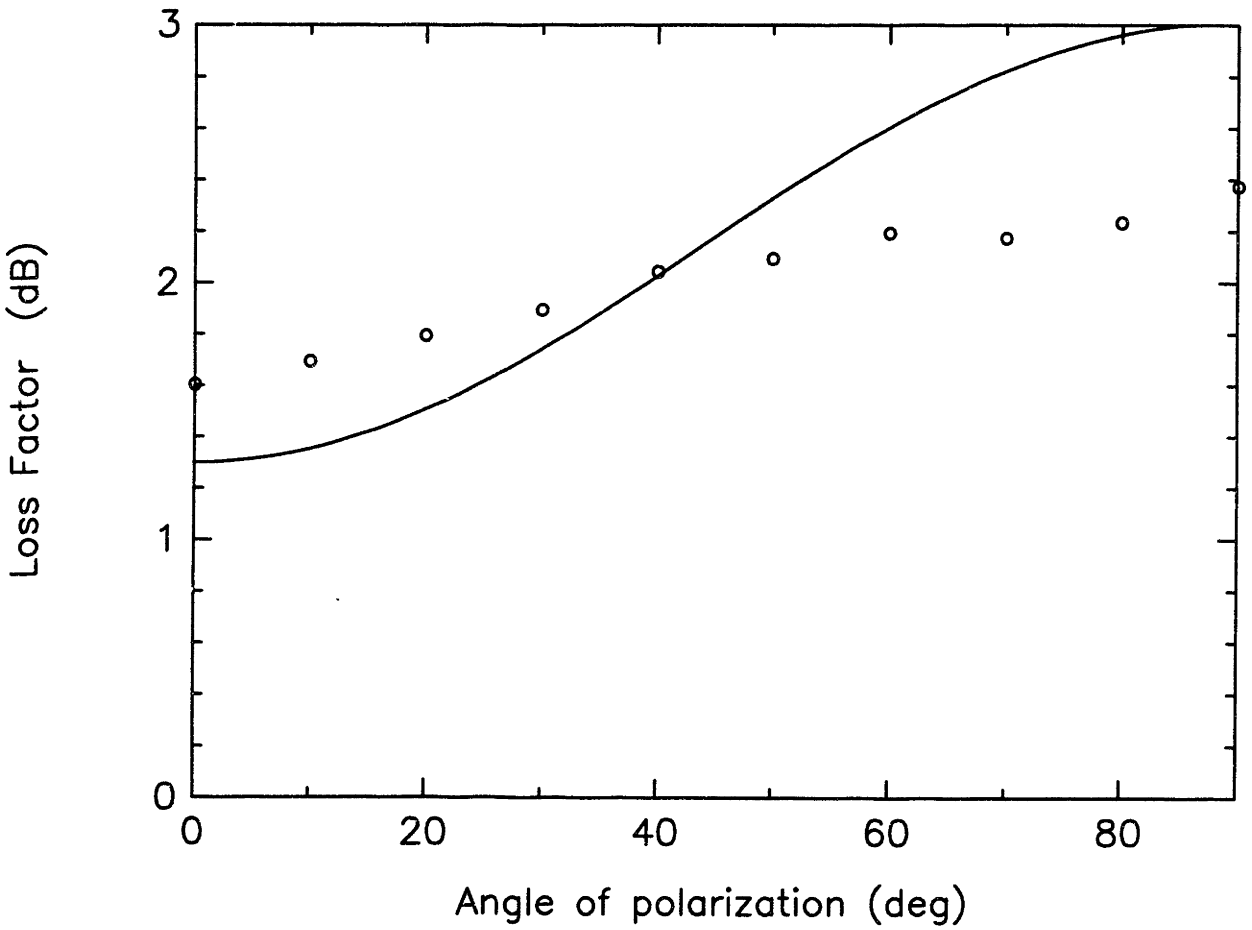

Figure 3-14: Comparison of theoretical loss factor and measurements as a function of polarization angle ψ_i, ($\theta_i = 90°$) for Douglas fir twigs.

Chapter 4

Radiative Transfer Theory for Active Remote Sensing: Discrete Scatterer Model

4.1 Introduction

In the remote sensing of geophysical terrains such as snow, ice and vegetation canopies, random medium models, including continuous medium and discrete scatterer approaches, have been applied to study volume scattering [1]. There has been a growing interest in the investigation of the clustering effects in electromagnetic wave scattering problems [24, 57]. The structures and the relative positions of the scatterers have been found to play important roles in scattering.

In the continuous random medium approach [15, 58], the permittivity fluctuation is described by a correlation function in which the variance and the correlation length represent the fluctuation strength and the geometry of the scatterers, respectively. The effective permittivity is evaluated to account for the attenuation and the phase delay of the wave propagation inside the medium. The distorted Born approximation is frequently used to calculate the scattered field.

In the discrete scatterer approach [18, 53, 59, 60], the medium is modeled as a collection of scatterers embedded in a background medium. Foldy's approximation [61]

can be used for sparsely distributed scatterers while quasi-crystalline approximation (QCA) and quasi-crystalline approximation with coherent potential [17, 62] can be used for dense media. QCA takes into account the interaction of the electromagnetic waves between correlated particles. The formulation uses bivariate particle statistics, or a pair correlation function, to provide a rigorous mathematical description of the particle placement. When the discrete scatterer approach is applied to vegetation, vegetation is usually modeled as a collection of canonically shaped dielectric scatterers such as discs and cylinders [20-22]. The internal field and the scattered field are estimated by various approximations, such as the finite cylinder approximation and the physical optics approximation. Backscattering cross sections of vegetation are evaluated as the sum of its components' backscattering cross sections, assuming independent scattering. Yueh *et al* [24] proposed a branching model in which the collective coherent scattering effect is considered by taking into account the phase shift due to the relative positions of the scatterers in the calculation of the scattered field. A significant difference in the bistatic scattering coefficients from independent scattering is obtained due to the coherent scattering effects. However, in approximating the induced current for each scattering component, the mutual interaction (multiple scattering) was not considered. In this chapter, the scattered fields calculated by the MoM code developed in the previous chapter are used in the radiative transfer equations. The mutual interactions between components of the scatterer are then accounted for in the calculation.

After obtaining the scattering function from a scatterer, radiative transfer theory is employed to study the scattering characteristics of a layer of medium containing the scatterers. Radiative transfer theory starts with the radiative transfer equations which govern the propagation of energy through the scattering medium. It lacks the mathematical rigor of wave theory which is based on Maxwell's equations. In radiative transfer theory, it is assumed that there is no correlation between fields and therefore, the addition of intensities is considered rather than the addition of fields. It has the advantage that the formulation is simple, and multiple scattering effects can be included rather straightforwardly. In this chapter, the extinction matrix and

phase matrix are calculated using the MoM and incorporated in the radiative transfer equation. The iterative first order solution of vector radiative transfer equation for active remote sensing is derived. Theoretical results of the backscattering coefficients from cylinder clusters with a planar bottom boundary condition are given.

4.2 Vector Radiative Transfer Equation for Active Remote Sensing

Consider a two-layer structure with discrete scatterers embedded in a homogeneous layer with a flat ground surface as shown in Fig. 4-1. The vector radiative transfer equation inside region 1 can be written as

$$\begin{aligned} \cos\theta \frac{d\overline{I}(\theta,\phi,z)}{dz} &= -\overline{\overline{\kappa}}_e(\theta,\phi)\cdot\overline{I}(\theta,\phi,z) \\ &\quad + \int_{4\pi} d\Omega' \overline{\overline{P}}(\theta,\phi;\theta',\phi')\cdot\overline{I}(\theta'\phi',z) \end{aligned} \tag{4.1}$$

$\overline{I}$ is the specific intensity that contains information on field intensities, polarizations and phase relations. It is defined as

$$\overline{I} = \begin{bmatrix} I_v \\ I_h \\ U \\ V \end{bmatrix} = \begin{bmatrix} <|E_v|^2>/\eta \\ <|E_h|^2>/\eta \\ 2Re<E_vE_h^*>/\eta \\ 2Im<E_vE_h^*>/\eta \end{bmatrix} \tag{4.2}$$

where η is the wave impedance.

Equation (4.1) states that as the specific intensity propagates through the medium in the direction of (θ,ϕ), it is attenuated by the medium ($\overline{\overline{\kappa}}_e$) through scattering and absorption losses, and enhanced by the scattered intensities due to scattering from all directions into the (θ,ϕ) direction. $\overline{\overline{\kappa}}_e$ is the extinction matrix that describes the attenuation of the specific intensity and $\overline{\overline{P}}$ is the phase matrix that describes the scattering of the specific intensity from the direction of (θ',ϕ') into the (θ,ϕ) direction.

The derivations of these matrices are given in the next section.

Since we are interested in simulating vegetation canopy, the sparse approximation can be assumed. The background permittivity of the canopy can be taken as that of the free space. Therefore the specific intensity at the upper interface ($z = 0$) is the same as the incident wave. At the lower interface, the reflection of the flat boundary can be described by the reflection matrix $\overline{\overline{R}}_{12}$. Mathematically, the boundary condition for equation (4.1) can be stated as

$$\overline{I}(\pi - \theta, \phi, z = 0) = \delta(\cos\theta - \cos\theta_o)\delta(\phi - \phi_o)\overline{I}_o \tag{4.3}$$

$$\overline{I}(\theta, \phi, z = -d) = \overline{\overline{R}}_{12}(\theta) \cdot \overline{I}(\pi - \theta, \phi, z = -d) \tag{4.4}$$

where

$$\overline{\overline{R}}_{12}(\theta) = \begin{bmatrix} |R_v(\theta)|^2 & 0 & 0 & 0 \\ 0 & |R_h(\theta)|^2 & 0 & 0 \\ 0 & 0 & Re(R_v(\theta)R_h^*(\theta)) & -Im(R_v(\theta)R_h^*(\theta)) \\ 0 & 0 & Im(R_v(\theta)R_h^*(\theta)) & Re(R_v(\theta)R_h^*(\theta)) \end{bmatrix} \tag{4.5}$$

R_v and R_h are the Fresnel reflection coefficients for the vertically and horizontally polarized waves, respectively.

4.3 Phase Matrix and Extinction Matrix

Consider a plane wave $\overline{E}_i$ propagating in (θ_i, ϕ_i) direction impinging upon a scatterer which gives rise to a scattered field $\overline{E}_s$ in (θ_s, ϕ_s) direction. The incident field is related to the scattered field through the scattering function matrix as follows:

$$\begin{bmatrix} E_{vs} \\ E_{hs} \end{bmatrix} = \frac{e^{ikr}}{r} \begin{bmatrix} f_{vv}(\theta_s, \phi_s; \theta_i, \phi_i) & f_{vh}(\theta_s, \phi_s; \theta_i, \phi_i) \\ f_{hv}(\theta_s, \phi_s; \theta_i, \phi_i) & f_{hh}(\theta_s, \phi_s; \theta_i, \phi_i) \end{bmatrix} \cdot \begin{bmatrix} E_{vi} \\ E_{hi} \end{bmatrix} \tag{4.6}$$

where E_{vi} and E_{hi} are the vertically and horizontally polarized components of the incident electric field, respectively, and vice versa for the scattered field components,

E_{vs} and E_{hs}. The scattered specific intensity is related to the incident specific intensity by the Stokes matrix in the following way [1].

$$\overline{I}_s = \frac{1}{r^2}\overline{\overline{L}}(\theta_s, \phi_s; \theta_i, \phi_i) \cdot \overline{I}_i \tag{4.7}$$

where

$$\overline{\overline{L}} = \begin{bmatrix} |f_{vv}|^2 & |f_{vh}|^2 \\ |f_{hv}|^2 & |f_{hh}|^2 \\ 2Re(f_{vv}f_{hv}^*) & 2Re(f_{vh}f_{hh}^*) \\ 2Im(f_{vv}f_{hv}^*) & 2Im(f_{vh}f_{hh}^*) \end{bmatrix} \begin{bmatrix} Re(f_{vv}f_{vh}^*) & -Im(f_{vv}f_{vh}^*) \\ Re(f_{hv}f_{hh}^*) & -Im(f_{hv}f_{hh}^*) \\ Re(f_{vv}f_{hh}^* + f_{vh}f_{hv}^*) & -Im(f_{vv}f_{hh}^* - f_{vh}f_{hv}^*) \\ Im(f_{vv}f_{hh}^* + f_{vh}f_{hv}^*) & Re(f_{vv}f_{hh}^* - f_{vh}f_{hv}^*) \end{bmatrix} \tag{4.8}$$

The phase matrix is obtained by averaging over size, shape and orientation of the scatterer. For example, the phase matrix of scatterer with identical shape but different orientation Eulerian angles α, β, γ with respect to the principal axis is

$$\overline{\overline{P}}(\theta, \phi; \theta', \phi') = n_o \int d\alpha \int d\beta \int d\gamma\, p(\alpha, \beta, \gamma)\overline{\overline{L}}(\theta, \phi; \theta', \phi') \tag{4.9}$$

where n_o is the number density of the scatterers, and $p(\alpha, \beta, \gamma)$ is the probability density function for the quantities α, β and γ.

The extinction matrix can be calculated by making use of the optical theorem. It is given by

$$\overline{\overline{\kappa}}_e(\theta, \phi) = \frac{2\pi n_o}{k} \begin{bmatrix} 2Im < f_{vv} > & 0 & Im < f_{vh} > & -Re < f_{vh} > \\ 0 & 2Im < f_{hh} > & Im < f_{hv} > & Re < f_{hv} > \\ 2Im < f_{hv} > & 2Im < f_{vh} > & Im < f_{vv} + f_{hh} > & Re < f_{vv} - f_{hh} > \\ 2Re < f_{hv} > & -2Re < f_{vh} > & -Re < f_{vv} - f_{hh} > & Im < f_{vv} + f_{hh} > \end{bmatrix} \tag{4.10}$$

where $f_{\alpha\beta}(\alpha, \beta = v, h)$ is the forward scattering function for an incident wave with β polarization and the scattered wave with α polarization, and <> denotes ensemble averaging over the orientation and size distribution of the scatterers.

In this chapter, cluster scatterers are considered. The scattering functions of such scatterers are calculated by the MoM code described in previous chapter. A Monte Carlo method is used in the calculation. Different realizations of the scatterers are formed according to the description of the scatterers. For a given scatterer, the average over the orientation taken. The phase matrix and the extinction matrix are obtained numerically.

4.4 Iterative Solution for Vector Radiative Transfer Equation

The vector radiative transfer equation is solved by an iterative method. The method is developed [1, 63] with the assumption that the attenuation is dominated by the absorption. In this case, the zeroth order solution is obtained by neglecting the last term of equation (4.1). The first order solution is calculated by substituting the zeroth order solution into the last term of equation (4.1). High order solutions can be obtained in the same manner.

By restricting the variable θ in the range of 0 to $\pi/2$, equation (4.1) can be split into two equations that couple the upward- and downward- going specific intensities. The radiative transfer equations inside region 1 can be written as

$$\cos\theta \frac{d\overline{I}(\theta,\phi,z)}{dz} = -\overline{\overline{\kappa}}_e(\theta,\phi)\cdot\overline{I}(\theta,\phi,z) + \overline{S}(\theta,\phi,z) \quad (4.11)$$

$$-\cos\theta \frac{d\overline{I}(\pi-\theta,\phi,z)}{dz} = -\overline{\overline{\kappa}}_e(\pi-\theta,\phi)\cdot\overline{I}(\pi-\theta,\phi,z) + \overline{W}(\pi-\theta,\phi,z) \quad (4.12)$$

where $\overline{I}(\theta,\phi,z)$ and $\overline{I}(\pi-\theta,\phi,z)$ are the upward going and the downward going specific intensities, respectively. The two source terms, $\overline{S}(\theta,\phi,z)$ and $\overline{W}(\pi-\theta,\phi,z)$, represent scattering from other directions into the direction of propagation. They are

given by

$$\overline{S}(\theta,\phi,z) = \int_0^{2\pi} d\phi' \int_0^{\pi/2} d\theta' \sin\theta' \Big[\overline{\overline{P}}(\theta,\phi;\theta'\phi') \cdot \overline{I}(\theta',\phi',z) + \overline{\overline{P}}(\theta,\phi;\pi-\theta'\phi') \cdot \overline{I}(\pi-\theta',\phi',z)\Big] \quad (4.13)$$

$$\overline{W}(\pi-\theta,\phi,z) = \int_0^{2\pi} d\phi' \int_0^{\pi/2} d\theta' \sin\theta' \Big[\overline{\overline{P}}(\pi-\theta,\phi;\theta'\phi') \cdot \overline{I}(\theta',\phi',z) + \overline{\overline{P}}(\pi-\theta,\phi;\pi-\theta'\phi') \cdot \overline{I}(\pi-\theta',\phi',z)\Big] \quad (4.14)$$

The boundary conditions for the above equations are as follows:

$$\overline{I}(\pi-\theta,\phi,z=0) = \overline{I}_o \delta(\cos\theta - \cos\theta_o)\delta(\phi-\phi_o) \quad (4.15)$$

$$\overline{I}(\theta,\phi,z=-d) = \overline{\overline{R}}_{12}(\theta) \cdot \overline{I}(\pi-\theta,\phi,z=-d) \quad (4.16)$$

where $\overline{\overline{R}}_{12}(\theta)$ is the reflectivity matrix and is given in (4.5).

4.4.1 Zeroth Order Solution

In the zeroth order solution, $\overline{S}$ and $\overline{W}$ are neglected. We have the eigenvalue equations given by

$$\cos\theta \frac{d\overline{I}^{(0)}(\theta,\phi,z)}{dz} = -\overline{\overline{\kappa}}_e(\theta,\phi) \cdot \overline{I}^{(0)}(\theta,\phi,z) \quad (4.17)$$

$$-\cos\theta \frac{d\overline{I}^{(0)}(\pi-\theta,\phi,z)}{dz} = -\overline{\overline{\kappa}}_e(\pi-\theta,\phi) \cdot \overline{I}^{(0)}(\pi-\theta,\phi,z) \quad (4.18)$$

The solutions are assumed to be in the form of $\exp(-\beta \sec\theta z)$. We have the eigenvalues β as

$$\overline{\beta} = \begin{pmatrix} 2ImK_1 \\ 2ImK_2 \\ i(K_1^* - K_2) \\ i(K_2^* - K_1) \end{pmatrix} \quad (4.19)$$

where K_1 and K_2 are the effective propagation constants through the medium and are given by

$$K_1 = k + \frac{n_o \pi}{k}[< f_{vv}(\theta,\phi;\theta,\phi) > + < f_{hh}(\theta,\phi;\theta,\phi) > + r] \quad (4.20)$$

$$K_2 = k + \frac{n_o \pi}{k}[< f_{vv}(\theta,\phi;\theta,\phi) > + < f_{hh}(\theta,\phi;\theta,\phi) > - r] \quad (4.21)$$

where

$$r = \sqrt{[< f_{vv}(\theta,\phi;\theta,\phi) > - < f_{hh}(\theta,\phi;\theta,\phi) >]^2 + 4 < f_{hv}(\theta,\phi;\theta,\phi) >< f_{vh}(\theta,\phi;\theta,\phi) >} \quad (4.22)$$

The sign of r is chosen such that the real part of r equals the real part of $< f_{vv} > - < f_{hh} >$.

We define a 4×4 eigenmatrix $\overline{\overline{E}}$ with column j as the eigenvector for β_j, $j = 1, 2, 3, 4$. For a medium with azimuthal symmetry, $\overline{\overline{E}}$ is given as,

$$\overline{\overline{E}} = \begin{pmatrix} 1 & 0 & 0 & 0 \\ 0 & 1 & 0 & 0 \\ 0 & 0 & 1 & 1 \\ 0 & 0 & -i & i \end{pmatrix} \quad (4.23)$$

Then this eigenmatrix satisfies the relation

$$\overline{\overline{E}} \cdot \overline{\overline{\beta}} = \overline{\overline{\kappa}}_e \cdot \overline{\overline{E}} \quad (4.24)$$

where

$$\overline{\overline{\beta}} = \overline{\overline{I}} \cdot \overline{\beta} \quad (4.25)$$

with $\overline{\overline{I}}$ as the 4×4 identity matrix. We decompose the Stokes vector into its characteristic modes with

$$\overline{J}(\theta,\phi,z) = \overline{\overline{E}}^{-1} \cdot \overline{I}^{(0)}(\theta,\phi,z) \quad (4.26)$$

Using $\overline{J}$, equation (4.17) can be decoupled into four ordinary differential equations.

In matrix form,

$$\cos\theta \frac{d}{dz}\overline{J}(\theta,\phi,z) = -\overline{\overline{\beta}}(\theta,\phi)\cdot\overline{J}(\theta,\phi,z) \tag{4.27}$$

Directly integrating equation (4.27) from $z' = -d$ to $z' = z$, we have

$$J_i(z)e^{\beta_i \sec\theta z} = J_i(z=-d)e^{-\beta_i \sec\theta d} \tag{4.28}$$

for each component of $\overline{J}$. We define a 4×4 diagonal matrix $\overline{\overline{D}}$,

$$\overline{\overline{D}}(\overline{\beta}(\theta,\phi),\sec\theta z') = \mathrm{diag}[e^{\beta_1(\theta,\phi)\sec\theta z'}, e^{\beta_2(\theta,\phi)\sec\theta z'}, \cdots, e^{\beta_4(\theta,\phi)\sec\theta z'}] \tag{4.29}$$

so that equation (4.28) can be expressed in a matrix form as

$$\overline{\overline{D}}(\overline{\beta}(\theta,\phi)\sec\theta z)\cdot\overline{J}(\theta,\phi,z) = \overline{\overline{D}}(-\overline{\beta}(\theta,\phi)\sec\theta d)\cdot\overline{J}(\theta,\phi,-d) \tag{4.30}$$

Recovering the original notation of $\overline{I}$, we have,

$$\overline{I}^{(0)}(\theta,\phi,z) = \overline{\overline{E}}\cdot\overline{\overline{D}}(-\overline{\beta}(\theta,\phi)\sec\theta(z+d))\cdot\overline{\overline{E}}^{-1}\cdot\overline{I}^{(0)}(\theta,\phi,-d) \tag{4.31}$$

Similarly, for the downward propagating wave from equation (4.18), which gives,

$$\overline{I}^{(0)}(\pi-\theta,\phi,z) = \overline{\overline{E}}\cdot\overline{\overline{D}}(\overline{\beta}(\pi-\theta,\phi)\sec\theta(z))\cdot\overline{\overline{E}}^{-1}\cdot\overline{I}^{(0)}(\pi-\theta,\phi,0) \tag{4.32}$$

Boundary conditions (4.15) and (4.16) are then used to solve equations (4.31) and (4.32). The zeroth order solution is given as

$$\begin{aligned}\overline{I}^{(0)}(\theta,\phi,z) &= \overline{\overline{E}}\cdot\overline{\overline{D}}(\overline{\beta}(\theta,\phi)\sec\theta(z+d))\cdot\overline{\overline{E}}^{-1}\cdot\overline{\overline{R}}_{12}\\ &\quad\cdot\overline{\overline{E}}\cdot\overline{\overline{D}}(-\overline{\beta}(\pi-\theta,\phi)d\sec\theta)\cdot\overline{\overline{E}}^{-1}\\ &\quad\cdot\overline{I}_o\delta(\cos\theta-\cos\theta_o)\delta(\phi-\phi_o)\end{aligned} \tag{4.33}$$

$$\begin{aligned}\overline{I}^{(0)}(\pi-\theta,\phi,z) &= \overline{\overline{E}}\cdot\overline{\overline{D}}(\overline{\beta}(\pi-\theta,\phi)z\sec\theta)\cdot\overline{\overline{E}}^{-1}\\ &\quad\cdot\overline{I}_o\delta(\cos\theta-\cos\theta_o)\delta(\phi-\phi_o)\end{aligned} \tag{4.34}$$

4.4.2 First Order Solution

The first order solution of the radiative transfer equation is obtained by evaluating the source terms $\overline{S}$ and $\overline{W}$ in equations (4.11) and (4.12) with the zeroth order solution. They are given as,

$$\begin{aligned}\overline{S}^{(0)}(\theta,\phi,z) &= \int_0^{2\pi} d\phi' \int_0^{\pi/2} d\theta' \sin\theta' \Big[\overline{\overline{P}}(\theta,\phi;\theta'\phi') \cdot \overline{I}^{(0)}(\theta',\phi',z) \\ &\quad + \overline{\overline{P}}(\theta,\phi;\pi-\theta'\phi') \cdot \overline{I}^{(0)}(\pi-\theta',\phi',z)\Big] \qquad (4.35)\\ \overline{W}^{(0)}(\pi-\theta,\phi,z) &= \int_0^{2\pi} d\phi' \int_0^{\pi/2} d\theta' \sin\theta' \Big[\overline{\overline{P}}(\pi-\theta,\phi;\theta'\phi') \cdot \overline{I}^{(0)}(\theta',\phi',z) \\ &\quad + \overline{\overline{P}}(\pi-\theta,\phi;\pi-0'\phi') \cdot \overline{I}^{(0)}(\pi-\theta',\phi',z)\Big] \qquad (4.36)\end{aligned}$$

Using the same procedure used for calculating the zeroth order solution, equations that relate the first order solution to the boundary values can be obtained. They are given as,

$$\begin{aligned}\overline{I}^{(1)}(\theta,\phi,z) &= \overline{\overline{E}} \cdot \overline{\overline{D}}(-\overline{\beta}(\theta,\phi)\sec\theta(z+d)) \cdot \overline{\overline{E}}^{-1} \cdot \overline{I}^{(1)}(\theta,\phi,-d) \\ &\quad + \overline{S}'(\theta,\phi,z) \qquad (4.37)\\ \overline{I}^{(1)}(\pi-\theta,\phi,z) &= \overline{\overline{E}} \cdot \overline{\overline{D}}(\overline{\beta}(\pi-\theta,\phi)\sec\theta(z)) \cdot \overline{\overline{E}}^{-1} \cdot \overline{I}^{(1)}(\pi-\theta,\phi,0) \\ &\quad + \overline{W}'(\pi-\theta,\phi,z) \qquad (4.38)\end{aligned}$$

where

$$\begin{aligned}\overline{S}'(\theta,\phi,z) &= \sec\theta \int_{-d}^{z} dz' \overline{\overline{E}} \cdot \overline{\overline{D}}(\overline{\beta}(\theta,\phi)\sec\theta(z'-z)) \cdot \overline{\overline{E}}^{-1} \\ &\quad \cdot \overline{S}^{(0)}(\theta,\phi,z') \qquad (4.39)\\ \overline{W}'(\pi-\theta,\phi,z) &= \sec\theta \int_{z}^{0} dz' \overline{\overline{E}} \cdot \overline{\overline{D}}(\overline{\beta}(\pi-\theta,\phi)\sec\theta(z'-z)) \cdot \overline{\overline{E}}^{-1} \\ &\quad \cdot \overline{W}^{(0)}(\pi-\theta,\phi,z') \qquad (4.40)\end{aligned}$$

Using the boundary conditions (4.15) and (4.16) and noting that the incident intensities have already been incorporated in the equations through the zeroth order

solution, we have,

$$\overline{I}^{(1)}(\pi-\theta,\phi,0) = 0 \tag{4.41}$$

$$\begin{aligned}\overline{I}^{(1)}(\theta,\phi,-d) &= \int_{-d}^{0} dz' \overline{\overline{R}}(\theta)\cdot\overline{\overline{E}}\cdot\overline{\overline{D}}(-\overline{\beta}(\pi-\theta,\phi)\sec\theta(z'+d)) \\ &\quad \cdot\overline{\overline{E}}^{-1}\cdot\overline{W}^{(0)}(\pi-\theta,\phi,z')\end{aligned} \tag{4.42}$$

Hence, combining equations (4.37), (4.38), (4.41) and (4.42), the first order solutions are given as

$$\begin{aligned}\overline{I}^{(1)}(\theta,\phi,z) &= \overline{\overline{E}}\cdot\overline{\overline{D}}(-\overline{\beta}(\theta,\phi)\sec\theta(z+d))\cdot\overline{\overline{E}}^{-1}\int_{-d}^{0} dz'\overline{\overline{R}}(\theta)\cdot\overline{\overline{E}} \\ &\quad \cdot\overline{\overline{D}}(\overline{\beta}(\pi-\theta,\phi)\sec\theta(z'+d))\cdot\overline{\overline{E}}^{-1}\cdot\overline{W}^{(0)}(\pi-\theta,\phi,z') \\ &\quad +\overline{S}'(\theta,\phi,z)\end{aligned} \tag{4.43}$$

$$\overline{I}^{(1)}(\pi-\theta,\phi,z) = \overline{W}'(\pi-\theta,\phi,z) \tag{4.44}$$

The first order solution at $z=0$ can be evaluated by carrying out the z' integration. It is given as

$$\begin{aligned}[\overline{I}^{(1)}(\theta,\phi,0)]_l &= \sec\theta\Big\{\overline{\overline{E}}\Big\}_{lk}\Big\{\overline{\overline{E}}^{-1}\cdot\overline{\overline{P}}(\theta,\phi;\pi-\theta_o,\phi_o)\cdot\overline{\overline{E}}\Big\}_{ki} \\ &\quad \frac{1-e^{-\beta_k(\theta,\phi)d\sec\theta-\beta_i(\pi-\theta_o,\phi_o)d\sec\theta_o}}{\beta_k(\theta,\phi)\sec\theta+\beta_i(\pi-\theta_o,\phi_o)\sec\theta_o}\Big\{\overline{\overline{E}}^{-1}\cdot\overline{I}_o\Big\}_i \\ &\quad +\sec\theta\Big\{\overline{\overline{E}}\Big\}_{lk}\Big\{\overline{\overline{E}}^{-1}\cdot\overline{\overline{P}}(\theta,\phi;\theta_o,\phi_o)\cdot\overline{\overline{E}}\Big\}_{ki} \\ &\quad \frac{e^{-\beta_k(\theta,\phi)d\sec\theta}-e^{-\beta_i(\theta_o,\phi_o)d\sec\theta_o}}{\beta_i(\theta_o,\phi_o)\sec\theta_o-\beta_k(\theta,\phi)\sec\theta}\Big\{\overline{\overline{E}}^{-1}\cdot\overline{\overline{R}}(\theta_o) \\ &\quad \cdot\overline{\overline{E}}\cdot\overline{\overline{D}}(-\overline{\beta}(\pi-\theta_o,\phi_o)d\sec\theta_o)\cdot\overline{\overline{E}}^{-1}\cdot\overline{I}_o\Big\}_i \\ &\quad +\sec\theta\Big\{\overline{\overline{E}}\cdot\overline{\overline{D}}(-\overline{\beta}(\theta,\phi)d\sec\theta)\cdot\overline{\overline{E}}^{-1}\cdot\overline{\overline{R}}(\theta)\cdot\overline{\overline{E}}\Big\}_{lk} \\ &\quad \Big\{\overline{\overline{E}}^{-1}\cdot\overline{\overline{P}}(\pi-\theta,\phi;\pi-\theta_o,\phi_o)\cdot\overline{\overline{E}}\Big\}_{ki} \\ &\quad \frac{e^{-\beta_k(\pi-\theta,\phi)d\sec\theta}-e^{-\beta_i(\pi-\theta_o,\phi_o)d\sec\theta_o}}{\beta_i(\pi-\theta_o.\phi_o)\sec\theta_o-\beta_k(\pi-\theta,\phi)\sec\theta}\Big\{\overline{\overline{E}}^{-1}\cdot\overline{I}_o\Big\}_i \\ &\quad +\sec\theta\Big\{\overline{\overline{E}}\cdot\overline{\overline{D}}(-\overline{\beta}(\theta,\phi)d\sec\theta)\overline{\overline{E}}^{-1}\cdot\overline{\overline{R}}(\theta)\cdot\overline{\overline{E}}\Big\}_{lk} \\ &\quad \Big\{\overline{\overline{E}}^{-1}\cdot\overline{\overline{P}}(\pi-\theta,\phi;\theta_o,\phi_o)\cdot\overline{\overline{E}}\Big\}_{ki}\end{aligned}$$

$$\frac{1-e^{-\beta_k(\pi-\theta,\phi)d\sec\theta-\beta_i(\theta_o,\phi_o)d\sec\theta_o}}{\beta_k(\pi-\theta,\phi)\sec\theta+\beta_i(\theta_o,\phi_o)\sec\theta_o}\Big\{\overline{\overline{E}}^{-1}\cdot\overline{\overline{R}}(\theta_o)$$
$$\cdot\overline{\overline{E}}\cdot\overline{\overline{D}}(-\overline{\beta}(\pi-\theta_o,\phi_o)d\sec\theta_o)\overline{\overline{E}}^{-1}\cdot\overline{I}_o\Big\}_i \tag{4.45}$$

where $[\overline{I}^{(1)}]_l$ represents the lth component of $\overline{I}^{(1)}$ and summations over the repeated indices are implied. The four terms in equation (4.45) represent four different scattering mechanisms. The first term represents scattering by a scatterer into the upper half-space. The second term corresponds to single scattering of the reflected wave by a scatterer. The third term represent scattering by a scatterer which is then reflected by the boundary before going back into the upper space. The last term corresponds to single scattering of the reflected wave which is further reflected by the boundary. The scattering mechanisms are depicted in Fig. 4-2.

4.5 Theoretical Results and Discussion

In this section, theoretical results of the backscattering coefficients of the two-layer medium are presented. The phase matrix in the radiative transfer equation has been evaluated using the scattering functions calculated by various methods. Firstly, the scattering functions are calculated by the MoM code developed in the previous chapter, in which the mutual interactions between the components have been accounted for (full numerical model). The full numerical results are compared with results obtained using two approximate methods. The first approximation used is the independent scattering model, where the elements of the phase matrix are calculated by the incoherent sum of the scattered power of the individual components. The scattered power is given as

$$|S|^2 = |S_o|^2 + \sum_{j=1}^{N} |S_j|^2 \tag{4.46}$$

where S_o is the scattered field from the center cylinder and S_j represents the response from the branch element j. The second approximate method is the coherent scattering model [24] in which the induced field is assumed to be the same as that in the

independent scattering model for individual components. However, the coherent sum of the fields rather than the incoherent sum of the intensities of the components is used in calculating the phase matrix elements. In this case, the relative positions of the components in the cluster that attribute to a phase shift in the field is accounted for. Mathematically, the scattered field from the cluster is given by

$$S = S_o + \sum_{j=1}^{N} S_j e^{i\theta_j} \tag{4.47}$$

where θ_j is the phase factor that accounts for the additional phase delay due to the relative position of the branch element and is given as

$$\theta_j = (\overline{k}_i - \overline{k}_s) \cdot \overline{r}_j \tag{4.48}$$

where $\overline{r}_j$ represents the branch element location, $\overline{k}_i$ and $\overline{k}_s$ are the wave vectors of the incident and scattered waves, respectively. The scattered power in this model is given as

$$|S|^2 = |S_o|^2 + \sum_{j=1}^{N} |S_j|^2 + 2\sum_{j=1}^{N} Re(S_o^* S_j e^{i\theta_j}) + \sum_{j=1}^{N}\sum_{i\neq j} S_i^* S_j e^{i(\theta_j - \theta_i^*)} \tag{4.49}$$

We consider a cluster with 10 branches. The geometrical configuration of the cylinder cluster is shown in Fig. 4-3. The cluster consists of a vertical center cylinder of radius 0.3 cm and of length 10 cm. There are five layers of branches distributed uniformly along the center cylinder. All the branches make an angle of 45^o with the center cylinder. The radius of the branch is 0.15 cm and the length is 2 cm. Two branches are arranged in the opposite direction to each other within a layer to form a pair. This pair of branches is attached to the center cylinder at a random azimuthal position. The permittivity of the cluster is $(11 + i4)\epsilon_o$. The frequency is 5.3 GHz. The scatterer is vertically oriented. Figs. 4-4 and 4-5 show, respectively, the absorption cross section and the total scattering cross section as the function of incidence angle of a single cluster for vertical polarization. Since the coherent scattering model assume the same internal field as the independent scattering model,

it has the same absorption cross section as the independent scattering model. The enhancement of the absorption is due to mutual interaction and it will be discussed in the next chapter. For the total scattering cross section, it is observed that coherent interfence increases the scattering loss (3dB at nadir) and mutual interaction also increases the scattering loss at nadir.

With the assumption that each scatterer is far apart compared to the wavelength, the radiative transfer theory is employed to calculate the backscattering coefficients for a two-layer medium containing the scatterers. The backscattering coefficients for HH, VV and HV polarizations as a function of incidence angle are shown in Figs. 4-6 through 4-8. The scatterers are vertically oriented and uniformly distributed in azimuthal direction. Ensemble average is performed over the orientation of the scatterers. It is observed that the coherent scattering model gives good estimates of the co-polarized returns (HH and VV). The difference between the approximate methods and the full numerical approach is larger for the case of cross-polarized returns. This is because the interactions between branches and the center cylinder give rise to cross-polarized returns which is not captured in the approximate methods.

To study the cross-polarized returns for the branching cluster, the branching angle of the scatterer is varied from 10 degrees to 90 degrees. The cross-polarized returns at nadir as a function of the branching angle is shown in Fig. 4-9. With small branching angles, the depolarization effect is small. The general trend is that the cross-polarized return increases with the branching angle. It is observed that there is larger discrepancy between the full numerical results and the approximate results for smaller branching angles. This is because mutual interaction is important for cross-polarized returns. At larger branching angles, a single component can give a significant cross-polarized return and the mutual interaction is less important in this case. To investigate the mechanism which accounts for the large different in cross-polarized returns, a calculation is carried out with the center cylinders of different radii. The results of the cross-polarized returns at nadir are shown in Fig. 4-10. The branching angle is chosen to be 10 degrees. The coherent scattering model and the independent scattering model give lower cross-polarized returns than the full numerical

numerical model. The difference increases for the larger center cylinder case. Both approximate methods have lower cross-polarized returns for the larger center cylinder case. This is due to the increase in attenuation with increasing cylinder size and no cross-polarized contribution from the center cylinder in the approximate methods. The numerical results show that the presence of the center cylinder is important for high cross-polarized returns. Since the center cylinder itself cannot give rise to high cross-polarized returns, the mechanism responsible for the high cross-polarized returns is the branch – center cylinder interaction. The wave bounces from branch to center cylinder back to other branches and gives high cross-polarized returns.

The co-polarized returns at nadir for the same set of scatterers are shown in Fig. 4-11. The difference between the numerical solution and the two other approximate solutions is smaller than that of the cross-polarized returns. The coherent model gives better estimates than the independent scattering model. The mutual interaction is small because of the small number of branches, and it is a weak function of the branching angle. When repeating the same calculation for various center cylinders, the results (Fig. 4-12) confirm that the mutual interaction is less important for co-polarized returns. The difference between the full numerical solution and the coherent scattering model becomes larger for a larger center cylinder. However, it is less significant for the co-polarized case than the cross-polarized case.

4.6 Summary

In this chapter, the first order iterative solution of the vector radiative transfer equation for active remote sensing is derived. The full numerical solution for a single branching scatterer has been used to evaluate the scattering functions for the phase matrix and extinction matrix in the radiative transfer equations. The backscattering coefficients are then calculated from the iterative solution. The solution accounts for the multiple scattering effects within the cluster and single scattering between the clusters. It is well suited for the calculation of locally dense media such as vegetation canopies. The numerical solutions are then compared with the solutions obtained

with different approximations. The results show that the coherent scattering model gives good estimates for co-polarized returns. For cross-polarized cases, both the independent and the coherent scattering models underestimate the backscattering returns. Cross-polarized returns are affected by the interaction between the components of the cluster and the two approximate methods do not account for this effect. By varying the branching angle of the cluster, it is shown that the mutual interaction is stronger for the smaller branching angle. The center cylinder in the cluster plays an important role in the cross-polarized returns. The triple bounce scattering mechanism, i.e. from branch to center cylinder back to branch, contributes to the high cross-polarized returns.

The solution of the two-layer random medium for the radiative transfer equations provides a means to study scattering mechanisms of complex clustering structures. Under the framework of radiative transfer theory, the model can easily be extended to a multi-layer random medium with a rough bottom boundary [63] in which the volume-surface interaction can be accounted for.

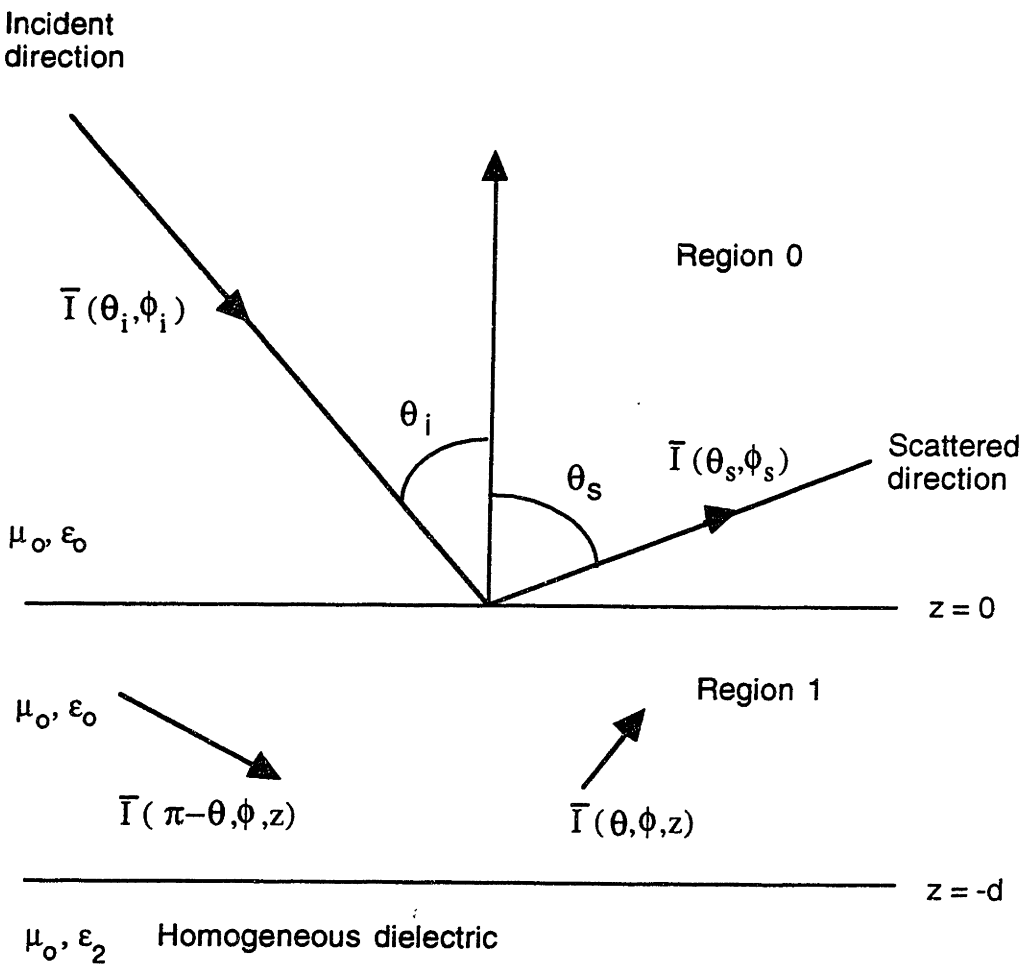

Figure 4-1: Configuration of two layer medium with planar interfaces containing discrete scatterers.

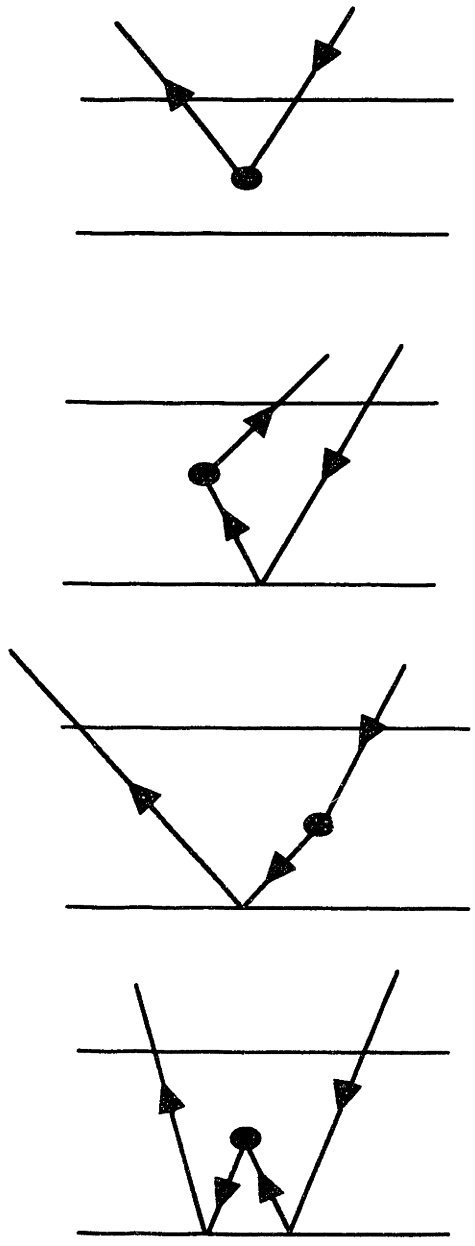

Figure 4-2: Four scattering mechanisms for single volume scattering in the presence of a reflective boundary.

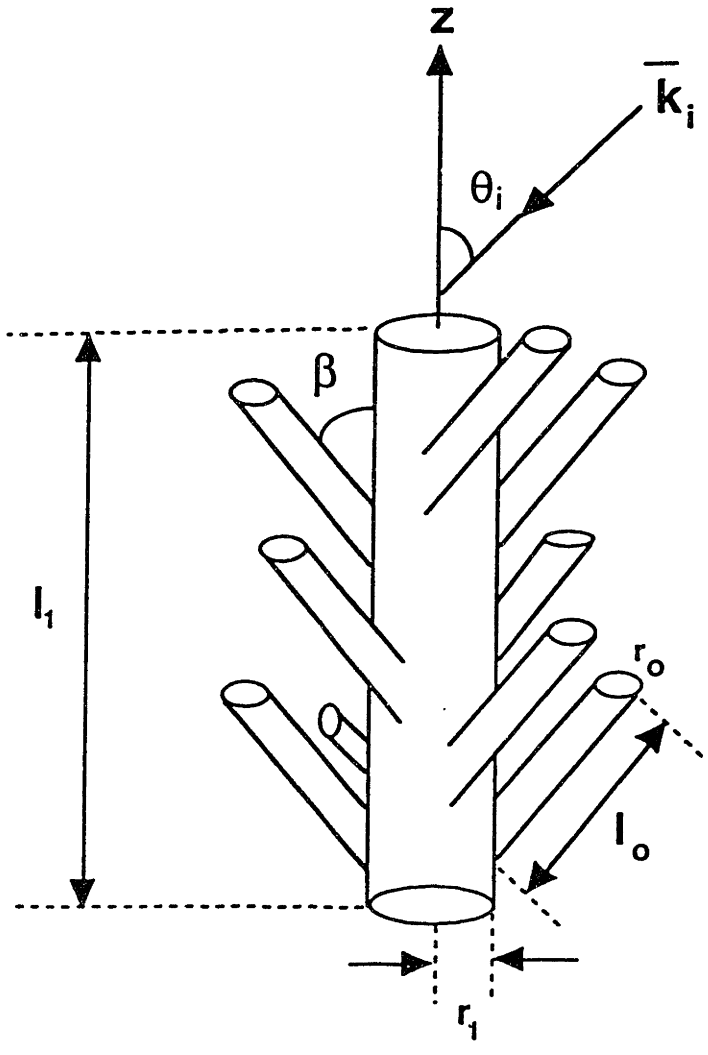

Figure 4-3: Configuration of the cluster. Center cylinder: length = 10 cm, radius = 0.3 cm; branching cylinder: length = 2 cm, radius = 0.15 cm, branching angle $\beta = 45°$; permittivity of the cluster = $(11 + i4)\epsilon_o$; frequency is 5.3 GHz; incidence angle = θ_i.

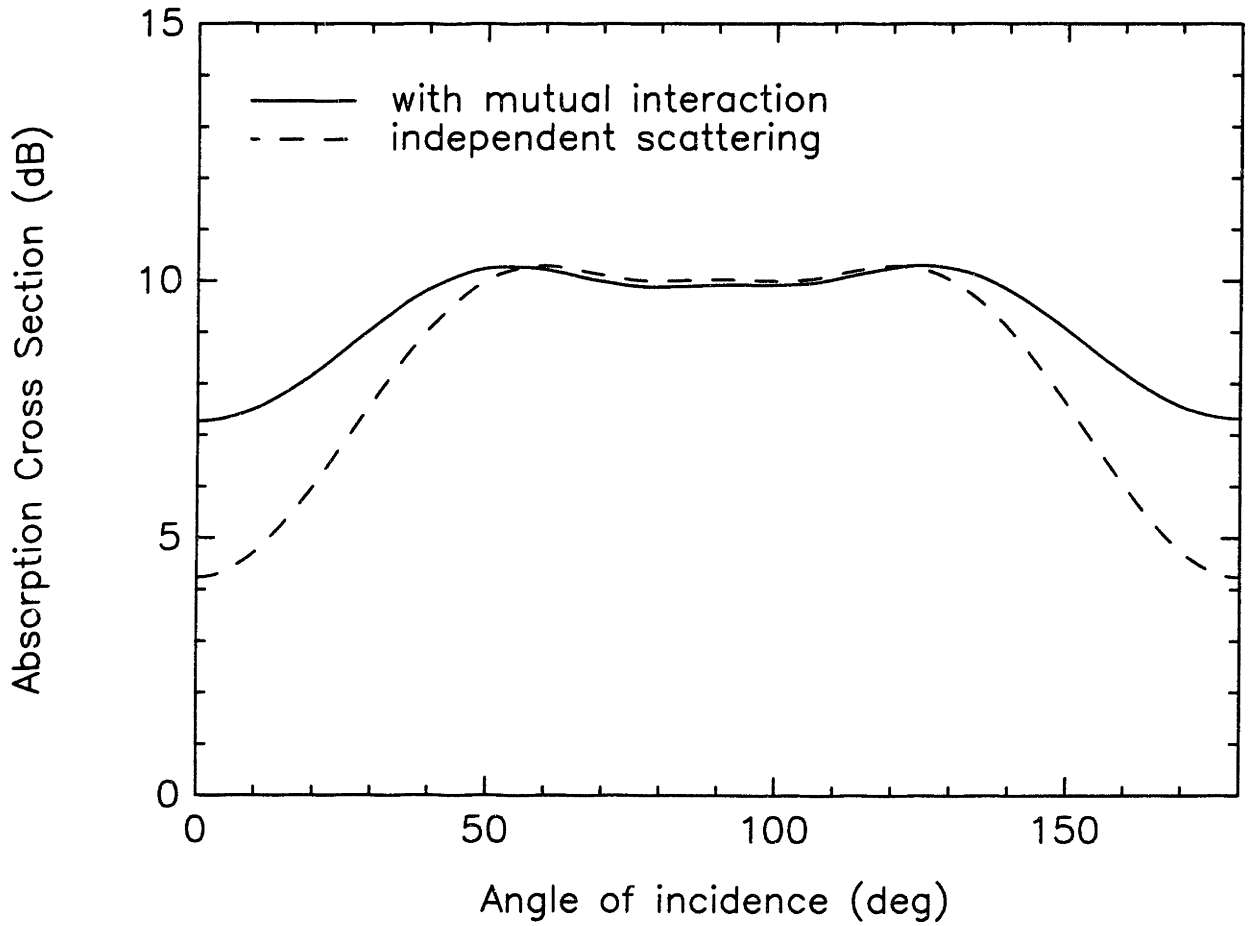

Figure 4-4: Absorption cross section as a function of incidence angle for vertical polarization. Number of branches is 10. Curves are normalized by $(\sigma_{ah}(90^o))_{ind}$ with the numerical value of -39.5 dBsm. Frequency is 5.3 GHz.

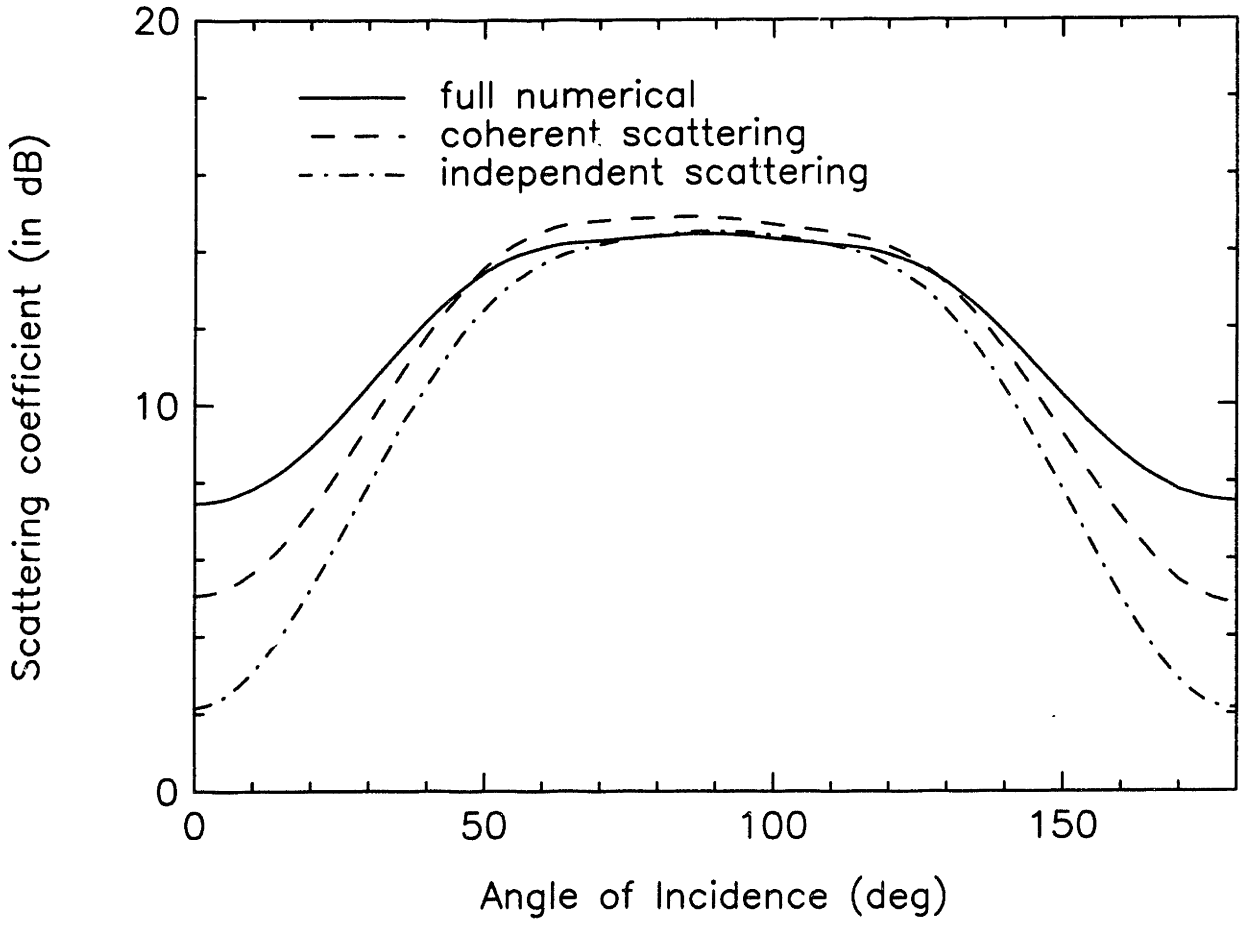

Figure 4-5: Absorption cross section as a function of incidence angle for vertical polarization. Number of branches is 10. Curves are normalized by $(\sigma_{sh}(90^o))_{ind}$ with the numerical value of -43.2 dBsm. Frequency is 5.3 GHz.

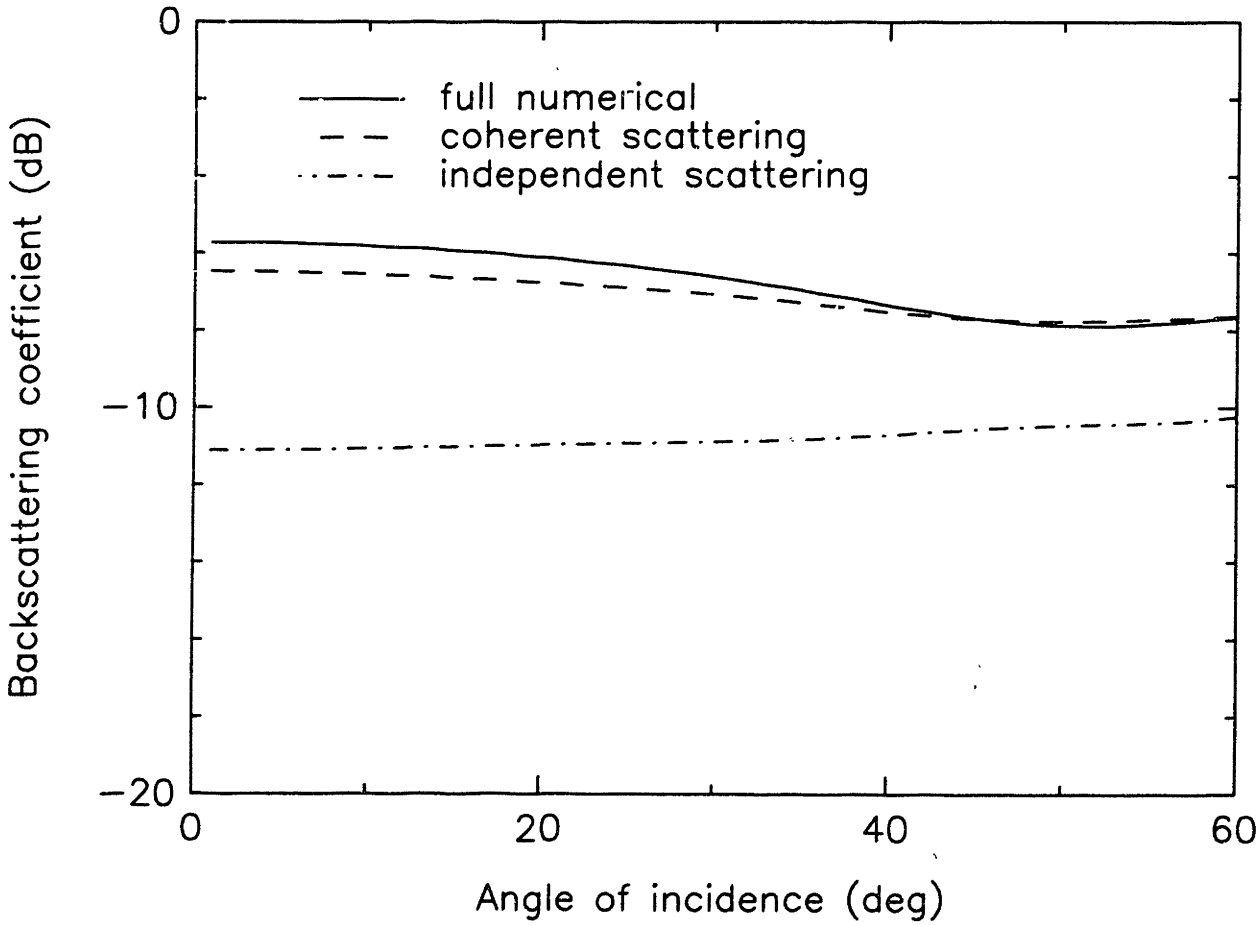

Figure 4-6: Backscattering coefficients for a two-layer medium — σ_{hh}, fractional volume $f = 0.5\%, \epsilon_s = (11 + i4)\epsilon_o$. The scattering layer has a thickness $d = 0.25$m and underlying half-space is flat and has a permittivity $\epsilon_{soil} = (10 + i2)\epsilon_o$. Frequency is 5.3 GHz. Number of branches for the scatterers is 10.

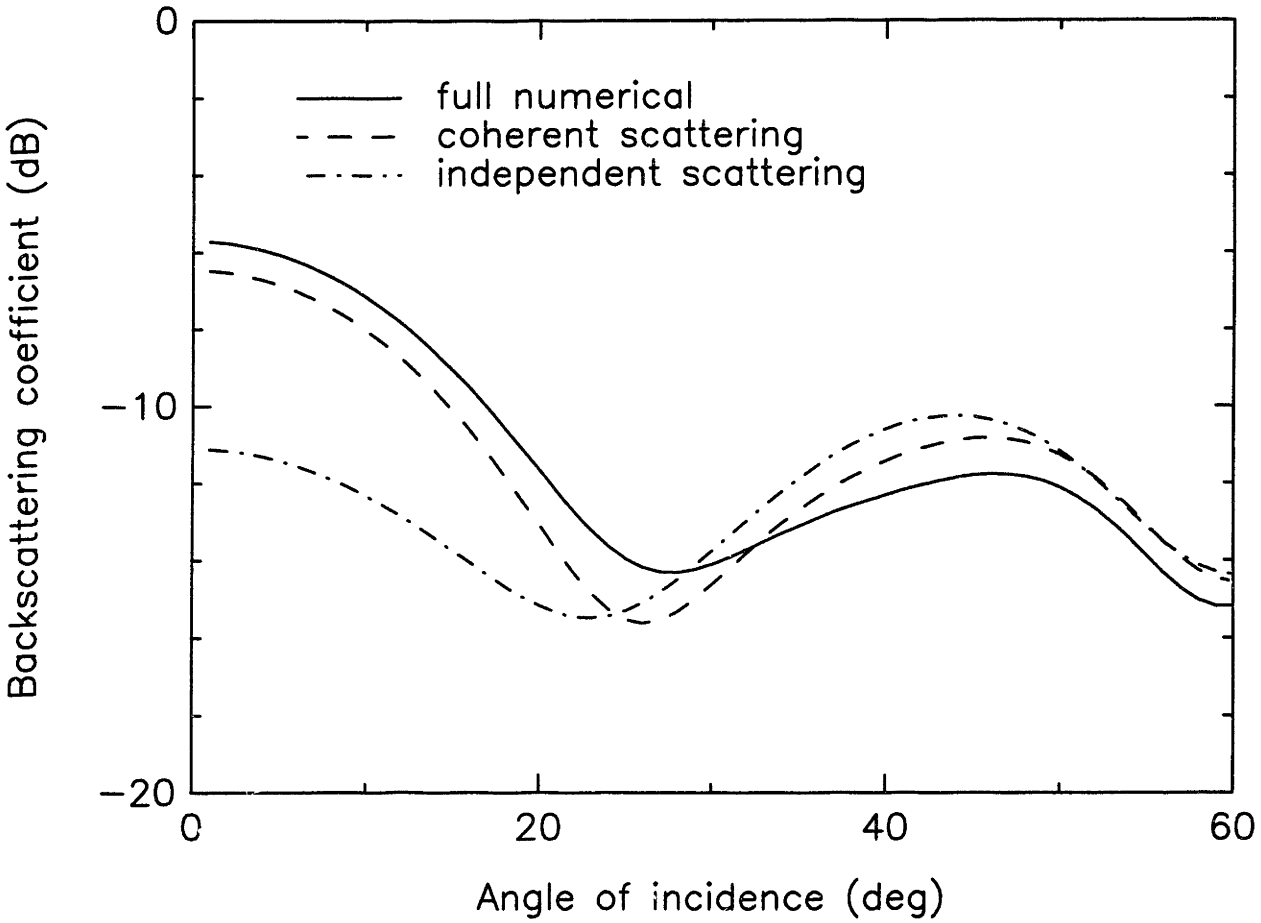

Figure 4-7: Backscattering coefficients for a two-layer medium — σ_{vv}, fractional volume $f = 0.5\%, \epsilon_s = (11 + i4)\epsilon_o$. The scattering layer has a thickness $d = 0.25$m and underlying half-space is flat and has a permittivity $\epsilon_{soil} = (10 + i2)\epsilon_o$. Frequency is 5.3 GHz. Number of branches for the scatterers is 10.

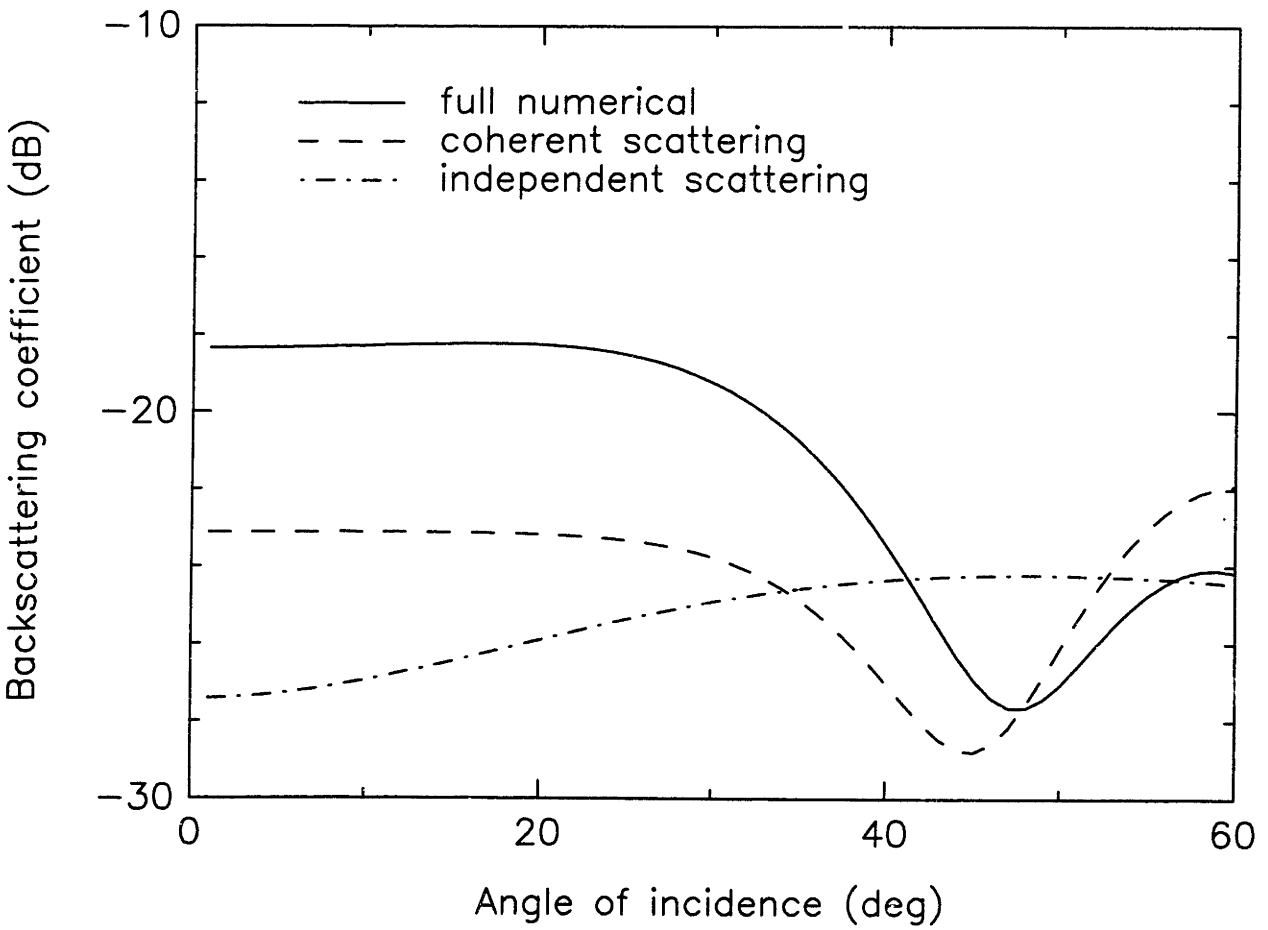

Figure 4-8: Backscattering coefficients for a two-layer medium — σ_{hv}, fractional volume $f = 0.5\%, \epsilon_s = (11 + i4)\epsilon_o$. The scattering layer has a thickness $d = 0.25$m and underlying half-space is flat and has a permittivity $\epsilon_{soil} = (10 + i2)\epsilon_o$. Frequency is 5.3 GHz. Number of branches for the scatterers is 10.

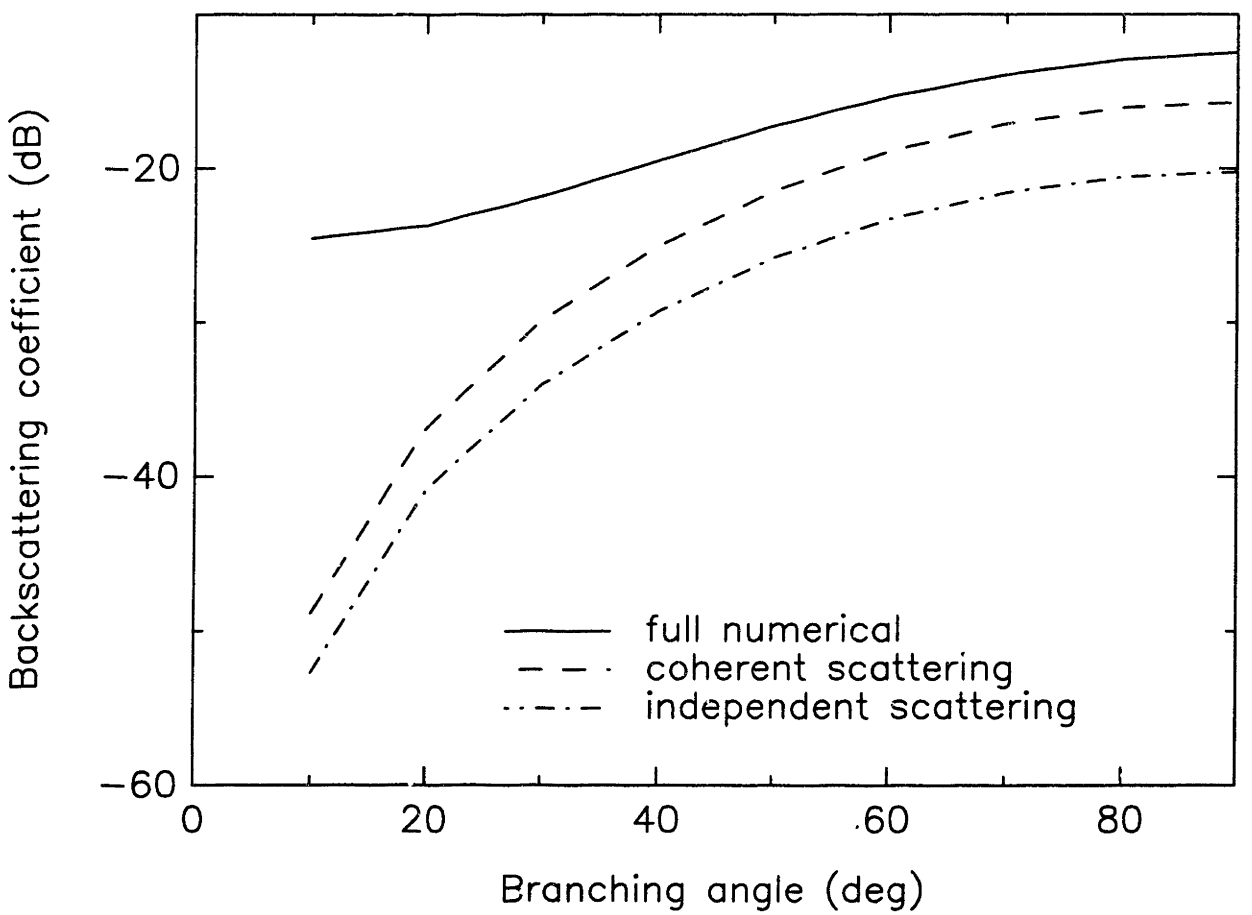

Figure 4-9: Backscattering coefficients for a two-layer medium — σ_{hv} at nadir, as a function of branching angle β. Fractional volume $f = 0.5\%, \epsilon_s = (11 + i4)\epsilon_o$. The scattering layer has a thickness $d = 0.25$m and underlying half-space is flat and has a permittivity $\epsilon_{soil} = (10 + i2)\epsilon_o$. Frequency is 5.3 GHz. Number of branches for the scatterers is 10.

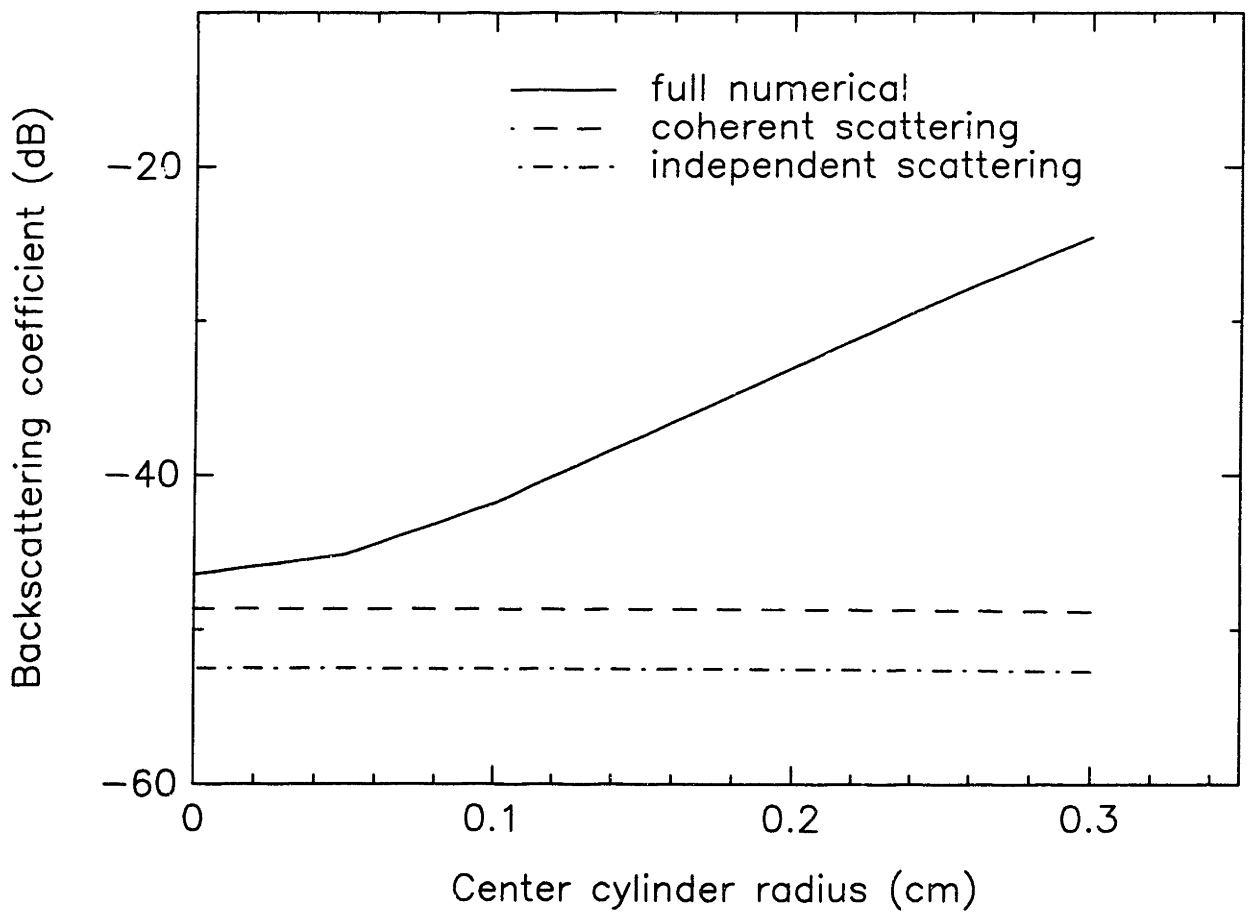

Figure 4-10: Backscattering coefficients for a two-layer medium — σ_{hv} as a function of the center cylinder diameter. Fractional volume $f = 0.5\%, \epsilon_s = (11 + i4)\epsilon_o$. The scattering layer has a thickness $d = 0.25$m and underlying half-space is flat and has a permittivity $\epsilon_{soil} = (10 + i2)\epsilon_o$. Frequency is 5.3 GHz. Number of branches for the scatterers is 10.

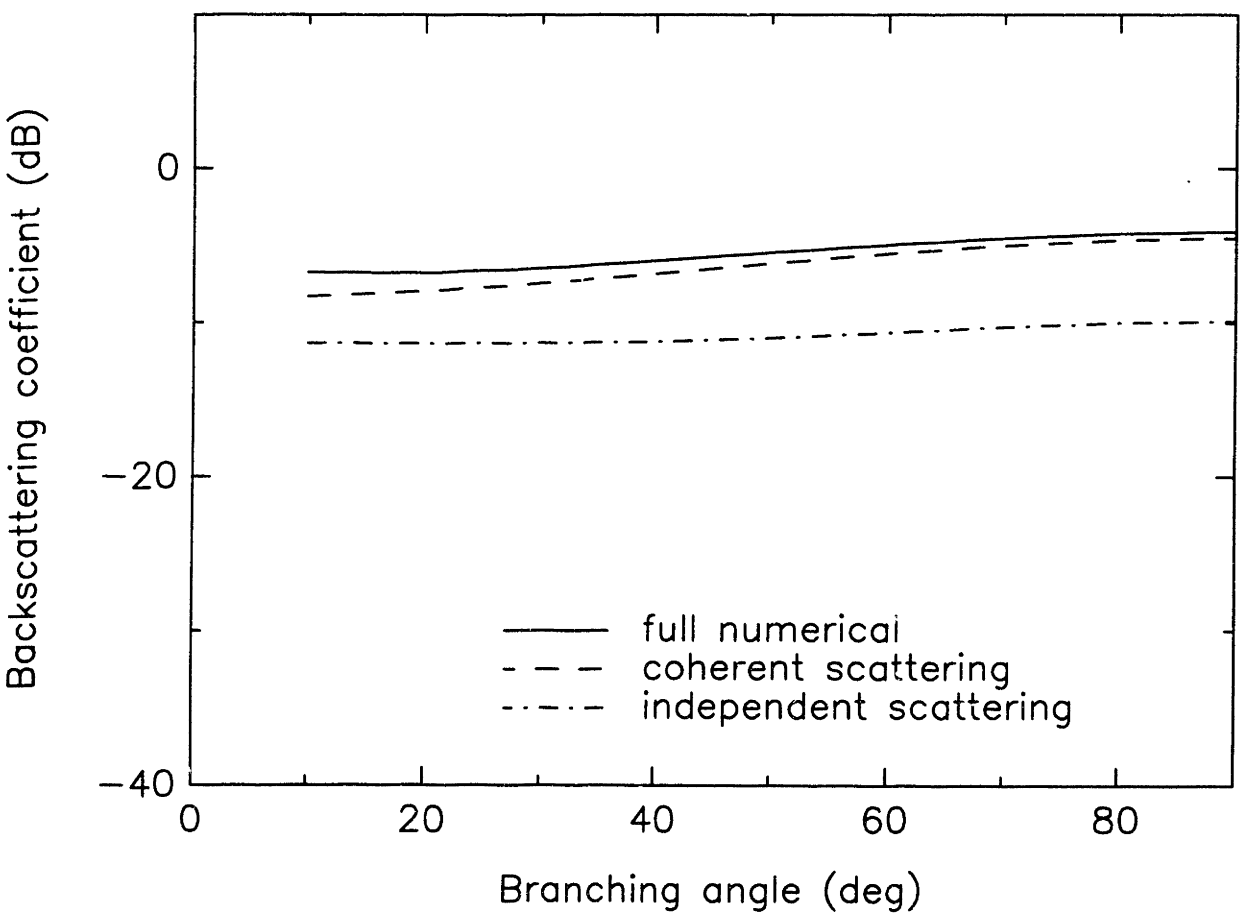

Figure 4-11: Backscattering coefficients for a two-layer medium — σ_{vv} at nadir as a function of branching angle β. Fractional volume $f = 0.5\%, \epsilon_s = (11 + i4)\epsilon_o$. The scattering layer has a thickness $d = 0.25$m and underlying half-space is flat and has a permittivity $\epsilon_{soil} = (10 + i2)\epsilon_o$. Frequency is 5.3 GHz. Number of branches for the scatterers is 10.

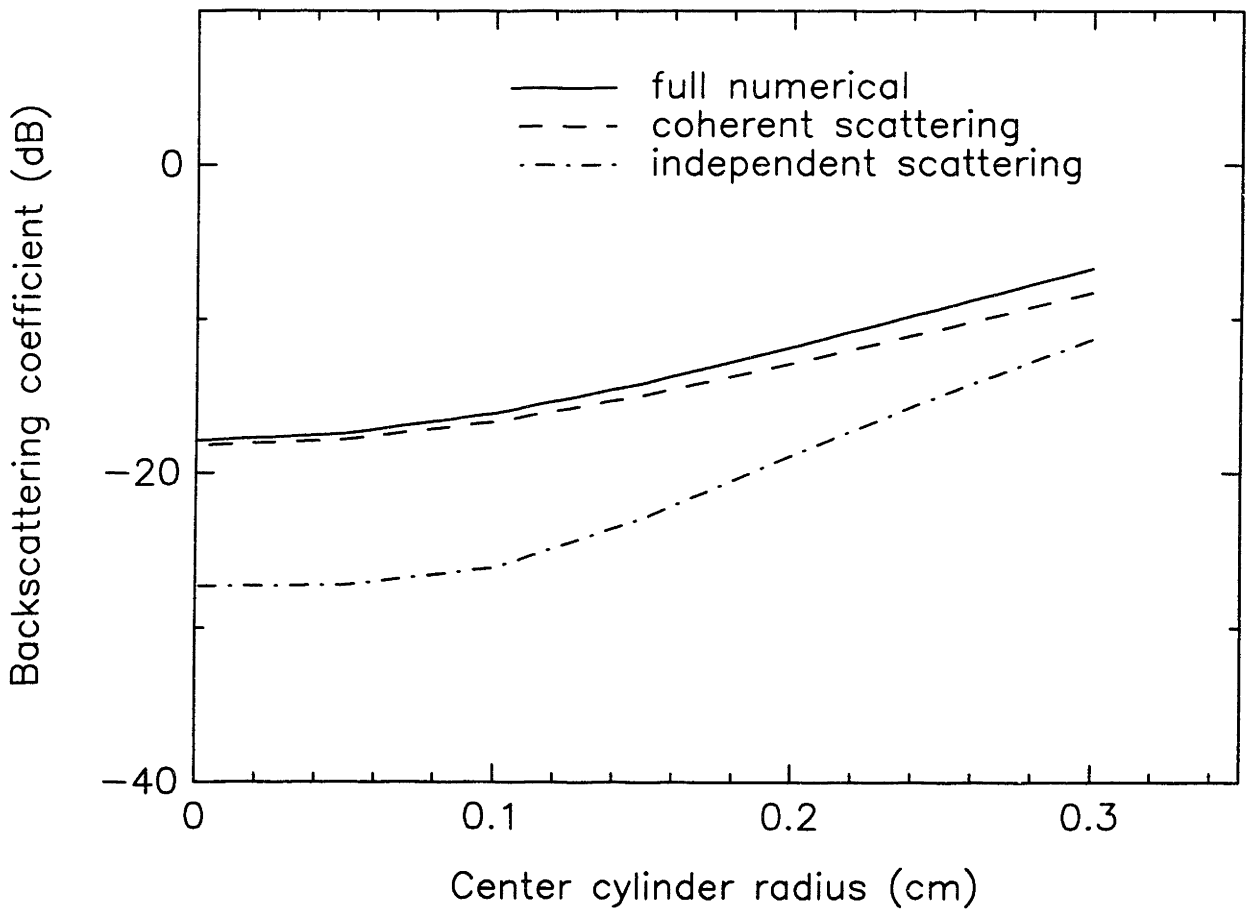

Figure 4-12: Backscattering coefficients for a two-layer medium — σ_{vv} as a function of the center cylinder diameter. Fractional volume $f = 0.5\%, \epsilon_s = (11 + i4)\epsilon_o$. The scattering layer has a thickness $d = 0.25$m and underlying half-space is flat and has a permittivity $\epsilon_{soil} = (10 + i2)\epsilon_o$. Frequency is 5.3 GHz. Number of branches for the scatterers is 10.

Chapter 5

Absorption Enhancement and Radiative Transfer Theory for Passive Remote Sensing

5.1 Introduction

In remote sensing of geophysical terrains such as snow, ice and vegetation canopies, different theoretical models have been developed to characterize the electromagnetic response and to interpret experimental data. For the discrete scatterer model, the medium is considered to be a collection of discrete scatterers embedded in a homogeneous background. In the radiative transfer approach, independent scattering assumption has been used to evaluate the phase functions, the scattering coefficients and the absorption coefficients. The classical relations are that for N particles, the scattering and absorption cross sections of N particles are given by

$$(\sigma_s)_{ind} = \sum_{i=1}^{N} \sigma_{si} \tag{5.1}$$

$$(\sigma_a)_{ind} = \sum_{i=1}^{N} \sigma_{ai} \tag{5.2}$$

where *ind* stands for independent, and σ_{si} and σ_{ai} are respectively the scattering and absorption cross sections of the ith particle as it exists alone. For a medium with a high concentration of particles, independent scattering is not valid. Such high particle concentration media can be divided in two categories; uniformly dense media and locally dense media. For uniformly dense media, for example snow and ice, the fractional volume of the scatterers is high and the collective scattering effects can be described by the dense media theory [1, 62]. In vegetation canopies, the fractional volume of particles is low, usually between 0.1% to 0.5%. However, scatterers like branches and leaves can occur in clusters. They are regarded as locally dense media. In media that exhibit locally dense properties, collective scattering and absorption effects are important.

The collective scatterering was first studied and applied in a branching vegetation model by Yueh *et al* [24]. The coherent scattering effect is taken into account by summing up the scattered fields due to each scatterer coherently and then calculating the scattered power. It gives rise to a significant difference in the bistatic scattering coefficients from independent scattering. However, the model did not account for the coherent mutual interactions between the components in the calculation of the induced field in each scatterer. Since the internal field in the model is assumed to be the same as the independent scattering, the absorption coefficients remain unchanged. In this chapter, we focus on the effect of mutual interaction on the collective scattering and absorption in locally dense media. The absorption of the cluster can be several times greater than the incoherent sum of its components as predicted by equation (5.2).

In section 5.2, we review the vector radiative transfer theory for passive remote sensing. In section 5.3, the method of solving the radiative transfer equations by discrete ordinates is given. In section 5.4, numerical results for the absorption cross sections of cylinder clusters are shown and interpreted. In section 5.5, we incorporate the absorption vectors and scattering functions for the cylinder clusters in the radiative transfer equation. The brightness temperatures are then calculated and compared with the results based on the independent and the coherent scattering models.

5.2 Vector Radiative Transfer Equation

The vector radiative transfer equation that governs the propagation of the specific intensity $\overline{I}$ is given by

$$\begin{aligned}\cos\theta\frac{d\overline{I}(\theta,\phi,z)}{dz} &= -\overline{\overline{\kappa}}_e(\theta,\phi)\cdot\overline{I}(\theta,\phi,z) \\ &\quad +\overline{\kappa}_a(\theta,\phi)CT+\int_{4\pi}d\Omega'\overline{\overline{P}}(\theta,\phi,\theta',\phi')\cdot\overline{I}(\theta'\phi',z)\end{aligned} \tag{5.3}$$

where $\overline{\overline{\kappa}}_e$ is the extinction matrix for the specific intensity due to the scatterer that accounts for losses from scattering and absorption, $\overline{\kappa}_a$ is the absorption coefficient vector, $\overline{\overline{P}}(\theta,\phi,\theta',\phi')$ is the phase matrix which relates the scattered intensities in the direction of $(\hat{\theta},\hat{\phi})$ to the incident intensities in the direction of $(\hat{\theta}',\hat{\phi}')$, T is the physical temperature, and C is a constant given by

$$C=\frac{K}{\lambda^2} \tag{5.4}$$

with K as the Boltzmann's constant (1.38×10^{-23} J/K) and λ the free space wavelength. The absorption vector can be expressed in terms of the number density of the scatterers and the absorption cross sections as follows:

$$\overline{\kappa}_a(\theta,\phi)=n_o\begin{bmatrix}\sigma_{a1}(\theta,\phi)\\ \sigma_{a2}(\theta,\phi)\\ \sigma_{a3}(\theta,\phi)\\ \sigma_{a4}(\theta,\phi)\end{bmatrix} \tag{5.5}$$

where

$$\sigma_{a1}(\theta,\phi) = \frac{4\pi}{k}Imf_{vv}(\theta,\phi;\theta,\phi)-\int d\Omega'\Big[|f_{vv}(\theta',\phi';\theta,\phi)|^2+|f_{hv}(\theta',\phi';\theta,\phi)|^2\Big] \tag{5.6}$$

$$\sigma_{a2}(\theta,\phi) = \frac{4\pi}{k}Imf_{hh}(\theta,\phi;\theta,\phi)-\int d\Omega'\Big[|f_{vh}(\theta',\phi';\theta,\phi)|^2+|f_{hh}(\theta',\phi';\theta,\phi)|^2\Big] \tag{5.7}$$

$$\begin{aligned}\sigma_{a3}(\theta,\phi) &= 2Re\Big\{\frac{2\pi i}{k}\Big[f_{vh}^*(\theta,\phi;\theta,\phi)-f_{hv}(\theta,\phi;\theta,\phi)\Big]\Big\} \\ &\quad -\int_{4\pi}d\Omega'\Big[f_{vv}(\theta',\phi';\theta,\phi)f_{vh}^*(\theta',\phi';\theta,\phi)+f_{hv}(\theta'\phi';\theta,\phi)f_{hh}^*(\theta'\phi';\theta,\phi)\Big]\end{aligned} \tag{5.8}$$

$$\sigma_{a4}(\theta,\phi) = 2Im\Big\{\frac{2\pi i}{k}\big[f^*_{vh}(\theta,\phi;\theta,\phi) - f_{hv}(\theta,\phi;\theta,\phi)\big]\Big\} \qquad (5.9)$$
$$- \int_{4\pi} d\Omega' \big[f_{vv}(\theta',\phi';\theta,\phi) f^*_{vh}(\theta',\phi';\theta,\phi) + f_{hv}(\theta'\phi';\theta,\phi) f^*_{hh}(\theta'\phi';\theta,\phi)\big]$$

$\sigma_{a1}(\theta,\phi)$ and $\sigma_{a2}(\theta,\phi)$ are, respectively, the absorption cross sections for the vertically and horizontally polarized waves in the propagation direction of (θ,ϕ).

Equation (5.3) differs from (4.1) by the term given by the emission vector $\overline{\kappa}_a CT$. In active remote sensing, a wave is launched by a transmitter to the medium and the radiated signal is usually much larger than the thermal emission so that the thermal emission can be neglected in active remote sensing. In passive remote sensing, since the thermal emission is the source term of the radiative transfer equation, and modeling the absorption of the medium becomes very important.

5.3 Method of Solution

In this section, the solution of the brightness temperatures of the layer of discrete scatterers overlying a flat surface is given. In passive remote sensing, the brightness temperature is measured. A brightness temperature vector is defined [60] in terms of the Stokes vector as

$$\overline{T}_B(\theta,\phi) = \frac{1}{C}\begin{pmatrix} I_v \\ I_h \\ U \\ V \end{pmatrix} \qquad (5.10)$$

where $C = K\epsilon/\epsilon_o\lambda^2$, with ϵ as the permittivity of the medium, and K is Boltzmann's constant.

For vegetation canopy, the medium can be assumed to be azimuthally symmetric in a statistical sense. In such a case, the third and fourth Stokes parameters are zero. The first and second Stokes parameters are independent of the angle ϕ, so the ϕ' integration can be carried out numerically and the resulting equations are in the

form of

$$\cos\theta\frac{d}{dz}I_v(\theta,z) = \kappa_{av}CT(z) - \kappa_{ev}I_v(\theta,z) + \int_o^\pi d\theta' \sin\theta' \Big[(v,v')I_v(\theta',z) + (v,h')I_h(\theta',z)\Big] \quad (5.11)$$

$$\cos\theta\frac{d}{dz}I_h(\theta,z) = \kappa_{ah}CT(z) - \kappa_{eh}I_h(\theta,z) + \int_o^\pi d\theta' \sin\theta' \Big[(h,v')I_v(\theta',z) + (h,h')I_h(\theta',z)\Big] \quad (5.12)$$

where

$$[\alpha(\theta),\beta(\theta')] = \int_o^{2\pi} d\phi' P_{\alpha,\beta}(\theta,\phi;\theta',\phi') \quad (5.13)$$

with $\alpha,\beta = v,h$ and $P_{vv} = P_{11}$. $P_{vh} = P_{12}$, $P_{hv} = P_{21}$ and $P_{hh} = P_{22}$. The phase matrix for the scatterers is the same as described in the previous chapter. To solve equations (5.11) and (5.12), a numerical approach using the discrete ordinates method is employed [59]. The equations are first discretized by approximating the integral with a finite sum by the Guassian quadrature formula.

$$\int_o^\pi d\theta' \sin\theta' [v(\theta),v(\theta')]I_v(\theta',z) = \sum_{j=-n}^{n} a_j [v(\theta),v_j]I_{v_j}(z) \quad (5.14)$$

where

$$v_j = v(\theta = \cos^{-1}\mu_j) \quad (5.15)$$

$$I_{v_j} = I_v(\theta = \cos^{-1}\mu_j) \quad (5.16)$$

$\cos\theta_j$ correspond to the zeroes (μ_j) of the Legendre polynomial $P_{2n}(\mu)$ and a_j are the coefficients the Christoffel weighting functions. The values of μ_j and a_j can be calculated by solving the Gauss-Legendre polynomials [48]. There are $2n$ μ_j values and $2n$ a_j values and

$$a_j = a_{-j} \quad (5.17)$$

$$\mu_j = -\mu_{-j} \quad (5.18)$$

After we further discretize the variable θ in (5.14) in θ_j directions, the integro-differential equations (5.11) and (5.12) are approximated by the following semi-discretized form,

$$\mu_i \frac{d}{dz} I_{vi}(z) = \kappa_{avi} CT - \kappa_{evi} I_{vi}(z) + \sum_{j=-n}^{n} a_j \Big[(v_i, v_j) I_{vj}(z) + (v_i, h_j) I_{hj}(z) \Big] \tag{5.19}$$

$$\mu_i \frac{d}{dz} I_{hi}(z) = \kappa_{ahi} CT - \kappa_{ehi} I_{hi}(z) + \sum_{j=-n}^{n} a_j \Big[(h_i, v_j) I_{vj}(z) + (h_i, h_j) I_{hj}(z) \Big] \tag{5.20}$$

where

$$I_{\beta i}(z) = I_\beta(\mu_i, z) \tag{5.21}$$

$$\kappa_{a\beta i} = \kappa_{a\beta}(\mu_i) \tag{5.22}$$

$$\kappa_{e\beta i} = \kappa_{e\beta}(\mu_i) \tag{5.23}$$

$$(\alpha_i, \beta_j) = [\alpha(\mu_i), \beta(\mu_j)] \tag{5.24}$$

for $i = \pm 1, \pm 2, \ldots, \pm n$. Equations (5.19) and (5.20) are first order inhomogeneous differential equations. To solve for the homogeneous solutions, we assume the solutions of the form $\exp(\alpha z)$. We have

$$I_{\beta i}(z) = I_{\beta i} e^{\alpha z} \tag{5.25}$$

Substituting equation (5.25) in (5.19) and (5.20), with the matrix notation, we obtain

$$\alpha \overline{\overline{\mu}} \cdot \overline{I}_u = -\overline{\overline{\kappa_e}} \cdot \overline{I}_u + \overline{\overline{F}} \cdot \overline{\overline{a}} \cdot \overline{I}_u + \overline{\overline{B}} \cdot \overline{\overline{a}} \cdot \overline{I}_d \tag{5.26}$$

$$-\alpha \overline{\overline{\mu}} \cdot \overline{I}_d = -\overline{\overline{\kappa_e}} \cdot \overline{I}_d + \overline{\overline{B}} \cdot \overline{\overline{a}} \cdot \overline{I}_u + \overline{\overline{F}} \cdot \overline{\overline{a}} \cdot \overline{I}_d \tag{5.27}$$

where $\overline{I}_u$ and $\overline{I}_d$ are $2n$ vectors denoting upward- and downward-going specific inten-

sities,

$$\overline{I}_u = \begin{bmatrix} I_{v1} \\ \vdots \\ I_{vn} \\ I_{h1} \\ \vdots \\ I_{hn} \end{bmatrix} \qquad \overline{I}_d = \begin{bmatrix} I_{v-1} \\ \vdots \\ I_{v-n} \\ I_{h-1} \\ \vdots \\ I_{h-n} \end{bmatrix} \tag{5.28}$$

and $\overline{\overline{\mu}}$, $\overline{\overline{\kappa}}_e$ and $\overline{\overline{a}}$ are $2n \times 2n$ diagonal matrices

$$\overline{\overline{\mu}} = \text{diag}[\mu_1, \mu_2, \cdots, \mu_n, \mu_1, \mu_2, \cdots, \mu_n] \tag{5.29}$$

$$\overline{\overline{\kappa}}_e = \text{diag}[\kappa_{ev1}, \kappa_{ev2}, \cdots, \kappa_{evn}, \kappa_{eh1}, \kappa_{eh2}, \cdots, \kappa_{ehn}] \tag{5.30}$$

$$\overline{\overline{a}} = \text{diag}[a_1, a_2, \cdots, a_n, a_1, a_2, \cdots, a_n] \tag{5.31}$$

and $\overline{\overline{F}}$ and $\overline{\overline{B}}$ are $2n \times 2n$ matrices

$$\overline{\overline{F}} = \begin{bmatrix} (v_1, v_1) & \cdots & (v_1, v_n) & (v_1, h_1) & \cdots & (v_1, h_n) \\ \vdots & & \vdots & \vdots & & \vdots \\ (v_n, v_1) & \cdots & (v_n, v_n) & (v_n, h_1) & \cdots & (v_n, h_n) \\ (h_1, v_1) & \cdots & (h_1, v_n) & (h_1, h_1) & \cdots & (h_1, h_n) \\ \vdots & & \vdots & \vdots & & \vdots \\ (h_n, v_1) & \cdots & (h_n, v_n) & (h_n, h_1) & \cdots & (h_n, h_n) \end{bmatrix} \tag{5.32}$$

$$\overline{\overline{B}} = \begin{bmatrix} (v_1, v_{-1}) & \cdots & (v_1, v_{-n}) & (v_1, h_{-1}) & \cdots & (v_1, h_{-n}) \\ \vdots & & \vdots & \vdots & & \vdots \\ (v_n, v_{-1}) & \cdots & (v_n, v_{-n}) & (v_n, h_{-1}) & \cdots & (v_n, h_{-n}) \\ (h_1, v_{-1}) & \cdots & (h_1, v_{-n}) & (h_1, h_{-1}) & \cdots & (h_1, h_{-n}) \\ \vdots & & \vdots & \vdots & & \vdots \\ (h_n, v_{-1}) & \cdots & (h_n, v_{-n}) & (h_n, h_{-1}) & \cdots & (h_n, h_{-n}) \end{bmatrix} \tag{5.33}$$

The number of homogeneous equations can be reduced from $4n$ to $2n$ by defining

$$\overline{I}_+ = \overline{I}_u + \overline{I}_d \tag{5.34}$$

$$\overline{I}_- = \overline{I}_u - \overline{I}_d \tag{5.35}$$

Equations (5.26) and (5.27) can be rewritten in terms of $\overline{I}_+$ and $\overline{I}_-$ as

$$\alpha\overline{\overline{\mu}} \cdot \overline{I}_- = \overline{\overline{A}} \cdot \overline{I}_+ \tag{5.36}$$

$$\alpha\overline{\overline{\mu}} \cdot \overline{I}_+ = \overline{\overline{W}} \cdot \overline{I}_- \tag{5.37}$$

where

$$\overline{\overline{A}} = -\overline{\overline{\kappa}}_e + \overline{\overline{F}} \cdot \overline{\overline{a}} + \overline{\overline{B}} \cdot \overline{\overline{a}} \tag{5.38}$$

$$\overline{\overline{W}} = -\overline{\overline{\kappa}}_e + \overline{\overline{F}} \cdot \overline{\overline{a}} - \overline{\overline{B}} \cdot \overline{\overline{a}} \tag{5.39}$$

Combining equations (5.36) and (5.37) gives the eigenvalue problem

$$(\overline{\overline{\mu}}^{-1} \cdot \overline{\overline{W}} \cdot \overline{\overline{\mu}}^{-1} \cdot \overline{\overline{A}} - \alpha^2\overline{\overline{I}})\overline{I}_+ = 0 \tag{5.40}$$

where $\overline{\overline{I}}$ is an identity matrix of $2n \times 2n$.

It can be observed from equation (5.40) that if α is an eigenvalue so is $-\alpha$. Equation (5.40) has $2n$ eigenvalues $\alpha_1^2, \alpha_2^2, \cdots, \alpha_{2n}^2$ and $2n$ eigenvectors $\overline{I}_{+1}, \overline{I}_{+2} \cdots, \overline{I}_{+2n}$. The solution of $\overline{I}_-$ can be expressed in terms of $\overline{I}_+$ by using equation (5.36). We define a $2n \times 2n$ eigenmatrix $\overline{\overline{E}}$ such that its jth column is the eigenvector $\overline{I}_{+j}$. Then the homogeneous solution for $\overline{I}_+$ and $\overline{I}_-$ are given by

$$\overline{I}_+ = \overline{\overline{E}} \cdot \overline{\overline{D}}(z) \cdot \frac{\overline{x}}{2} + \overline{\overline{E}} \cdot \overline{\overline{U}}(z+d) \cdot \frac{\overline{y}}{2} \tag{5.41}$$

$$\overline{I}_- = \overline{\overline{Q}} \cdot \overline{\overline{D}}(z) \cdot \frac{\overline{x}}{2} - \overline{\overline{Q}} \cdot \overline{\overline{U}}(z+d) \cdot \frac{\overline{y}}{2} \tag{5.42}$$

where

$$\overline{\overline{Q}} = \overline{\overline{\mu}}^{-1} \cdot \overline{\overline{A}} \cdot \overline{\overline{E}} \cdot \overline{\overline{\alpha}}^{-1} \tag{5.43}$$

$$\overline{\overline{D}}(z) = \text{diag}[e^{\alpha_1 z}, e^{\alpha_2 z}, \cdots, e^{\alpha_{2n} z}] \tag{5.44}$$

$$\overline{\overline{U}}(z) = \text{diag}[e^{-\alpha_1 z}, e^{-\alpha_2 z}, \cdots, e^{-\alpha_{2n} z}] \tag{5.45}$$

$$\overline{\overline{\alpha}} = \text{diag}[\alpha_1, \alpha_2, \cdots, \alpha_{2n}] \tag{5.46}$$

The solutions of the upward and downward propagating intensities, $\overline{I}_u$ and $\overline{I}_d$ can be obtained by making use of equations (5.34) and (5.35) and the addition of the particular solutions to equations (5.19) and (5.20). They are given by

$$\overline{I}_u = C\overline{T} + (\overline{\overline{E}} + \overline{\overline{Q}}) \cdot \overline{\overline{D}}(z) \cdot \overline{x} - (\overline{\overline{E}} - \overline{\overline{Q}}) \cdot \overline{\overline{U}}(z+d) \cdot \overline{y} \tag{5.47}$$

$$\overline{I}_d = C\overline{T} + (\overline{\overline{E}} - \overline{\overline{Q}}) \cdot \overline{\overline{D}}(z) \cdot \overline{x} - (\overline{\overline{E}} + \overline{\overline{Q}}) \cdot \overline{\overline{U}}(z+d) \cdot \overline{y} \tag{5.48}$$

where $\overline{T}$ is a $2n$ vector with each element equal to the temperature T. $\overline{x}$ and $\overline{y}$ are to be determined from the boundary conditions. The boundary conditions are, in matrix form,

$$\overline{I}_d(z=0) = 0 \tag{5.49}$$

$$\overline{I}_u(z=-d) = \overline{\overline{r}}_{12} \cdot \overline{I}_d(z=-d) + \overline{\overline{t}}_{21} \cdot C\overline{T}_2 \tag{5.50}$$

where

$$\overline{\overline{r}}_{12} = \text{diag}[r_{v12_1}, r_{v12_2}, \cdots, r_{v12_n}, r_{h12_1}, r_{h12_2}, \cdots, r_{h12_n}] \tag{5.51}$$

$$\overline{\overline{t}}_{21} = \text{diag}[t_{v21_1}, t_{v21_2}, \cdots, t_{v21_n}, t_{h21_1}, t_{h21_2}, \cdots, t_{h21_n}] \tag{5.52}$$

and $\overline{T}_2$ is a $2n$ vector with each element equals to the physical temperature of the half-space below $z = -d$. $r_{\alpha 12}$ and $t_{\alpha 21}$ are, respectively, the Fresnel reflectivity and transmissivity for polarization α at the interface $z = -d$.

After determining the unknown constants x's and y's, the brightness temperature

$\overline{T}_B$ is given by

$$\overline{T}_B = \frac{1}{C}\overline{I}_u(z=0) \tag{5.53}$$

5.4 Absorption Enhancement

The geometrical configuration of the cylinder cluster is shown in Fig. 5-2. Numerical results are calculated for the following parameters. The cluster consists of a vertical center cylinder of radius 0.3 cm and of length 10 cm. There are five layers of branches distributed uniformly and randomly along the center cylinder. All the branches make an angle of 45^o with the center cylinder. The radius of the branch is 0.15 cm and its length is 2 cm. Two branches are arranged in the opposite direction to each other within a layer to form a pair. This pair of branches is attached to the center cylinder at random azimuthal positions. The permittivity of the cluster is $(11+i4)\epsilon_o$. All the quantities of the absorption cross section are normalized by dividing by the independent scattering absorption cross section $(\sigma_a)_{ind}$ as given by equation (5.2) for the horizontal polarization at incidence angle of 90^o. The frequency is 5.3 GHz.

In the first case, we consider such a cluster with 10 branches. The variation of absorption cross section with incidence angle θ for two polarizations is shown in Figs. 5-3 and 5-4. At nadir, there is a difference between two polarizations. The cluster exhibits azimuthal asymmetry due to a few number of branches. It should be noted that the center cylinder is much larger than the branching ones and the effect of the center cylinder is dominant in this case. The absorption cross section for the horizontal polarization obtained from independent scattering model is not sensitive to the changes in the incidence angle. This is because the absorption is proportional to the square of the magnitude of the internal field and the incident electric field vector does not change with incidence angle for horizontal polarization. The small variation with incidence angle is due to the contribution from the branches. If there are enough branches to exhibit azimuthal symmetry, such variations will diminish. The variation with incidence angle is much larger for the vertical polarization case because the incident electric field vector changes with the incident angle. The differ-

ence between the present model and the independent scattering model is due to the mutual interactions between the components of the cluster. The vertical polarization case has a large enhancement at nadir. The internal field from the independent scattering model can be regarded as the first order internal field. The incident electric field has a small tangential component on the center cylinder and hence a small first order internal field. However, the induced fields on the branches can generate a larger tangential component on the center cylinder which facilitates the penetration of the electric field into the center cylinder. This mutual interaction creates a significant change in the internal field and the absorption is several times larger than that of the independent scattering case. At 90^o incident angle, the first order internal field for the center cylinder is already high and the enhancement is not significant.

The second case we consider is a cluster with 48 branches. The number of branching layers has been increased to 12. Within each layer, four branches are arranged at right angles to each other. They are then attached to the center cylinder at random azimuthal locations. The results are shown in Figs. 5-5 and 5-6. We observe that the cluster exhibits azimuthal symmetry due to the large number of branches. The results at nadir for the two polarizations are approximately the same. In Fig. 5-5, as predicted previously, the independent scattering curve for the horizontal polarization does not change with incidence angle. Significant enhancements are observed for both polarizations at nadir. However, for the vertical polarization, the absorption with mutual interaction is less than that from independent scattering at large incident angles. This is due to the blocking of the center cylinder and the branches which results in lower internal fields. The horizontal polarization only excites a small internal field for the center cylinder, so that the near field interaction always enhances the absorption. Without considering the structure of cluster, the independent scattering predicts a symmetric absorption cross section with 90^o incident angle. It should be noted that even though the absorption cross section does not obey inversion symmetry, the extinction cross section does. The explanation is that, by combining optical theorem

and reciprocity, we obtain

$$\begin{aligned}\sigma_e(\theta) &= \frac{4\pi}{k} Im(f_{pp}(\theta;\theta)) = \frac{4\pi}{k} Im(f_{pp}(\pi-\theta;\pi-\theta)) \\ &= \sigma_e(\pi-\theta) \end{aligned} \tag{5.54}$$

where k is the wavenumber, σ_e is the extinction cross section, f_{pp} is the forward scattering function and $p = v, h$. The extinction cross sections show the inversion symmetry in Figs. 5-9 and 5-10. The extinction cross sections are calculated from the optical theorem. Energy conservation is observed in the calculation to 99% accuracy.

To study the relative importance of the absorption enhancement and blocking, we repeat the case 2 with the center cylinder removed. The results are shown in Figs. 5-7 and 5-8. Blocking lowers the internal fields of all the branches, and without the center cylinder, no significant enhancement is made for the horizontal polarization to counter the effect of blocking. Therefore at large incidence angles, the absorption from the numerical model is lower than that of the independent scattering model for both polarizations.

5.5 Brightness Temperature Calculation

In this section, theoretical results based on the MoM calculation of the scattering function of the scatterer are presented and compared with results obtained from approximate methods. The brightness temperature is calculated for a two-layer medium embedded with vertically oriented clusters. The bottom surface is flat and the reflection matrix is given by equation (5.51). The phase matrix is evaluated in three different ways. First, it is calculated by the MoM for the cluster, in which the interactions between all components are fully accounted for (full numerical model). It is then compared with the independent scattering model in which the incoherent sum of its components is used to evaluate the phase matrix and the extinction matrix (independent scattering model). The third method is the coherent scattering model [24] in which the internal fields of the components are assumed to be the same as that

of independent scattering while the phase shift due to the relative positions of the scatterers is accounted for in the calculation of the scattered field. The phase matrix is evaluated using this model and the extinction matrix is calculated by the addition of the absorption cross section and the total scattering cross section.

In the first case, the brightness temperature for a half-space configuration with vertically oriented scatterers is calculated. The 10-branch scatterer described in the previous section is used. Ten realizations are generated for the branching scatterers to obtain the average brightness temperature. The radiometer frequency is 5.3 GHz. The canopy has a fractional volume $f = 0.5\%$ and a permittivity $\epsilon_s = (11+i4)\epsilon_o$. The physical temperature of the canopy is 300 K. The results for vertical and horizontal polarizations are shown in Figs. 5-11 and 5-12. The brightness temperature for the half-space medium is closely related to the ratio of the absorption coefficient κ_a and the extinction coefficient κ_e. These two quantities are functions of the observation angle. The extinction coefficient κ_e is equal to the sum of the scattering coefficient κ_s and the absorption coefficient κ_a. As mentioned in the previous section, for the 10-branch case, absorption enhancement is observed. The independent scattering model gives the highest brightness temperature because it ignores the coherent effect and yields the lowest scattering coefficient. Although it gives a low κ_a, it does not completely compensate for the underestimation of κ_s. As a result, the ratio of the κ_a/κ_e is highest among the three methods. When the scattering coefficient is calculated by the coherent scattering model, it has a higher value than the independent scattering model. With κ_a obtained from the independent scattering model, it has a lower ratio of κ_a/κ_e, and hence lower brightness temperature. The ratios of κ_a to κ_e obtained from the three methods are shown in Figs. 5-13 and 5-14. The coherent scattering model provides a good estimate of the brightness temperature for the vertical polarization. It underestimates the brightness temperature for the horizontal polarization at low observation angles because it does not account for the absorption enhancement, which is particularly high at that range.

We then increase the absorption of the scatterers by changing their permittivity to $(11+i8)\epsilon_o$ (case 2). The calculation of the brightness temperature for a half-space

scattering medium is repeated. The results are shown in Figs. 5-15 and 5-16. As the absorption increases, the brightness temperature increases. It also increases the relative importance of the absorption effects. As a result, the coherent scattering model gives a worse estimate than in case 1.

The thermal emission from the two-layer configuration modeling a vegetation canopy overlying on a flat ground surface is also calculated (case 3). The permittivity of the ground is $\epsilon_{soil} = (16 + i4)\epsilon_o$ while the ground and the canopy temperatures are both 300 K. The thickness (d) of the vegetation canopy is 25 cm. The optical depth $\kappa_e d/\cos\theta$ varies for different models. The full numerical approach gives the highest optical depth while the independent scattering model gives the lowest. The optical depth indicates how well the overlying layer shields the half-space underneath. Figs. 5-17 and 5-18 show the brightness temperatures for the two polarizations. For the vertically polarized brightness temperature, the Brewster angle effect [64] is observed. With the interaction between surface and volume scattering, the brightness temperatures obtained from the full numerical approach can be higher than the other two approximate methods, depending on the properties of the ground surface and the canopy thickness. At small observation angles, the brightness temperature is related to the ground surface emissivity. Therefore the Brewster angle effect is observed for the vertical polarization. The brightness temperature of the horizontal polarization decreases with increasing observation angle at that range. As the observation angle increases, the optical depth increases and the half-space limit is approached. This explains why the brightness temperature for the horizontal polarization rises at large observation angles. The effect of canopy thickness is studied by varying it from 10 cm and 100 cm. The brightness temperatures observed at 8.4^o are shown in Figs. 5-19 and 5-20. The brightness temperatures from the full numerical approach in this case are higher than the two approximate methods when the canopy thickness is small because it shields the bottom half-layer more effectively. The difference decreases as the thickness of the canopy increases. As the half-space limit is approached, the brightness temperatures from full numerical approach fall between that of independent scattering model and the coherent scattering model.

A 48-branch scatterer described in the previous section is used in the brightness temperature calculation (case 4). The same parameters as the first case are used. The scatterer has a more complicated structure, and both blocking and absorption enhancement occur. The brightness temperatures for a half-space configuration are shown in Figs. 5-21 and 5-22. The independent scattering model fails in this case. The number of branches is large and the coherent scattering effect is significant. The coherent scattering model gives a good estimate of the ratio κ_a/κ_e, although it does not give accurate results individually. The calculation is repeated with a canopy thickness of 25cm (case 5). The results are shown in Figs. 5-23 and 5-24. In general, the coherent scattering model in these cases gives a good estimate of the brightness temperatures. The difference between the full numerical model and the coherent scattering model for vertical polarization at large observation angles in the two-layer medium is larger than the half-space medium, which is due to the inaccuracy in the optical depth.

As mentioned in the previous chapter, when the branching angle is small, the mutual interactions will be strong and the full numerical method will give the most accurate results. To illustrate the point, the 48 branch-clusters with branching angles of 15^o and 75^o are used in the calculation. All other parameters remain the same as the previous cases. The brightness temperatures of the vertical polarization with 15^o branching angle clusters for the half-space medium (case 6) and the two-layer medium of thickness 25 cm (case 7) are shown in Figs. 5-25 and 5-26, respectively. The corresponding cases for the 75^o branching angle clusters are shown in Figs. 5-27 and 5-28. The difference between models can be as large as 30K for some observation angles.

5.6 Summary

In this chapter, we derived the numerical solution to the vector radiative transfer equation for the thermal emission from a layer of random medium overlying a flat ground surface. A branching scatterer is used for the calculation of the absorption

coefficients and the brightness temperatures. The absorption is found to be enhanced by the mutual interactions between the branching components. Blocking is another important factor in the clustering effect. In the calculation of brightness temperature, the elements of the phase matrix and the extinction matrix are evaluated under various assumptions. Numerical results show that the coherent scattering model gives a better estimate of the brightness temperatures than the independent scattering model for the half-space cases. Both the independent scattering model and the coherent scattering model underestimate the optical depth of the random medium layer. For scatterers with large number of branches, the independent model has been shown to be inadequate. When the mutual interactions between the components of the cluster are strong, full numerical method must be used. The use of the MoM to evaluate the scattering functions provides an accurate solution. The accurate solution can then be used to improve and verify approximate methods.

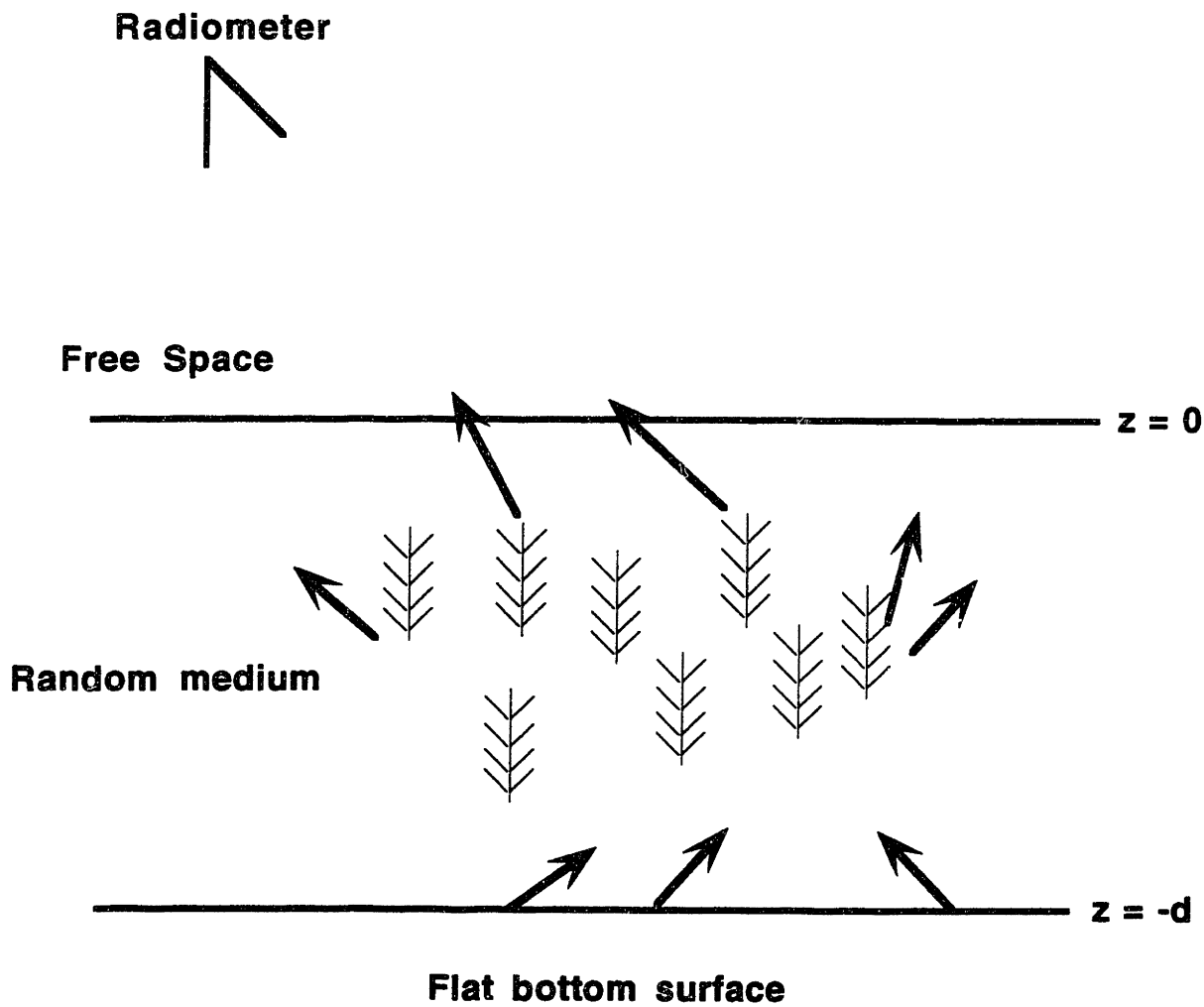

Figure 5-1: Geometrical configuration of the problem.

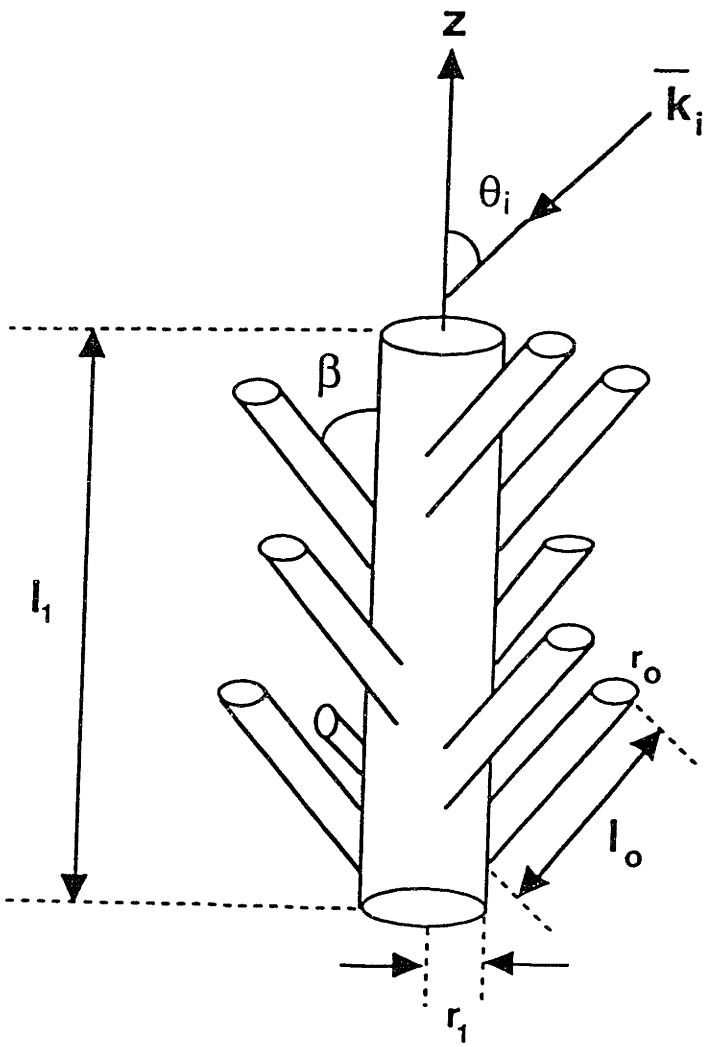

Figure 5-2: Configuration of the cluster. Center cylinder: length = 10 cm, radius = 0.3 cm; branching cylinder: length = 2 cm, radius = 0.15 cm, branching angle $\beta = 45°$; permittivity of the cluster = $(11 + i4)\epsilon_o$; frequency is 5.3 GHz; incidence angle = θ_i.

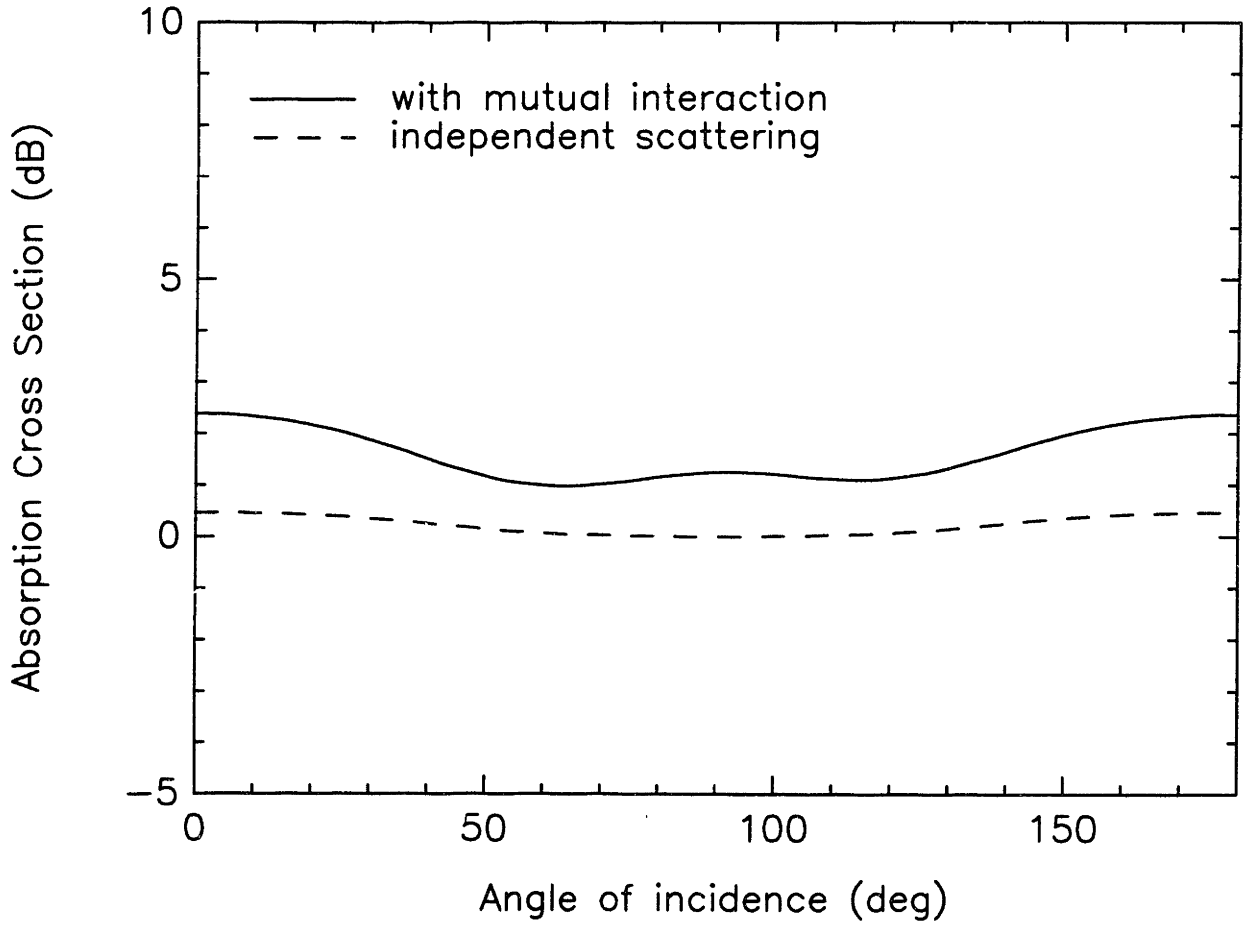

Figure 5-3: Absorption cross section as a function of incidence angle for horizontal polarization. Number of branches is 10. Curves are normalized by $(\sigma_{ah}(90^o))_{ind}$ with the numerical value of -39.5 dBsm.

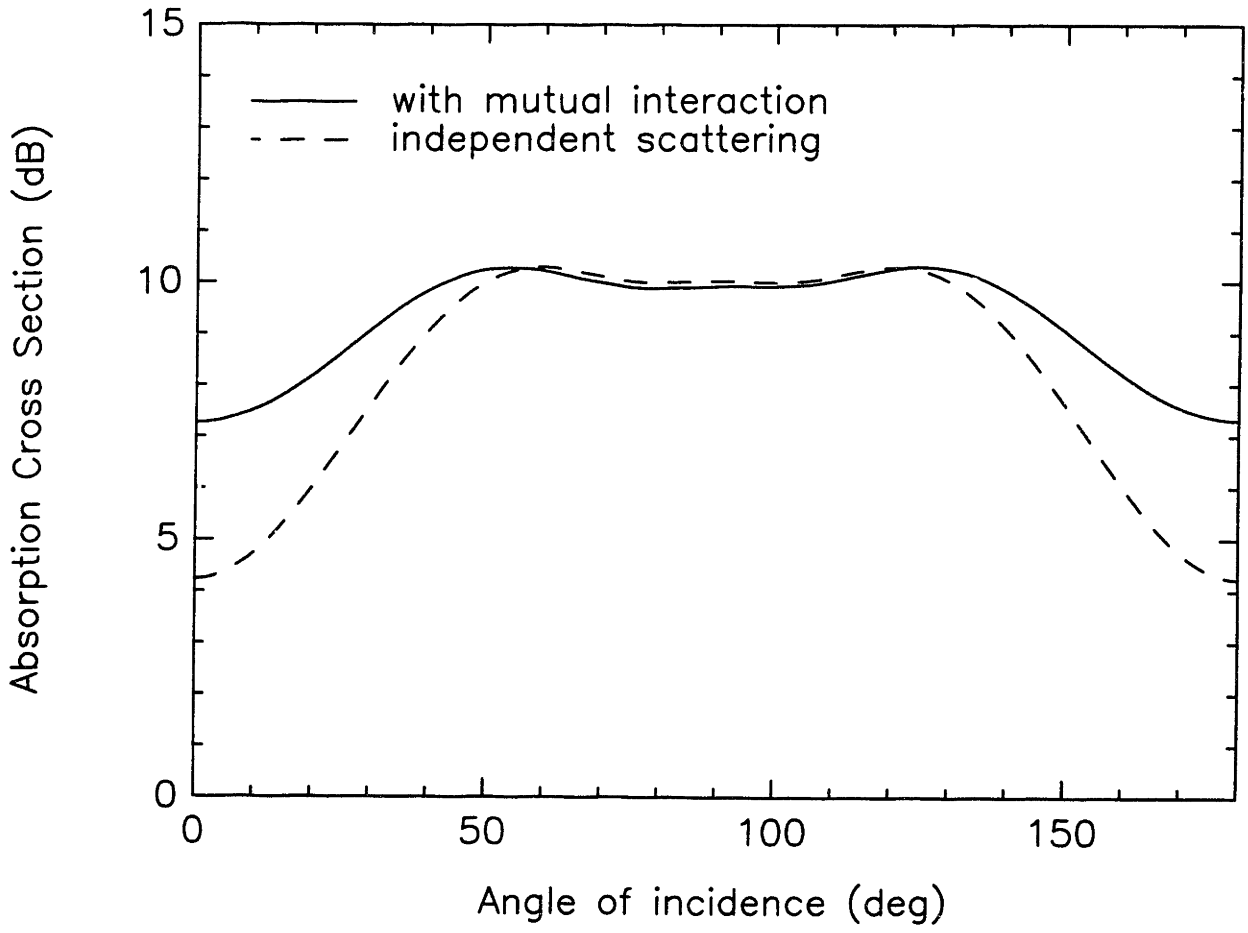

Figure 5-4: Absorption cross section as a function of incidence angle for vertical polarization. Number of branches is 10. Curves are normalized by $(\sigma_{ah}(90^o))_{ind}$ with the numerical value of -39.5 dBsm.

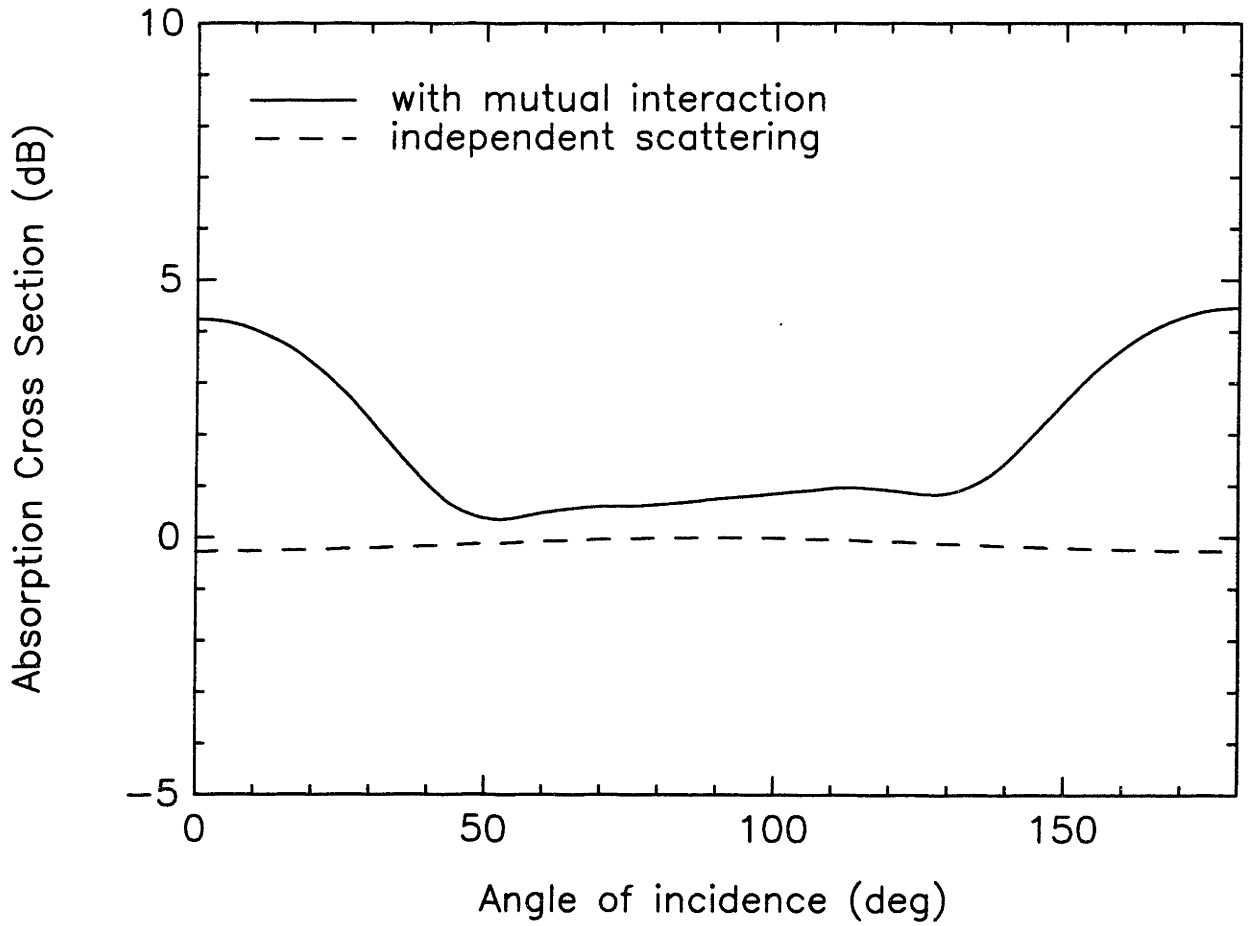

Figure 5-5: Absorption cross section as a function of incidence angle for horizontal polarization. Number of branches is 48. Curves are normalized by $(\sigma_{ah}(90^o))_{ind}$ with the numerical value of -30.7 dBsm.

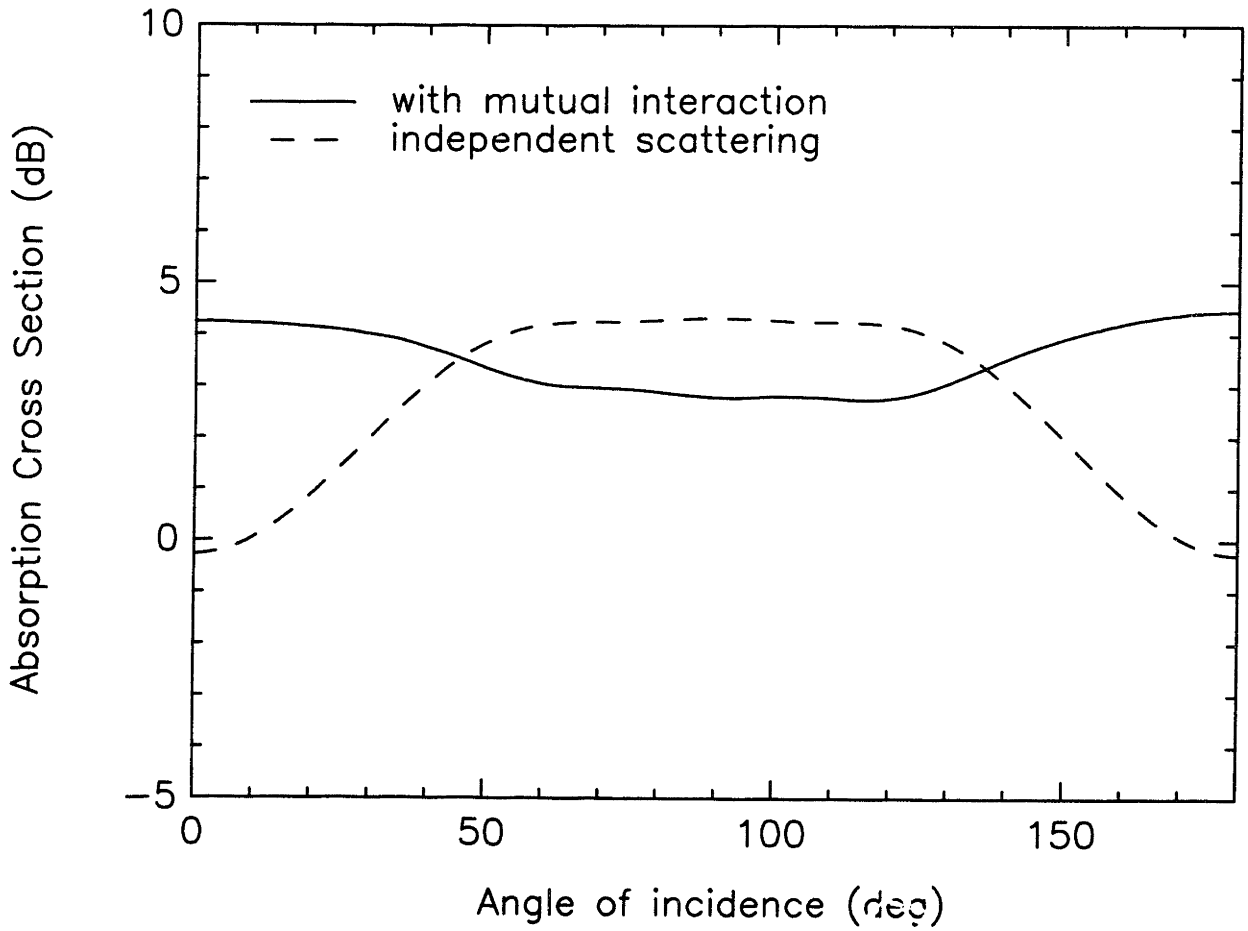

Figure 5-6: Absorption cross section as a function of incidence angle for vertical polarization. Number of branches is 48. Curves are normalized by $(\sigma_{ah}(90°))_{ind}$ with the numerical value of -30.7 dBsm.

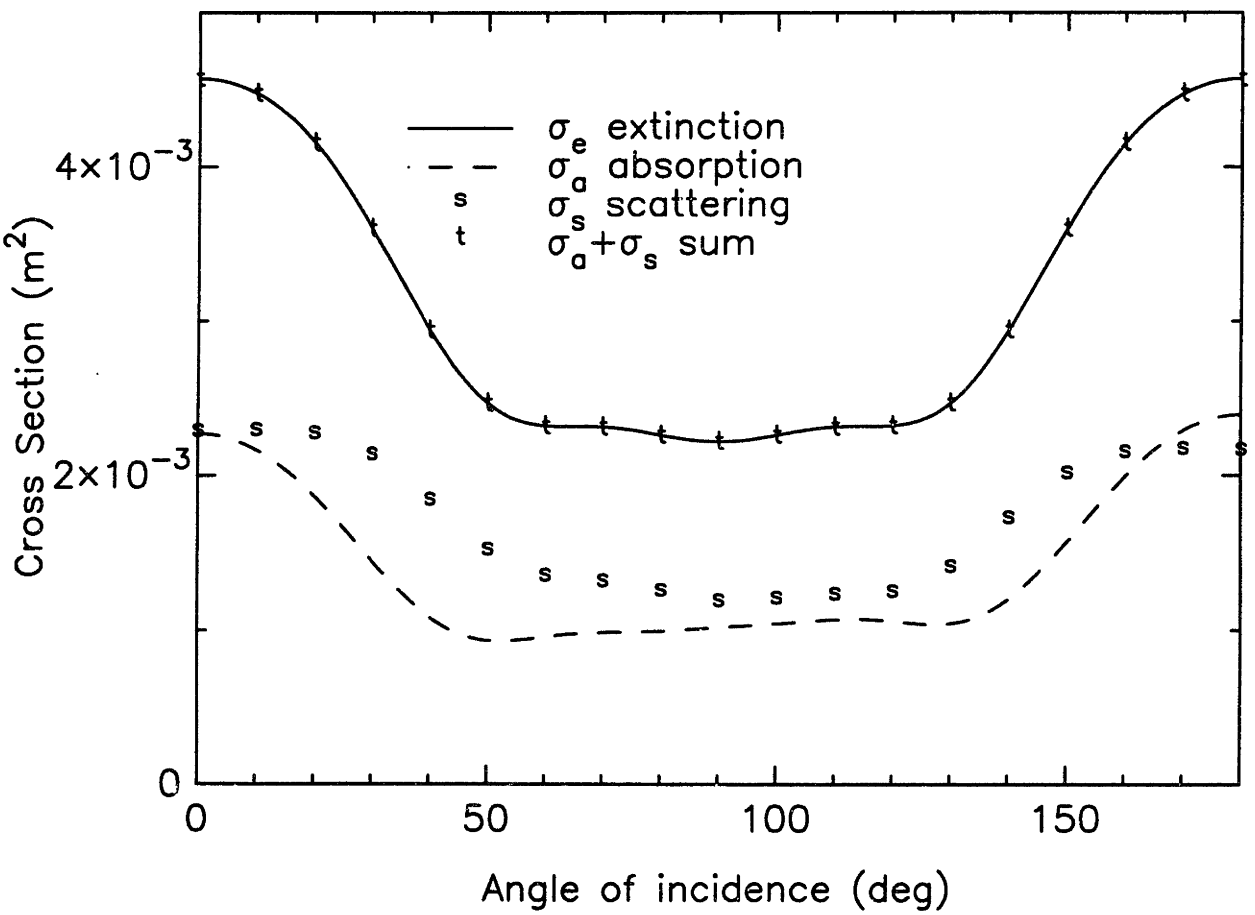

Figure 5-7: Cross sections as a function of incidence angle for horizontal polarization. The number of branches is 48.

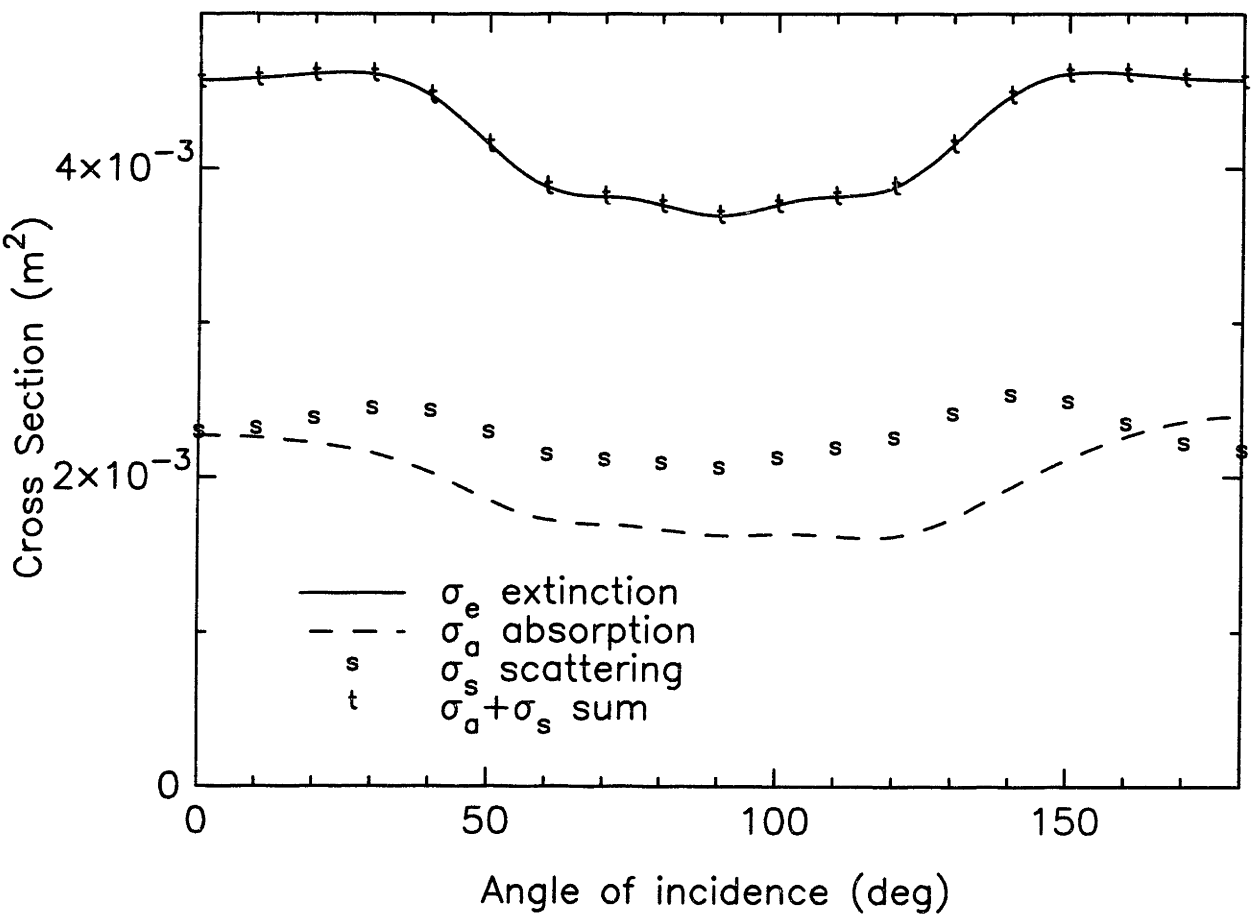

Figure 5-8: Cross section as a function of incidence angle for vertical polarization. Number of branches is 48.

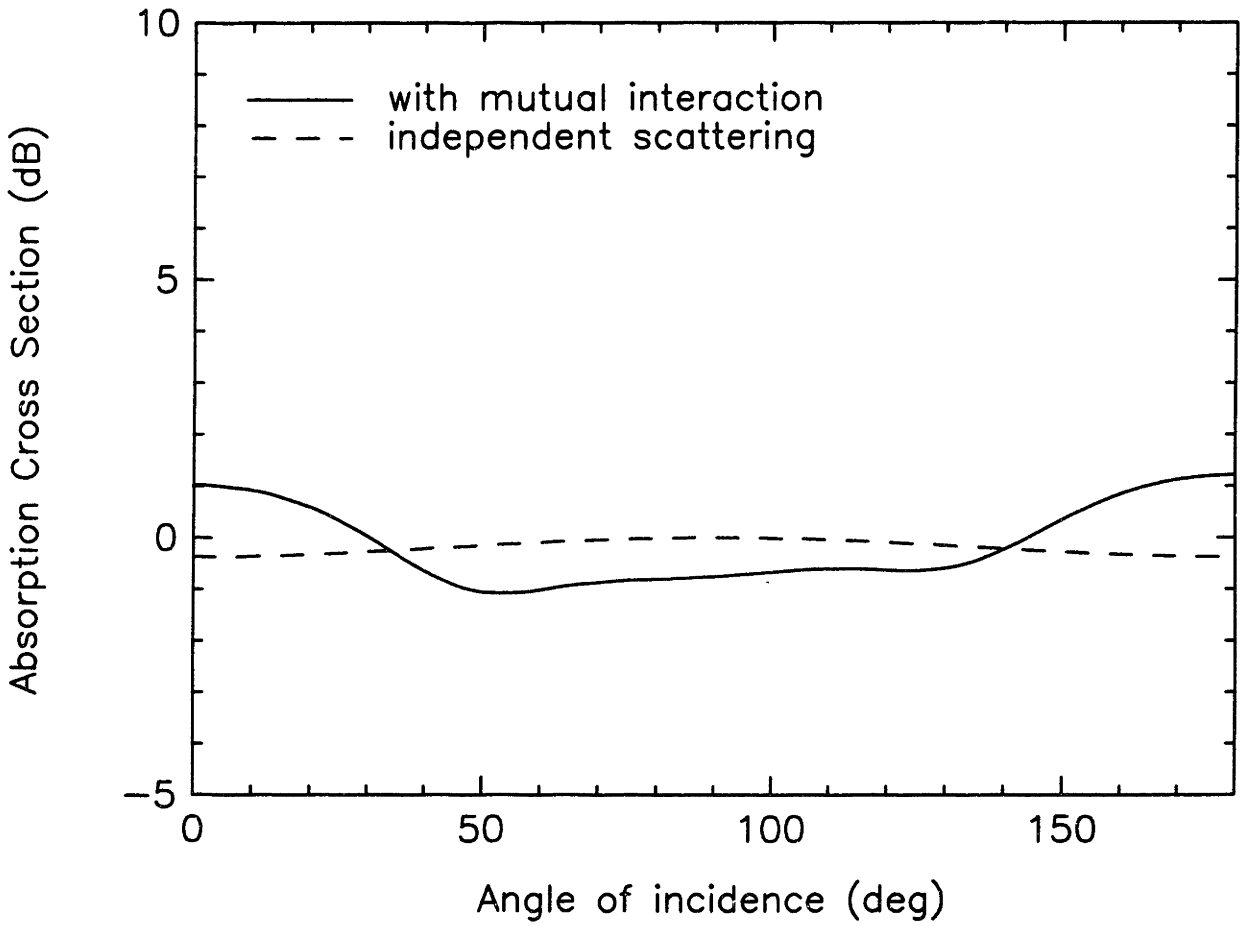

Figure 5-9: Absorption cross sections as a function of incidence angle for horizontal polarization. Number of branches is 48. Center cylinder is removed from the cluster. Curves are normalized by $(\sigma_{ah}(90°))_{ind}$ with the numerical value of -30.9 dBsm.

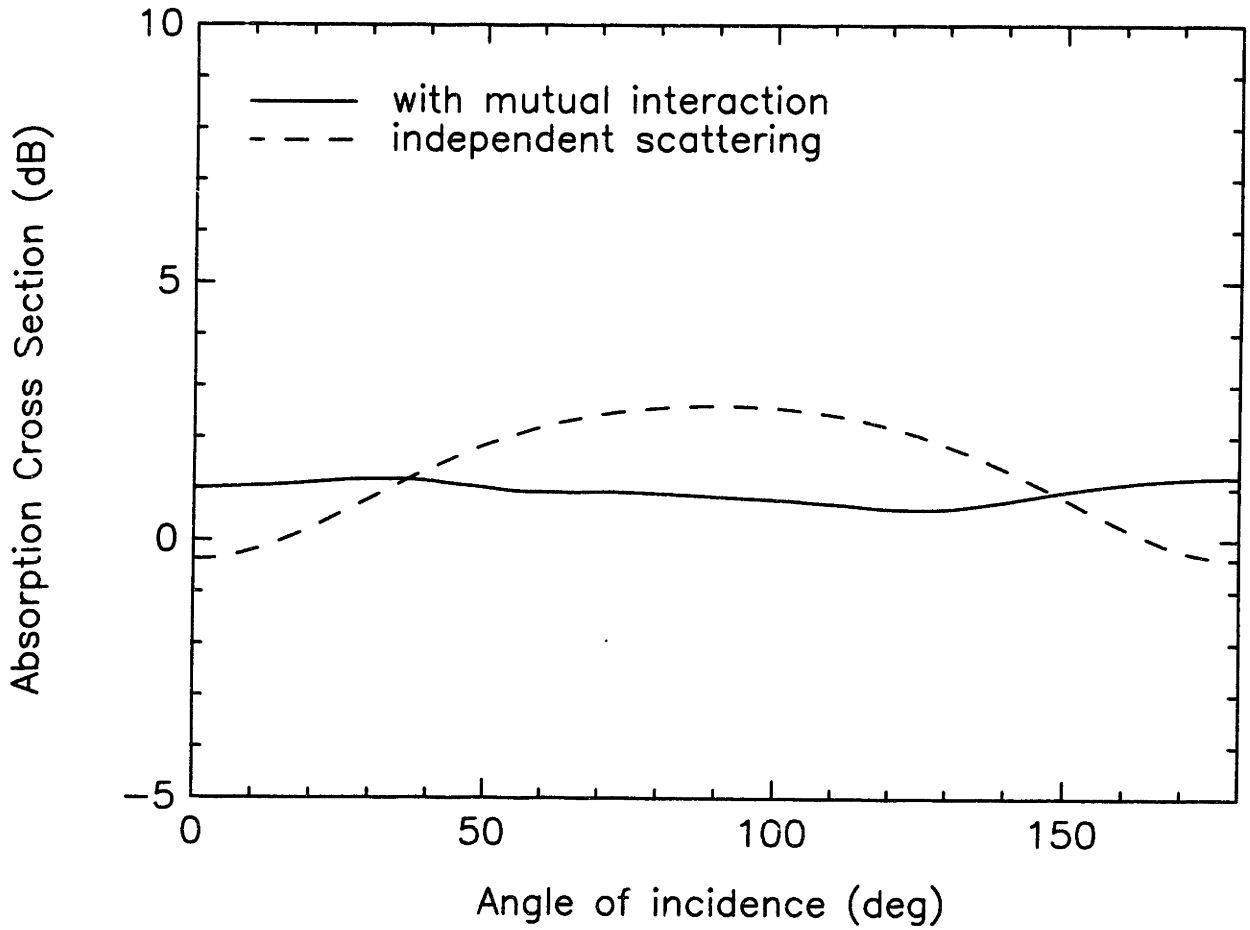

Figure 5-10: Absorption cross section as a function of incidence angle for vertical polarization. Number of branches is 48. Center cylinder is removed from the cluster. Curves are normalized by $(\sigma_{ah}(90^o))_{ind}$ with the numerical value of -30.9 dBsm.

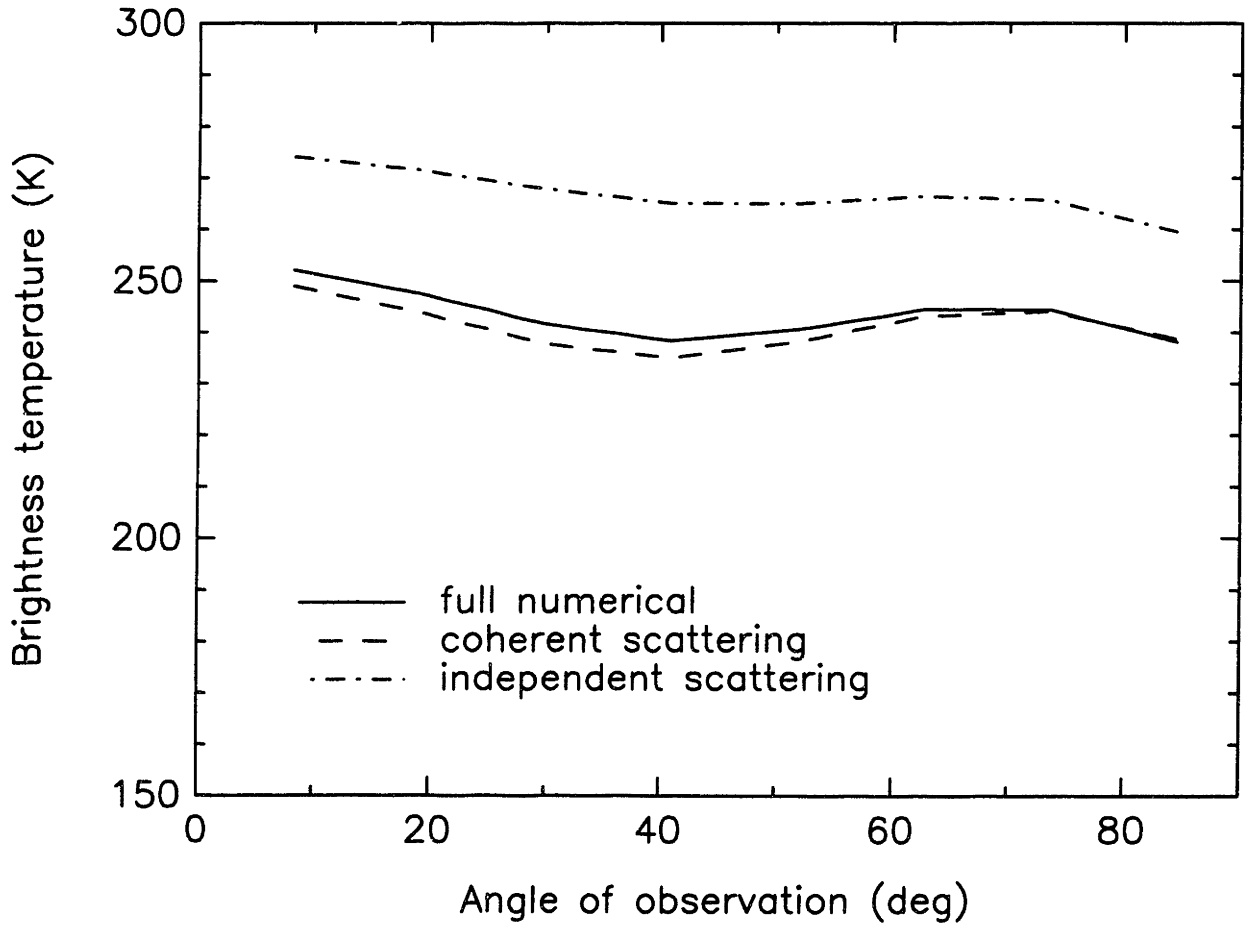

Figure 5-11: Brightness temperature of a half-space medium embedded with vertically oriented scatterers — T_{Bh}, $f = 0.5\%, \epsilon_s = (11 + i4)\epsilon_o$. Frequency is 5.3 GHz. Number of branches for the scatterers is 10.

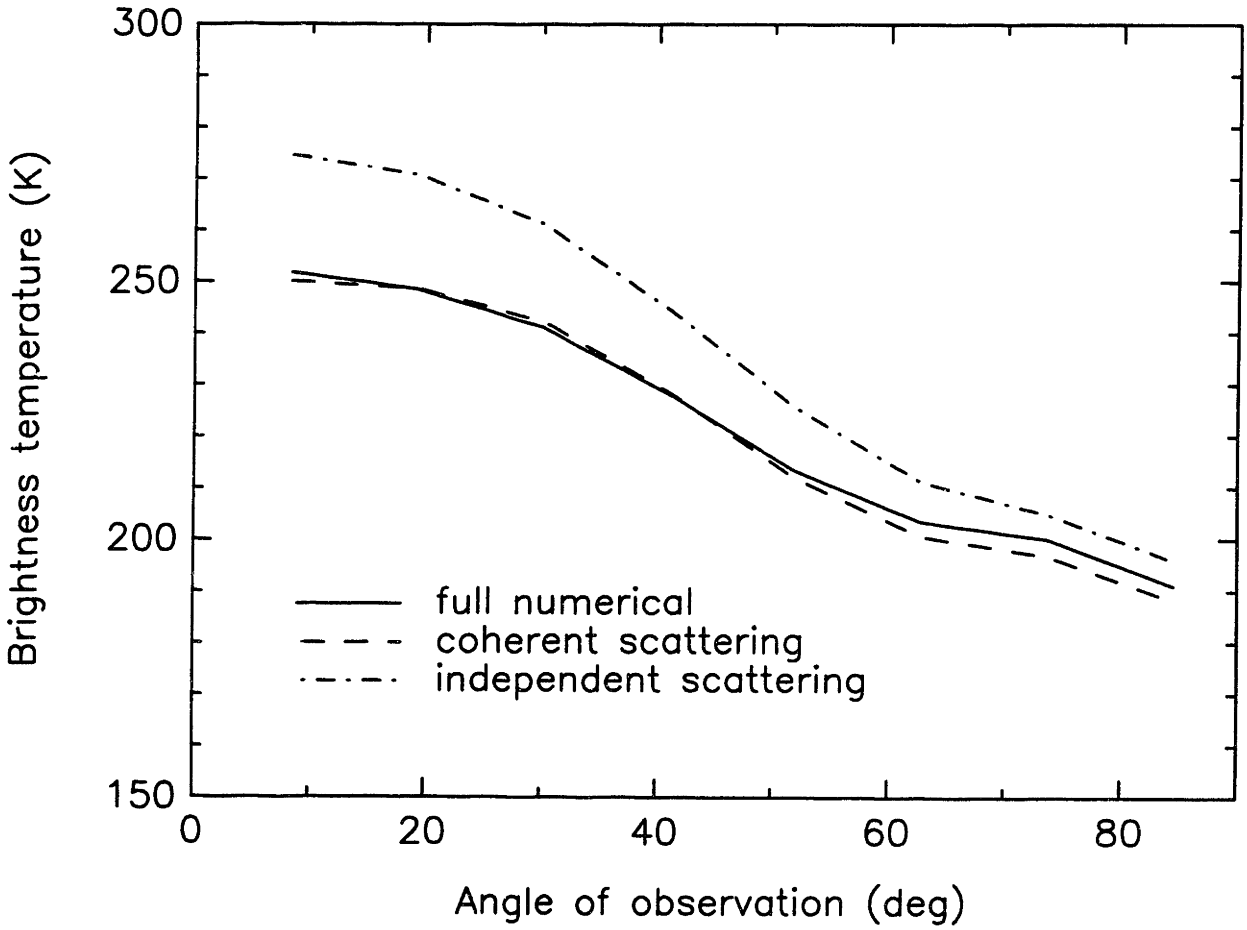

Figure 5-12: Brightness temperature of a half-space medium embedded with vertically oriented scatterers — T_{Bv}, $f = 0.5\%, \epsilon_s = (11 + i4)\epsilon_o$. Frequency is 5.3 GHz. Number of branches for the scatterers is 10.

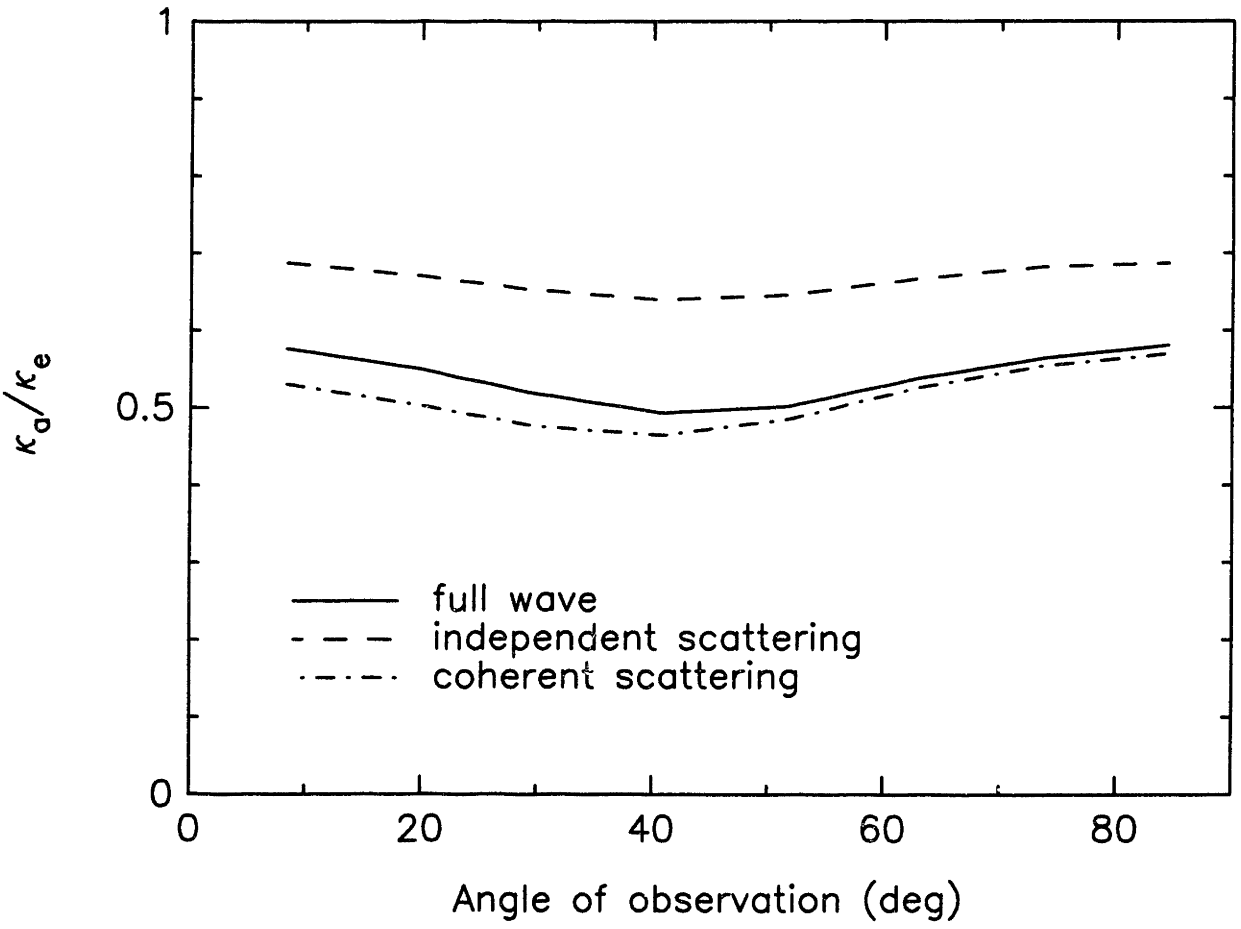

Figure 5-13: Ratio of κ_a to κ_e for horizontal polarization — case 1.

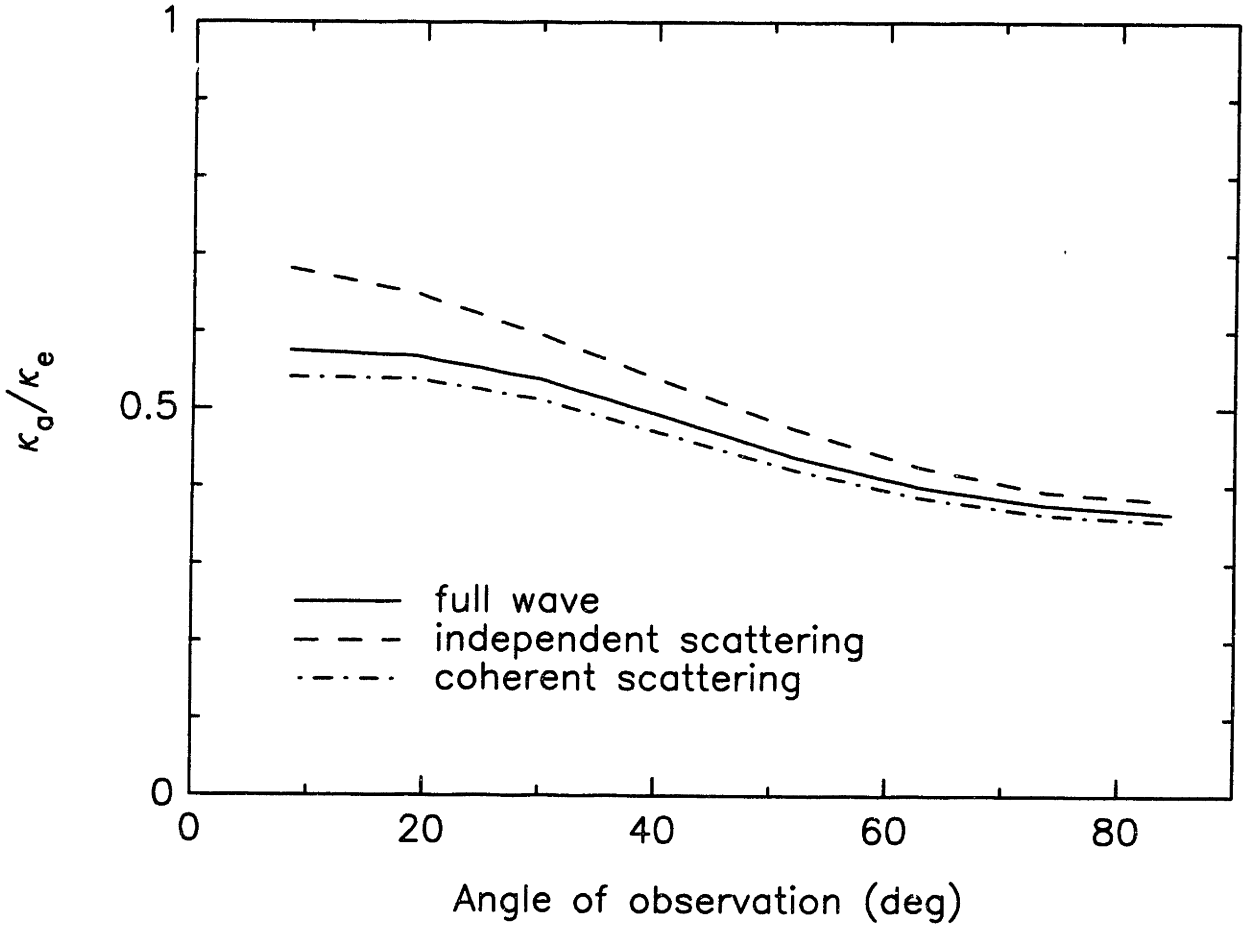

Figure 5-14: Ratio of κ_a to κ_e for vertical polarization — case 1.

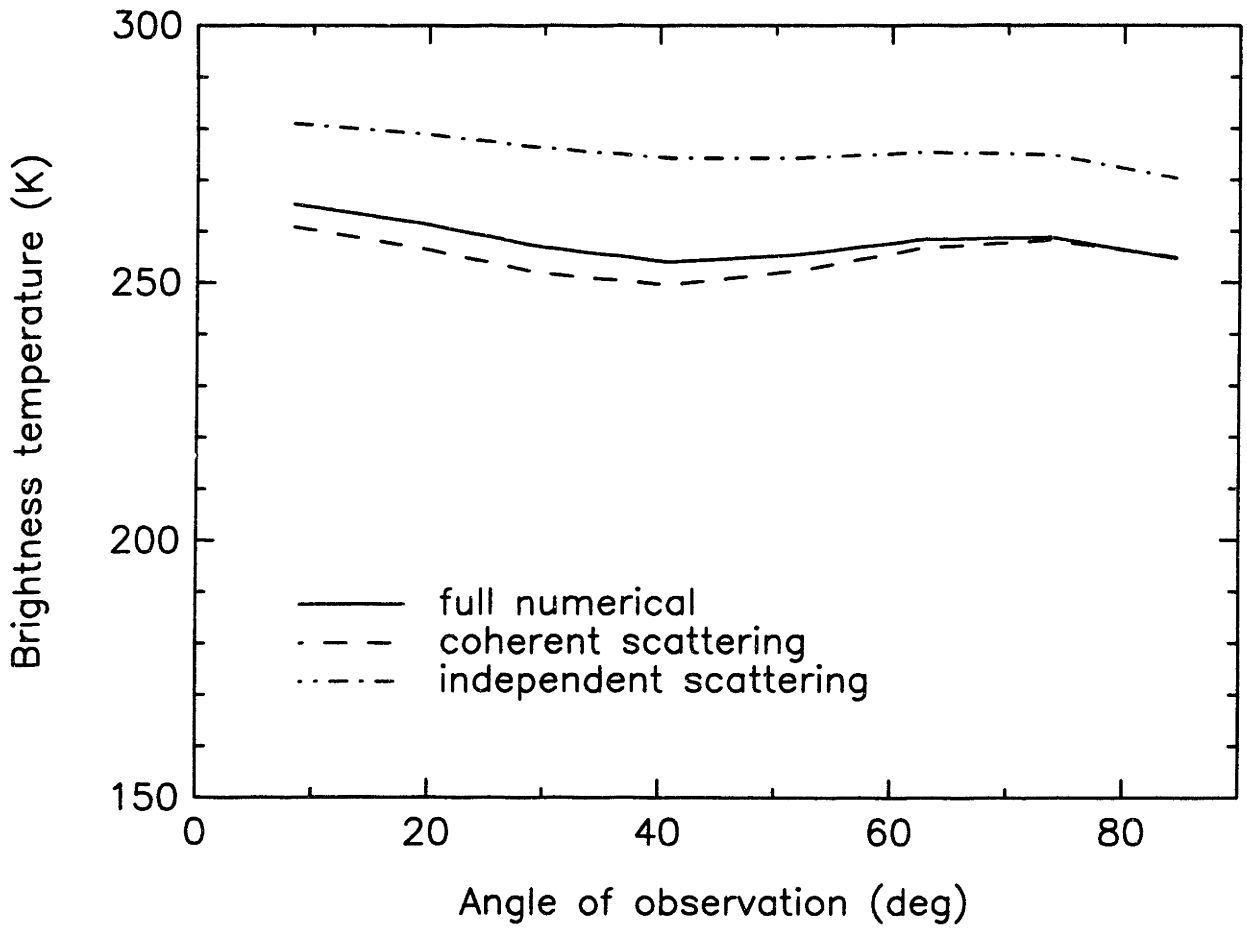

Figure 5-15: Brightness temperature of a half-space medium embedded with vertically oriented scatterers — T_{Bh}, $f = 0.5\%, \epsilon_s = (11 + i8)\epsilon_o$. Frequency is 5.3 GHz. Number of branches for the scatterers is 10.

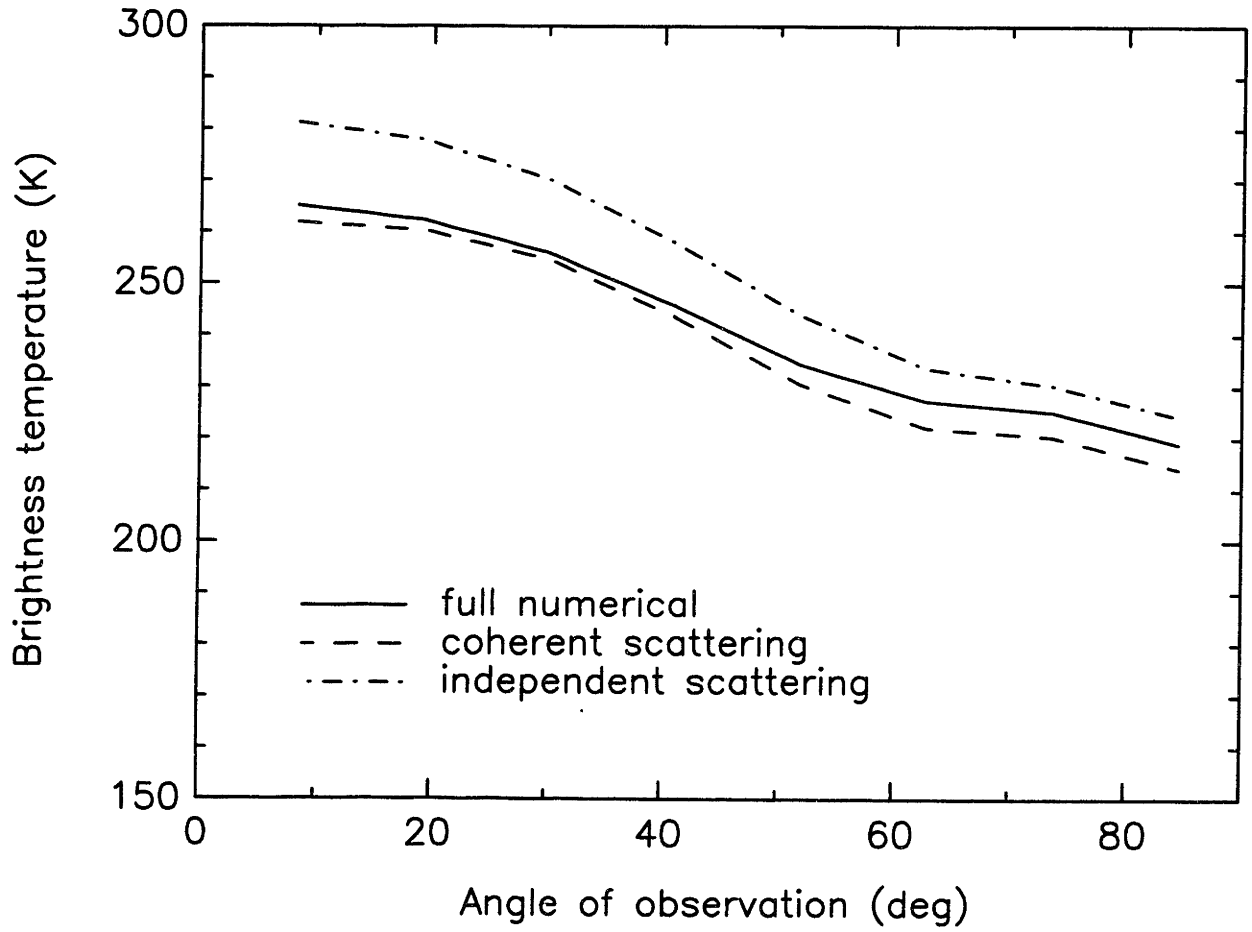

Figure 5-16: Brightness temperature of a half-space medium embedded with vertically oriented scatterers — T_{Bv}, $f = 0.5\%, \epsilon_s = (11+i8)\epsilon_o$. Frequency is 5.3 GHz. Number of branches for the scatterers is 10.

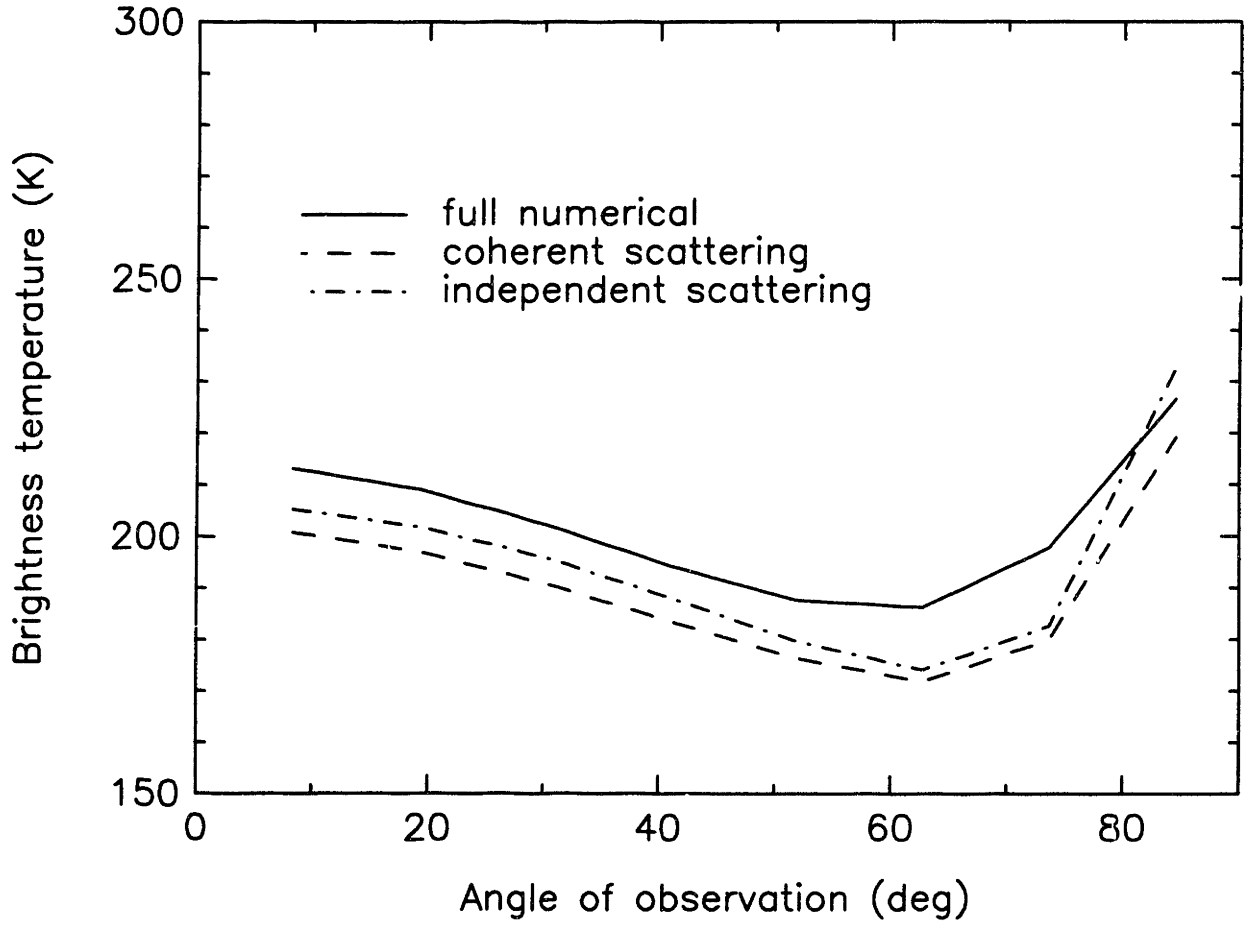

Figure 5-17: Brightness temperature of a two-layer medium — T_{Bh}, $f = 0.5\%, \epsilon_s = (11 + i4)\epsilon_o$. Scattering layer has a thickness $d = 0.25$m and underlying half-space is flat and has a permittivity $\epsilon_{soil} = (16 + i4)\epsilon_o$. Frequency is 5.3 GHz. Number of branches for the scatterers is 10.

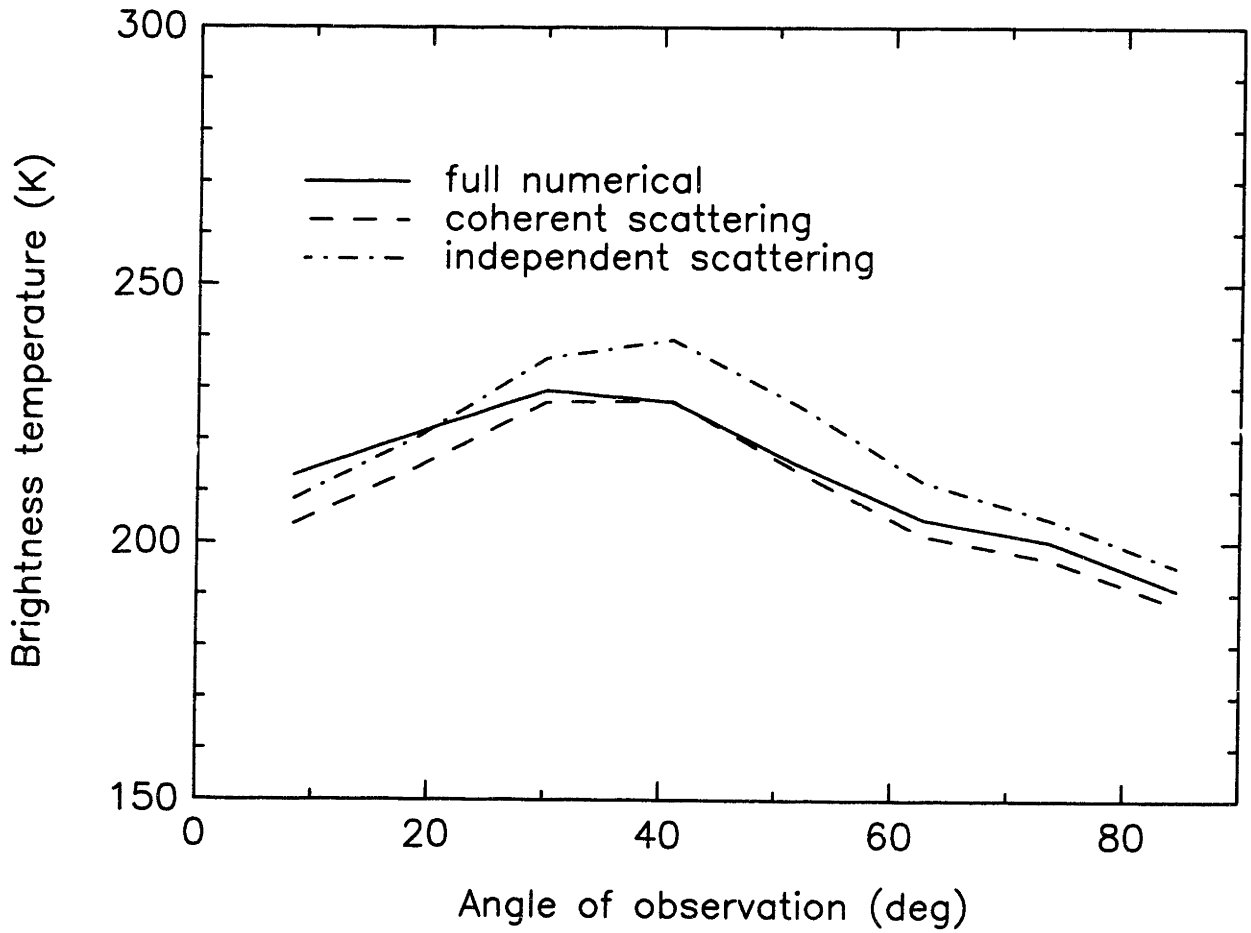

Figure 5-18: Brightness temperature of a two-layer medium — T_{Bv}, $f = 0.5\%, \epsilon_s = (11 + i4)\epsilon_o$. Scattering layer has a thickness $d = 0.25$m and underlying half-space is flat and has a permittivity $\epsilon_{soil} = (16 + i4)\epsilon_o$. Frequency is 5.3 GHz. Number of branches for the scatterers is 10.

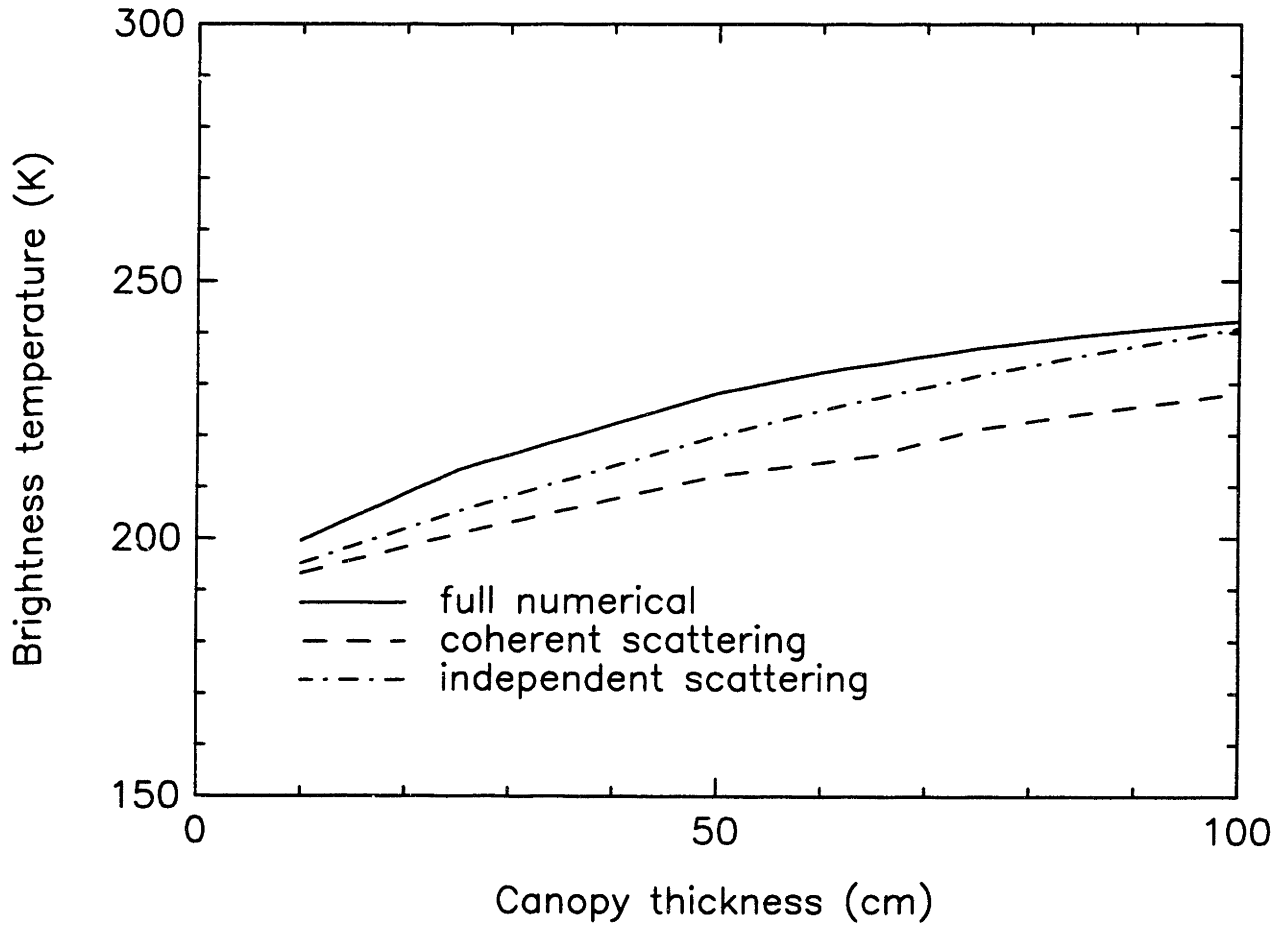

Figure 5-19: Brightness temperature of a two-layer medium — T_{Bh} at observation angle = 8.4°, $f = 0.5\%, \epsilon_s = (11 + i4)\epsilon_o$. Underlying half-space is flat and has a permittivity $\epsilon_{soil} = (16 + i4)\epsilon_o$. Frequency is 5.3 GHz. Number of branches for the scatterers is 10.

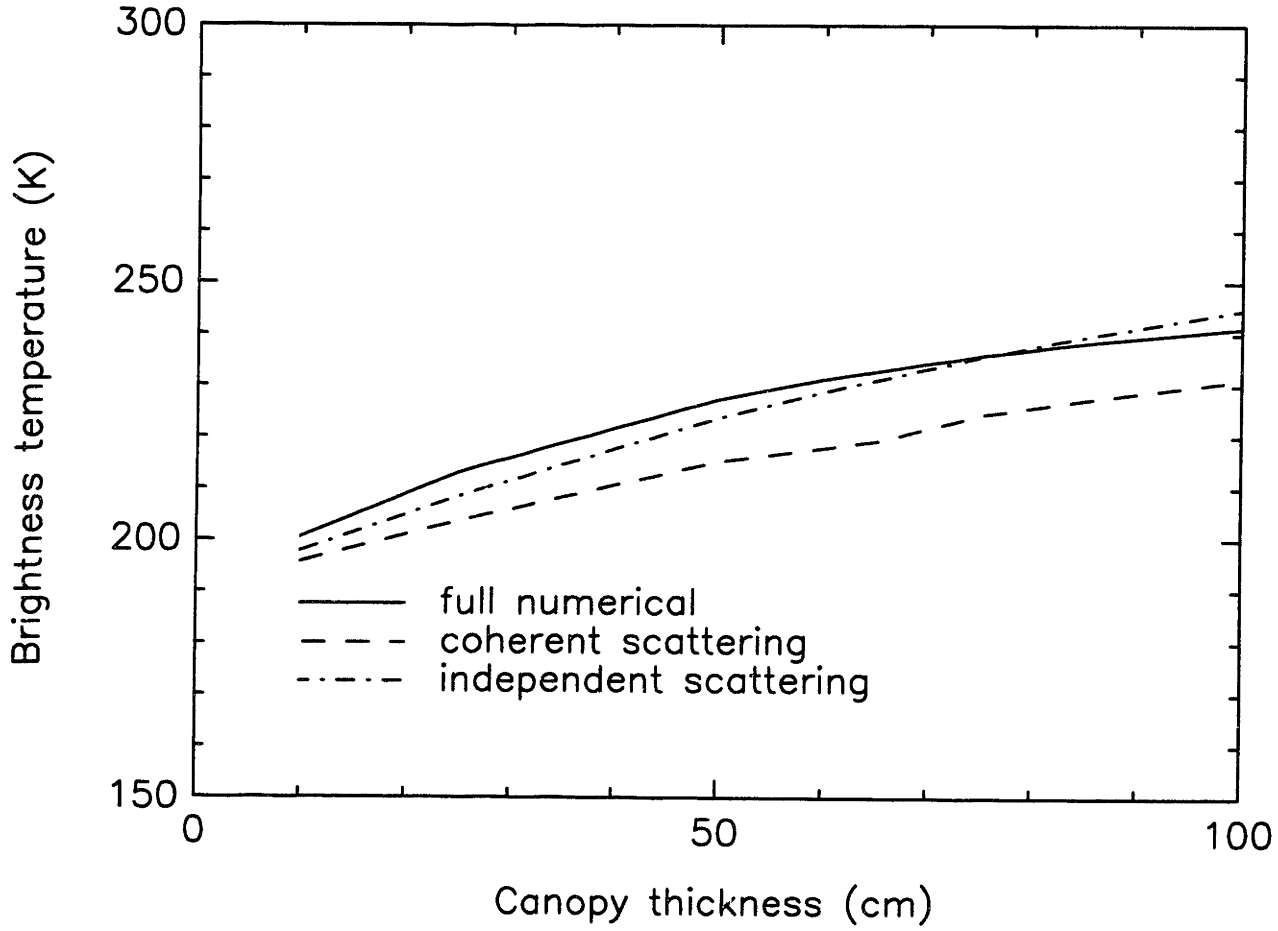

Figure 5-20: Brightness temperature of a two-layer medium — T_{Bv} at observation angle = 8.4^o as a function of canopy thickness d, $f = 0.5\%, \epsilon_s = (11 + i4)\epsilon_o$. Underlying half-space is flat and has a permittivity $\epsilon_{soil} = (16 + i4)\epsilon_o$. Frequency is 5.3 GHz. Number of branches for the scatterers is 10.

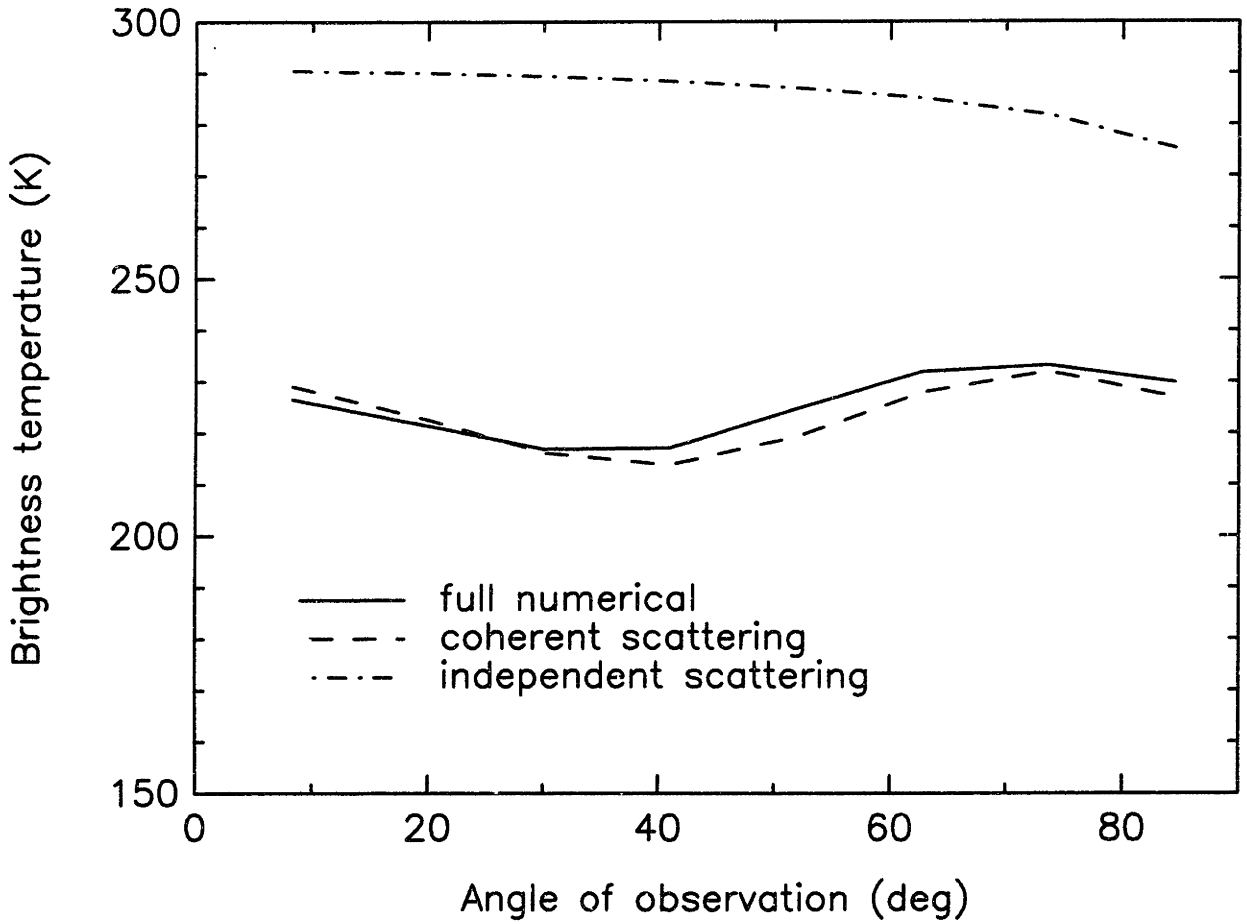

Figure 5-21: Brightness temperature of a half-space medium — T_{Bh}, $f = 0.5\%, \epsilon_s = (11 + i4)\epsilon_o$. Frequency is 5.3 GHz. Number of branches for the scatterers is 48.

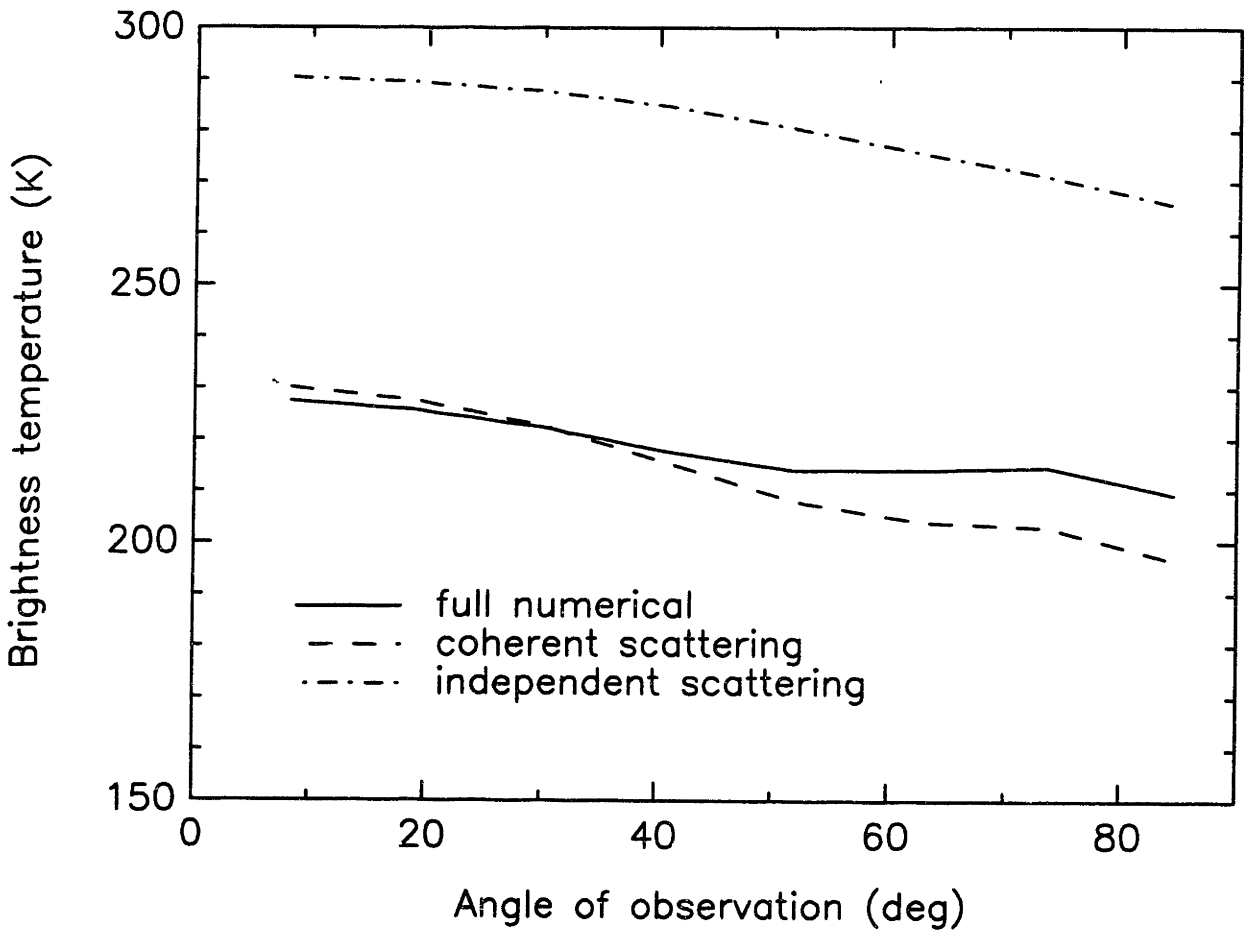

Figure 5-22: Brightness temperature of a half-space medium — T_{Bv}, $f = 0.5\%, \epsilon_s = (11 + i4)\epsilon_o$. Frequency is 5.3 GHz. Number of branches for the scatterers is 48.

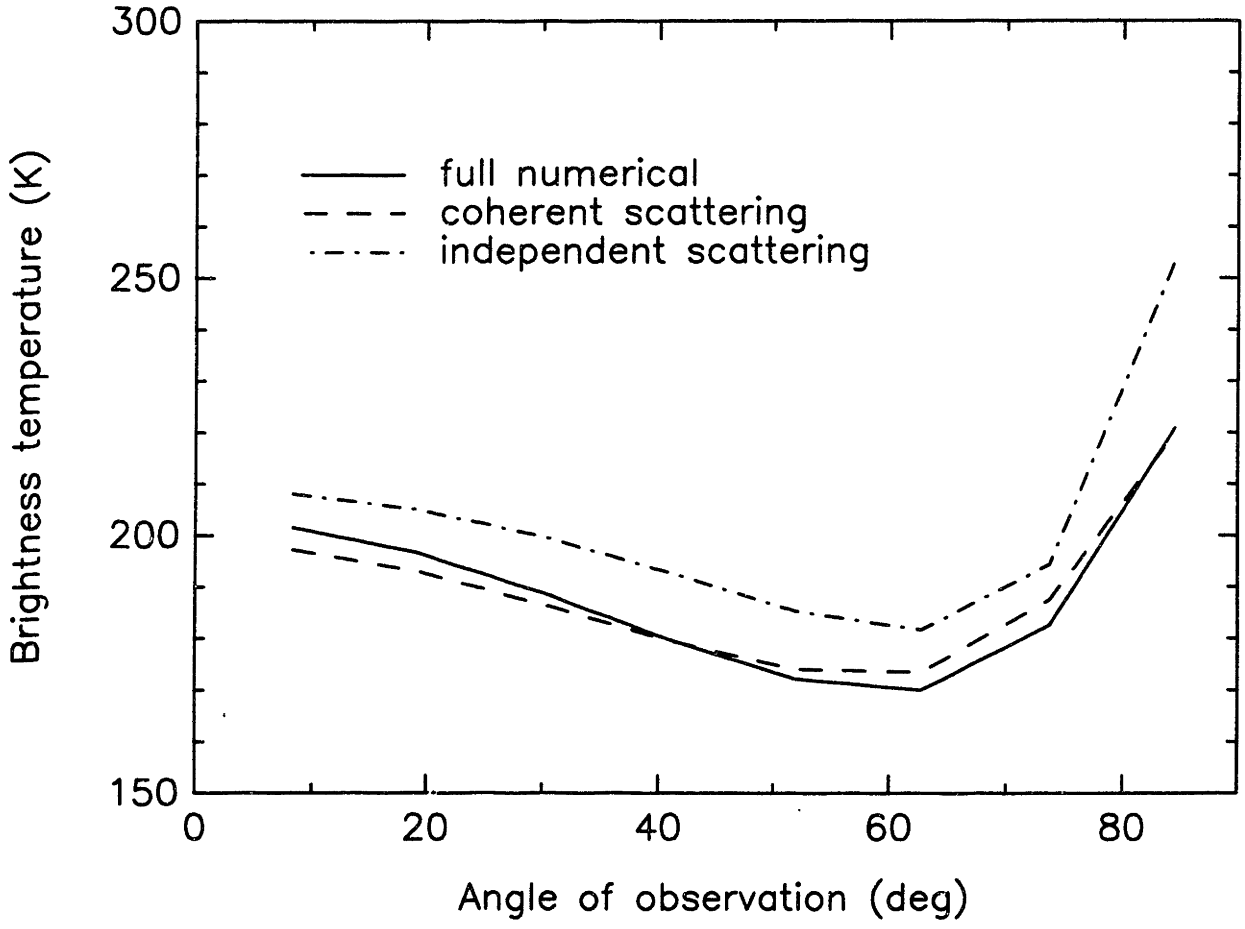

Figure 5-23: Brightness temperature of a two-layer medium — T_{Bh}, $f = 0.5\%, \epsilon_s = (11 + i4)\epsilon_o$. Scattering layer has a thickness $d = 0.25$m and underlying half-space is flat and has a permittivity $\epsilon_{soil} = (16 + i4)\epsilon_o$. Frequency is 5.3 GHz. Number of branches for the scatterers is 48.

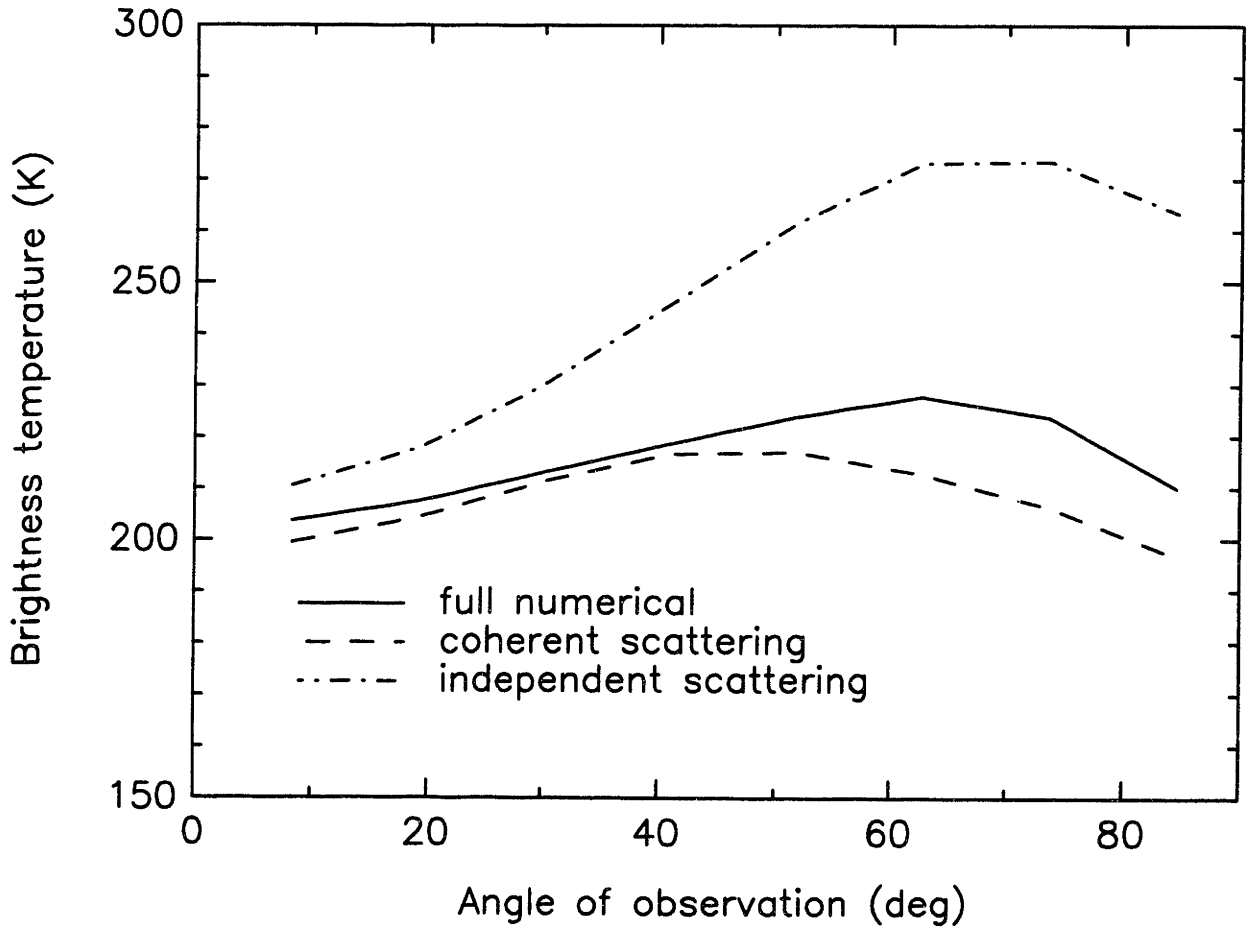

Figure 5-24: Brightness temperature of a two-layer medium — T_{Bv}, $f = 0.5\%, \epsilon_s = (11 + i4)\epsilon_o$. Scattering layer has a thickness $d = 0.25$m and underlying half-space is flat and has a permittivity $\epsilon_{soil} = (16 + i4)\epsilon_o$. Frequency is 5.3 GHz. Number of branches for the scatterers is 48.

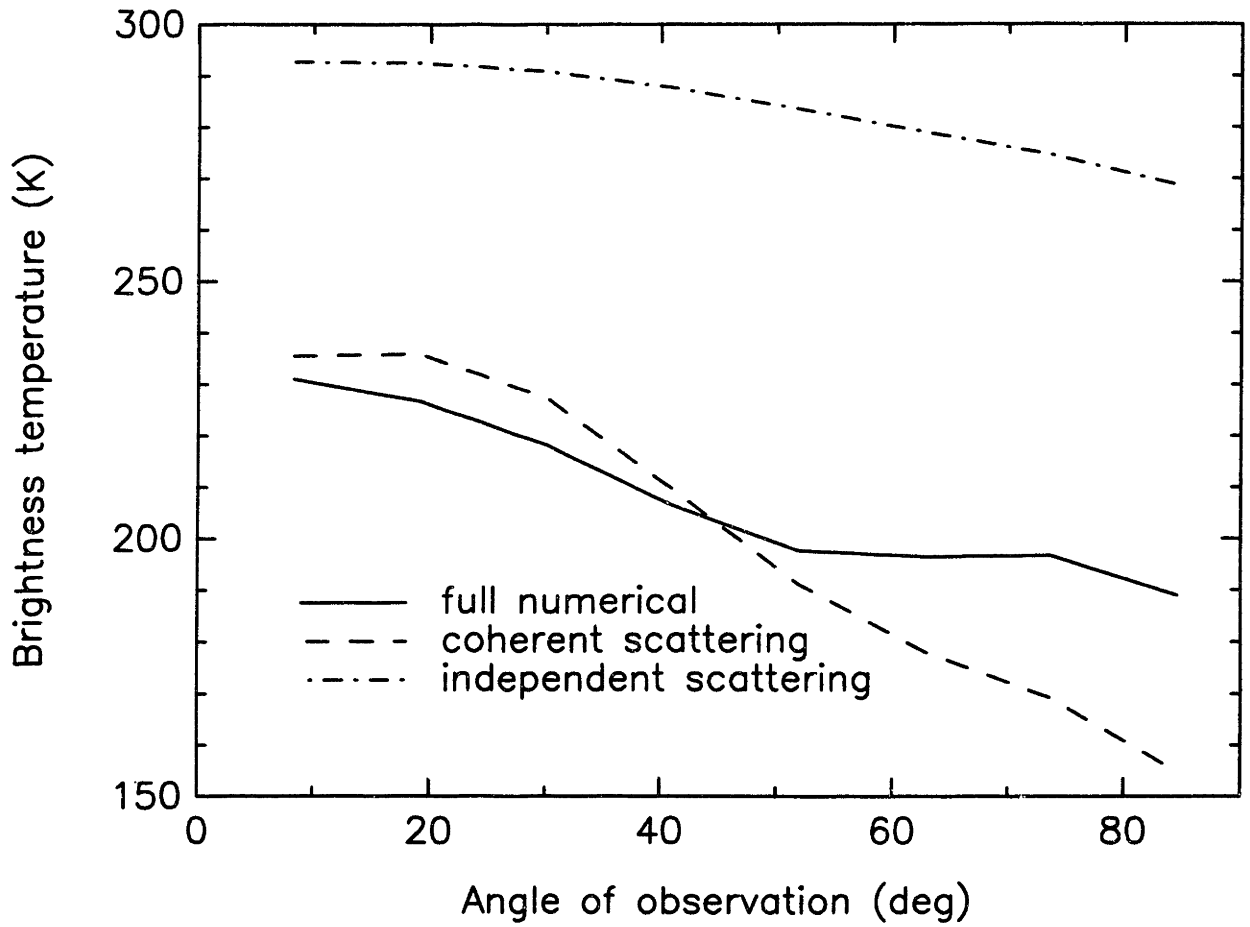

Figure 5-25: Brightness temperature of a half-space medium — T_{Bv}, $f = 0.5\%, \epsilon_s = (11 + i4)\epsilon_o$. Frequency is 5.3 GHz. Number of branches for the scatterers is 48. Branching angle β is 15^o.

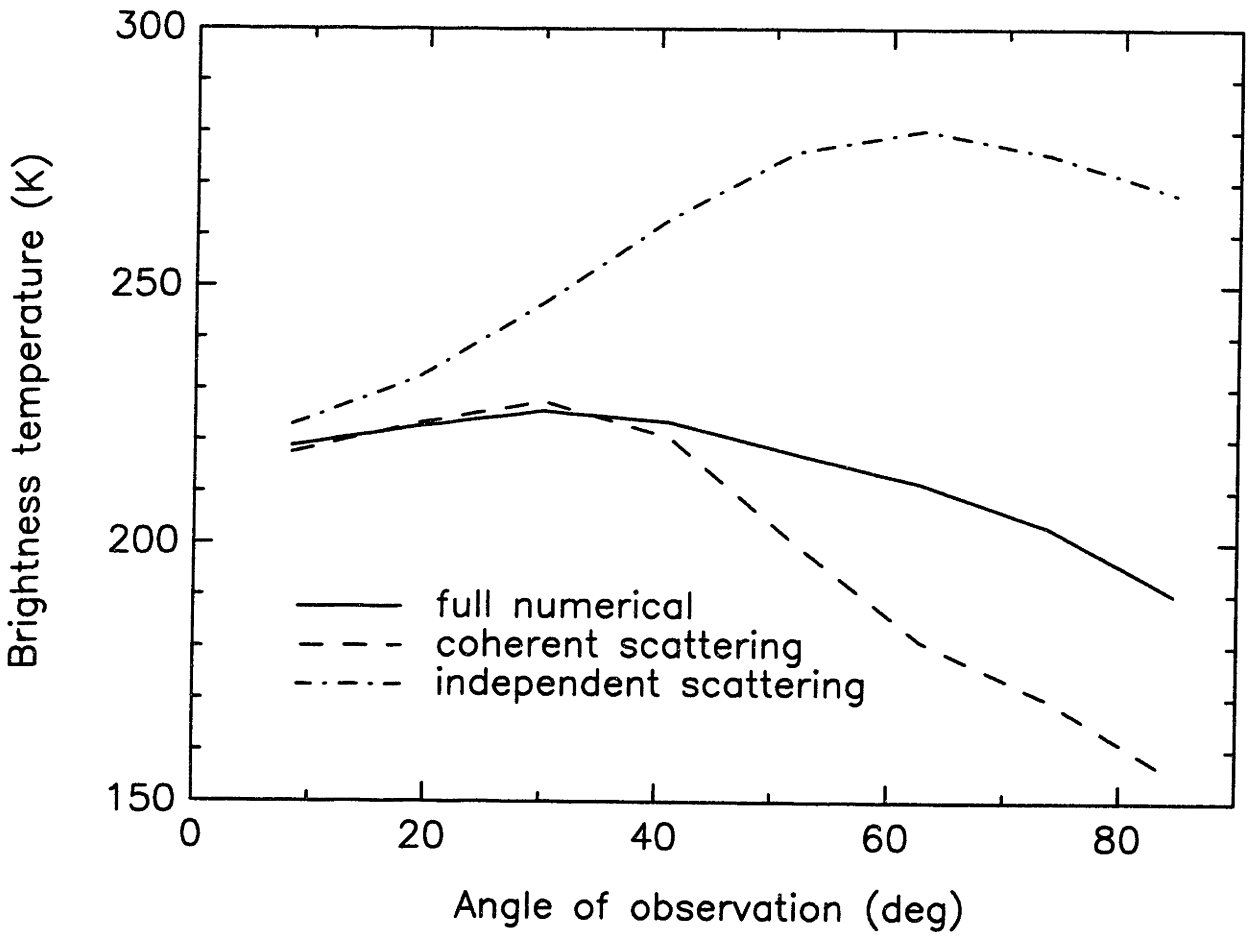

Figure 5-26: Brightness temperature of a two-layer medium — T_{Bv}, $f = 0.5\%, \epsilon_s = (11 + i4)\epsilon_o$. Scattering layer has a thickness $d = 0.25$m and underlying half-space is flat and has a permittivity $\epsilon_{soil} = (16 + i4)\epsilon_o$. Frequency is 5.3 GHz. Number of branches for the scatterers is 48. Branching angle β is 15^o.

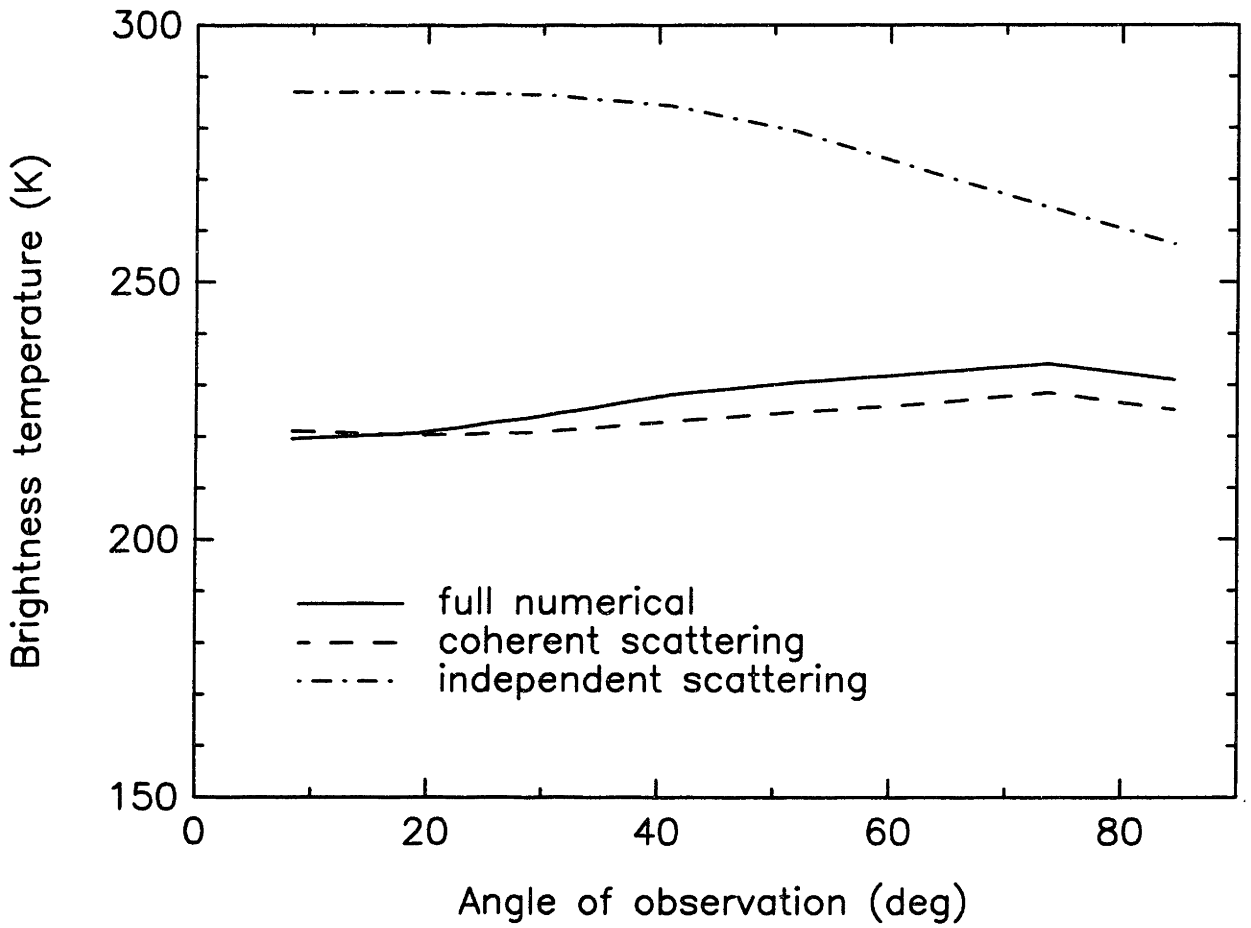

Figure 5-27: Brightness temperature of a half-space medium — T_{Bv}, $f = 0.5\%, \epsilon_s = (11 + i4)\epsilon_o$. Frequency is 5.3 GHz. Number of branches for the scatterers is 48. Branching angle β is 75^o.

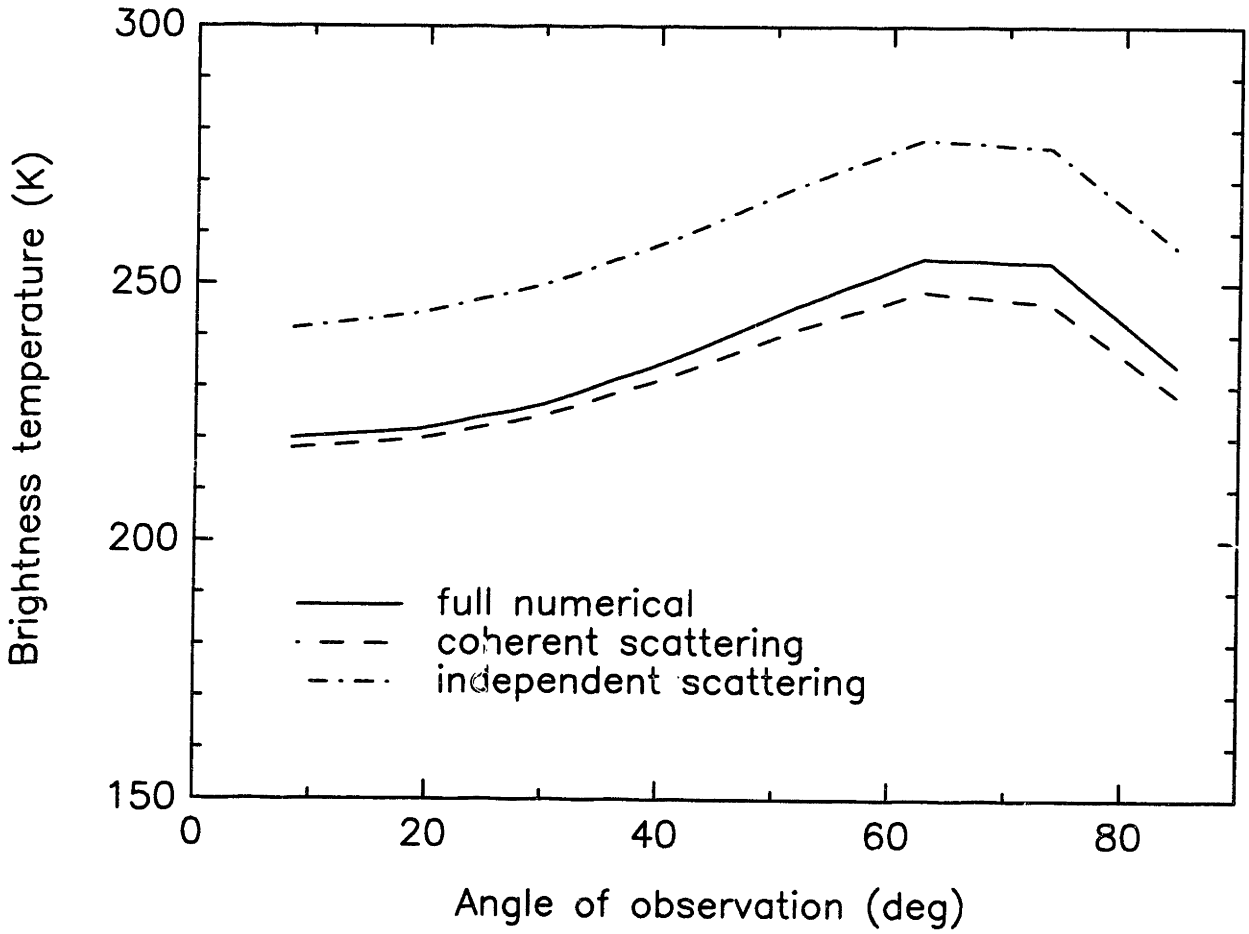

Figure 5-28: Brightness temperature of a two-layer medium — T_{Bv}, $f = 0.5\%, \epsilon_s = (11 + i4)\epsilon_o$. Scattering layer has a thickness $d = 0.25$m and underlying half-space is flat and has a permittivity $\epsilon_{soil} = (16 + i4)\epsilon_o$. Frequency is 5.3 GHz. Number of branches for the scatterers is 48. Branching angle β is 75^o.

Chapter 6

Iterative Solvers for Large Linear Systems of Equations in Parallel Virtual Machine

6.1 Introduction

In Chapters 4 and 5, we have shown that numerical methods provide accurate solutions. However, numerical solutions require a considerably large computer resource. As the structure becomes larger and more complicated, the scattering problems can lead to linear systems with a large number of unknowns. Parallel computation can be employed to solve such a large linear system of equations efficiently. There are different approaches to solving electromagnetic wave scattering problems, with each resulting in a different form of matrix equation. In finite difference and finite element methods, a sparse matrix is formed. The matrix is complex and usually non-Hermitian. When the mesh for these methods is chosen to consist of non-intersecting surfaces, the matrix will have a block tridiagonal structure. On the other hand, the method of moments solution requires solving a dense complex matrix. Depending on the choice of basis functions and test functions, the resulting matrix can either be symmetric or non-symmetric. In this chapter, two programs (BICONG) and (BICGSTAB) are developed to solve the block tridiagonal and general matrix problems, respectively, by

making use of multiple processors, to demonstrate the potential of parallel computing.

Program BICONG has been developed to solve sparse systems of linear equations with block tridiagonal structure that arise from the discretization of elliptic differential equations in three dimensions. BICONG and BICGSTAB are iterative solvers using the preconditioned biconjugate gradient method and the preconditioned biconjugate squared method, respectively. They are implemented in parallel virtual machine (PVM). PVM is a macro library code that runs on a UNIX network. The use of PVM gives us access to more CPU power as well as memory and allows us to solve large problems that cannot be fitted into a single machine.

BICONG and BICGSTAB are written in modular forms so that users can supply the preconditioner of their choice, and select a solver for the preconditioner. Two different algorithms are used in BICONG depending on whether the matrix is symmetric or non-symmetric. BICGSTAB is developed based on BICONG and is used to solve general dense complex matrix equations. Numerical experiments using BICONG for solving linear systems arising from three-dimensional complex Helmholtz equations are reported. We compare two preconditioning techniques: point preconditioning using incomplete Cholesky factorization and block preconditioning using diagonal blocks modified by row balancing. Although point preconditioning gives competitive performance on a single machine, it is not suitable for parallel implementation because it requires a lot of communication. Block preconditioning with row balancing requires fewer iterations than that without row balancing.

The performance of BICONG is evaluated in terms of computational cost and communication cost over the network. The breakdown of the timing data shows that communication cost is negligible. However, load balancing is an important consideration. Using a larger number of machines to solve a problem is not necessarily faster because one slow machine can slow down the whole solution process. We develop a simple load balancing scheme in which an user can prescribe the number of blocks to be solved by each type of machine. This load balancing scheme significantly improves performance. To test BICONG's efficiency in parallel implementation, standalone tests using four IBM RS/6000 workstations were performed. A speed up of 3.6 for

a large problem with 262,144 unknowns was obtained. The solver can easily achieve 80% efficiency in parallelization.

Section 6.2 describes the iterative solver (BICONG) for block tridiagonal systems of equations. In section 6.3, a similar solver (BICGSTAB), which can be used to solve general dense complex matrix equations is described. The results of numerical experiments are discussed in section 6.4. Concluding remarks are given in section 6.5.

6.2 Iterative Solver for Block Tridiagonal Systems of Equations

This section describes a solver (BICONG) developed to solve block tridiagonal systems of equations with complex valued elements. BICONG can solve systems of equations that arise from discretization of Maxwell's equations with a harmonic time dependence. When the nodes of 3-D finite element or finite difference meshes can be partitioned into a family of non-intersecting surfaces, then only adjacent surfaces will be coupled. The block tridiagonal system will have the form

$$Ax = b \tag{6.1}$$

where

$$A = \begin{bmatrix} D_1 & E_1 & & & & \\ C_2 & D_2 & E_2 & & & \\ & \ddots & \ddots & \ddots & & \\ & & \ddots & \ddots & \ddots & \\ & & & C_{n-1} & D_{n-1} & E_{n-1} \\ & & & & C_n & D_n \end{bmatrix}.$$

The diagonal blocks D contain matrix elements coupling nodes on the same surface, blocks E above the diagonal contain matrix elements coupling one surface to the next adjacent surface, and C to the previous surface. For a 3-D simulation of an induction log, the number of unknowns can be more than a million [65]. For a large sparse

matrix, iterative methods are usually more efficient than direct elimination [66]. A commonly used iterative method is the conjugate gradient (CG) method which first proposed by Hestenes and Stiefel [67] to solve Hermitian positive definite matrices. Different variants of the method were developed to extend the method to solve non-Hermitian matrices [68-72]. BICONG uses the preconditioned biconjugate gradient method to solve equation (6.1). The biconjugate gradient method is a variant of CG. It gives good results in solving a non-Hermitian matrix [72-74]. BICONG is implemented to run on parallel virtual machine (PVM). PVM [75] is a software system that permits a network of heterogeneous Unix computers to be used as a single large parallel computer.

6.2.1 Method of Solution

The preconditioned biconjugate gradient algorithm is a Lanczos-based Krylov subspace method for non-Hermitian matrices. The following notations are used:

$[x, y] = \sum_n x_n y_n =$ scalar product without complex conjugation

$(x, y) = \sum_n x_n^* y_n =$ scalar product with complex conjugation

$A = [a_{ij}] =$ general square complex matrix

$A^* = [a_{ij}^*] =$ complex conjugate of A

$A^T = [a_{ji}] =$ transpose of A

$A^H = [a_{ji}^*] =$ Hermitian transpose of A

Let M be an easily invertible approximation of A, then the algorithm can be written as follows:

Algorithm 1

Initialize:

$r_o \leftarrow b - Ax_o$
$\tilde{r}_o \leftarrow r_o$
$n \leftarrow 0$

begin loop:

$z_n \leftarrow M^{-1} r_n$
$\tilde{z}_n \leftarrow (M^H)^{-1} \tilde{r}_n$
if $(n = 0)$ *then*
  $p_n \leftarrow z_n$
  $\tilde{p}_n \leftarrow \tilde{z}_n$
else
  $\beta_n \leftarrow (\tilde{r}_n, z_n)/(\tilde{r}_{n-1}, z_{n-1})$
  $p_n \leftarrow z_n + \beta_n p_{n-1}$
  $\tilde{p}_n \leftarrow \tilde{z}_n + \beta_n^* \tilde{p}_{n-1}$
end if
$\alpha_n \leftarrow (\tilde{r}_n, z_n)/(\tilde{p}_n, Ap_n)$
$x_{n+1} \leftarrow x_n + \alpha_n p_n$
$r_{n+1} \leftarrow r_n - \alpha_n A p_n$
$\tilde{r}_{n+1} \leftarrow \tilde{r}_n - \alpha_n^* A^H \tilde{p}_n$
$n \leftarrow n + 1$
test for convergence; exit loop if converged

end loop.

The algorithm simplifies if A and M are symmetric complex matrices. If we change the initialization of $\tilde{r}_o$ to $\tilde{r}_o = r_o^*$, then $\tilde{r}_n = r_n^*$, and $\tilde{p}_n = p_n^*$ for all n. The algorithm can be restated as follows:

Algorithm 2

Initialize:

$r_o \leftarrow b - Ax_o$
$n \leftarrow 0$

begin loop:

$z_n \leftarrow M^{-1} r_n$
if $(n = 0)$ *then*
  $p_n \leftarrow z_n$
else
  $\beta_n \leftarrow [r_n, z_n]/[r_{n-1}, z_{n-1}]$
  $p_n \leftarrow z_n + \beta_n p_{n-1}$
end if
$\alpha_n \leftarrow [r_n, z_n]/[p_n, Ap_n]$
$x_{n+1} \leftarrow x_n + \alpha_n p_n$
$r_{n+1} \leftarrow r_n - \alpha_n A p_n$
$n \leftarrow n + 1$
test for convergence; exit loop if converged

end loop.

BICONG includes an implementation of both algorithms. Since the matrix obtained from Maxwell's equations with harmonic time dependence from finite element or finite difference discretization is complex and symmetric, we will concentrate on algorithm 2 from now on. The algorithm will break down if the denominators in computing α_n or β_n becomes zero. That is, if

$$[r_n, z_n] = 0 \tag{6.2}$$

or if

$$[p_n, Ap_n] = 0 \tag{6.3}$$

However, this type of breakdown is very rare and can be circumvented by restarting with a different initial vector x_o.

A good convergence rate depends on finding a suitable preconditioner. BICONG

is written in a modular form such that users can supply the preconditioner of their choice. Several papers in the literature discuss the use of block preconditioners in CG methods [76-80]. We choose the modified diagonal block as preconditioner in the numerical experiments because it requires little work in forming and no communication cost for solving the preconditioner. The block preconditioner is formed by modifying the diagonal blocks of the original matrix with row balancing. Mathematically,

$$M_{ij} = D_{ij} + \delta_{ij} \sum_{l} (A_{il} - D_{il}) \tag{6.4}$$

where D are the diagonal blocks and δ is the kronecker delta function.

6.2.2 Implementation

A schematic diagram showing the major modules in BICONG is shown in Fig. 6-1. BICONG consists of the master program BICONGHOST and the node program BICONGNODE. BICONGHOST is responsible for the coordination. BICONGNODE is the program that actually does the calculation. A flow chart for BICONG is given in Fig. 6-2. Two libraries of subroutines are used, namely BLAS (basic linear algebra subroutines) and SLAP [81] (sparse linear algebra package). When BICONGHOST is invoked, it reads in a parameter file that specifies the problem. BICONGHOST then enrolls the number of nodes specified by the user. It reads the matrix A and the right hand side b from the data files and broadcasts the submatrices and subvectors to the nodes. BICONGHOST assumes that all the submatrix blocks have the same size. It reads in the submatrices in sequential order, starting from the block with the lowest row numbers. Within the same row, the block with lower column numbers will be read first. For the matrix in equation (6.1), the order is as follows: $D_1, E_1, C_2, D_2, E_2, \cdots, C_n, D_n$.

Each submatrix is ordered with the local numbering, i.e. a submatrix a of order N will be represented by a_{ij}, $1 \leq i, j \leq N$. Subroutines were written to interface BICONG with a given matrix format. The format used is the row-indexed sparse storage mode [48]. To represent a matrix A of logical size $N \times N$, the row-indexed

scheme sets up two one-dimensional arrays, call them ija and sa. The first of these stores integer values; the second stores the matrix elements values. The storage rules are:

1. The first N locations of sa store A's diagonal matrix elements, in order. (Note that diagonal elements are stored even if they are zero).

2. Each of the first N locations of ija stores the index of the array sa that contains the first nonzero off-diagonal element of the corresponding row of the matrix. (If there are no off-diagonal elements for that row, it is one greater than the index in sa of the most recently stored element of a previous row.)

3. Location 1 of ija is always equal to $N + 2$.

4. Location $N+1$ of ija is one greater than the index in sa of the last off-diagonal element of the last row. Location $N + 1$ of sa is not used and can be set arbitrarily.

5. Entries in sa at locations greater than $N + 1$ contain A's off-diagonal values, ordered by rows and, within each row, ordered by columns.

6. Entries in ija at locations greater than $N + 1$ contain the column number of the corresponding element in sa.

For compactness, ija is then put into the complex array A, followed by sa. The first element of ija is stored in $\mathrm{Re}(A(1))$ and the second element of ija is stored in $\mathrm{Im}(A(1))$ and so on. Modifications of the interface subroutines have to be made for machines whose memory storage of two integers is not equivalent to one complex number. Most current workstations use IEEE arithmetic and conform to this requirement.

Submatrices and subvectors that contain the same rows must reside in the same node. BICONGNODE then forms the preconditioner. The advantage of the choice of diagonal block as preconditioner becomes apparent. No communication is required in forming and solving the preconditioner. An iterative solver using the preconditioned conjugate gradient method with incomplete Cholesky factorization is implemented

for solving the equation $Mz = r$ in BICONGNODE. If a direct solver, for example from LAPACK [82], is desirable, users can invoke it by changing the solver subroutine SOLVE2.

When we examine algorithms 1 and 2, we see that only the matrix vector multiplication step requires communication between nodes. The communication time can be minimized if each node stores consecutive blocks rather than separate blocks. In each iteration, α and β have to be updated before the calculation can continue. These are the bottlenecks of the algorithms. The faster machines have to wait for the slowest machine to calculate the partial sums for α and β. In order to improve the performance of the solver, a simple load balancing scheme is used. Users can specify the number of blocks that each type of machine will process. This load balancing scheme is helpful when BICONG is run in a heterogeneous network with large differences in computational power between different machines.

6.3 Iterative Solver for Unsymmetric Linear Systems of Equations

This section describes the solver (BICGSTAB) developed to solve unsymmetric linear systems of equations with complex valued elements. BICGSTAB can solve systems of equations that arise from the method of moments solution for electromagnetic scattering problems. The resulting matrix, in general, will be dense and unsymmetric. A variant of biconjugate gradient method, named BICGSTAB [83], is implemented to solve the systems of equations. BICGSTAB is derived from Conjugate Gradients-Squared (CGS) method [72] and it is more reliable than CGS. The advantage of using BICGSTAB over the biconjugate gradient method is that it does not require the transpose of the matrix. In order to utilize PVM, the matrix must be partitioned into smaller submatrices and stored in different nodes. For a dense matrix, it is not practical to obtain its transpose by transporting submatrices from one node to another. Another alternative is to store both the submatrix and its corresponding submatrix of the transpose matrix in one node. This produces larger memory

requirements on the system. A transpose-free algorithm can be used to avoid this problem. A comparative study of preconditioned Lanczos methods for nonsymmetric linear systems can be found in literature [84]. The choice of BICGSTAB is mainly due to its similarity to BICONG in structure and that only a slight modification is required for the implementation.

6.3.1 Method of Solution

Using the same notations as the previous section, the algorithm can be written as follows:

Algorithm 3

Initialize:

$r_o \leftarrow b - Ax_o$
$\tilde{r} \leftarrow r_o$
$n \leftarrow 1$

begin loop:

$\rho_{n-1} = (\tilde{r}, r_{n-1})$
if $(n = 1)$ *then*
  $p_n \leftarrow r_{n-1}$
else
  $\beta_{n-1} \leftarrow (\rho_{n-1}/\rho_{n-2})/(\alpha_{n-1}/w_{n-1})$
  $p_n \leftarrow r_{n-1} + \beta_{n-1}(p_{n-1} - w_{n-1}v_{n-1}$
end if
$z_n \leftarrow M^{-1}p_n$
$v_n \leftarrow Az_n$
$\alpha_n \leftarrow \rho_{n-1}/(\tilde{r}, v_n)$
$s_n \leftarrow r_{n-1} - \alpha_n v_n$
$\tilde{s}_n \leftarrow M^{-1}s_n$
$t_n \leftarrow A\tilde{s}_n$
$w_n \leftarrow (t_n, s_n)/(t_n, t_n)$
$x_n \leftarrow x_{n-1} + \alpha_n z_n + w_n \tilde{s}_n$
$r_n \leftarrow s_n - w_n t_n$
$n \leftarrow n + 1$
test for convergence; exit loop if converged

end loop.

6.3.2 Implementation

BICGSTAB is derived from BICONG. The basic modules in BICONG can be used in the development of BICGSTAB. BICGSTAB consists of the master program BICSGTABHOST and the node program BICGSTABNODE. The master program is responsible for the coordination and the node program does the calculation. The differences between BICONG and BICGSTAB are the matrix format and the matrix partition. The matrix A in equation (6.1) is partitioned into stripes of submatrices, each of which has the same number of columns as A. The partition of A can be illustrated as follows:

$$A = \begin{bmatrix} \text{---} & A_1 & \text{---} \\ \text{---} & A_2 & \text{---} \\ & \vdots & \\ \text{---} & A_p & \text{---} \end{bmatrix}$$

All the submatrices have the same size. BICGSTABHOST reads the submatrices in sequential order, starting from the block with the lowest row number. The submatrix is of the size $l \times N$, where $l = N/p$ and the matrix A is of the size $N \times N$. The submatrices are then sent out to the nodes. Unlike BICONG, each node has to keep the full vectors for the calculation. In the preconditioning step, the diagonal of the matrix A is chosen as the preconditioner and the solution of the equation $Mz = p$ is performed in BICGSTABHOST.

6.4 Numerical Experiments

To test the performance of BICONG, two test problems were used. We present the results of solving a complex Helmholtz equation. The equation,

$$\nabla^2\phi + k^2\phi = -\rho \tag{6.5}$$

with

$$k^2 = \omega^2\epsilon\mu + i\omega\mu\sigma,$$

governs the propagation of electromagnetic waves, where ω is the angular frequency, ϵ the permittivity, μ the permeability, and σ the conductivity.

In the first case, we used the finite-element method to discretize equation (6.5) for an induction case, i.e. $k^2 = i\omega\mu\sigma$. There are two materials with a 10:1 contrast ratio in k^2 in a rectangular box in the computational domain. Plane waves propagate into the box and are reflected at the interface between the two materials. The geometrical configuration of the problem is shown in Fig. 6-3. The values of the solution at the boundary points are calculated analytically by using the reflection and transmission coefficients. Thus a Dirichlet problem is set up for testing. Table 6.1 shows the computer time required to obtain a solution with a relative deviation of of 0.0001 for various grid sizes with different preconditioners. The relative deviation is defined as

$$\delta = \frac{|x_n - x_{n-1}|}{|x_n|}. \tag{6.6}$$

The grid is of equal spacing in all directions and with the size of $n \times n \times p$, where p is the number of processors. As n increases with p fixed, block preconditioning becomes more effective because it solves the 2-D $(n \times n)$ problem exactly in the preconditioning step. When we compare the results of using the preconditioners with or without row balancing, we observe that row balancing improves the performance. Without row balancing, the preconditioning step is not solving the corresponding 2-D problem exactly, and hence gives a slower convergence rate. On the other hand, point preconditioning using incomplete Cholesky factorization remains competitive except in the last case ($n = 128$). However, the parallel implementation of point preconditioning requires more communication and is less attractive than block preconditioning.

Table 6.2 shows the breakdown of the time spent in the calculation. The communication time is taken as the maximum of the time spent in communication for all nodes. We see that communication cost is insignificant in all cases. For the cases of large n, load balancing becomes an important consideration. In the above timings, no load balancing scheme was used and each node processed one diagonal block and its corresponding off-diagonal blocks in the calculation.

grid size $n \times n \times p, p = 16$	$n = 16$	$n = 32$	$n = 64$	$n = 128$
point preconditioning (single machine) (sec)	7.2	75	1030	14140
block preconditioning (single machine) (sec)	20.5	121	498	2087
block preconditioning (16 machines) (sec)	135	158	451	520
block preconditioning (16 machines) (sec) without row balancing	134	125	618	1140

Table 6.1: Performance of BICONG with different preconditioner.

grid size $n \times n \times p, p = 16$	$n = 16$	$n = 32$	$n = 64$	$n = 128$
wall clock time (sec)	78	64	699	1127
CPU time (sec)	9	34	523	1015
communication time (sec)	0.4	1.1	4.1	8.0

Table 6.2: Breakdown of time spent in the calculation.

For the second problem, we solve the same equation but with different right hand sides. A vertical magnetic dipole is placed above a rectangular box with a contrast of 2:1 in k^2 ($k^2 = i\omega\mu\sigma$). The geometrical configuration is shown in Fig. 6-4. A field due to a vertical magnetic dipole can be characterized by H_z only, and it is the solution of the Helmholtz equation. The values on all the boundary points of the box are calculated analytically [43] and are given as,

$$H_{1z} = -\frac{iIA}{8\pi}\int_{-\infty}^{\infty} dk_{rho}\frac{k_\rho^3}{k_{1z}}H_0^{(1)}(k_\rho\rho)[e^{ik_{1z}|z|} + R_{12}^{TE}e^{ik_{1z}z+2ik_{1z}d_1}] \tag{6.7}$$

$$H_{2z} = -\frac{iIA}{8\pi}\int_{-\infty}^{\infty} dk_{rho}\frac{k_\rho^3}{k_{1z}}H_0^{(1)}(k_\rho\rho)T_{12}^{TE}e^{ik_{2z}(z+d_1)+ik_{1z}d_1} \tag{6.8}$$

$$\tag{6.9}$$

where

$$R_{12}^{TE} = \frac{k_{1z} - k_{2z}}{k_{1z} + k_{2z}}, \qquad T_{12}^{TE} = \frac{2k_{1z}}{k_{1z} + k_{2z}},$$

$k_{iz} = (k_i^2 - k_\rho^2)^{1/2}$, and A is the area of the small electric current loop simulating a magnetic dipole.

A standalone performance test was carried out on three IBM RS/6000 model 560

grid size $n \times n \times n$	$n = 16$	$n = 24$	$n = 32$	$n = 64$
1 RS/6000 (sec)	14	63	134	3383
4 RS/6000 (sec)	6.4	23	45	992

Table 6.3: Performance of BICONG in a homogeneous platform.

grid size $n \times n \times n$	$n = 16$	$n = 24$	$n = 32$	$n = 64$
1 RS/6000 (sec)	14	63	134	3383
16 machines, no load balancing (sec)	92	50	176	5215
16 machines, with load balancing (sec)	102	34	92	1510

Table 6.4: Performance of BICONG with and without load balancing.

workstations and one IBM RS/6000 model 580, with various grid sizes. The results are compared with those from one single machine in Table 6.3. The solver shows good performance in parallelization on a homogeneous platform. For a heterogeneous platform with SUN Sparc 2, Sparc 10 and IBM RS/6000 machines, a simple load balancing scheme is used in which the more powerful machines (RS/6000) have been assigned to process more blocks than the others. The results are compared with results without any load balancing scheme in Table 6.4. The load balancing scheme improves the performance significantly.

No computer timing is performed on testing BICGSTAB. However, BICGSTAB has been used for the method of moments calculations described in Chapter 3. It is not as efficient as BICONG in terms of parallelization and the motivation of using PVM is mainly due to the memory requirement.

6.5 Summary

A block tridiagonal solver BICONG is implemented in PVM. It can solve a complex non-Hermitian matrix with tridiagonal block structure. Two different algorithms based on the preconditioned biconjugate gradient method are implemented in BICONG for symmetric and non-symmetric matrices. BICONG achieved more than

80% efficiency in parallelization when tested in a homogeneous platform (efficiency defined as speed up divided by the number of processors). A simple load balancing scheme of assigning different number of blocks according to the computational power of the machines improved the performance. BICGSTAB is the extension of BICONG. It is used to solve general complex matrix problems. The advantage of BICGSTAB over the biconjugate gradient method is that it does not require the transpose of the matrix. BICGSTAB has been applied to solve the matrix problems that arise from the method of moments formulation described in Chapters 2 and 3. However its performance is less impressive than BICONG because it is difficult to find an effective preconditioner to implement in parallel computation.

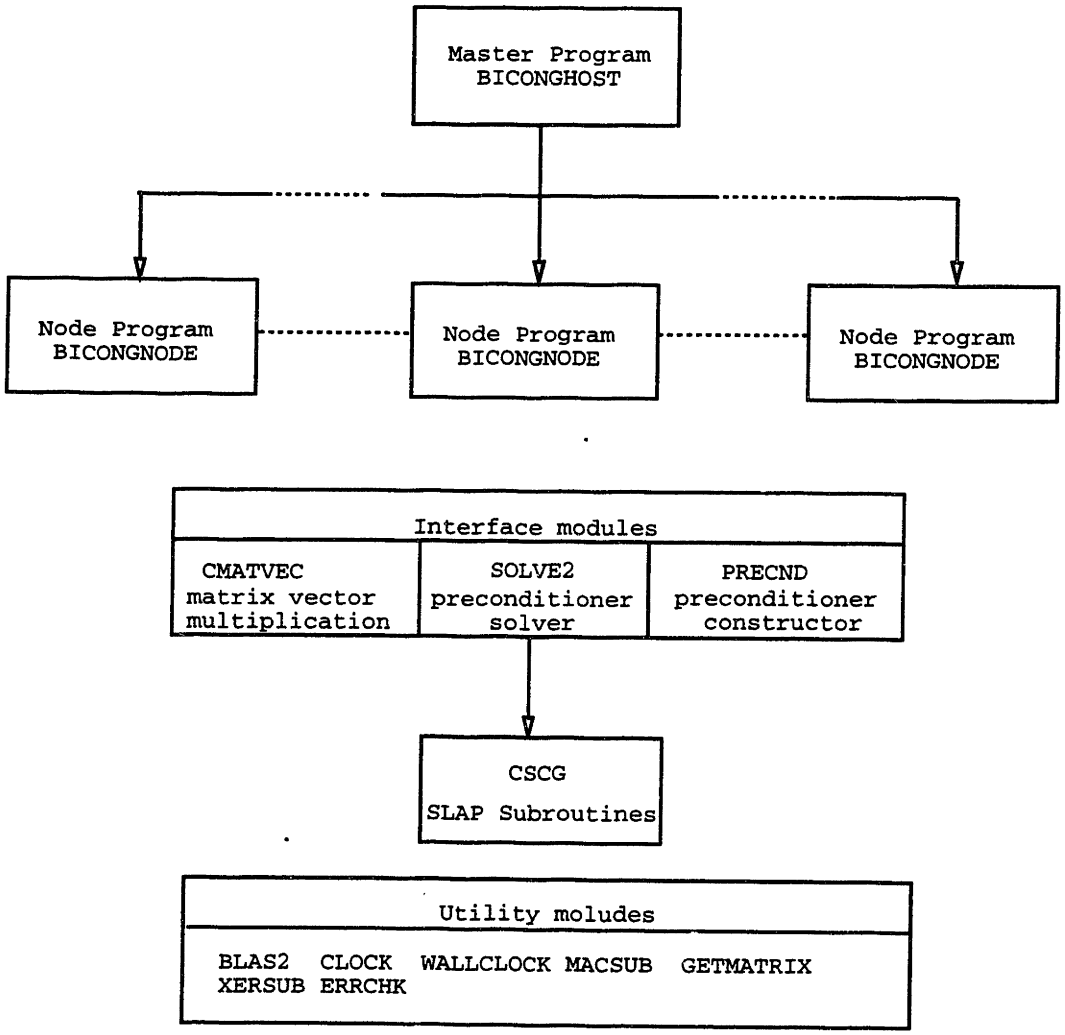

Figure 6-1: Block diagram showing the modules of BICONG.

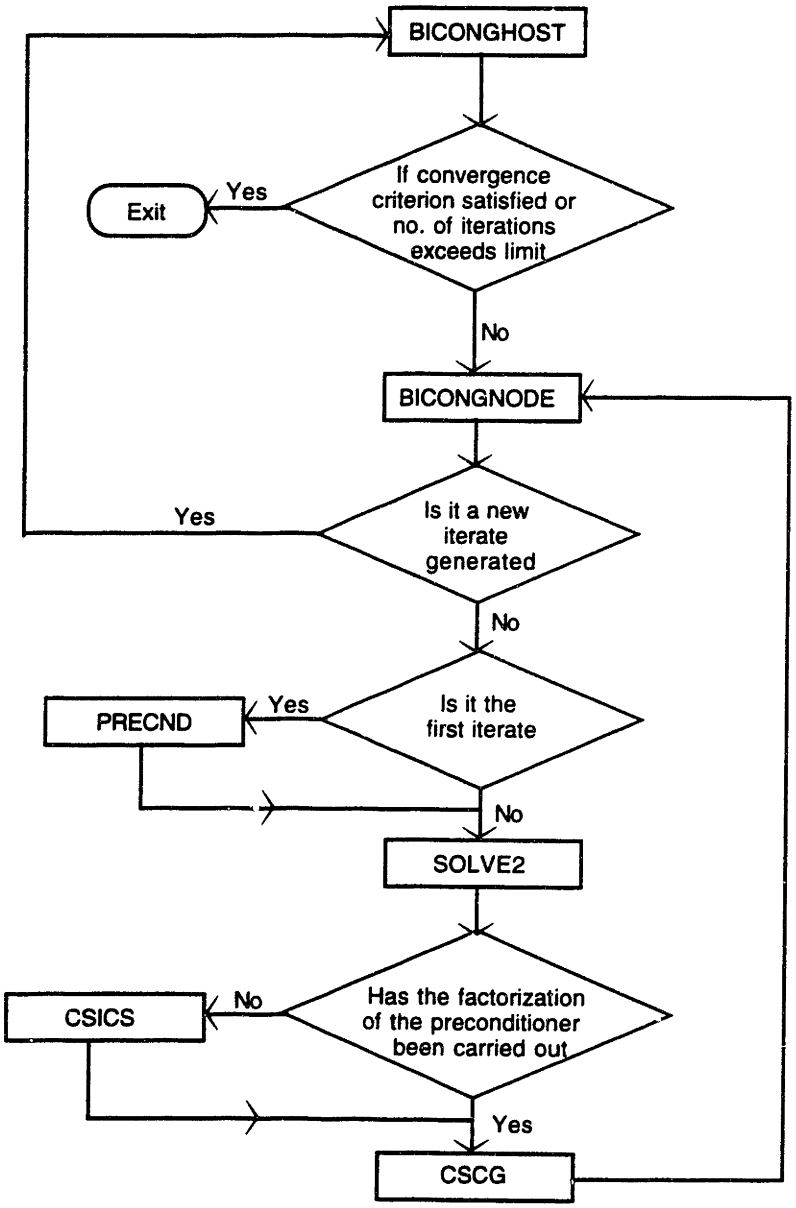

Figure 6-2: Flow chart for BICONG.

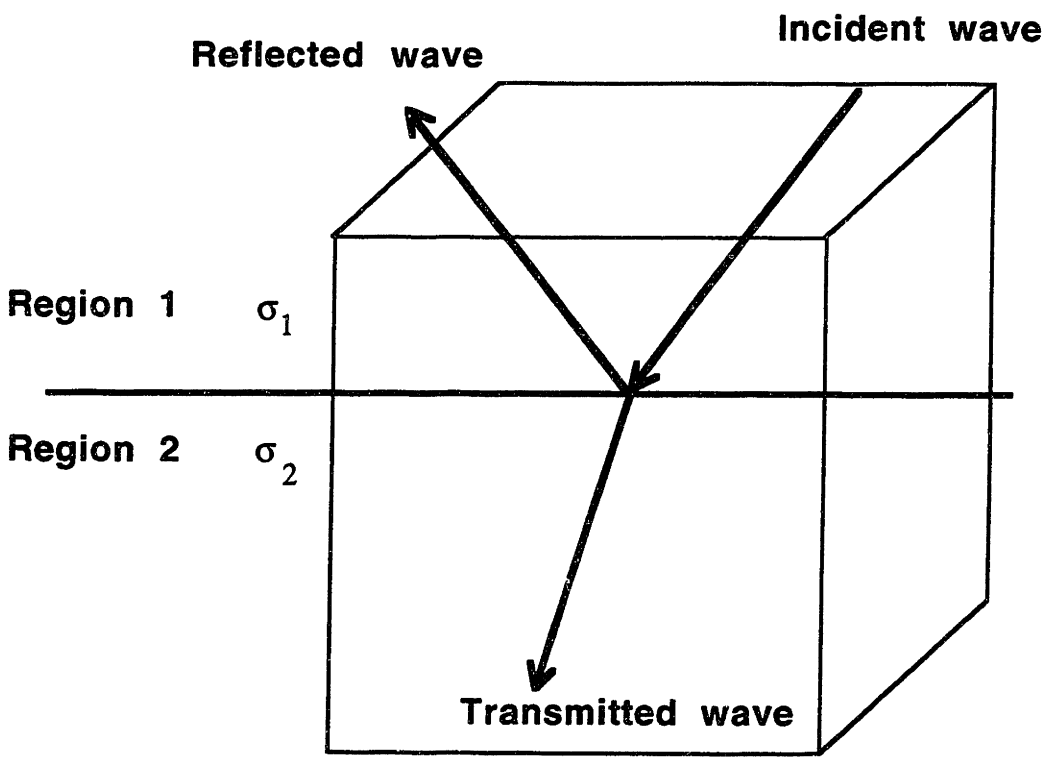

Figure 6-3: Geometrical configuration of the test problem 1.

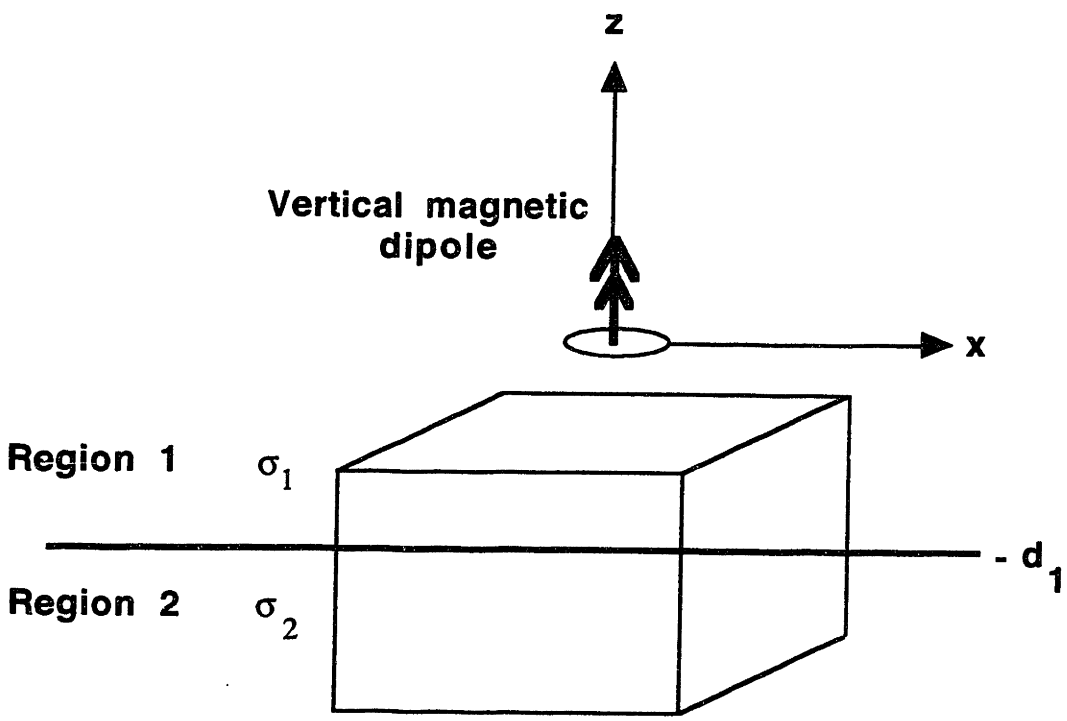

Figure 6-4: Geometrical configuration of the test problem 2.

Chapter 7

Summary

In this thesis, we studied the effect of mutual interaction in the scattering behavior of locally dense vegetation. The radiative transfer theory is modified by defining the phase matrix and extinction coefficient as, respectively, the bistatic cross section per unit volume of space and the extinction cross section per unit volume of space. The limit of the volume of space is taken such that the collective scattering effects of the particles within the volume are taken into account. The scattering functions of the scatterers within the volume of space are obtained from the numerical solution of Maxwell's equations, and hence all the interactions between different components of the cluster are retained. Because of low fractional volume, the interaction between two remotely separated scatterers is small, thus the use of radiative transfer theory is justified. Analytical iterative solution method is used in the active case to calculate backscattering coefficients and Gaussian quadrature method is used in the passive case to calculate brightness temperatures.

In Chapter 2, a volume scattering model using scatterers with multi-scale branching structures is developed to investigate the scattering characteristics of vegetation canopies. A branching scatterer is approximated by a thin perfectly conducting wire structure. The method of moments (MoM) formulation based on reaction integral equations is employed in the calculation. The frequency, angle, and polarization dependencies of the electromagnetic scattering characteristics from the branching model are studied. The scatterer models the shape of a vegetation cluster but not its electro-

magnetic properties. However, the trend of a flat frequency response curve is obtained in the calculation which is observed in experimental data. As a next step, a dielectric model is developed to study the branching, multi-scale scatterers in electromagnetic wave scattering.

In Chapter 3, a MoM approach is used to compute both the scattered fields and absorption by thin cylinder structures. It has been applied to calculate the scattering function for coniferous leaves, and with the Foldy's approximation for a sparse medium, attenuation coefficients are calculated. Good agreement between the model and observations is obtained at X-band frequency on various forest components. The MoM code is applied to study the clustering effects exhibited by vegetation. The code accounts for the mutual interaction between the components of the structure, and it can be used to construct the phase matrix and extinction matrix in the radiative transfer equations.

In Chapter 4, the first order iterative solution of the vector radiative transfer equations for active remote sensing is derived. The full numerical solution for a single branching scatterer is used to evaluate the scattering functions for the phase matrix and extinction matrix in the radiative transfer equations. The backscattering coefficients are then calculated using iterative method. This solution accounts for the multiple scattering effect within the cluster and single scattering between the clusters. The numerical solutions are then compared with the solutions obtained with different approximations. The results show that the coherent scattering model gives a good estimate for co-polarized returns. For cross-polarized cases, both the independent and the coherent scattering models are shown to be less accurate. Cross-polarized returns are strongly influenced by interactions between the components of the cluster and the approximate methods used do not account for this effect. By varying the branching angle of the cluster, it is shown that for smaller branching angles, mutual interaction is stronger and hence larger difference with approximate methods. The center cylinder in the cluster plays an important role in the cross-polarized returns. The triple bounce scattering mechanism, i.e. from branch to central cylinder back to branch, attributes to the high cross-polarized returns.

The numerical solution of the vector radiative transfer equation for the thermal emission from a layer of random medium overlying a flat ground surface is derived in Chapter 5. A branching scatterer is used for the calculation of the absorption coefficients and the brightness temperatures. The absorption is found to be enhanced by the mutual interactions of the branching components. Blocking is another important factor in the clustering effect. In the calculation of brightness temperature, the elements of the phase matrix and the extinction matrix are evaluated under various assumptions. Numerical results show that the coherent scattering model gives a better estimate of the brightness temperatures than the independent scattering model for the half-space cases. Both the independent and the coherent scattering model underestimate the optical depth of the random medium layer.

A better understanding of the clustering effects is obtained through the numerical investigation. For scatterers with large number of branches, the independent model is shown to be inadequate. The coherent scattering model for branching structure improves the estimate of the scattering characteristics. However, since the internal field in the model is assumed to be the same as the independent scattering model, mutual interaction is not included. Using the MoM approach, it is shown that both the absorption and the scattering losses are enhanced by mutual interaction.

Finally, parallel computing is introduced to handle the computationally intensive electromagnetic wave scattering problems. Two iterative algorithms are implemented by using the parallel virtual machine (PVM). Numerical experiments are carried out to evaluate the effectiveness of different preconditioners. The block tridiagonal solver has shown promising results in term of the efficiency of parallelization. The dense matrix iterative solver is less attractive because of the difficulty of implementing an effective preconditioner in parallel. However, the use of PVM in the dense matrix problems provides access to increased memory so that large scattering problems can be solved.

In this thesis, we have shown that numerical methods provide accurate solutions when mutual interaction is strong, which cannot be handled with existing approximate methods. Suggestions for future work are to improve modeling of locally dense

medium with both analytical and numerical approaches. Coherent scattering model provided reasonable results in some cases. It may be possible to improve the model by incorporating high order terms to account for mutual interaction. Only thin cylinder structures have been studied for the clustering effects in this thesis. A possible extension is to study scatterers with different structures, for example, discs and thick cylinders. However, the computational requirement will be very demanding for large and complicated scatterers. PVM has a potential to handle large problems efficiently and development of a parallel MoM code can provide a tool to study the behavior of locally dense medium.

Appendix A

Notations

In this appendix, brief description of the definitions of the polarization coordinate systems, the scattering functions, the Stokes vector used in this thesis will be presented.

Consider an incident plane wave with the electric field vector given by

$$\overline{E}_i = (\hat{v}_i E_{vi} + \hat{h}_i E_{hi}) e^{i\overline{k}_i \cdot \overline{r}} \tag{A.1}$$

impinging upon a scatterer. The far field spherical scattered wave can be expressed as

$$\overline{E}_s = (\hat{v}_s E_{vs} + \hat{h}_s E_{hs}) = \frac{e^{ikr}}{r} \overline{\overline{F}}(\theta_s, \phi_s; \theta_i, \phi_i) \cdot \overline{E}_i \tag{A.2}$$

where $\overline{k}$ is the wave vector of the wave propagating in the direction (θ, ϕ), defined as

$$\overline{k} = k_o(\sin\theta\cos\phi\hat{x} + \sin\theta\sin\phi\hat{y} + \cos\theta\hat{z}) \tag{A.3}$$

and k_o is the free space wavenumber. The horizontal and vertical polarization vectors of the electric field are defined as

$$\begin{aligned} \hat{k}_i &= \sin\theta_i\cos\phi_i\hat{x} + \sin\theta_i\sin\phi_i\hat{y} + \cos\theta_i\hat{z} \\ \hat{h}_i &= \frac{\hat{z} \times \hat{k}_i}{|\hat{z} \times \hat{k}_i|} \end{aligned} \tag{A.4}$$

$$= -\sin\phi_i\hat{x} + \cos\phi_i\hat{y} \tag{A.5}$$

$$\hat{v}_i = \frac{\hat{h}_i \times \hat{k}_i}{|\hat{h}_i \times \hat{k}_i|}$$

$$= \cos\theta_i\cos\phi_i\hat{x} + \cos\theta_i\sin\phi_i\hat{y} - \sin\theta_i\hat{z} \tag{A.6}$$

$$\hat{k}_s = \sin\theta_s\cos\phi_s\hat{x} + \sin\theta_s\sin\phi_s\hat{y} + \cos\theta_s\hat{z} \tag{A.7}$$

$$\hat{h}_s = \frac{\hat{z} \times \hat{k}_s}{|\hat{z} \times \hat{k}_s|}$$

$$= -\sin\phi_s\hat{x} + \cos\phi_s\hat{y} \tag{A.8}$$

$$\hat{v}_s = \frac{\hat{h}_s \times \hat{k}_s}{|\hat{h}_s \times \hat{k}_s|}$$

$$= \cos\theta_s\cos\phi_s\hat{x} + \cos\theta_s\sin\phi_s\hat{y} - \sin\theta_s\hat{z} \tag{A.9}$$

where θ_i, ϕ_i and θ_s, ϕ_s are the polar and azimuthal angles of the incident and the scattered k vectors. The wave vector and the polarization vectors are depicted in Fig. A-1.

The scattering matrix $\overline{\overline{F}}(\theta_s, \phi_s; \theta_i, \phi_i)$ is of the form

$$\overline{\overline{F}}(\theta_s, \phi_s; \theta_i, \phi_i) = \begin{pmatrix} f_{vv}(\theta_s, \phi_s; \theta_i, \phi_i) & f_{vh}(\theta_s, \phi_s; \theta_i, \phi_i) \\ f_{hv}(\theta_s, \phi_s; \theta_i, \phi_i) & f_{hh}(\theta_s, \phi_s; \theta_i, \phi_i) \end{pmatrix} \tag{A.10}$$

where $f_{\alpha\beta}(\theta_s, \phi_s; \theta_i, \phi_i)$ is the scattering function for an incident wave of β-polarization and propagating in the (θ_i, ϕ_i) direction and the corresponding α-polarized scattered wave propagating in the (θ_s, ϕ_s) direction. The Stokes vector associated with the incident wave is given by

$$\overline{I}_i = \begin{pmatrix} I_{vi} \\ I_{hi} \\ U_i \\ V_i \end{pmatrix} = \frac{1}{\eta} \begin{pmatrix} E_{vi}E_{vi}^* \\ E_{hi}E_{hi}^* \\ 2Re(E_{vi}E_{hi}^*) \\ 2Im(E_{vi}E_{hi}^*) \end{pmatrix} \tag{A.11}$$

and the scattered Stokes vector is given by [63],

$$\overline{I}_s = \begin{pmatrix} I_{vs} \\ I_{hs} \\ U_s \\ V_s \end{pmatrix} = \frac{1}{\eta} \lim_{\substack{r\to\infty \\ A\to\infty}} \frac{r^2}{A\cos\theta_s} \begin{pmatrix} < E_{vs}E_{vs}^* > \\ < E_{hs}E_{hs}^* > \\ 2Re < E_{vs}E_{hs}^* > \\ 2Im < E_{vs}E_{hs}^* > \end{pmatrix} \tag{A.12}$$

where η is the characteristic impedance, θ_s is the scattered angle, A is the illuminated area and <> denotes ensemble average. The scattered and the incident Stokes vectors are related by the Muller matrix ($\overline{\overline{M}}$) as follows:

$$\overline{I}_s = \overline{\overline{M}} \cdot \overline{I}_i = \begin{pmatrix} M_{11} & M_{12} & M_{13} & M_{14} \\ M_{21} & M_{22} & M_{23} & M_{24} \\ M_{31} & M_{32} & M_{33} & M_{34} \\ M_{41} & M_{42} & M_{43} & M_{44} \end{pmatrix} \cdot \overline{I}_i \tag{A.13}$$

where

$$M_{11} = \lim_{A\to\infty} \frac{1}{A\cos\theta_s} < |f_{vv}|^2 > \tag{A.14}$$

$$M_{12} = \lim_{A\to\infty} \frac{1}{A\cos\theta_s} < |f_{vh}|^2 > \tag{A.15}$$

$$M_{13} = \lim_{A\to\infty} \frac{1}{A\cos\theta_s} Re < f_{vv}f_{vh}^* > \tag{A.16}$$

$$M_{14} = -\lim_{A\to\infty} \frac{1}{A\cos\theta_s} Im < f_{vv}f_{vh}^* > \tag{A.17}$$

$$M_{21} = \lim_{A\to\infty} \frac{1}{A\cos\theta_s} < |f_{hv}|^2 > \tag{A.18}$$

$$M_{22} = \lim_{A\to\infty} \frac{1}{A\cos\theta_s} < |f_{hh}|^2 > \tag{A.19}$$

$$M_{23} = \lim_{A\to\infty} \frac{1}{A\cos\theta_s} Re < f_{hv}f_{hh}^* > \tag{A.20}$$

$$M_{24} = -\lim_{A\to\infty} \frac{1}{A\cos\theta_s} Im < f_{hv}f_{hh}^* > \tag{A.21}$$

$$M_{31} = \lim_{A\to\infty} \frac{1}{A\cos\theta_s} 2Re < f_{vv}f_{hv}^* > \tag{A.22}$$

$$M_{32} = \lim_{A\to\infty} \frac{1}{A\cos\theta_s} 2Re < f_{vh}f_{hh}^* > \tag{A.23}$$

$$M_{33} = \lim_{A\to\infty} \frac{1}{A\cos\theta_s} Re < f_{vv}f_{hh}^* + f_{vh}f_{hv}^* > \quad (A.24)$$

$$M_{34} = -\lim_{A\to\infty} \frac{1}{A\cos\theta_s} Im < f_{vv}f_{hh}^* - f_{vh}f_{hv}^* > \quad (A.25)$$

$$M_{41} = \lim_{A\to\infty} \frac{1}{A\cos\theta_s} 2Im < f_{vv}f_{hv}^* > \quad (A.26)$$

$$M_{42} = \lim_{A\to\infty} \frac{1}{A\cos\theta_s} 2Im < f_{vh}f_{hh}^* > \quad (A.27)$$

$$M_{43} = \lim_{A\to\infty} \frac{1}{A\cos\theta_s} Im < f_{vv}f_{hh}^* + f_{vh}f_{hv}^* > \quad (A.28)$$

$$M_{44} = \lim_{A\to\infty} \frac{1}{A\cos\theta_s} Re < f_{vv}f_{hh}^* - f_{vh}f_{hv}^* > \quad (A.29)$$

and A is the illuminated area, r is the observation distance and $f_{\alpha\beta}$ is the elements of the scattering matrix.

The backscattering coefficients are given by:

$$\sigma_{vv} = 4\pi\cos\theta M_{11} \quad (A.30)$$

$$\sigma_{vh} = 4\pi\cos\theta M_{12} \quad (A.31)$$

$$\sigma_{hv} = 4\pi\cos\theta M_{21} \quad (A.32)$$

$$\sigma_{hh} = 4\pi\cos\theta M_{22} \quad (A.33)$$

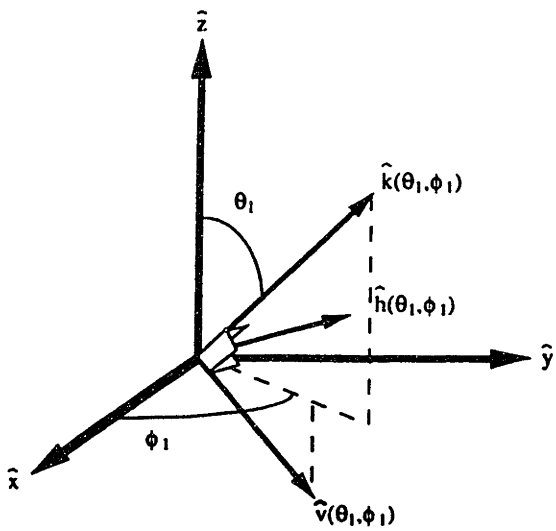

Figure A-1: Illustration of the wave vector and the horizontal and vertical polarization vectors.

Appendix B

Mutual Impedance of Sinusoidal Monopoles

In this appendix, we will give the closed form expansion for the mutual impedance of the sinusoidal monopoles that is required for filling the impedance matrix Z [27].

B.1 Nonplanar-Skew Case

Let the filamentary source monopole be located on the z-axis from z_1 to z_2, and the receiving monopole on the t-axis from t_1 to t_2 as shown in Fig. B-1. The receiving monopole lies in the place $y = d$. The sinusoidal currents on the source and receiving monopoles are

$$I(z)\hat{z} = \frac{I_1 \sinh \gamma(z_2 - z) + I_2 \sinh \gamma(z - z_1)}{\sinh \gamma d_1}\hat{z} \tag{B.1}$$

and

$$\bar{I}(t)\hat{t} = \frac{\bar{I}_1 \sinh \gamma(t_2 - t) + \bar{I}_2 \sinh \gamma(t - t_1)}{\sinh \gamma d_1}\hat{t} \tag{B.2}$$

where (I_1, I_2) and $(\bar{I}_1, \bar{I}_2)$ are the endpoint currents of the two monopoles and have values of either 1 and 0, $d_1 = z_2 - z_1$ and $d_2 = t_2 - t_1$. The mutual impedance of the two monopoles is defined as

$$Z = -\int_{t_1}^{t_2} \bar{I}(t)\hat{t} \cdot \overline{E}(t)dt \tag{B.3}$$

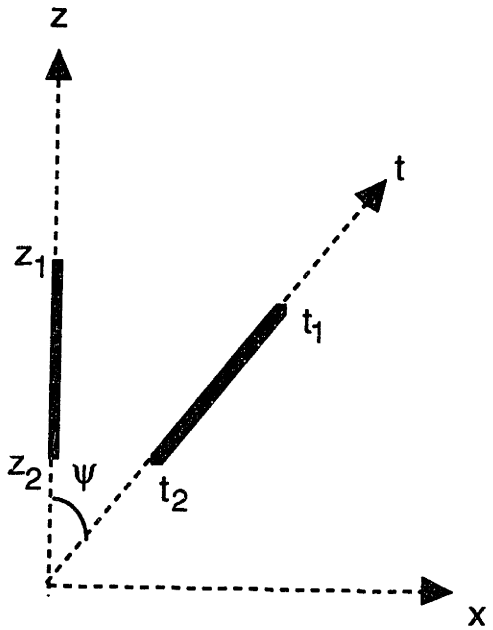

Figure B-1: Nonplanar skew monopoles.

where $\overline{E}(t)$ is the field produced by the source.

$$\overline{E} = \overline{E}_\rho + \overline{E}_z + \overline{E}_i \tag{B.4}$$

$\overline{E}_\rho$ and $\overline{E}_z$ are the field components due to the current in the source filament, $\overline{E}_i$ is the field due to the charges at the endpoints of the source filament. It is given by

$$\overline{E}_i = (-1)^{i+1} I_i \frac{\eta}{4\pi\gamma} \nabla \frac{e^{-\gamma R_i}}{R_i} \qquad i = 1, 2 \tag{B.5}$$

$$\eta = \sqrt{\frac{\mu}{\epsilon}}$$

The derivation can be found in [27, 28, 31]. The final expression for Z_{ij} is given as

$$\begin{aligned} Z_{ij} &= (-1)^{i+j} B[e^{t_n}(e^{z_m} G_{22} - e^{-z_m} G_{12}) - e^{-t_n}(e^{z_m} G_{21} - e^{-z_m} G_{11})] \qquad \text{(B.6)} \\ B &= \frac{\eta}{16\pi \sinh \gamma d_1 \sinh \gamma d_2} \end{aligned}$$

$$m = 2/i, \quad n = 2/j$$

$$i = 1, \quad \text{if } I_1 = 1 \quad I_2 = 0$$

$$i = 2, \quad \text{if } I_2 = 1 \quad I_1 = 0$$
$$j = 1, \quad \text{if } \bar{I}_1 = 1 \quad \bar{I}_2 = 0$$
$$j = 2, \quad \text{if } \bar{I}_2 = 1 \quad \bar{I}_1 = 0$$

The functions G_{kl} are defined as follows:

$$\begin{aligned} G_{kl} &= F(R_2 + mz_2 + nt - i\beta) + F(R_2 + mz_2 + nt + i\beta) \\ &\quad -F(R_1 + mz_1 + nt - i\beta) - F(R_1 + mz_1 + nt + i\beta) \end{aligned} \tag{B.7}$$

where

$$\begin{aligned} m = (-1)^k, \qquad & n = (-1)^l \\ \beta &= md_1 \cot\psi + n\frac{d}{\sin\psi} \\ \cos\psi &= \hat{t} \cdot \hat{z} \\ i &= \sqrt{-1} \end{aligned}$$

and

$$F(\alpha + i\beta) = e^{i\gamma\beta} \int_{\alpha_1 + i\beta}^{\alpha_2 + i\beta} \frac{e^{-\gamma w}}{w} dw \tag{B.8}$$

α is a function of t, $\alpha_1 = \alpha(t_1), \alpha_2 = \alpha(t_2)$.

B.2 Parallel Monopole Mutual Impedance

The configuration is shown in Fig. B-2. The mutual impedance is special case of the previous subsection.

$$\begin{aligned} Z_{ij} &= -(-1)^{i+j} \frac{\eta}{8\pi \sinh\gamma d_1 \sinh\gamma d_2} \{e^{-\gamma(t_n - z_m)}[F(R_2 - t + z_2) - F(R_1 - t + z_1)] \\ &\quad + e^{\gamma(t_n - z_m)}[F(R_2 + t - z_2) - F(R_1 + t - z_1)]\} \end{aligned} \tag{B.9}$$

where

$$R_i = \sqrt{d^2 + (t - z_i)^2}$$

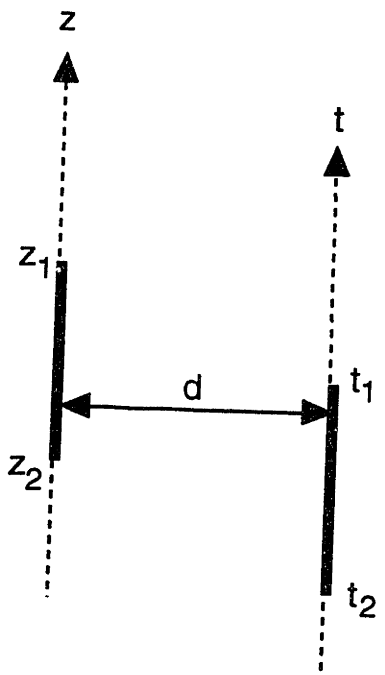

Figure B-2: Parallel monopoles.

References

[1] L. Tsang, J. A. Kong, and R. T. Shin. *Theory of Microwave Remote Sensing.* Wiley-Interscience, New York, 1985.

[2] S. Brown, A. E. Lugo, and B. Liegel, editors. *The Role of Tropical Forests on the World Carbon Cycle.* NTIS, Springfield, 1980.

[3] T. T. Wilheit, A. T. C. Chang, M. S. V. Rao, E. B. Rodgers, and J. S. Theon. A satellite technique for quantitatively mapping rainfall rates over the ocean. *Journal of Applied Meteorology*, 16(5), 1977.

[4] F. T. Ulaby, R. K. Moore, and A. K. Fung. *Microwave Remote Sensing: Active and Passive.* Addison-Wesley, Reading, 1981.

[5] F. MacIntyre. *Ocean Science.* W. H. Freeman, San Francisco, 1977.

[6] T. Le Toan, A. Beaudoin, J. Riom, and D. Guyon. Relating forest biomass to SAR data. *IEEE Transactions on Geoscience and Remote Sensing*, 30(2), 1992.

[7] J. R. Wang. An overview of the measurements of soil moisture and modeling of moisture flux in FIFE. *Journal of Geophysical Research*, 97(D17), 1992.

[8] F. T. Ulaby, A. Aflam, and M. C. Dobson. Effects of vegetation cover on radar sensitivity to soil moisture. *IEEE Transactions on Geoscience and Remote Sensing*, 20(4), 1982.

[9] T. T. Wilheit. A model for microwave emissisivity of the ocean's surface as a function of wind speed. *IEEE Transactions on Geoscience Electronics*, 17(4), 1978.

[10] F. J. Wentz. Measurement of oceanic wind vector using satellite microwave radiometers. *IEEE Transactions on Geoscience and Remote Sensing*, 30(5), 1992.

[11] A. P. Cracknell, editor. *Remote Sensing in Meteorology, Oceanography and Hydrology.* Ellis Horwood, Chichester, 1981.

[12] D. K. Hall and J. Martinec. *Remote Sensing of Ice and Snow.* Chapman and Hall, New York, 1985.

[13] J. J. Van Zyl and H. A. Zebker. Imaging radar polarimetry. *Progress in Electromagnetics Research*, volume 3, chapter 5. Elsevier, New York, 1990.

[14] D. L. Evans and J. J. Van Zyl. Polarmetric imaging radar: Analysis tools and applications. *Progress in Electromagnetics Research*, volume 3, chapter 7. Elsevier, New York, 1990.

[15] L. Tsang and J. A. Kong. Scattering of electromagnetic waves from random media with strong permittivity fluctuations. *Radio Science*, 16(3), 1981.

[16] L. Tsang and J. A. Kong. Scattering of electromagnetics waves from a half space of densely distributed dielectric scatterers. *Radio Science*, 18(6), 1983.

[17] L. Tsang and J. A. Kong. Effective propagation constant for coherent electromagnetic waves in media embedded with dielectric scatterers. *Journal of Applied Physics*, 53(11), 1982.

[18] R. H. Lang and J. S. Sidhu. Electromagnetic backscattering from a layer of vegetation: A discrete approach. *IEEE Transactions on Geoscience and Remote Sensing*, 21(1), January 1983.

[19] M.A. Karam and A. K. Fung. Electromagnetic scattering from a layer of finite length randomly oriented, dielectric, circular cylinders over a rough interface with application to vegetation. *International Journal of Remote Sensing*, 9(6), 1988.

[20] M. A. Karam, A. K. Fung, and Y. M. M. Antar. Electromagnetic wave scattering from some vegetation samples. *IEEE Transactions on Geoscience and Remote Sensing*, 26(6), 1988.

[21] S. L. Durden, J. J. van Zyl, and H. A. Zebker. Modeling and observation of the radar polarization signature of forest areas. *IEEE Transactions on Geoscience and Remote Sensing*, 27(3), 1989.

[22] R. H. Lang and H. A. Saleh. Microwave inversion of leaf area and inclination angle distributions from backscattered data. *IEEE Transactions on Geoscience and Remote Sensing*, 23(5), 1985.

[23] D. M. Le Vine, A. Schneider, R. H. Lang, and H. G. Carter. Scattering from thin dielectric disks. *IEEE Transactions on Antenna Propagation*, 33(12), 1985.

[24] S. H. Yueh, J. A. Kong, J. K. Jao, R. T. Shin, and T. LeToan. Branching model for vegetation. *IEEE Transactions on Geoscience and Remote Sensing*, 30(2), 1992.

[25] J. H. Richmond. Radiation and scattering by thin wire structures in complex frequency domain. Technical Report CR-2396, NASA, 1974.

[26] J. H. Richmond. Computer program for thin wire structures in a homogeneous conducting medium. Technical Report CR-2399, NASA, 1974.

[27] C. W. Chuang, J. H. Richmond, N. Wang, and P. H. Pathak. New expressions for mutual impedance of nonplanar- skew sinusoidal monopoles. *IEEE Transactions on Antennas and Propagation*, 38(2), 1990.

[28] J. H. Richmond and N. H. Geary. Mutual impedance of nonplanar-skew dipoles. *IEEE Transactions on Antennas and Propagation*, 23(3), 1975.

[29] R. F. Harrington. *Field Computation by Moment Methods.* The Macmillian Company, New York, 1968.

[30] J. J. H. Wang. *Generalized Moment Methods in Electromagnetics– Formulation and Computer Solution in Integral Equations.* John Wiley & Sons, New York, 1991.

[31] J. H. Richmond and N. H. Geary. Mutual impedance between coplanar-skew dipoles. *IEEE Transactions on Antennas and Propagation*, 18(3), 1970.

[32] B. B. Mandelbrot. *Fractal: Form, Chance and Dimension.* W. H. Freeman and Company, San Francisco, 1977.

[33] P. E. Oppenheimer. Real time design and animation of fractal plants and trees. *Computer Graphics*, 20(4), 1986.

[34] F. T. Ulaby and M. C. Dobson. *Handbook of Radar Scattering Statistics for Terrain.* Artech House, Inc., Norwood, 1989.

[35] N. Morita. Surface integral representations for electromagnetic scattering from dielectric cylinders. *IEEE Transactions on Antennas and Propagation*, 26(2), 1978.

[36] S. M. Rao, D. R. Wilton, and A. W. Glisson. Electromagnetic scattering by surfaces of arbitrary shape. *IEEE Transactions on Antennas and Propagation*, 30(3), 1982.

[37] D. E. Livesay and K. M. Chen. Electromagnetic fields induced inside arbitrarily shaped biological bodies. *IEEE Transactions on Microwave Theory and Techniques*, 22(12), 1974.

[38] K. Tanaka and M. Kojima. Volume integral equations for analysis of dielectric branching waveguide. *IEEE Transactions on Microwave Theory and Techniques*, 36(8), 1988.

[39] K. K. Mei. Unimoment method of solving antenna and scattering problems. *IEEE Transactions on Antennas and Propagation*, 22(6), 1974.

[40] S. K. Chang and K. K. Mei. Application of the unimoment method to electromagnetic scattering of dielectric cylinders. *IEEE Transactions on Antennas and Propagation*, 24(1), 1976.

[41] B. H. McDonald and A. Wexler. Finite-element solution of unbounded field problems. *IEEE Transactions on Microwave Theory and Techniques*, 20(12), 1972.

[42] J. M. Jin and V. V. Liepa. Application of hybrid finite element method to electromagnetic scattering from coated cylinders. *IEEE Transactions on Antennas and Propagation*, 36(1), 1988.

[43] W. Chew. *Electromagnetic Waves and Fields in Inhomogeneous Media.* Van Nostrand Reinhold, New York, 1990.

[44] A. D. Yaghjian. Electric dyadic Green's functions in the source region. *Proceeding of IEEE*, 68(2), 1980.

[45] A. Q. Howard and D. B. Seidel. Singularity extraction in kernel functions in a closed region problem. *Radio Science*, 13(3), 1978.

[46] S. Lee, J. Boersma, C. Law, and G. A. Deschamps. Singularity in Green's function and its numerical evaluation. *IEEE Transaction on Antennas and Propagation*, 28(3), 1980.

[47] O. D. Kellogg. *Foundations of Potential Theory.* Dover, New York, 1953.

[48] W. H. Press, B. P. Flannery, S. A. Teukolsky, and W. T. Vetterling. *Numerical Recipes.* Cambridge University Press, New York, 2nd edition, 1992.

[49] B. T. Draine. The discrete-dipole approximation and its application to interstellar graphite grain. *The Astrophysical Journal*, 333, 1988.

[50] C. Su. Calculation of electromagnetic scattering from a dielectric cylinder using the conjugate gradient method and FFT. *IEEE Transactions on Antennas and Propagation*, 35(12), 1987.

[51] T. K. Wu and L. L. Tsai. Scattering from arbitrarily-shaped lossy dielectric bodies of revolution. *Radio Science*, 12(5), 1977.

[52] E. Mougin, A. Lopes, and T. LeToan. Microwave propagation at X band in cylindrical-shaped forest components: attenuation observations. *IEEE Transactions on Geoscience and Remote Sensing*, 28(1), 1990.

[53] R. H. Lang. Electromagnetic backscattering from a sparse distribution of lossy dielectric scatterers. *Radio Science*, 16(1), 1981.

[54] A. Ishimaru and C. W. Yeh. Matrix representation of the vector radiative transfer equations for randomly distributed nonspherical particles. *Journal of the Optical Society of America A*, 1(4), 1984.

[55] E. Mougin and A. Lopes. Microwave propagation at X band in cylindrical-shaped forest components: interpretation of attenuation observations. *IEEE Transactions on Geoscience and Remote Sensing*, 28(3), 1990.

[56] F. T. Ulaby and M. A. El Rayes. Microwave dielectric spectrum of vegetation. Part II: Dual-dispersion model. *IEEE Transactions on Geoscience and Remote Sensing*, 25(5), 1987.

[57] K. Sarabandi, P. F. Polatin, and F. T. Ulaby. Monte Carlo simulation of scattering from a layer of vertical cylinders. *IEEE Transactions on Antenna Propagation*, 41(2), 1993.

[58] L. Tsang and J. A. Kong. Wave theory for microwave remote sensing of a half-space random medium with three-dimensional variations. *Radio Science*, 14(3), 1979.

[59] L. Tsang, J. A. Kong, and R. T. Shin. Radiative transfer theory for active remote sensing of a layer of nonspherical particles. *Radio Science*, 19(2), 1984.

[60] L. Tsang and J. A. Kong. Scattering of electromagnetic waves from a half space of densely distributed dielectric scatterers. *Radio Science*, 18(6), 1983.

[61] L. L. Foldy. The multiple scattering of waves. *Physical Review*, 67, 1945.

[62] L. Tsang. Dense media radiative transfer theory for dense discrete random media with spherical particles of multiple sizes and permittivities. *Progress in Electromagnetics Research*, volume 6, chapter 5. Elsevier, New York, 1992.

[63] H. C. Han. *Electromagnetic Wave Phenomena in Inhomogeneous and Anisotropic Media.* PhD thesis, Massachusetts Institute of Technology, EECS, 1992.

[64] J. A. Kong. *Electromagnetic wave theory.* Wiley & Sons Inc., New York, 1990.

[65] R. Freedman and J. P. Vogiatzis. Theory of induced polarization logging in a borehole. *Geophysics*, 51(9), 1986.

[66] L. A. Hageman and D. M. Young. *Applied Iterative Methods.* Academic Press, New York, 1981.

[67] M. R. Hestenes and E. Stiefel. Methods of conjugate gradients for solving linear systems. *Journal of the National Bureau of Standards*, 49(6), 1952.

[68] R. Freund. On conjugate gradient type methods and polynomial preconditioners for a class of complex non-Hermitian matrices. *Numerische Mathematik*, 57, 1990.

[69] R. Freund. Conjugate gradient-type methods for linear systems with complex symmetric coefficient matrices. *SIAM Journal of Scientific and Statistical Computing.*, 13(1), 1992.

[70] Y. Saad. Krylov subspace methods for solving large unsymmetric linear systems. *Mathematical Computation*, 37(155), 1981.

[71] R. Fletcher. Conjugate gradient methods for indefinite systems. *Lecture Notes in Mathematics 506.* Springer-Verlag, New York, 1976.

[72] P. Sonneveld. A fast lanczos-type solver for non-symmetric linear systems. *SIAM Journal on Scientific and Statistical Computing*, 10(1), 1989.

[73] G. N. Minerbo and P. E. Saylor. Iterative solution of maxwell's equations in three dimensions. *Proceedings of the Schlumberger Software Conference 90*, 1990.

[74] P. Joly and R. Eymard. Preconditioned biconjugate gradient methods for numerical reservoir simulation. *Journal of Computational Physics*, 91, 1990.

[75] A. Geist, A. Beguelin, J. Dongarra, W. Jiang, R. Manchek, and V. Sunderam. Parallel virtual machine user's guide and reference manual. Technical Report ORNL/TM-12187, Oak Ridge National Laboratory, 1993.

[76] P. Concus, G. H. Golub, and G. Meurant. Block preconditioning for the conjugate gradient method. *SIAM Journal on Scientific and Statistical Computing*, 6(1), 1985.

[77] Y. Notay. Conditioning analysis of modified block incomplete factorizations. *Linear Algebra and its Applications*, 154, 1991.

[78] M. Magolu. Modified block-approximate factorization strategies. *Numerische Mathematik*, 61(1), 1992.

[79] M. Magolu and Y. Notay. On the conditioning analysis of block approximate factorization. *Linear Algebra and its Applications*, 154, 1991.

[80] M. Tismenetsky. A note on block preconditioner. *Applied Mathematics Letters*, 4(2), 1991.

[81] M. K. Seager and A. Greenbaum. Sparse linear algebra package. Available from the National Energy Software Center, Argonne National Laboratory, Argonne, Illinois, 1988.

[82] E. Anderson, Z. Bai, C. Bischof, J. Demmel, J. Dongarra, J. Du Croz, A. Greenbaum, S. Hammarling, A. McKenney, S. Ostrouchov, and D. Sorensen. *LAPACK Users' Guide*. SIAM, Philadelphia, 1992.

[83] H. A. Van der Vorst. BI-CGSTAB: a fast and smoothly converging variant of BI-CG for the solution of nonsymmetric linear systems. *SIAM Journal on Scientific and Statistical Computing*, 13(2), 1992.

[84] C. H. Tong. A comparative study of preconditioned lanczos methods for nonsymmetric linear systems. Technical Report SAND91-8240B, Sandia National Laboratories, September 1992.

Biographical Note

Wai Chung Au was born in Hong Kong on March 10, 1966. He received the B.A. and M.A. degrees from Trinity College, Cambridge University, UK, in 1988 and 1992, respectively. He received the M.S. degree in Aeronautics and Astronautics from Massachusetts Institute of Technology, Cambridge, MA, in 1991. In the years as a graduate student, he served as a research assistant.

His research interest is in the area of microwave remote sensing and application of parallel computing to electromagnetic problems.

He is a felllow of Cambridge Commonwealth Society and a member of Sigma Xi.